LUX-ZEPLIN Dark Matter Searches: Development of Optical and Source Based Calibration Systems

Thesis submitted in accordance with the requirements of
the University of Liverpool for the degree of Doctor in Philosophy
by

Billy Boxer

March 2021

Department of Physics
Oliver Lodge Laboratory
University of Liverpool

Abstract

Resounding evidence from astrophysical and cosmological observations strongly implies that the bulk of the Universe's mass is comprised of a non-luminous and near collisionless substance, Dark Matter (DM). Searches conducted to directly observe the scattering of the lead DM candidate, the Weakly Interacting Massive Particle (WIMP), with nuclei are reaching unprecedented levels of sensitivity.

The LUX-ZEPLIN (LZ) experiment will utilise a multi-tonne dual phase xenon Time Projection Chamber (TPC) to push the WIMP parameter space to regions where the elastic scattering of neutrinos arises as an irreducible background. To achieve this level of sensitivity, LZ has instrumented an outer layer of the liquid xenon and the water tank, that houses the detection volumes, to veto gamma and neutron single-scatter in the TPC, which could otherwise mimic the response of a WIMP interacting with a xenon nucleus.

The accurate calibration of the energy and timing responses for all three instrumented detection volumes (TPC, liquid xenon skin, and outer detector) is imperative to the overall sensitivity goal of LZ. To achieve this, LZ has developed a calibrated source deployment system that allows for the accurate and precise positioning of gamma and neutron sources between the detection volumes. Furthering this, the TPC is surrounded by ten acrylic tanks containing a total of 17 tonnes of gadolinium-loaded liquid scintillator, which themselves sit in the outer detector, which is filled with 228000 litres of water. 120 8-inch photomultiplier tubes are positioned on the walls of the outer detector with their windows directed toward the TPC. In order to calibrate these photomultiplier tubes, an optical calibration system has been designed.

Also described in this thesis are the results of an Effective Field Theory (EFT) WIMP search analysis using 3.14×10^4 kg·day exposure collected by the LUX collaboration between 2014 and 2016. This analysis builds on the previously produced limits from LUX by extending the region of considered nuclear recoil energies to ∼180 keV. By performing a binned Profile Likelihood, the 90% confidence exclusion limits on the non-relativistic WIMP couplings to the nucleon operators derived from a model-independent EFT were determined. Exclusion limits are set on the inelastic EFT WIMP-nucleon recoils in the isoscalar basis and were either competitive with published results or world-leading in some phase-space regions for certain operators at specific values of the mass splitting.

Declaration

This thesis contains the work I conducted as a member of the LUX-ZEPLIN collaboration on the optical calibration system under the supervision of Dr Sergey Burdin at the University of Liverpool, and the calibrated source deployment system under the supervision of Dr Maurits Van der Grinten at UKRI RAL.

Figure 2.2 and Figure 2.1 are from a paper produced in collaboration with Robert Poole-McKenzie, Dr Andreea S. Font, Dr Ian G. McCarthy, Sam G. Stafford, and Shaun T. Brown from the Astrophysics Research Institute at Liverpool John Moores University, and Dr Sergey Burdin from the Oliver Lodge Laboratory at the University of Liverpool. I developed the code to produce the differential recoil rates and the resultant spin-independent cross-section using detector parameters from published information from direct detection experiments.

My work on the LUX-ZEPLIN calibrated source deployment system is given in §4.1. The system was developed and built by members of the LUX-ZEPLIN collaboration at RAL: Dr Maurits Van der Grinten, Sergey Balashov and Andrei Khazov. I made multiple trips through my PhD to RAL. I worked extensively with Andrei to perform quality assurance tests on the system during different stages of its development. Further to this, I developed the protocol and code to allow for the calibrated source deployment system's operation by Ignition, producing a graphical user interface to facilitate the execution of a calibration deployment. Unfortunately, due to the travel restrictions and delays due to Covid-19, I was not able to obtain the commissioning data myself.

My work on the LUX-ZEPLIN optical calibration system included the initial development of the main structure for the self-monitoring systems and the optical calibration system's overall design. I was directly involved with the test performed at the early stages of the research and development of the system's electronic components, designed by Ashley Greenall and Sam Powel from the University of Liverpool. I produced multiple scripts and quality assurance tests during the system's development. I created several bespoke fibre optic components: 3D printed housings, 3D printed couplers and the 3-way splitter.

I manufactured all the pulser and photodiode boards and developed the control software for the photodiode board.

This thesis's final chapter contains the work I performed under Dr Sergey Burdin's supervision within the LUX collaboration regarding the WS2014-16 high-NR effective field theory analysis. My work mainly focused on developing the signal models required for both the inelastic and elastic analyses. I wrote the top-level notebook to produce the recoil spectra for the nucleon level operators from a Mathematica package developed by nuclear theorists. From these recoil models, I generated the signal model energy and spatial probability distribution functions and the relevant energy cuts. Additionally, I was involved in reprocessing the ^{83m}Kr models. Finally, I was the sole analyser of the inelastic signal models. I ensured the coding framework would be compatible and ran the analysis to produce the nucleon operator inelastic limits.

Acknowledgements

I have come to know the physics department at the Univerity of Liverpool quite well. It is not only where I conducted these postgraduate studies but also where I received my MPhys. Because of this, there are far too many people to thank specifically, for those who are not mentioned explicitly; thank you! I would like to thank Ashley G. and Sam P. for developing the OCS electronics and always being ready to help address any questions or concerns I had during their testing. Additionally, I would like to thank Peter C., and Paul S. from the AMW for the production of the 3D printed components I designed for the OCS, those currently at or retired from the Detector Fabrication Facility, and Tony S. for always providing a solution to a problem whether it was wholly inane or genuinely perplexing. Angie R., Julie C. and Marj R., thank you so much. Without people like you, I would never get any paperwork filed correctly or even know that I was meant to be doing so. I would also like to acknowledge the School of Physical Sciences Director of Postgraduate Research, Tim V., for your help to champion the student's side through the fall out of the pandemic; thank you.

Additionally I would like to thank Will T. for the countless times you have replied to my coding questions, for going above and beyond to help when personal issues arose, and stepping in for my best man at my wedding.

My work involving the CSD required me to make several trips to RAL. I thoroughly enjoyed my time working there alongside Sergey B. and Andrei K. I extend my thanks for always accommodating me in the labs, for the range of topics that would be discussed over coffee, and specifically to Andrei for kindly offering to give me lifts to and from the lab.

Without the tireless and seemingly endless efforts of Greg R. and Shaun A., the LUX WS2014-16 high-NR analysis would never have got to the point of producing meaningful results, let alone ones that were publishable. Thank you both for pushing through even on the days when things seemed their at bleakest.

Mum, thank you for helping me through my education at every step and always being

there to help me weigh up the consequences of my decisions in life.

Simon, one of my closest friends, thank you for giving me the support I needed to keep my own mental health from deteriorating; I am sure I will be returning the favour over the next year as you approach the deadline of your studies. Also, I couldn't figure out any other way, so yeah, platypus.

To my darling wife Leigh, I truly thank you, and I say that with the deepest connotation I have ever had with these words. We started this journey together over ten years ago. Shortly after it started we moved to different Universities. The three years without you were incredibly difficult but we got them. I had the honour and privilege to marry you during my postgraduate studies, by far the most incredible day of my life. Thank you for supporting me through this and being there to keep me going when I've been at my worst. I love you, eternally.

Unfortunately, during my PhD, I lost a very dear friend of mine to a tragic accident. He was one of the three fundamental pillars within my friendship group from the age of 13. A bright and cheerful soul with a passion for furthering himself. I have countless stories of the antics we got caught up in during our formative years, and each and every one is filled with his beaming smile. I am, in part, who I am today because of the time I spent with him. Mental health problems within young men are a rising issue that we still are failing to address. The stigma around the subject and attitudes of some towards it continue to deter open conversation. This is by no means an attempt to heal the wounds caused but to show a deep appreciation towards a person I hold dear to my heart.

This thesis is dedicated
in the honour and memory of
James William Faragher.

Contents

List of Figures

List of Tables

Acronyms

ΛCDM Lambda Cold Dark Matter

ADC Analog-to-Digital Converter

ALP Axion Like Particle

BBN Big Bang Nucleosynthesis

BSM Beyond the Standard Model

CEνNS Coherent Elastic Neutrino-Nucleus Scattering

CI Confidence Interval

CMB Cosmic Microwave Background

CP Charge Parity

CSD Calibrated Source Deployment

DD Deuterium-Deuterium

DM Dark Matter

EFT Effective Field Theory

ER Electron Recoil

FPGA Field Programmable Gate Array

FSS Fibre Support Structure

GdLS Gadolinium-loaded Liquid Scintillator

GXe Gaseous Xenon

ICV Inner Cryostat Vessel

LAr Liquid Argon

LLAMA LUX Legacy Analysis Monte Carlo Application

LUX Large Underground Xenon

LXe Liquid Xenon

LZ LUX-ZEPLIN

MACHO Massive Compact Halo Object

MOND Modification Of Newtonian Dynamics

NEST Noble Element Simulation Technique

NR Nuclear Recoil

OCC Optical Calibration Card

OCS Optical Calibration System

OCV Outer Cryostat Vessel

OD Outer Detector

PBH Primordial Black Hole

PDF Probability Density Function

PLR Profile Likelihood Ratio

PMT Photomultiplier Tube

POI Parameter Of Interest

PQ Peccei-Quinn

PTFE Polytetrafluoroethylene

QA Quality Assurance

RFR Reverse Field Region

ROI Region Of Interest

S1 Prompt Scintillation Signal

S2 Delayed Proportional Scintillation Signal

SC Slow Control

SD Spin-Dependent

SHM Standard Halo Model

SI Spin-Independent

SM Standard Matter

SURF Sanford Underground Research Facility

TPC Time Projection Chamber

VUV Vacuum UltraViolet

WIMP Weakly Interacting Massive Particle

WS WIMP Search

Introduction

Since the founding of astronomical photography in the mid-19th century, discrepancies have arisen between observations and the general expectation of the Universe we live in. Initial attempts were made to explain some of these phenomena via the introduction of massive non-luminous bodies, or by a mechanism which absorbs the light on its path[1]. The first dynamic evidence for these bodies' involved modelling the Milky Way as a gas acting under gravity. Using this model an estimation of the system's size and the velocity dispersion of the stars can be calculated. It was speculated that up to 90% of the bodies within the galaxy must either be dark or too dim to detect[2] [1]. An upper limit of density was set, with a high enough value that the implications conflicted with observed star velocities. Inevitably this led to contention, and the coining of the phrase 'Dark Matter' (DM), about this new form of matter[3] [2]. Some argued that the discrepancies fell within an order of magnitude and that the quantity of dark matter would either equate to or be less than that of visible matter[4] [3]. By using a quantitative model that described the shape and size of the Milky Way as a flat distribution of stars rotating about a Galactic pole[5] [4], the relationship between the motion of stars and their velocity dispersion was established, leading to the first estimates on the local DM density of 6.3×10^{-24} g/cm^3.

Our current understanding is that DM may have been an essential influence on large-scale structure formation in the Universe. The Lambda Cold Dark Matter (ΛCDM) model relies on large quantities of non-baryonic non-relativistic DM becoming gravitationally bound in the early Universe. This then aids in the seeding process required for ordinary matter to form the astronomical bodies seen today. Remarkably, this model requires the

[1] Arthur Ranyard (1894) concluded that dark structures were the likely cause of the dark region observed in the sky's Opiuchi neighbourhood.

[2] Lord Kelvin (1904) "Many of our stars, perhaps a great majority of them, may be dark bodies".

[3] Henri Poincare (1906) when examining Lord Kelvin's work used the term "matière obscure".

[4] Ernst Opik (1915) concluded it was unlikely that there was a significant mass contribution from unseen matter.

[5] Kapteyn (1932) developed the model and his student, Oort, produced an independent and consistent estimate.

mass contributions to be five times greater from DM than baryons. It is highly likely that the DM contribution is from one or more particles, which is not explainable by the Standard Model. A threefold approach is currently being used: (1) the LHC is searching for DM produced in particle colliders, (2) ground and orbital based telescopes to detect the DM self-annihilation signature, (3) direct searches for the scattering of DM with nuclei, which tend to favour models reliant on a weak-mediator. The last of these, the direct detection of DM, has many challenges, with the majority associated with the expected exceptionally low interaction rate. Observing such an event with certainty requires a sensitive readout system in an ultra-low background environment. The LUX-ZEPLIN (LZ) experiment is one of the few cutting edge experiments seeking to detect DM using a Liquid Xenon (LXe) TPC. By implementing rigorous cleanliness and radiation screening campaigns, LZ aims to reduce the expected rate of the background event dramatically; especially those that induce a nuclear recoil response. LZ will also use a layered detector structure to allow for the vetoing of coincidence signals found between the separate sections to further aid in reducing non DM like signals.

This thesis starts with the critical cosmological and astronomical evidence for DM which motivate the extensive search over many decades. A description of the leading particle candidates, Weakly Interacting Massive Particles (WIMPs) and axions, is given, followed by a summary of collider production results, indirect detection and direct detection experiments in the search for DM.

More relevant to direct detection is the local density of DM. The most recent estimations of which will be shown in Chapter 2 along with the expected velocities and velocity distribution of DM bound to the Milky Way. Additionally, the formulation behind the standard scattering interactions will be shown. The remainder of this chapter will describe the non-relativistic Effective Field Theory (EFT) of DM. This will be used in the closing chapter to re-examine parameter space previously ruled out by simpler interaction models.

Chapter 3 will outline the unique properties of LXe and why it has become the target of choice for direct DM searches; especially those that use Time Projection Chambers (TPCs). This chapter will then describe the main detection volumes of the LZ experiment, the expected backgrounds during operation, the intended calibrations and the proposed WIMP Search (WS) strategy.

Two systems vital to the calibration of the PhotoMultiplier Tubes (PMTs) used within LZ, the Calibrated Source Deployment (CSD) system and the Optical Calibration System (OCS) will be described along with some of the critical tests performed during the

development of these systems.

The closing chapter of this thesis will report the analysis of the inelastic WIMP-nucleon non-relativistic EFT using the WIMP Search (WS) data collected between 2014 and 2016 by the Large Underground Xenon (LUX) experiment. This chapter will start with a description of the LUX detector before giving an overview of the general WS2014-16 EFT analysis (data selection, backgrounds and signal models) and the resultant limits on the isoscalar coupling to the inelastic EFT operators.

Chapter 1

Dark Matter Physics/Puzzle/Problem

Consistent evidence [5, 6, 7] continues to indicate non-baryonic non-luminous matter comprising most of the matter abundance in the Universe. Many solutions exist to either account for or reconcile this Dark Matter (DM). There is a strong case that this matter is comprised of a new form of particle outside the Standard Model. As of yet, no such particle has been discovered. However, its properties are highly constrained by indirect searches and cosmological requirements [8, 9, 10].

Key features that outline the current understanding of the properties of DM are given in this opening chapter; starting with a summary of the most substantial astronomical and cosmological evidence. A description of the favoured particle candidates, and some not so favoured, will be given. Finally, an overview of the detection methods of the prime particle candidate, Weakly Interacting Massive Particles (WIMPs), concludes the chapter.

1.1 Astronomical and Cosmological Motivation

By the early 20th Century it had become apparent that estimates of the masses of astronomical bodies, such as galaxies and galaxy clusters, differed depending on the method used to calculate them. Estimates of the mass obtained through studying the rotational velocity of entities within the body greatly exceeded the mass determined through the body's luminosity[1] [12]. Development of this comparative observation style led to robust measurements of the rotational velocity of stars in different galaxies, highlighting the

[1] Zwicky (1933) observed that the mass of the Coma Cluster was not in agreement with the mass required to generate velocities of bodies in its outer edge.

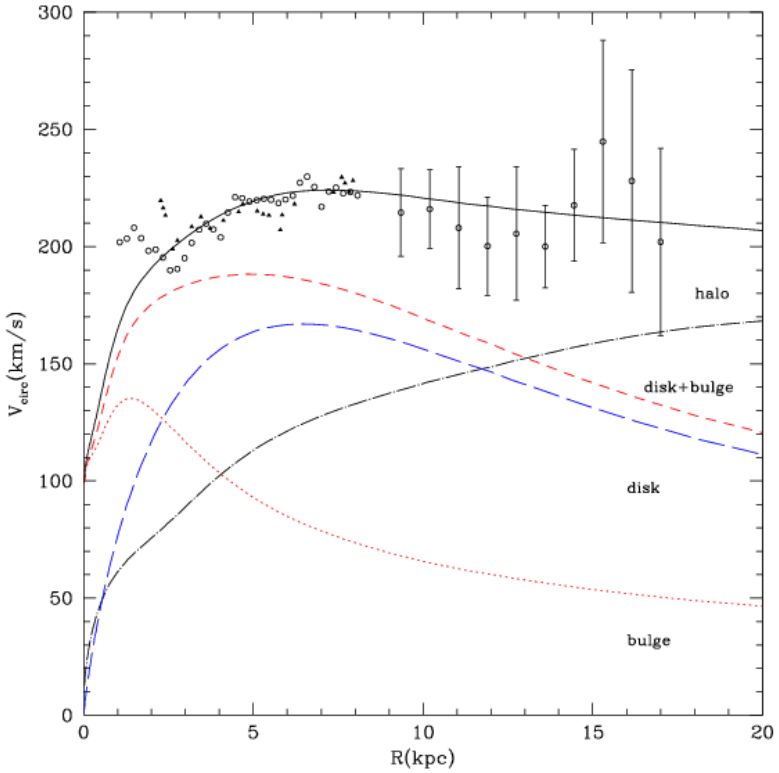

Figure 1.1: Rotational curve of the Milky Way determined through the variations in circular velocity for bound objects as a function of radial distance from galactic nucleus. The model shown includes angular momentum exchange, and shows the contribution from different components. The forms of these distributions indicate that DM contribution dominates at greater radii [11].

extent of these discrepancies[2]. The velocity distribution was expected to increase with radius from the galactic nucleus, then decline as $1/\sqrt{radius}$. Nevertheless, the observed data disagreed with the expected relationship between radial distance with the expected convolution from the known distributions. The velocity tended to increase linearly and then flatten out, with the effect extending beyond the visible radius [13, 14]. As shown in Figure 1.1, this flatness could be accounted for by modifying the relative masses of the galactic bulge and galactic disk, and by adding a new component with a different spatial distribution [5]. Coincidentally, this distribution satisfied the same relation as expected from a self-gravitational gas of non-interacting particles; supporting the hypothesis of DM's presence. This new component, the halo, can extend to ten times the galactic disc's size and contains 80% of its total mass.

[2]Vera Rubin and Ford W. Kent (1970) began studying the rotational velocity of stars in the Andromeda galaxy.

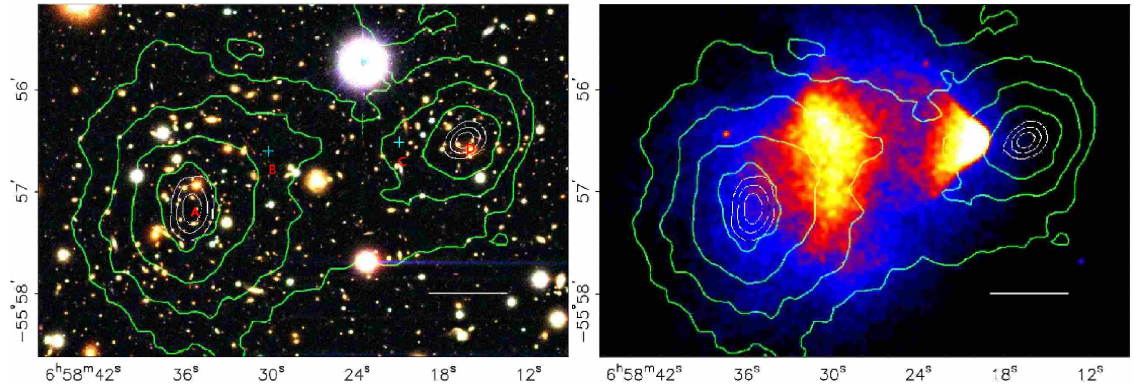

Figure 1.2: **Left** The Magellan telescope image showing the merging cluster 1E 0657·558. **Right** Chandra X-ray image of the same cluster. For both panels, given in green are the outer contours of the weak lensing which start at 0.16 kpc and increase inwards in steps of 0.07 kpc [6].

General relativity states that massive objects warp the space-time around them. Light, which propagates along null-geodesics, when travelling near such an object will curve in accordance with the distortion [15]. Any particle that acts gravitationally can induce lensing[3]. Bound systems of DM in the foreground of a light source, such as a galaxy, should produce a noticeable lensing effect. Therefore complementary measurements of the mass distribution via a lensing effect and one based on luminosity, should resolve any spatial separation between the bulk of the mass in the body and its luminous content.

Cluster 1E0657-558, i.e. the Bullet Cluster, was a prime candidate for such measurements. Formed by the merger of two smaller clusters, it is theorised that when the gases within the clusters passed through each other, they would interact hindering travel; while any dark component would only experience gravitational influence. Figure 1.2 shows the luminous component, imaged by the Chandra X-ray satellite, of the Bullet Cluster being displaced from the majority of the mass, obtained from Hubble weak lensing measurements [16]. This observation was clear evidence of the existence of a new form of collisionless non-baryonic matter, and empirical proof of the existence of DM [6].

The most compelling cosmological evidence for DM stems from serendipitous roots. Initially perceived as noise in a radio-astronomy experiment[4], the Cosmic Microwave Back-

[3]Three categories: strong can produce multiple images of the same object, or create arcs; weak has no noticeable distortion but statistically discernible; and microlensing occurs when a much smaller object produces the distortion.

[4]Arno Penzias and Robert Wilson are rumoured to have believed the signal originally came from pigeons nesting on the antenna.

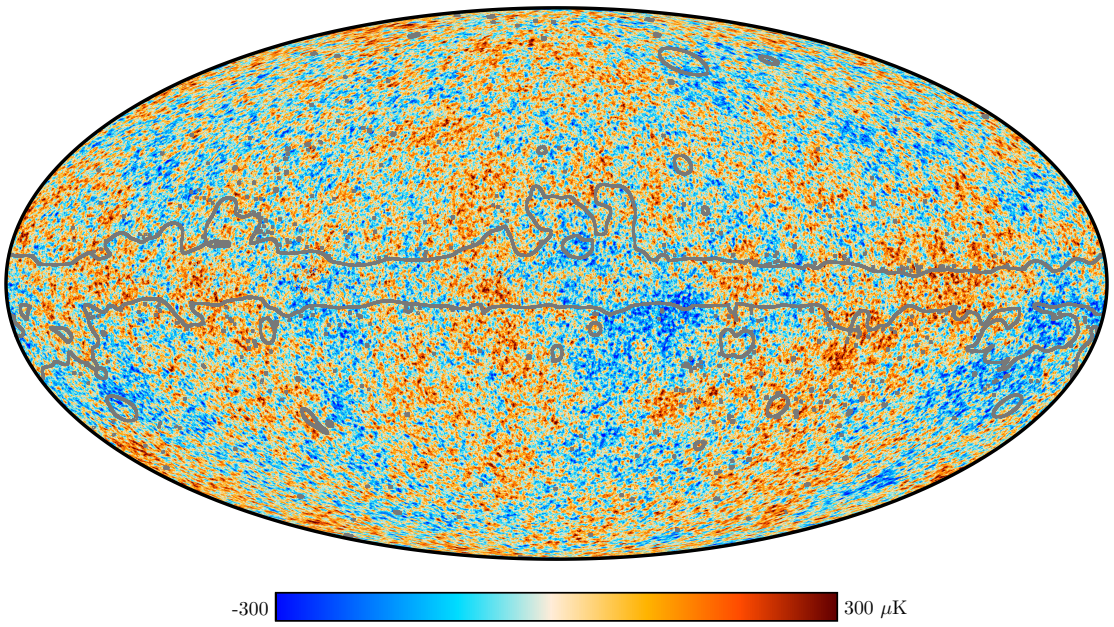

Figure 1.3: CMB temperature map, showing anisotropy variations of 600 μK. Extracted from the Planck satellite full sky survey 2018 results. Source: Planck Collaboration and the ESA.

ground (CMB) was first observed in 1965 [17]. A near isotropic, T = 2.728 ± 0.004 K, black body distribution of microwave frequency photons emitted during the very early Universe (∼300,000 years after the Big Bang) [18]. The CMB offered the first proof of Big Bang Nucleosynthesis (BBN) and an invaluable probe into the distribution of mass in the early Universe. During these early stages of the Universe's development, its temperature was around 3000 K; allowing a hot dense plasma to form between baryons, electrons and photons [19]. This plasma was maintained by a reversible process: $p + e^- \leftrightarrow H + \gamma$. As the Universe cooled, through expansion, temperatures dropped below that required for hydrogen to ionise. Stable hydrogen began to form whilst still being coupled to the photons (the period of recombination). With a decreasing number of free electrons, the photons' mean free path increased; allowing them to propagate in the now transparent Universe. These photons contained an imprint of their previous couplings, the remnants of which can be observed today in the surface of last scattering.

COBE conducted the first high precision measurement of the CMB during the 1990s. The data collected was able to show that despite being highly isotropic, there were significant fluctuations in the CMB. From this data, it was possible to prove the Universe is flat in curvature [18]. Since then, a vast effort has gone into improving the resolution of these measurements to a degree where these anisotropies are known to a high precision.

Most notably are the results from WMAP [20], and the Planck [21, 8] satellites, giving the most precise measurements to date of the CMB. Figure 1.3 shows the most recent data collected by the ESA's Planck satellite, with a maximum temperature variation of 0.0006 K.

The source of these anisotropies originate from quantum fluctuations in the early Universe. Over time these were stretched on a cosmological scale and later developed into density fluctuations. During recombination, the motion of matter can be considered a harmonic oscillator; where first gravitational attraction pulls objects in to form sites of over-density. Then, once the system's pressure becomes too great, a pressure wave forces the gas of particles to rarefy. When decoupling begins, the locations with the greatest density will generate a larg gravitational potential for the photons to overcome. Nowadays the variation in the potential can be observable by the degree of redshift attributed to the photons coming from a specific region of the Universe [22]. By taking a power spectrum of the CMB, as shown in Figure 1.4, it is possible to see the acoustic peaks produced by

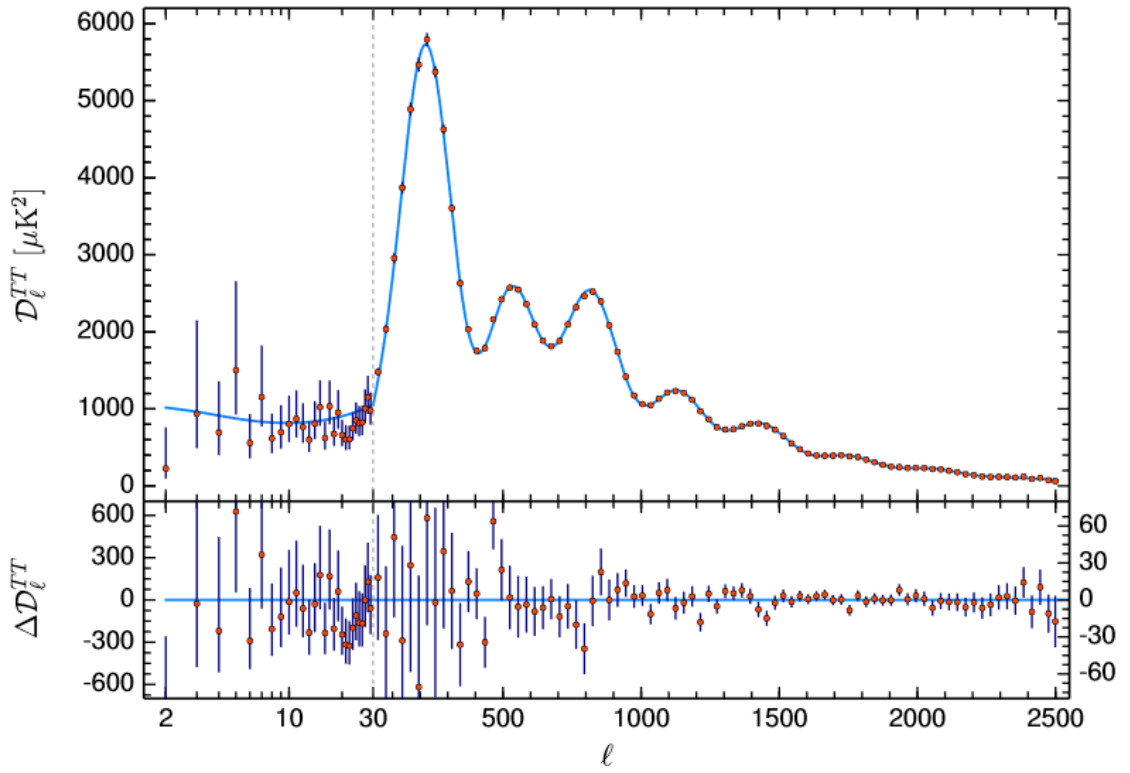

Figure 1.4: CMB temperature power spectrum from the 2018 Planck data. The ΛCDM model best fit (blue line) is in good agreement with data points (red dots) for all bar the lowest multipole moment. Error bars are the $\pm 1\sigma$ uncertainty and the lower panel contains the residual plot [8].

the fluctuations prior to the surface of last scattering. The anisotropies lead to a non-flat power spectrum with clear acoustic oscillations at multipoles (l) $\geq$ 100. The positions and amplitudes of these peaks allow for a determination of the size, composition and shape of the Universe. A flat universe is expected to have the first multipole at l ~200; which is the current perceived view[5]. More interestingly, the other peaks are highly influenced by the abundance and types of matter in the Universe. A high baryonic abundance, Ω_b, would require the over-dense regions to be denser and the rarefied less rarefied; increasing the photons' energy loss when decoupling. A high Ω_b would be observed as a suppression of the second peak. Higher modes are sensitive to the ratio of matter to radiation, Ω_m / Ω_r; a higher ratio implies lower amplitudes. The most recent determination of these abundances, obtained from the Planck satellite [8], are:

$$\Omega_\Lambda = 0.6847 \pm 0.0073 \tag{1.1.1a}$$

$$\Omega_m = 0.3153 \pm 0.0073 \tag{1.1.1b}$$

$$\Omega_b h^2 = 0.0224 \pm 0.0001, \tag{1.1.1c}$$

where Ω_Λ is the Dark Energy abundance. Dark Energy will not be explored in this thesis; please see [24, 25] for a well-rounded summary.

A completely independent evaluation of these abundances can be extrapolated from BBN, the process by which the lightest elements[6], other than hydrogen, began to form during the early Universe [26]. Prior to this, protons and neutrons were in equilibrium: $p + e^- \leftrightarrow n + \nu_e$. Once the temperature decreased to T $\sim$ 1 MeV, unbound neutrons began to decay with a 10 minute half-life. Further cooling, T $\sim$ 0.7 MeV, prevented dissociation of light nuclei by photons; allowing deuterium and helium to form. Helium's higher binding energy makes dissociation harder, increasing its relative primordial abundance to deuterium. Therefore, it is possible to determine the number of protons to neutrons in the Universe by comparing the ratios of light elements. Dependent on the required time for the necessary change in temperatures, a differing value for these ratios is retrieved. The deuterium:hydrogen ratio, as shown by Figure 1.5, is the most sensitive to variations in the baryon-photon ratio $n = n_b/n_\gamma$; where a smaller value of n implies a greater number of photons and thus an increased probability for dissociation. This increased dissociation causes a later start to BBN and reduces the number of light nuclei produced. The observed ratio of $n = (5.921 \pm 0.051) \times 10^{-10}$ [7] is in good agreement with that obtained from CMB

[5] This is not without contention, with good arguments supporting a closed Universe [23].

[6] Being: D, ^{3}He, ^{4}He and ^{7}Li.

constraints [8] and gives a baryonic abundance from BBN studies of:

$$\Omega_b h^2 = 0.02235 \pm 0.00016 \pm 0.00033, \tag{1.1.2}$$

akin to n, is consistent with the values set from the CMB data shown on page 6. With knowledge of these abundances, it is possible to extrapolate the non-baryonic contribution to the matter density, i.e. the contribution from DM:

$$\Omega_{dm} h^2 = 0.120 \pm 0.001, \tag{1.1.3}$$

resulting in ∼80% of the mass density and ∼24.5% of the total energy of the Universe being attributed to DM[7].

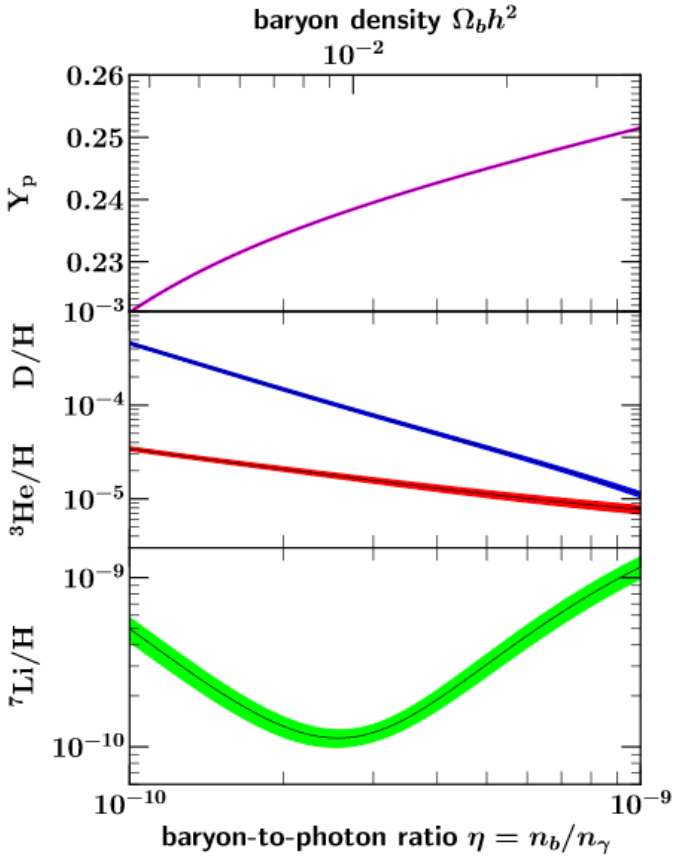

Figure 1.5: Standard BBN models for the abundances of light elements (D, ^{3}He, ^{4}He and ^{7}Li) as function of the baryon-to-photon ratio. All abundances have been normalised to that of hydrogen, and Yp denotes the yield of ^{4}He. A value of $N_\nu = 3$ and a neutron lifetime of $\tau_n = 879.4 \pm 0.6$ s was used. Bands on the lines indicate the 1σ error [27].

[7] Using a Hubble parameter of h ∼0.7. The Hubble parameter is the ratio of the distance of an object to its recession velocity in an expanding universe and can be used to define the scale of the universe.

1.2 Dark Matter Candidates

Many candidate particles and theories attempt to either directly reconcile or explain the presence of this unaccounted mass. Some of these candidates will be discussed briefly. The two most popular particle candidates, the axion and the WIMP, will be discussed in more depth, focusing on the latter.

The independent determinations of the matter abundances from the CMB power spectrum and BBN strongly infer the presence of a non-baryonic massive particle. Measurements of the Bullet Cluster set an upper limit on this particle's self interaction cross-section of $\sigma/\mathrm{m} < 0.7\ \mathrm{cm}^2/\mathrm{g}$ [28]. These measurements also indicate the particle does not absorb or emit light; therefore, it is either electrically neutral or possesses a fractional charge. Constraints from detection and requirements from structure-formation simulations set the bounds on this charge relative to the charge of an electron: $\epsilon \leq 7.6 \cdot 10^{-4}\ (\mathrm{MeV/T})^{1/2}$ and $\epsilon \leq 2.2 \cdot 10^{-4}\ (\mathrm{MeV/T})^{1/2}$ respectively [29, 30]. Furthermore, strong interactions can be ruled out; otherwise, isotopes with enormous masses would be present. The requirement of long term stability, or to have a lifetime greater than the age of the Universe, is set as the particle's influence has been persistent throughout this time.

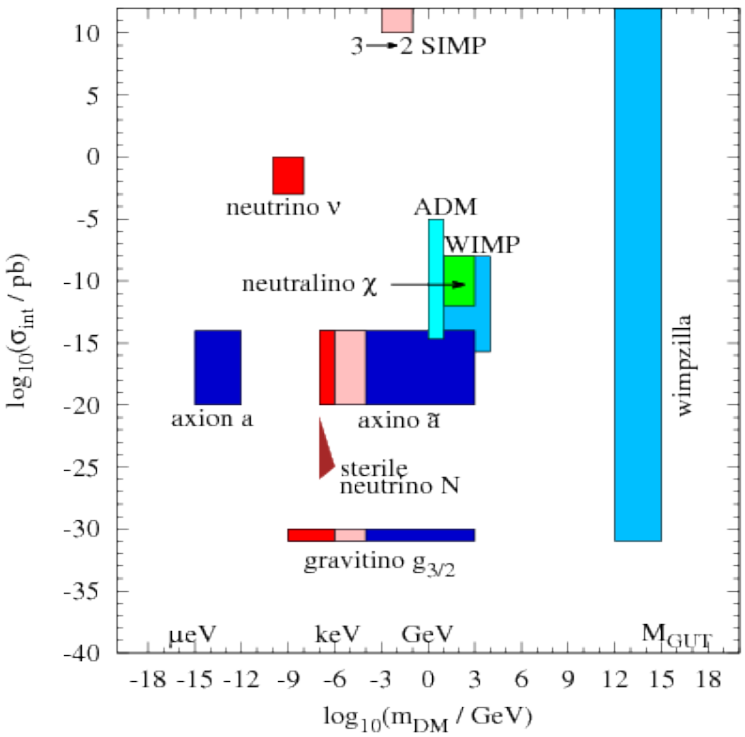

Figure 1.6: Parameter space of interaction cross-section and DM mass covered by various DM candidates. Cold DM models are shown in blue, warm in pink and hot are in red [31].

Moreover, its abundance must be enough to meet the observed DM density. It must be cold at the epoch of the structure-formation, as hot (i.e. relativistic) DM produces a larger free-streaming length than cold. Larger free-streaming lengths are known to produce inconsistencies between simulations and the large scale structure known to exist in the Universe [31]. In contrast, simulations based on the Lambda Cold Dark Matter (ΛCDM) model have shown significant success at replicating these structures. Cold DM simulations are not without problems[8], often missing required substructures such as satellites [33]. With masses at the keV scale, warm DM can provide a solution to this [34], yet introduces a differing set of inconsistencies.

The menagerie of current DM candidates spans many orders of magnitude both in mass and size of the cross-section for interacting with Standard Matter (SM), as shown in Figure 1.6. Some of those listed in this plot, plus a few other theories are given in briefly below:

- **Neutrinos:** Due to their notably light masses, neutrinos would be considered hot DM. It will be later shown that neutrinos are neither abundant enough nor massive enough to be a major contributor to the DM abundance. Despite this, they are still highly significant in the search for DM as they provided the phenomenological landscape for the WIMP hypothesis.

- **MOND:** Modification Of Newtonian Dynamics (MOND) takes the view that there is not a form of new matter in the Universe, it is just that our current understanding of galactic and universal dynamics is incomplete. By slight modifications to Newton's laws, it is possible to construct a viable solution to the DM problem [35]. Despite this, no current combination of modifications can lead to replicating the variety of large scale structures observed in the Universe. One example is DM's inclusion within MOND models to explain X-ray bright systems [36].

- **Dark Baryons:** Generally considered in the form of Massive Compact Halo Objects (MACHOs). The EROS-2 collaboration have highly constrained the contribution of MACHOs' to be a small per cent of the Milky Way's halo; making them too scarce to account for the mass discrepancy [37].

- **Primordial Black Holes:** A very different consideration is that the mass deficit originates from a vast number of Primordial Black Holes (PBHs). These PBHs form prior to the BBN epoch [38], and would weaken the requirement for non-baryonic

[8] For a short review of the issues with small scale structures within ΛCDM simulations; please see [32]

DM to be present in the Universe. The coalescing of two of these PBHs [39] is a potential source of the first gravitational wave observed by LIGO [40]. Interesting as it is, the likelihood of DM being PBHs is highly constrained [41].

- **Hexa-Quarks:** With each discovery of a new stable Bose-Einstein condensate (bosonic, isoscalar) hexa-quark matter [42], comes the testing of its viability as a candidate for DM. Uranus's heat production excluded the h-dibaryon; the expected flux caused by the annihilation-capture equilibrium process for such a particle was not in agreement with measurements [43]. The d*(2380) hexa-quark, with a mass of 2380 MeV/c^2, is made of six light quarks, three up and three down; and has a radius smaller than that of a proton. Significant production of such a particle during the phase transition from the quark-gluon plasma into hadronic matter makes this a potential new light DM candidate [44]. Lack of observation of such condensates in the Universe is pinned to the fact that within larger massed condensates, the electron and muon component would be sufficient enough for the system to become a heavy neutral atom, hence obscuring any electromagnetic signature. This however is in direct contradiction with observation of such heavy neutral atoms in the heliosphere by the IBEX_Lo satellite; with too little an abundance to contribute toward DM [45].

- **Dark Photons:** A viable DM candidate exists in the form of a light vector boson, which is stable on cosmological timelines; given the mass is $< 2m_e$. This boson, the dark photon (V), has several production mechanisms: scattering with SM in the early Universe under the conversions $\gamma e^{\pm} \rightarrow V e^{\pm}$ or $e^{+}e^{-} \rightarrow V\gamma$; resonant photo-dark photon conversion; or, akin to the axion, by some form of misalignment mechanism.

1.2.1 Axions

Another category of potential DM candidates arises from other areas of physics that require the need for Beyond the Standard Model (BSM) particles. One prime example of this category is the axion or Axion Like Particle (ALP).

Non-observation of the neutron's electric dipole moment indicates a negligible level of Charge Parity (CP) violation, which was in stark contradiction to predictions using quantum chromodynamics [46]. To resolve what is known as the Strong CP problem,

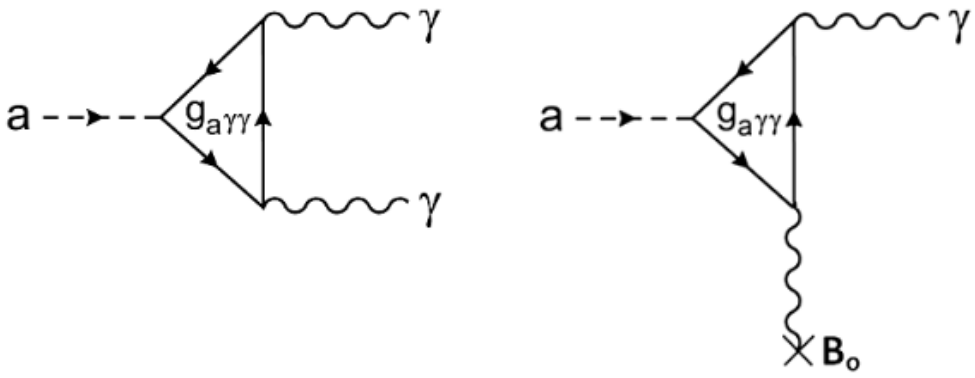

Figure 1.7: Feynman diagram for axion decay to photons and the Primakoff effect, where an axion converts to a photon in the presence of a magnetic field B_0 [55].

a new symmetry was proposed. This Peccei-Quinn (PQ) symmetry[9] gives a means to construct a Lagrangian within QCD in a manner that ensures CP conservation [47, 48]. CP symmetry is both hidden and global. With spontaneous breaking occurring at an energy scale of f_a; resulting in the generation of a massive pseudo-Goldstone boson [49, 50]. This new extremely light pseudoscalar particle, the axion, has a mass inversely proportional to f_a:

$$f_a \simeq (0.6\,eV)\frac{10^6\,GeV}{m_a}. \tag{1.2.1}$$

Experimental bounds for f_a constrain the scale to be greater than that of weak symmetry breaking [51]; implying a very light axion $10^{-6} \leq m_a \leq 10^{-3} eV/c^2$ [52]. This light mass brings the likelihood of the axion being the main contributor to the observed quantity of DM in the Universe into some doubt; as a very high abundance of axions would be required [50]. Thermal production of the axion in the early Universe, would attribute relativistic velocities to the axion and hence would be considered as hot DM. Through the re-alignment mechanism, it has been proposed that axions may be non-relativist, reconciling it as a cold DM candidate [53]. Additionally, axions have a further mechanism by which they could form the required abundances to meet observations; by forming Bose-Einstein condensates [54].

With such a small mass, and low interaction cross-section, detection of the axion poses great difficulties. ALPs share some properties of the axion without being directly linked to PQ symmetry; this alleviates some of the constraints and widens the viable parameter space. Axions and ALPs can couple to photons through the decay channel $a \rightarrow \gamma\ \gamma$, but the strength of the coupling is only considered a free parameter for ALPs [56]. Most

[9] Taking its name from the theorist who introduced the model, Roberto Peccei and Helen Quinn.

searches for these particles utilise a technique initially adopted in the resonant production of mesons; bombardment of the nucleus with photons, known as the Primakoff effect [57]. By inverting this process, it is possible to produce photons from an axion-photon interaction, shown in Figure 1.7. Experimentally, one photon in the interaction vertex is supplied by applying a magnetic field, allowing the axion to convert into a single photon. Detection of this photon would infer the presence of an axion traversing the region which the magnetic field had been applied[56].

The ADMX collaboration is attempting to utilise the Primakoff effect to detect axions emitted from the Milky Way's DM halo [55]. ADMX uses a strong magnetic field in a high Q microwave[10] in an attempt to induce axion-photon conversion. Another strategy attempting to exploit the Primakoff effect is the light-through the wall method. This effect involves detecting the light produced on the opposite side of an opaque material, on which a laser is incident. A photon interacting with the medium is thought to convert to an axion, allowing it to transverse through the material, and is then converted back to a photon on the other side [58]. Not all detection methods rely on this effect; some attempt to observe the direct detection of an axion interacting with a medium either through the axio-electric effect or a process akin to the photoelectric effect. The Large Underground Xenon (LUX) collaboration placed limits of $g_{ae} < 3.5 \times 10^{-12}$ for massless solar axions and for ALPs in a mass range of 1-16 keV/c^2: $g_{ae} < 4.2 \times 10^{-13}$ [59].

1.2.2 WIMPS

Possibly the most favoured of the hypothesised DM candidates is the WIMP, primarily due to being non-relativistic at the point of departure from thermal equilibrium. First, consider a particle in thermal and chemical equilibrium with the rest of the Universe. These particles would be undergoing a constant process of annihilation into and formation from lighter particles.

Expansion of the Universe drives the reduction in this particle's number density, n_χ. This reduction continues until the point where their reaction rate, Γ, has decreased to below the expansion rate of the Universe, $H(t)$:

$$H(t) \geq n_\chi \langle \sigma_{ann} \rangle. \tag{1.2.2}$$

At this stage, the particle is no longer able to annihilate at a sufficient rate to maintain equilibrium; this mechanism is called "Freeze-out". The remaining mass, the relic abun-

[10]The quality factor (Q) of the microwave cavity, and acts a measure of the amount of energy loss at the frequency of operation.

dance, of the particle can then be compared to the DM abundance observed by PLANCK. The following is an outline of the thermal production mechanism for DM, the freeze-out mechanism and the results which motivate the WIMP hypothesis and the extensive search for a BSM particle matching its characteristics. The derivation follows that in Ref. [60].

Thermal Production

A DM candidate's present-day relic abundance can be determined through an understanding of the time evolution of its number density. For a given particle in kinetic equilibrium, whether fermion (- sign) or boson (+ sign), the occupancy number phase space is given by:

$$f = \frac{1}{e^{(E-\mu)}/T \pm 1}. \tag{1.2.3}$$

The chemical potential, μ, is a conserved quantity in interactions involving particles in chemical equilibrium. When integrated in phase space a series of parameters describing a weakly interacting gas of particles, with g internal degrees of freedom, is generated; with properties given by Eq. (1.2.4 - 1.2.6):

$$n = \frac{g}{(2\pi^3)} \int f(\mathbf{p}) d^3p \tag{1.2.4}$$

$$\rho = \frac{g}{(2\pi^3)} \int E(\mathbf{p}) f(\mathbf{p}) d^3p \tag{1.2.5}$$

$$p = \frac{g}{(2\pi^3)} \int \frac{|\mathbf{p}|^2}{3E(\mathbf{p})} f(\mathbf{p}) d^3p, \tag{1.2.6}$$

where n is the number density of particles, ρ the energy density and p the pressure of the gas. By considering a scenario where there are no number changing processes, these densities can remain constant under an iso-entropic time evolution of the Universe. To do so, the densities are normalised by a time dependent volume, $a(t)^{-3}$; which is linked to the entropy density via $s = S/a^3$. When applied to the number density in Eq. (1.2.4), the particle's yield as a function of the number density and entropy is found to be constant,

$$Y = \frac{n}{s}. \tag{1.2.7}$$

The evolution of the entropy and energy densities as functions of temperature can now be written as:

$$s = \frac{2\pi^2}{45} g_{*s} T^3 \tag{1.2.8}$$

and,

$$\rho = \frac{\pi^2}{30} g_* T^4. \tag{1.2.9}$$

The effective number of degrees of relativistic freedom for each is given by:

$$g_{*s} = \sum_{bosons} g \left(\frac{T_i}{T}\right)^3 + \frac{7}{8} \sum_{fermions} g \left(\frac{T_i}{T}\right)^3 \tag{1.2.10}$$

$$g_{*} = \sum_{bosons} g \left(\frac{T_i}{T}\right)^4 + \frac{7}{8} \sum_{fermions} g \left(\frac{T_i}{T}\right)^4 . \tag{1.2.11}$$

Here T is temperature of plasma in equilibrium, and T_i is the effective temperature of each particle type. By solving the number density in the relativistic limit, the yield of such a particle can be extrapolated as:

$$n = \frac{g_{\mathit{eff}}}{\pi^2}\zeta(3)T^3 \tag{1.2.12}$$

$$Y_{eq} = \frac{45}{2\pi^4}\zeta(3)\frac{g_{\mathit{eff}}}{g_{*s}} \approx 0.278\frac{g_{\mathit{eff}}}{g_{*s}}, \tag{1.2.13}$$

where $g_{\mathit{eff}} = g$ for bosons and 3/4g for fermions. For non-relativistic particles, the number density and the yield at equilibrium of such a particle is given by the following:

$$n = g_{\mathit{eff}} \left(\frac{mT}{2\pi}\right)^{3/2} e^{-m/T} \tag{1.2.14}$$

$$Y_{eq} = \frac{45}{2\pi^4} \left(\frac{\pi}{8}\right)^{1/2} \frac{g_{\mathit{eff}}}{g_{*s}} \left(\frac{m}{T}\right)^{3/2} e^{-m/T}. \tag{1.2.15}$$

Time Evolution

The application of time evolution allows for the determination of the present-day values for the number density. In general this is achieved by applying the covariant form of the Liouvilles operator to the phase space distribution function:

$$\hat{L}[f] = C[f], \tag{1.2.16}$$

where $C[f]$ is a dimensionless operator containing the number changing process and $\hat{L}$ is the Liouville operator defined as:

$$\hat{L} = p^\mu \frac{\partial}{\partial x^\mu} - \Gamma^\mu_{\sigma p} p^\sigma p^\rho \frac{\partial}{\partial p^\mu}, \tag{1.2.17}$$

where $\Gamma^\mu_{\sigma p}$, the affine connection, is introduced to account for the influence of gravity. When considering the Universe to be Friedmann-Robertson-Walker like, $f(x^\mu, p^\mu) = f(t, E)$, the Liouville operator can be written as:

$$\begin{aligned} \hat{L} &= E\frac{\partial}{\partial t} - \Gamma^0_{\sigma p} p^\sigma p^\rho \frac{\partial}{\partial E} \\ &= E\frac{\partial}{\partial t} - H|\mathbf{p}|^2 \frac{\partial t}{\partial E}. \end{aligned} \tag{1.2.18}$$

Here $H = \frac{\dot{a}}{a}$ is the Hubble parameter. Finally, by integrating over the phase space, a link can be established to the time evolution of number density:

$$\begin{aligned} \frac{g}{(2\pi)^3}\int \frac{\hat{L}|f|}{E} d^3\mathbf{p} = \frac{g}{(2\pi)^3}\int \frac{C|f|}{E} d^3\mathbf{p} \\ = \frac{dn}{dt} + 3Hn. \end{aligned} \tag{1.2.19}$$

Collisionless Operator

The collisionless operator encodes the microphysics of particle interactions; including any number changing processes (those that create or destroy particles). From here, the following nomenclature is adopted: SM particles will be referred to by A and B, and DM as 1 and 2. For the annihilation process of SM to DM, and vice versa, the corresponding phase space for the particles is:

$$d\Pi_i = \frac{g_i}{(2\pi)^3}\frac{d^3\mathbf{p_i}}{2E_i} \tag{1.2.20}$$

$$\begin{aligned} \frac{g}{(2\pi)^3}\int \frac{C|f|}{E} d^3\mathbf{p} = -\int d\Pi_A d\Pi_B d\Pi_1 d\Pi_2 (2\pi)^4 \delta(p_A + p_B - p_1 - p_2) \\ \left[|\mathcal{M}_{12\to AB}|^2 f_1 f_2 (1 \pm f_A)(1 \pm f_B) - |\mathcal{M}_{AB\to 12}|^2 f_A f_B (1 \pm f_1)(1 \pm f_2)\right], \\ = -\int d\Pi_A d\Pi_B d\Pi_1 d\Pi_2 (2\pi)^4 \delta(p_A + p_B - p_1 - p_2) \\ \left[|\mathcal{M}_{12\to AB}|^2 f_1 f_2 - |\mathcal{M}_{AB\to 12}|^2 f_A f_B\right]. \end{aligned} \tag{1.2.21}$$

$(1 \pm f_i)$ accounts for the viable phase space of produced particles, taking into account fermions (-) and bosons(+). Assuming no CP violation in the DM sector (T invariant), $|\mathcal{M}_{12\to AB}|^2 = |\mathcal{M}_{AB\to 12}|^2 \equiv |\mathcal{M}|^2$, and energy conservation in annihilation, $E_A + E_B = E_1 + E_2$, gives:

$$f_A f_B = f_A^{eq} f_B^{eq} = e^{\frac{E_A + E_B}{T}} = e^{\frac{E_1 + E_2}{T}} = f_1^{eq} f_2^{eq}. \tag{1.2.22}$$

Placing Eq. (1.2.22) into Eq. (1.2.21), and using the fact that SM particles are in equilibrium, the final phase space for the collisionless operator can be written as:

$$\frac{g}{2\pi^3}\int \frac{C|f|}{E} d^3\mathbf{p} = -\langle\sigma v\rangle (n^2 - n_{eq}^2), \tag{1.2.23}$$

where $\langle\sigma v\rangle$ is the thermal average cross-section:

$$\langle\sigma v\rangle \equiv \frac{1}{n_{eq}^2}\int d\Pi_A d\Pi_B d\Pi_1 d\Pi_2 (2\pi)^4 \delta(p_A + p_B - p_1 - p_2) |\mathcal{M}|^2 f_1^{eq} f_2^{eq}. \tag{1.2.24}$$

By combining Eq. (1.2.19) and (1.2.23), the Boltzmann equation is retrieved:

$$\frac{dn}{dt} + 3Hn = -\langle\sigma v\rangle^2 (n^2 - n_{eq}^2). \tag{1.2.25}$$

The above can be treated as an equilibrium restoring equations. When $Hn < \langle\sigma v\rangle n^2$, the right hand side dominates, giving:

$$0 \approx n - n_{eq}; \tag{1.2.26}$$

therefore, the number density traces its equilibrium value $n \equiv n_{eq}$. When $Hn > \langle\sigma v\rangle n^2$, the right hand side can be neglected and the resultant equation, $dn/n = -3\, da/a$, implies $n \propto a^{-3}$ as:

$$\begin{aligned} H &= da/dt/a, \\ dn/dt/n &= 3H = -3da/dt/a, \\ dn/n &+ 3da/a = 0, \end{aligned} \tag{1.2.27}$$

which has a solution of $n(a) = C/(a^3)$. This is equivalent to saying DM particles no longer annihilate and any remaining decrease in the number density is directly linked to an increase in the scale factor of the Universe. From here it is then common practice to simplify the Boltzmann equation with the yield and with a dimensionless variable[11]:

$$\begin{aligned} \frac{dY}{dx} &= \frac{-sx\langle\sigma v\rangle}{H(m)}(Y^2 - Y_{eq}^2) \\ &= \frac{\lambda\langle\sigma v\rangle}{x^2}(Y^2 - Y_{eq}^2), \end{aligned} \tag{1.2.28}$$

where:

$$\frac{dY}{dt} = \frac{dY}{dx}\frac{dx}{dt} = \frac{dY}{dx}Hx, \tag{1.2.29}$$

and:

$$\begin{aligned} \lambda &\equiv \frac{2\pi^2}{45}\frac{M_P g_{*s}}{1.66 g_*^{1/2}} m \\ &\approx 0.26 \frac{g_{*s}}{g_*^{1/2}} M_p m, \end{aligned} \tag{1.2.30}$$

where M_P is the Planck mass.

Yield at Freeze-Out

It is only correct to consider the contribution of relativistic particles to the DM abundance. $e^{\pm}$, γ, ν and $\bar{\nu}$ all decouple at a few MeV, and hence their yield is depicted by Eq. (1.2.13). With no dependence on x_f, a direct calculation can be performed; in which

[11] The dimensionless variable will be treated as x = m/T.

$g_* = g_{*s} = 10.75$ accounts for the number of relativistic degrees of freedom[12]. From this the relic density of neutrinos can then be determined:

$$\begin{aligned}\Omega h^2 &= \frac{\sum_i m_{\nu i} Y_\infty s_0 h^2}{\rho_c} \\ &\equiv \frac{\sum_i m_{\nu i}}{91eV}.\end{aligned} \tag{1.2.31}$$

Equation (1.2.31) implies that for neutrinos to be a significant contributor $\sum_i m_{\nu i} \equiv 9eV$ must hold. Current experimental upper bounds, $\sum_i m_{\nu i} \leq 0.3eV$, indicate this is not the case, and that the neutrino contribution is less than 3 % of the total DM abundance: $\Omega h^2 \leq 0.003$.

For non-relativistic particles, only an approximate solution can be obtained, due to the dependence on x_f; being the previously defined dimensionless quantity when the temperature is set to that at the time of freeze out. To perform this approximation the quantity $\Delta_Y \equiv Y - Y_{eq}$ is required. In early stages of the Universe, $1 < x \ll x_f$, the yield of a particle follows the equilibrium set by $Y \equiv Y_{eq}$. With the assumption $d\Delta_Y/dx = 0$, the difference in the yields is:

$$\Delta_Y = \frac{\frac{dY_{eq}}{dx}}{Y_{eq}} \frac{x^2}{2\lambda \langle \sigma v \rangle}; \tag{1.2.32}$$

giving a difference at freeze-out of:

$$\Delta_Y = \frac{x_f^2}{2\lambda \langle \sigma v \rangle}. \tag{1.2.33}$$

For later times $x \gg x_f$ assume $Y \gg Y_{eq}$ and hence $\Delta_\infty \equiv Y_\infty$ giving:

$$\frac{d\Delta_Y}{dx} \equiv \frac{\lambda \langle \sigma v \rangle}{x^2} \Delta_Y^2. \tag{1.2.34}$$

Treating the above as a separable equation, it is possible to perform an integration from the period of freeze-out to the present day. Additionally, by expanding the thermally averaged cross-section in powers of x^{-1}, as $\langle \sigma v \rangle = a + \frac{b}{x}$, a final yield is obtained:

$$\frac{1}{\Delta_{Y_\infty}} = \frac{1}{\Delta_{Y_f}} + \frac{\lambda}{x_f}\left(a + \frac{b}{2x_f}\right) \tag{1.2.35}$$

$$\Delta_{Y_\infty} = Y_\infty = \frac{x_f}{\lambda(a + \frac{b}{2x_f})}. \tag{1.2.36}$$

[12] For one neutrino family number of degrees of freedom is $g_{eff} = 3g/4 = 3/2$.

With this it is now possible to calculate the relic density:

$$\begin{aligned}\Omega_\chi h^2 &= \frac{m_\chi Y_\infty s_0 h^2}{\rho_c} \\ &\approx \frac{10^{-10} GeV^{-2}}{a + \frac{b}{40}} \\ &\approx \frac{3 \times 10^{-27} cm^3 s^{-1}}{a + \frac{b}{40}}.\end{aligned} \tag{1.2.37}$$

Finally by reintroducing the thermally average cross-section, which from now will be referred to as the annihilation cross-section for brevity, it can be seen in Eq. (1.2.38) that the relic density is inversely proportional to the annihilation cross-section and independent of the mass of the particle.

$$\Omega_\chi h^2 \approx \frac{3 \times 10^{-27}\ cm^3 s^{-1}}{\langle \sigma v \rangle}. \tag{1.2.38}$$

Therefore; in order for these particles to be the majority, if not sole, contributor to the DM abundance, they would require an annihilation cross-section of $\langle \sigma v \rangle \sim 3 \times 10^{-26}$ $\mathrm{cm^3 s^{-1}}$. Being on the weak scale, this provides strong motivation to observe BSM particles interacting via weak interactions. It is important to note that a larger cross-section results in a greater delay before the departure from equilibrium; reducing the produced relic density.

When considering the scenario where DM can self-annihilate to SM particles, through some existing or new gauge boson, a cross-section equivalent to $G_F m_\chi^2$ (where $G_F = 1.16 \times 10^{-5}$ $\mathrm{GeV^{-2}}$) would retrieve the correct relic density for DM with masses on the GeV scale; hence defining the prime search region for the majority of current dedicated DM searches. Combining this expected mass with an annihilation cross-section expected to be at the weak scale, leads to the motivation behind the WIMP-hypothesis [13]. Currently WIMP-like DM has not been experimentally ruled out, and is at this time the most extensively sought form of DM.

1.3 Particle Dark Matter Detection Strategies

When considering DM to be of a particle (χ) nature, a Feynman-like diagram can be constructed to show the potential interactions with SM particles (X). By doing so, as in Figure 1.8, it is possible to show the association between the three detection strategies, being:

[13] This is also the most significant contention with the WIMP-hypothesis; as both were derived using some strong assumptions.

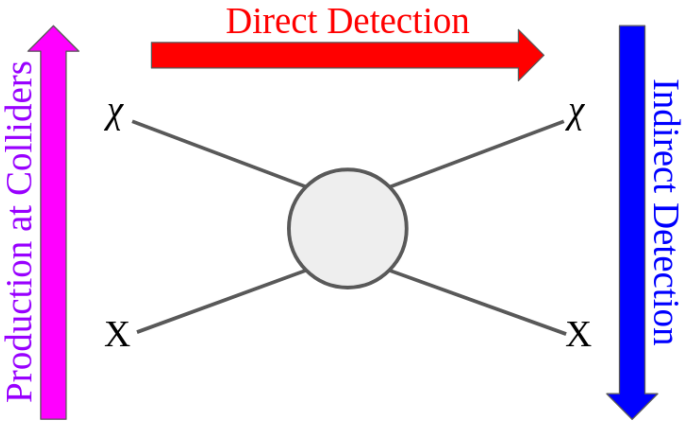

Figure 1.8: Feynman like diagram for the interaction between SM particles (X) and DM (χ). Indicated by the arrows is the approaches used by the three detection strategies.

- **Direct detection** is based on the observation of the scattering of an incoming DM particle with a SM target, $\chi X \rightarrow \chi$X.
- **Indirect detection** search for the annihilation signature of DM into SM products, $\chi\chi \rightarrow$ XX. The DM is normally considered to have gathered to a sufficient quantity to induce annihilation at sources of large gravitational potential such as Galactic centres, the Sun and even the Earth.
- **Collider production**, XX $\rightarrow \chi\chi$, attempt to look for the signature of DM products (generally missing energy) from the annihilation of highly energetic standard model particles.

The remainder of this chapter will discuss these three strategies in more detail.

1.3.1 Indirect Detection

Considering the vast array of astrophysical indications towards DM's existence, it is only natural to further explore space for possible evidence of this new particle. The general principle of indirect detection is to observe the annihilation or decay products of DM, which have become gravitationally bound to the centre of astrophysical objects such as planets, stars, and galaxies. These products (gammas, neutrinos, electrons, positrons, protons, antiprotons and even antideuterium) would be discernible as an anomalous flux; each with a detection signature dependent on the undertaken decay channel [61]. Therefore, this form of DM search is sensitive to the decay of DM. Indirect detection also has the unique capability to probe the distribution of low-velocity DM within the galactic disk; due to

its greater probability of accumulating in massive astronomical bodies [62]. Astronomical sources of particular interest are galactic clusters and the Milky Way's galactic centre and halo.

Indirect detection also has a strong dependency on the product of the thermally averaged cross-section and the velocity of DM; which is directly linked to the chosen model for the halo profile, discussed later in §2.2. The uncertainties presented by different models can alter the $(\sigma_\chi v)$ by an order of magnitude. With this in mind, observation of an anomalous flux from DM annihilation, for a given piece of apparatus, is highly dependent on the astronomical source, DM abundance and particle phenomenology. To account for these variations, a diverse range of methods are employed[14]: Cherenkov telescopes (H.E.S.S. [63] and CTA [64]), neutrino telescopes (IceCube [65] and ANTARES [66]), and particle detectors in balloons and satellites (Planck [21] and FERMI [9]). All of which provide distinct and complementary techniques, with differing backgrounds and systematic uncertainties to the other two search strategies.

Below is an outline of some of the leading particle candidates being explored for an anomalous flux, the experiments involved and the constraints they set on either the DM annihilation cross-section or the DM-nucleon scattering cross-section.

Gamma-Rays

Some of the strongest limits on the DM annihilation cross-section stem from observations of gamma-rays by satellites, notably Fermi, or ground-based Cherenkov telescopes. Gamma-rays have become a favoured signal as it is possible to locate the source of their emission; they do not experience significant scattering to produce distortion. Additionally, a negligible absorption probability allows for inference of the mechanism by which they were produced; achieved through making observations across the energy spectrum [67]. Interestingly the data collected by the Fermi revealed an excess around the Milky Way's centre; peaking at an energy of 2-3 GeV [68]. Initial attempts to attribute this to DM [69] hold less credibility than solutions that involve unresolved point sources; such as millisecond pulsars [70]. Lack of an observable signal from the combined analysis of 15 dwarf spheroidal galaxies, by the Fermi-LAT collaboration, places a constraint on the DM annihilation cross-section of $< 3 \times 10^{-26} \mathrm{cm}^3/\mathrm{s}^2$ for DM masses below 100 $\mathrm{GeV/c}^2$ in both the bottom and τ channels [9].

[14] Some of these were never intended to detect DM, with primary focus on other physics.

Positrons and Antiprotons

Annihilation of DM in most models results in the production of equal parts of matter and antimatter. Therefore, the detection of a discernible excess of antimatter particles, in this case primarily antiprotons and positrons, originating from an unknown astrophysical source could indicate the presence of DM. In 2008, PAMELA observed a clear rise in the Milky Way's positron fraction proportional to the energy, for energies above 10 GeV [71]. Later this was confirmed by both Fermi-LAT and AMS-02 [10], this is a clear postulate of DM annihilation in the galactic halo. It is essential to consider alternatives sources of the signal, such as pair production within the magnetosphere of a pulsar [72, 73]. Moreover, the required annihilation cross-section for this excess is inconsistent with constrains set by other experiments [74].

Neutrinos

Another particle that may indicate the presence of DM through the observation of an anomalous flux is the neutrino. Neutrinos can easily escape from astrophysical sources in which they are generated and travel long distance without perturbation; making the local DM density the only required astrophysical parameter. Other particle types require an accurate description of the galactic distribution of DM. Additionally, these will be high energy neutrinos (E > 10 GeV), making it possible to distinguish them from those produced in nuclear reactions in the Sun (E $\lesssim$ 20 MeV) [75]. The exact coupling of DM to the SM is not known. Therefore, several decay channels representing different energy regions are used to set a benchmark to compare results: $b\bar{b}$, W^+W^- and $\tau^+\tau^-$ [15]. Detection of the annihilation, or decay of DM at the centre of either the Earth or the Sun is only possible through neutrinos; being the only product able to escape these dense bodies. The Earth and the Sun are not expected to be sources of high energy neutrinos; consequently, any anomilous flux would be relatively background free. The only significant contribution to the background would be from the production of neutrinos from cosmic ray interactions in the atmosphere of the Sun [76, 77].

Once equilibrium has been achieved between the annihilation and capture rates, the solar neutrino flux, $d\Phi_\nu/dE_\nu$, can be related to the annihilation rate of DM, Γ_A; as given by Eq. (1.3.1).

$$\frac{d\Phi_\nu}{dE_\nu} = \frac{\Gamma_A}{4\pi D^2}\frac{dN_\nu}{dE_\nu}. \tag{1.3.1}$$

In turn this can be related to the DM-nucleon cross-section given in Eq. (1.3.2) [78].

[15] A 100% branching fraction is assumed to ignore any model dependencies.

Through this it is possible to place constraints on the spin-dependent DM-nucleon interaction cross-section for the null result on the detection of an anomalous high energy neutrino flux from the Sun by IceCube, and ANTARES [65, 66]. Being primarily made of hydrogen, the Sun can be considered a proton-rich target; hence allowing for a constraint to be set on the spin-dependent cross-section. The most abundant isotopes in the Earth's inner core, the mantle and the crust are Fe, Si and O; all spin-0 atoms. Therefore, neutrinos originating from the centre of the Earth allow for a spin-independent analysis to be conducted. Measurements of Earth originating neutrinos tend to contain greater uncertainties than solar as the Earth is unlikely to have reached equilibrium between the annihilation and capture rates due to its relative age. An assumption on the annihilation cross-section is consequently required [79].

1.3.2 Collider Production

When considering colliders, the mindset needs to be altered slightly. It is no longer possible to directly confirm whether a new particle is indeed DM. Once a stable neutral particle has been identified with a plausible mass and cross-section in the week scale, it would require external verification from astrophysical or cosmological based studies. Despite this it is still very appealing to seek the route of production of new particles for later association towards DM; especially with the unprecedented, 13.3 TeV centre of mass energies now obtainable by the LHC. The LHC's current beyond the Standard Model search strategy incorporates comprehensive searches for potential DM candidates [80, 81].

Direct and indirect experiments are influenced by the chosen DM cosmological model, and its associated uncertainties; which is not the case for collider production. This provides excellent complementarity, but with a drawback: the parameter space has many degrees of freedom. Assumptions are needed on either the type of interaction (vector, axial-vector or scalar) with its respective couplings, the mediator's mass, or the DM mass. Therefore, the relevant assumptions must be clearly stated alongside any comparison to direct and indirect limits.

In collider production, three main signal mechanisms are used to identify events originating from a potential DM candidate: (1) a significant amount of missing energy from the reconstructed event coinciding with an initial-state radiation, (2) missing energy plus the recoil of a visible particle, and (3) through resonant mass searches. It is not only hadronic colliders that present a pathway towards the identification of potential DM candidates. Electron-positron colliders offer a much cleaner interaction and hence reduced complexity

to the analysis. Experiments such as Belle are currently motivated towards searches for the production of two photons. This production method is indicative of the decay of an ALP, which as previously mentioned are a one of the prime DM candidates [82]. More recently, there have been thoughts to introduce further fixed-target experiments with dedicated focus towards DM searches at CERN, JLAB, FNAL and SLAC; which pose their own unique difficulties when searching for a non-interacting particle.

1.3.3 Direct Detection

Direct detection experiments aim to observe the elastic or inelastic scattering of a DM candidate with a target's nuclei or electrons. The exact rate, R, of the interaction depends on the mass of the interacting DM particle m_{DM}, the target nucleus mass m_N, the scattering cross section σ, the local dark matter density ρ_0 and the escape velocity v_{esc} of DM from the halo. When considering interactions with nuclei, the differential rate as a function of the energy of the recoiling nucleus, E_R, takes the form [83, 78]:

$$\frac{dR(E_R,t)}{dE_R} = nN_T \int_{v_{\text{min}}} vf(\vec{v},t)\frac{d\sigma(E_R,v)}{dE_R}d\vec{v} = \frac{\rho}{m_\chi m_A}\int_{v_{min}} vf(\vec{v})\frac{d\sigma(E_R,v)}{dE_R}d\vec{v}, \quad (1.3.2)$$

where n is the number density of DM and N_T is the number of target atoms. A derivation of the differential interaction rate (and the kinematic association between E_R and the minimum velocity for the incident DM (v_{min}) is given in §2.1, the cross section in §2.3, and the DM velocity distribution $f(v)$ and local density in §2.2. Here m_A refers to the mass of the target nucleus (A). One thing to note is the number of unknown values within Eq. (1.3.2): ρ_o, $f(v)$, m_{DM} and σ. By making assumptions on the astrophysical model, values for ρ_0 and $f(v)$ can be defined and allow for a search to by performed in the m_χ - $\sigma_{\chi N}$. parameter space[16].

Experimental design has little control on the rate other than the choice and quantity of detection material, as well as the location of the detector. The latter is an important factor in controlling backgrounds induced from environmental and cosmic origins. The cross-section, in general, is split into two components of the couplings within its Lagrangian. An axial-vector term which gives rise to a the Spin-Dependent (SD) interaction $\sigma^{\text{SD}}_{\chi-N}$, and a term from the scalar and vector couplings which result in a Spin-Independent (SI) interaction σ^{SI}. Both are derived in §2.3 where it will be shown that the SD interaction

[16]It will be shown later on that direct detection experiments prefer to set limits on the WIMP-nucleon cross-section ($\sigma_{\chi N}$) rather than the the WIMP-nucleus ($\sigma_{\chi N}$).

is enhanced in targets with sizeable angular momentum, while SI receives an enhancement for targets with a higher atomic mass ($\frac{dR(E_R,t)}{dE_R} \propto A^2$).

Backgrounds

With such a low expected interaction rate, direct detection experiments are considered a rare event search where understanding of the background events is critical. The origins of these events can be broken down into three categories: radioactive decay of the materials that comprise the detector, cosmics and decays from the surrounding environment. To reduce background events from the detector material itself many experiments have placed an intensive effort into producing a highly stable, radio-pure, shielded detector in recent years; with each generation of detectors driving the detection threshold to ever lower energies. Typical interaction detection thresholds are now a few keV. However, techniques such as those that exploit Bremsstrahlung or the Migdal effect have shown the capability of observing sub-keV interactions [84]. These techniques give improved sensitivity for lower mass DM. By locating the detector deep underground, and surrounding it with further shielding, the contribution of cosmics towards the observed background rate is dramatically reduced. Further reduction is achievable by adding a suitable veto system for muon, gamma and neutron interactions with the main detector.

The event rate of DM interactions in a direct detection experiment scales directly with the detectable volume, setting the overall sensitivity. Increasing the sensitivity comes with a drawback; the increased likelihood of observing neutrinos scattering elastically with electrons and coherent neutrino scattering with nuclei in the target. It is not possible to shield from neutrinos. Therefore, the continuous flux from both solar and atmospheric neutrinos represents an irreducible background. Experiments are attempting to circumvent this 'neutrino floor' by designing the detectors to identify the direction of the incoming particle [85]. Events that appear to originate from the Sun would be discernible, allowing observation of the annual modulation induced by the Earths changing direction with respect to the DM originating from the halo. The rotation of the Earth about the Sun also causes a variation in the velocity of the incident DM particle. If the detector is in a suitable location, then this modulation in the rate may also be observable [86].

Direct Detection Experiments and Constraints

Direct detection searches are currently focused towards the detection of WIMP-like DM; with searches for other DM candidates such as axions, ALPS and dark photons also being

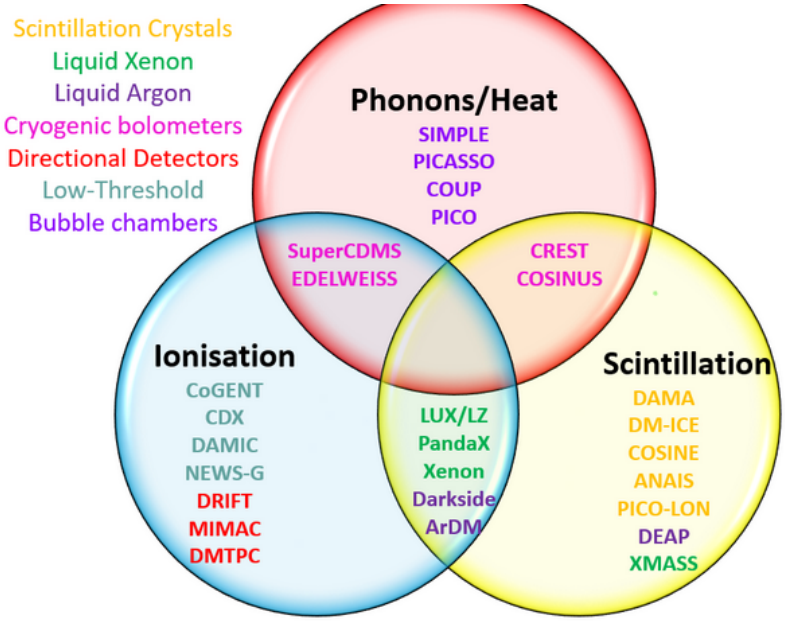

Figure 1.9: Venn diagram of the different direct detection experiments grouped by type of detected energy deposition. Each detector name is coloured according to the type of detector and indicated in the key in the top left. Information in part collated from [87].

undertaken. Experiments are generally categorised into the type of detection material they use (semiconducting crystals, superheated liquids, noble liquids and multi-atomic crystals, for example) and the type of energy deposition they attempt to observe. Figure 1.9 shows the grouping of different direct detection experiments based on whether they observe an ionisation (charge), scintillation (light) or phonon (heat) signature. The mechanism for producing these energy depositions from an incoming particle interaction with a xenon atom is given in §3.1, and how the ionisation and scintillation signals are then observed within a Time Projection Chamber (TPC) in §3.2. A list of the main experiments, their target material, fiducial mass [17], the limit set on the SI cross-section, the DM mass this was achieved at, and the reference of the relevant analysis paper is given in Table 1.1.

Solid-state cryogenic detectors combine bolometric techniques with the readout of either charge or light. A wide range of target materials have been used: SuperCDM at Soudan uses a combination of silicon and germanium [93], pure germanium such as EDELWEISS at Laboratoire Souterrain de Modane [99] and calcium tungsten oxide (CaO_4W) is used as the detection volume of CRESST at Laboratori Nazionali del Gran Sasso (LNGS) [98]. This choice of detection material allows for an optimised search for low mass DM; down to ~ 0.2 GeV/c^2. SuperCDMS placed an upper limit on DM interacting with elec-

[17] The fiducial mass is the mass contained within the detector's volume from which signals are considered.

Experiment	Target	Fiducial mass [kg]	Cross Section [cm^2]	DM mass [GeV/c^2]	Ref.
High mass (>5 GeV/c^2)					
XENON1T	Xe	1042	4.1×10^{-47}	30	[88]
PandaX-II	Xe	364	8.6×10^{-47}	40	[89]
LUX	Xe	118	1.1×10^{-46}	50	[90]
DEAP-3600	Ar	2000	3.9×10^{-45}	50	[91]
DarkSide-50	Ar	46	1.14×10^{-44}	100	[92]
SuperCDMS	Ge	12	1.0×10^{-44}	100	[93]
Low mass (<5 GeV/c^2)					
Ionisation only					
XENON1T	Xe	1042	3.6×10^{-41}	3	[94]
DarkSide-50	Ar	20	1.0×10^{-41}	2	[95]
High voltage ionisation					
CDMSLite	Ge	0.6	2.0×10^{-40}	2	[96]
Single scintillation photon					
LUX	Xe	118	8.0×10^{-40}	2.5	[97]
Phonon and scintillation					
CRESST	CaO_4W	0.023	1.0×10^{-39}	2	[98]

Table 1.1: Best constraints on the WIMP-nucleon SI cross-section at both high and low masses. Low mass searches have been group by the type of signature the analysis was conducted on.

trons for masses between (0.5 - 104) MeV/c^2, dark photon kinetic mixing for masses in range (1.5 - 40) eV/c^2 [100] and whilst running in a high-bias detector environment (CDMSLite) has set bounds on the SI cross-section of 2×10^{-40} cm^2 for DM mass of 2 GeV/c^2 [96].

A multitude of direct detection searches have opted to use Liquid Argon (LAr) or Liquid Xenon (LXe) as the target material. The majority of these searches use a TPC; the mechanism of this type of detector will be given in §3.2 with specific reference given to the LUX-ZEPLIN (LZ) experiment. Figure 1.10 shows that LXe TPCs currently provide the best constraints for the SI cross-section for WIMP-like DM ($\gtrapprox$ 2GeV/c^2) interaction with a nucleon. Analysis of the Nuclear Recoil (NR) ionisation and scintillation signals have allowed these experiment to probe masses down to $\approx$ 6 GeV/c^2. The most stringent

limit on the cross-section for SI interactions of 2.1×10^{-47} cm^2 at 30 GeV/c^2 was set by the XENON1T experiment at LNGS [88]. Other leading LXe TPCs include the LUX experiment previously at the Sanford Underground Research Facility (SURF) [90] and PandaX-II at China Jinping Underground Laboratory (CJPL) [89]. LAr TPCs suffer from having a higher required energy threshold for the interaction, but benefit from having the capability to perform pulse shape discrimination to identify Electronic Recoil (ER) from NR interactions. Currently the most stringent SI limits from LAr TPCs are being set by DEAP-3600 at SNOLAB [91] and DarkSide-50 at LGNS [92].

For lower mass searches both XENON1T and DarkSide-50 have employed an ionisation channel only search; elevating the need to have a detectable scintillation signal thus reducing the minimum recoil energy threshold of the detector and allowing studies of DM masses of $\propto 2$ GeV/c^2. The LUX collaboration, for their low mass analysis, instead opted to maintain observing the combined ionisation and charge signatures while considering scintillation signals containing only a single observed photon. By doing so, they were able to maintain the ability to discriminate between NR and ER events, unlike in an ionisation channel only search.

Currently, the next generation of liquid noble TPCs is under construction: DarkSide-20k at LNGS [101], LZ at SURF [102], PandaX-4T at CJPL [103] and XENONnT at LGNS [104]. These detectors will have a significantly increased fiducial mass and reduced background; leading to an expected increase in the sensitivity of SI DM interactions by 1-2 orders of magnitude, potentially reaching the neutrino floor.

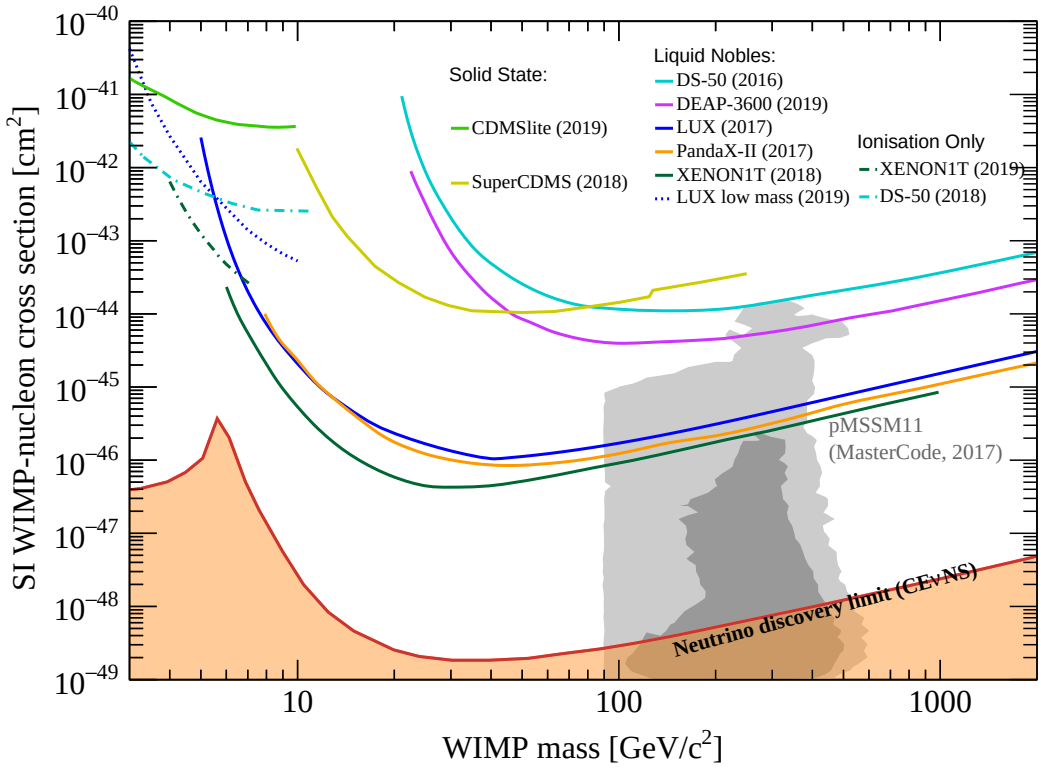

Figure 1.10: Upper limits on the SI WIMP-nucleon cross-section as a function of WIMP mass from various LAr TPCs, LXe TPCs and solid-state detectors. Low mass searches from liquid noble TPCs are indicated by dotted and dashed lines. Individual references and overall limit of included experiment are given in Table 1.1. The background arising from coherent scattering of neutrinos with the target is given by the shaded region [105, 106]. Additionally, the favoured regions from the pMSSM11 model scans have been included [107]. Figure updated from [108] with consent from the author.

Chapter 2

Direct Detection of WIMPs

With such compelling evidence and complementarity in search techniques, outlined in Chapter 1, it is quite remarkable that DM has persistently eluded detection. This chapter will focus on direct detection techniques, specifically the direct detection of WIMP-nucleon interactions. It will start with the interaction's kinematics used to derive the critical formula in direct detection searches, the differential interaction rate. Following this will be an outline of the local astrophysical DM properties: local density and velocity distributions. The chapter concludes with the derivation of both the SI and SD WIMP-nucleon cross-sections and the resultant differential rate for both interaction types.

2.1 WIMP-Nucleus Interaction Rate

One of the key quantities in direct detection is the recoil energy of the recoiling nucleus, E_R. WIMPs, being non-relativistic DM particles, with mass m_χ and velocity v are expected to elastically scatter with a nucleus of mass m_A, with a recoil energy dependent on the DM scattering angle θ [78]:

$$E_R = \frac{1}{2} m_\chi v^2 \frac{4 m_\chi m_A}{(m_\chi + m_A)} \frac{1 + cos\theta}{2}. \tag{2.1.1}$$

A maximum recoil energy occurs when the collision is head on and $m_\chi = m_A$. Taking a typical halo velocity of $v \sim 200$ kms^{-1}:

$$E_R^{max} = \frac{1}{2} m_\chi v^2 = \frac{1}{2} \left(\frac{m_\chi}{1\text{GeV}} \right) \text{keV}. \tag{2.1.2}$$

For a $m_\chi \sim 100$ GeV/c^2, the maximum recoil energy is expected to be ~50 keV; setting the search Region Of Interest (ROI) for the majority of direct detection experiments. Using the same estimated velocity, and a local DM density of $\rho_0 = 0.3$ GeV cm^{-3}, details of

both given in §2.2, it is possible to estimate the local flux of DM particles[1]:

$$\Phi = nv = \frac{v\rho}{m} \approx \frac{10^7}{m_{\mathrm{DM}}}\ \mathrm{cm}^{-2}\mathrm{s}^{-1}; \tag{2.1.3}$$

where n is the number density. From this, the expected rate, R, of DM particles observed within a detector is given by:

$$R = N/t = nvN_T\sigma. \tag{2.1.4}$$

N being the number of observed DM particles, N_T the number of target nuclei, σ the interaction cross-section and t the time of the observation. As previously shown there is a range of recoil energies that can be induced. With a spectrum of recoils such as this, it is better to describe the number of detected particles based on this energy dependency:

$$\frac{dR}{dE_R} = nvN_T\frac{d\sigma}{dE_R}. \tag{2.1.5}$$

The velocity of halo DM is not a fixed value, but a distribution. Integrating over all possible velocities, in the detector frame, with corresponding probability distribution, gives:

$$\frac{dR}{dE_R} = nN_T\int_{v_{\mathrm{min}}} vf(\vec{v})\frac{d\sigma}{dE_R}d\vec{v}. \tag{2.1.6}$$

The value for the minimum velocity, v_{min}, is set by the specific detector threshold of observable recoil energy, $E_{R,Threshold}$:

$$v_{\mathrm{min}} = \sqrt{m_\chi E_{R,Threshold}/2\mu_{\chi A}^2}. \tag{2.1.7}$$

For WIMPs, $\mu_{\chi A} = (m_\chi \times m_A)/(m_\chi + m_A)$, is the reduced mass of the WIMP-nucleus system. Additionally, by converting from the number of targets to a detector mass, M_T, the familiar form of the differential rate[2] is retrieved:

$$\frac{dR}{dE_R} = \frac{\rho}{m_\chi m_A}\int_{v_{min}} vf(\vec{v})\frac{d\sigma}{dE_R}d\vec{v} = \frac{2\rho}{m_\chi}\int_{v_{min}} vf(\vec{v})\frac{d\sigma}{d|q|^2}d\vec{v}, \tag{2.1.8}$$

where $q = \sqrt{2m_A E_R}$ is the exchange momentum of the interaction.

2.2 Local Astrophysical Dark Matter Properties

A thorough understanding of DM's astrophysical properties in our Galaxy is crucial for direct and indirect detection. This section will describe the local density, the expected distribution and the velocities of DM bound within our Galaxy.

[1] The resultant flux is on the same scale as expected from a weak interaction.

[2] $N_T = \epsilon\frac{M_T}{m_N}$, and assuming a detectors efficiency at the ranges of recoil energies of ϵ=1.

Local Dark Matter Density

The differential interaction rate, Eq. (2.3.16), shows a dependence on the local DM density, ρ_0. The uncertainty of ρ_0 imposes limitations on the accuracy and precision of any DM measurements or constraints. Methods to ascertain a value of ρ_0 fall into two categories: local measures generally observe tracer star motion in the vicinity of the Sun; while galactic measures derive ρ_0 from observations of rotation curves. However, this does require assumptions on the shape of the galactic halo [109]. One of the leading uncertainties on ρ_0 stems from the contribution from baryons to the local dynamic mass [110]. This is specifically distinct in methods involving tracer stars, where the motion is influenced by the baryon and DM potentials. The variation in measured value is significant in both global and local measures. Galactic measures place ρ_0 in the range 0.2 - 0.6 GeV/cm^3, while recent studies of data from Gaia place local values at 0.1 - 1.5 GeV/cm^3 (depending on the studied star type) [111]. Figure 2.1 shows how this uncertainty on ρ_0 influences the overall sensitivity to SI WIMP-nucleon interactions in a LXe TPC direct detection experiment. It can be seen that ρ_0 simply acts as a scaling value (as evident by its placement in Eq. 1.3.2). Within direct detection experiments it has become customary to set ρ_0 ~0.3 GeV/cm^3; allowing for ease of comparison between the limits set by different experiments. A drawback does arise in the scenario of a viable WIMP-nucleon event being detected; the uncertainty on ρ_0 would result in uncertainties on the exact mass and cross-section of

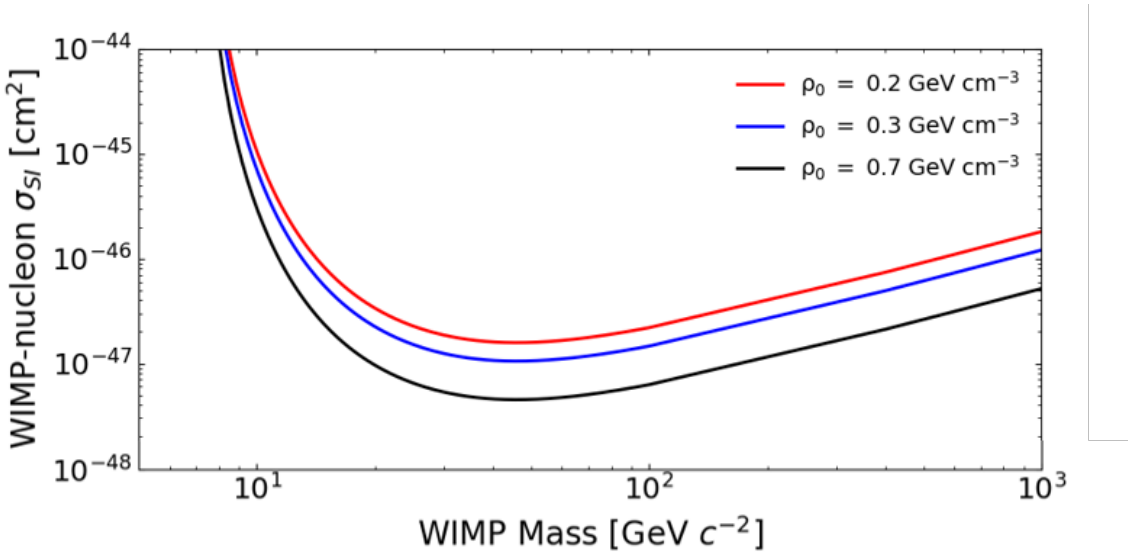

Figure 2.1: Influence of the uncertainty of ρ_0 on the expected SI WIMP-nucleon interaction cross-section as a function of WIMP mass [110].

the WIMP[3].

Dark Matter Velocity Distribution

To date, measurements of the local velocity distribution of DM are not possible, placing a high reliance on simulated models. It has been commonplace in experiments to use a simple isotropic, isothermal (or a Navarro-Frenk-White profile [112]) sphere of DM, the Standard Halo Model (SHM) [113]; with $\rho(r) \propto r^{-2}$. The SHM assumes a Maxwellian velocity distribution, $f(\vec{v})$ with a dispersion of $\sigma_v = v_0/\sqrt{2}$; v_0 being the average local circular velocity. Formulaically the SHM extends to infinity, truncating at the escape velocity ($v_{\rm esc}$) places the constraint that the DM must be bound to our Galaxy, to do so the Heaviside function, Θ, is used [114]:

$$f(\vec{v}) = \frac{1}{(2\pi\sigma_v^2)^{3/2} N_{\rm esc}} \exp\Big(-\frac{|\vec{v}|^2}{2\sigma_v^2}\Big)\ \Theta(v_{\rm esc} - |\vec{v}|). \tag{2.2.1}$$

To allow the integral of σ_v to be unitary, as required in the rate formula, the Maxwellian is renormalised by:

$$N_{\rm esc} = \mathrm{erf}(z) - 2z\ \exp(-z^2)/\pi^{1/2}, \tag{2.2.2}$$

where erf() is the error function and $z = v_{\rm esc}/v_0$. By truncating the function based on conditions of the WIMP velocities, these being the previously mentioned z, along with $x = v_{\rm min}/v_0$ and $y = |V_E|/v_0$ ($|V_E|$ being the velocity of the Earth with regards to the DM halo), a calculable form is retrieved [83]:

$$\int_{v_{\rm min}}^{v_{\rm max}} \frac{f(\vec{v})}{v} = \begin{cases} \frac{1}{v_0 y} & \text{if } z < y,\ x < |y-z| \\ \frac{1}{2N_{\rm esc} v_0 y}\left[\mathrm{erf}(x+y) - \mathrm{erf}(x-y) - \frac{4}{\sqrt{\pi}} y e^{-z^2}\right] & \text{if } z > y,\ x < |y-z| \\ \frac{1}{2N_{\rm esc} v_0 y}\left[\mathrm{erf}(z) - \mathrm{erf}(x-y) - \frac{2}{\sqrt{\pi}}(y+z-x) e^{-z^2}\right] & \text{if } |y-z| < x < y+z \end{cases} . \tag{2.2.3}$$

In this form, the velocity distribution can be parameterised by three velocities: v_0, $v_{\rm esc}$ and $v_{\rm min}$. As previously stated v_0 is the average local circular velocity. An assumption is made that the Sun's rotational velocity around the Milky Way's centre, $v_0 = 220$ km s^{-1}, matches this value. The assumption may be valid, however measurements of the velocity have been shown to vary depending on the study performed; recent observations give a

[3]It should be noted the mass of the WIMP also appears in the recoil energy spectrum and with a sufficient number of observed events this uncertainty would decrease.

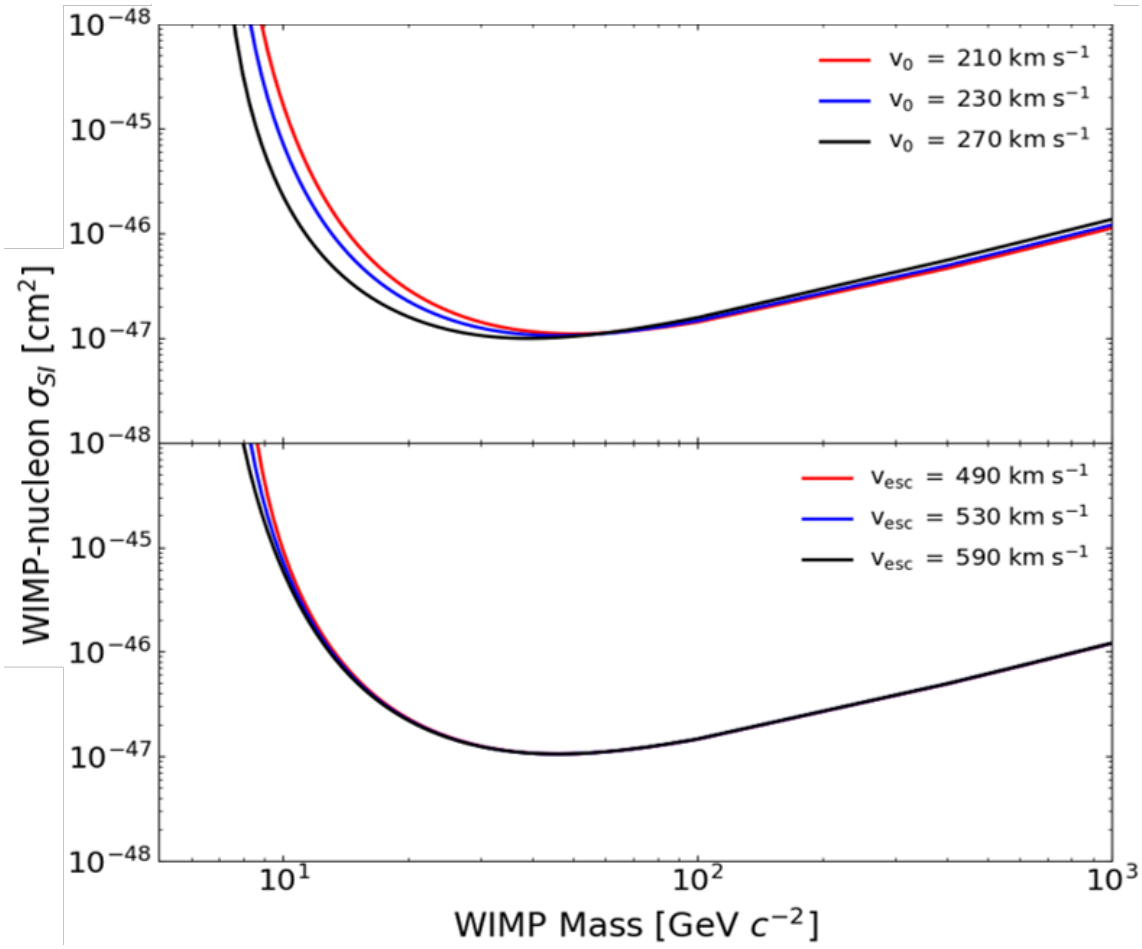

Figure 2.2: Influence of the uncertainty on v_0 (**top**) and v_{esc} (**bottom**) on the expected SI WIMP-nucleon interaction cross-section as a function of WIMP mass. Edited from version presentation in [110].

value of 238 ± 15 km s^{-1} [115]. It is commonplace in direct detection experiments to use $v_{esc} = 544$ km s^{-1}; originating from the RAVE survey of 12 high-velocity stars. More recently, data obtained by the Gaia satellite has led to revisions of this number; initially placing it at 580 ± 63 km s^{-1} [116] and revised again to 528^{+24}_{-25} km s^{-1} [117]. Finally, v_{min} can have a range of values as given by Eq. (2.1.7).

Figure 2.2 shows how the uncertainties on v_0 (**top**) and v_{esc} (**bottom**) influence the overall sensitivity to SI WIMP-nucleon interactions in a LXe TPC direct detection experiment. Variations in v_0 have more of an impact on the overall SI WIMP-nucleon cross-section for low masses, with any deviations becoming negligible by ~ 40 GeV/c^2. Variations in v_{esc} only cause marginal changes in the sensitivity for the very lightest WIMP masses generally considered in LXe TPC DM searches.

Another source of potential uncertainty stems from the assumed model of the velocity

distribution itself. Recent data collected by the Gaia satellite suggests that the velocity distribution of halo DM in the Milky Way is not purely homogeneous and isotropic as described by the SHM [118, 119]. In fact, it appears that a significant fraction of the Milky Way's halo DM is comprised of a strongly radially anisotropic population, which should also be considered along with the components of the SHM; this new model is referred to as SHM++. Within [118] the authors construct a five parameter analytic model to describe the DM halo with the inclusion of this new population. These parameters include the three original from the SHM: the circular velocity, the local escape velocity and local DM density, and two additional parameters: the anisotropy and density of this new component. A separate determination of the SHM++ is given in [119], where they have used metal-poor halo stars as effective traces of the DM in the halo. In contrast to the SHM, the SHM++ is shifted to higher velocities with an elongated tail. These changes are heavily influenced by the assumed larger values attributed to v_0 and v_{esc}, and are not solely attributed to the introduction of an anisotropic component [118]. The influence of the anisotropy is most significant in the notable increase of the velocity distribution's peak height. Additionally, the dispersion within the SHM++ is decreased, making this distribution cooler than a halo comprising only a homogeneous round isotropic component. Many direct detection DM experiments still opt to use the SHM over the SHM++. In part, this is due to the substantial discrepancies found in [118, 119] by studies conducted using Auriga high-resolution magneto-hydrodynamical simulations [120], suggesting that additional studies need to be performed before adoption of the new model into general analyses.

2.3 Spin Independent and Spin Dependent WIMP-Nucleon Cross-Sections

Along with the WIMP mass, the other key parameter for direct detection searches is the WIMP-nucleon interaction cross-section. As previously mentioned, this interaction can either have a dependence on the spin of the interacting particles or not. The following section will go through the derivation of the SI and SD WIMP-nucleon cross-section, following the procedure set out in [78]. The WIMP-nucleon cross-section can be related to the momentum transfer, and the WIMP-nucleon scattering amplitude, $\mathcal{M}$, by:

$$\frac{d\sigma}{d|q|^2} = \frac{1}{\pi v^2}|\mathcal{M}|^2. \tag{2.3.1}$$

As $|\mathcal{M}|^2 = \pi G_F^2 C F^2(q)$, the momentum dependency of the target nucleus can be factorised out into a nuclear form factor, $F^2(q)$. This form factor contains information on the nature

of the interaction. G_f is the standard Fermi constant, and C is a dimensionless variable containing the details of the interaction. Thus, Eq. (2.3.1) can be rewritten as:

$$\frac{d\sigma}{d|q|^2} = \frac{G^2}{v^2} F^2(q). \tag{2.3.2}$$

For non-relativistic scattering, only the interactions which do not vanish in the limit of zero-momentum transfer are considered to be allowed, with all others being suppressed. The corresponding cross-section, $\sigma_{0\chi A}$, will be referred to as the zero-momentum cross-section from here, and when integrating over $d|q|^2$:

$$\sigma_{0\chi A} = \int_0^{4\mu_{\chi A}^2 v^2} \frac{d\sigma}{d|q|^2}(q=0)\, d|q|^2 = 4G_F^2 \mu_{\chi A}^2 C. \tag{2.3.3}$$

The lack of form factor suppression in the above makes it somewhat arbitrary and therefore should only be taken as a representation of the interaction cross-section. Placing this into Eq. (2.3.2), gives:

$$\frac{d\sigma}{d|q|^2} = \frac{\sigma_{0\chi A}}{4\mu_{\chi A}^2 v^2} F^2(q). \tag{2.3.4}$$

To allow for complementary limits to be set by different target nuclei, it is better to work with the WIMP-nucleon zero-momentum cross-section. Doing so only preserves two forms of interaction: Spin Independent (SI) and Spin-Dependent (SD).

Spin Independent Interactions

SI interactions are scalar and have an effective WIMP-nucleon Lagrangian of [78]:

$$\mathcal{L}_{SI} = f_p \bar{\chi}\chi\bar{p}p + f_n \bar{\chi}\chi\bar{n}n, \tag{2.3.5}$$

with a scattering amplitude of:

$$|\mathcal{M}_{SI}|^2 = [f_p Z + f_n(A-Z)]^2; \tag{2.3.6}$$

hence C_{SI} becomes:

$$C_{SI} = \frac{1}{\pi G_F^2}[f_p Z + f_n(A-Z)]^2. \tag{2.3.7}$$

This results in a zero-momentum cross-section for WIMP-nucleon interaction of:

$$\sigma_{0\chi N} = \frac{4\mu_{\chi N}^2}{\pi}[f_p Z + f_n(A-Z)]^2. \tag{2.3.8}$$

A and Z take their normal meanings of atomic mass and atomic number respectively. From this point a restriction to isospin conserving models ($f_p \sim f_n \sim f_N$) will be applied[4]:

$$\sigma_{0\chi N=} = \frac{4\mu_{\chi A}^2}{\pi} f_N A^2 = \frac{\mu_A^2}{\mu_N^2} A^2 \sigma_{0\chi A}. \tag{2.3.9}$$

[4]The majority of spin-independent direct detection searches focus on such models.

The presence of A^2 in Eq. (2.3.9) is the cause of the well known enhancement in scattering rate observed with increasing atomic mass of the target. The above cross-section, when substituted into Eq. (2.1.8) gives the SI differential recoil spectrum for WIMP-nucleon elastic scattering to be:

$$\left(\frac{dR}{dE_R}\right)_{SI} = \frac{2\rho_0}{m_\chi}\int_{v_{min}} vf(\vec{v})\left(\frac{A^2\sigma_0}{4\mu_N^2 v^2}F^2(q)\right)d\vec{v}. \tag{2.3.10}$$

Spin Dependent Interactions

Consideration of SD, axial interactions, requires a different Lagrangian. The following is specific to spin 1/2 Majorana WIMPs [78]:

$$\mathcal{L}_{SD} = f_p\bar{\chi}\gamma^\mu\gamma 5\chi\bar{p}\gamma_\mu\gamma 5p + f_n\bar{\chi}\gamma^\mu\gamma 5\chi\bar{n}\gamma_\mu\gamma 5n. \tag{2.3.11}$$

The convention is to equate the scattering amplitude to the spin content of nucleons in the nucleus. By using $f_N = \sqrt{2G_f}a_N$ the scattering amplitude is written as:

$$|\mathcal{M}_{SD}|^2 = 8G_F^2\frac{J+1}{J}[a_p\langle S_p\rangle + a_n\langle S_n\rangle]^2, \tag{2.3.12}$$

where $\langle S_p\rangle$ and $\langle S_n\rangle$ are the proton and neutron spin contents. This gives a dimensionless quantity for SD interactions of:

$$C_{SD} = \frac{8}{\pi}\frac{J+1}{J}[a_p\langle S_p\rangle + a_n\langle S_n\rangle]^2, \tag{2.3.13}$$

and a corresponding cross-section of:

$$\sigma_{0\chi A} = \frac{32}{\pi}G_F^2\mu_N^2\frac{J+1}{J}[a_p\langle S_p\rangle + a_n\langle S_n\rangle]^2. \tag{2.3.14}$$

Under the single shell model assumptions [78], it is valid to consider that the total spin contribution of a nucleus ($\langle S_N\rangle$) is only from the unpaired nucleon[5], and this is the reason why searches for SD WIMP-nucleon interactions favour proton or neutron rich targets. Converting Eq. (2.3.3) by the ratio of $\sigma_{0\chi A}$ to the number of free nucleons in the nucleus and substituting in Eq. (2.3.13), allows the conversion between the WIMP-nucleon and the WIMP-nucleus zero-momentum-transfer cross-section[6]:

$$\sigma_{0\chi A} = \frac{4}{3}\frac{J+1}{J}\frac{\mu_A^2}{\mu_N^2}\langle S_N)\rangle^2\sigma_{0\chi N}. \tag{2.3.15}$$

Finally the differential rate for SD WIMP-proton (neutron) interactions can be written as:

$$\left(\frac{dR}{dE_R}\right)_{SD} = \frac{2\rho_0}{m_\chi}\int_{v_{min}} vf(\vec{v})\left(\frac{1}{3\mu_N^2 v^2}\frac{J+1}{J}\langle S_N\rangle^2\sigma_{0\chi N}F^2(q)\right)d\vec{v}. \tag{2.3.16}$$

[5] i.e. for an unpaired neutron, $\langle S_p\rangle$ =0.

[6] Assuming that $J_N = \langle S_N\rangle$.

Form Factor

The last term to discuss in the scattering rate equation, other than astrophysical parameters, is the form factor $F^2(q)$. The form factor incorporates the physics of the scattering amplitude of an incoming particle on a signal atom. With DM velocities expected to be $v/c \sim 10^{-3}$, nuclear recoils will have energies of no more than a few tens of keV; smaller than the typical nuclear binding energy per nucleon.

For SI interactions, the Helm form factor, solid spherical atoms with a smooth density of nucleons from the skin to the centre, is adopted [121]:

$$F(q)^2 = \left(\frac{3j_i(qr_n)}{qr_n}\right)^2 e^{-q^2s^2}, \tag{2.3.17}$$

where the inverse of the momentum transfer, $q \equiv \sqrt{2m_N E_R} \sim \mathcal{O}(10 \text{ - } 100)$ MeV, is of the same order as nuclear radii, $R \sim A^{1/3}$ fm; therefore, a DM particle will not resolve a nucleus as a point-like object. Here j_i is the Bessel function, r_n is the reduced nucleon radius[7] and s is the nucleon skin depth ($\sim$ 1 fm). An interesting effect occurs as the de Broglie wavelength of the incident particle approaches the size of the atomic radius ($\lambda_b = h/q \approx r_n$); a loss of coherence occurs due to the particle no longer being able to resolve the atom. Therefore, a significantly reduced interaction rate is expected at a recoil energy which is governed by the atomic mass of the target:

$$E_R \approx 0.7 \frac{h^2}{2m_N \cdot A^{2/3}}. \tag{2.3.18}$$

Figure 2.3 shows the form factor for several different elements, where the atomic number stated has been weighted based on the relative natural abundance of each isotope; the loss of coherence can be seen in the Xe line.

[7] It is common to adopt the Lewin-Simth parameterisation [83], where $r_n = \sqrt{c^2 + 7/3\pi^2 a^2 - 5s^2}$, $c = 1.23\text{A}^{1/3}$-0.6 fm and a = 0.52 fm.

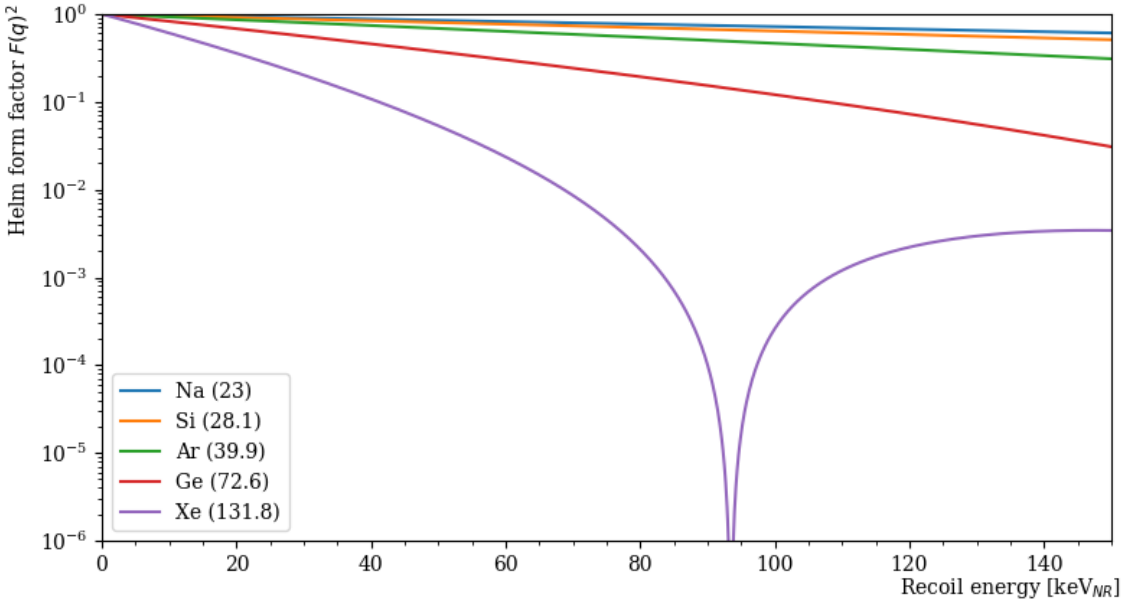

Figure 2.3: Form factor of various elements represented by atomic weight given by relative natural abundances.

2.4 Effective Field Theory; A Model Independent Approach

With ever-improving SI and SD WIMP-nucleon limits being set by direct detection experiments, the assumption of a momentum-independent WIMP-nucleon interaction becomes less acceptable. In both the SI and SD interaction, the momentum-dependence is suppressed due to the WIMPs' non-relativistic velocities in the nucleus frame; hence, both use a zero-momentum cross-section. However, this assumption may oversimplify the dynamics of the interaction. The momentum-independent interaction may have some momentum-dependent component, which could suppress the momentum-independent terms and leave only those that are momentum-dependent. Additionally, when considering the interaction on a nucleon rather than a nucleus scale, the interaction's momentum is no longer negligible. The characteristic momentum transfer of the interaction given by the inverse of the size of the nucleus. When considering the parton scale, this is no longer small and assumes that the momentum transfer is non-negligible [122]. For these reasons, it appears that the best approach would be to consider the WIMP-nucleon interaction in a model-independent way. As DM does not fit in the SM, and knowledge of its physics at high-energy scales is not known, the most valid description of the interaction would be produced through an Effective Field Theory (EFT) [123].

EFTs allow for a parameterisation of an unknown model to an arbitrary accuracy by only describing the physics at some scale [123]; this could be in terms of energy, momentum or velocity as in quantum electrodynamics. Using velocity as an example and setting the scale to v^2, the detailed dynamics of the interaction would be described up to some cut off scale $\Lambda^2 >> v^2$ for $\frac{\Lambda^2}{v^2}$. The physics at higher scales is not neglected; it is simply folded into the dynamics by integrating out the delta functions [124].

To prevent divergences arising in the derivation, power counting according to [125] is applied. The result is an understanding of the relevant degrees of freedom in the interaction, which could highlight any underlying symmetries. From these symmetries a leading-order description can be developed and the Lagrangian to describe the interaction can be written.

With the extensive framework of possible WIMP-nucleon interactions and the lack of detection through the simple SI and SD models, it is only natural to apply an EFT to WIMP DM through direct detection. Fitzpatrick et al. have developed such an EFT where all possible interactions in the non-relativistic limit for fermionic WIMP-nucleon scatter have been determined [126]. The resultant form factors that describe all possible interactions have been scripted into a Mathematica package by Anand et al. [127], which

allows for a determination of the expected differential recoil rate for these interactions.

To allow for the determination of WIMP-nucleon scatters in the scenario where there is some form of energy transfer between the WIMP and the nucleon, Barello et al. [84] shows the modifications required to the derivation presented in [126], where they note that the only changes to the scattering amplitude and hence resultant form factors can be accounted for by an additional term associated to the velocity of the interaction. Inelastic transitions are interesting, as they could be an indication of a potential underlying sub-structure within WIMPs.

The following is the derivation set out by Fitzpatrick et al. in [126] including, where appropriate, the modifications by Barello et al. [128] to allow for the determination of inelastic[8] scattering rates within this non-relativistic model-independent approach to WIMP-nucleon interactions.

2.4.1 Kinematics and Allowed Operators

The WIMP-nucleon scattering can be considered as a four-field contact interaction [126]. A field is associated to each of the incoming and outgoing WIMPs (χ) and nucleons (N). The corresponding interaction Lagrangian is given as:

$$\mathcal{L}_{\text{int}} = c\chi^{+}\mathcal{O}_{\chi}\chi^{-}N^{+}\mathcal{O}_{N}N^{-} \equiv c\mathcal{O}\chi^{+}\chi^{-}N^{+}N^{-}. \tag{2.4.1}$$

Here $\mathcal{O}$ has been introduced to represent the effective operators, and c (the effective operator coefficient) to account for any higher-order physics not included due to the lack of consideration of the mediator in the interaction.

From this, it is possible to construct a generalised description of all possible and allowed WIMP-nucleon interactions within the imposed four-field symmetries, all of which must be Galilean invariant as this is a non-relativistic theory. Within this framework, the exchange momentum ($\vec{q}$), the WIMP velocity in the nucleon frame ($\vec{v} \equiv \vec{v}_{\chi,\text{in}} - \vec{v}_{N,\text{in}}$), and the spins of the particles ($\vec{S}_{\chi}$ and $\vec{S}_{N}$) are all Galilean invariant.

For inelastic interactions, the kinematics require alteration, where the dynamics of the scatter are described by:

$$\chi_1(\vec{p})\ N(\vec{k}\,) \rightarrow \chi_2(\vec{p}\,')\ N(\vec{k}\,')\ , \tag{2.4.2}$$

which includes the incoming (χ_1) and outgoing (χ_2) WIMP, and the nucleon N. Additionally $\vec{p}$ and $\vec{p}\,'$, and $\vec{k}$ and $\vec{k}'$ are the initial and final momenta of the WIMP and

[8] Focus is given to the inelastic derivation as this will be used later in the analysis presented in Chapter 5.

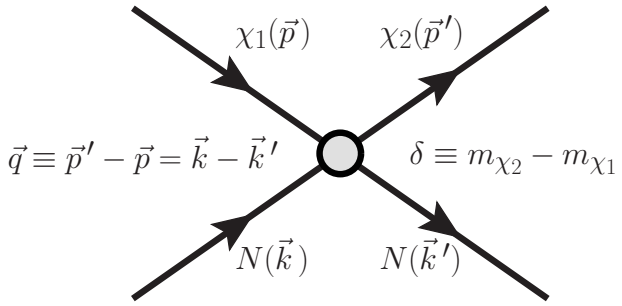

Figure 2.4: Diagram of the inelastic WIMP-nucleon interaction [128].

nucleon respectively. An illustration of this is given in Figure 2.4, where a new term ($\delta_m = m_{\chi_2} - m_{\chi_1}$) is introduced to account for the mass splitting between the incoming and outgoing WIMP. To leading order δ_m is the required energy to allow a transition to occur. A positive δ_m implies that WIMPs will favour scattering with heavy nuclei, and there should be an expected increase in the annual modulation signal [129]. Whereas a negative δ_m provides an interesting scenario where the transition is exothermal, potentially implying some underlying substructure to WIMPs, which allows for excitation of internal degrees of freedom [130]. In order to perform a consistent expansion of velocities, the exact mass splitting must scale with $\delta_m \sim O(v^2)$ and splitting should be considered in the range $\delta \sim 100\text{keV}\left(\frac{\text{m}_\chi}{100\text{GeV}}\right)$.

To determine the degrees of freedom within the velocity expansion of this EFT for inelastic interactions, a common velocity shift is applied to the Galilean invariant constraints[9]. This results in two relevant boost invariant vectors:

$$\vec{v} \equiv \vec{v}_{\chi_1} - \vec{v}_{N_{in}} = \vec{p}/m_{\chi_1} - \vec{k}/m_N,$$
$$\vec{q} = \vec{p}\,' - \vec{p} = \vec{k} - \vec{k}'.$$

As a result of introducing δ_m, $\vec{p} - \vec{p}\,'$ is no longer fully Galilean invariant; in contrast to the elastic derivation. However, it is still invariant to leading order in a velocity expansion and hence holds as a valid approximation for a non-relativistic theory. In addition to the invariant vectors there are two boost invariant scalars: the WIMP masses and δ_m.

The next stage of the derivation is to impose Hermiticity on the interaction. Parameters such as $\vec{S}_\chi$ and $\vec{S}_N$ are already Hermitian, but those related to $\vec{q}$ and $\vec{v}$ are not. As $\vec{q}$ is anti-Hermitian, it can simply be replaced with the complex conjugated form $i\vec{q}$. However, this is not the case for $\vec{v}$, which requires a replacement with the velocity perpendicular to

[9] An alternative derivation taking the non-relativistic limits from the relativistic expansion is also given in [128].

the momentum transfer ($\vec{v}^{\perp}$).

Before proceeding further with the derivation of the kinematics of the interaction, both [128] and [126] construct orthogonal vectors[10] in the centre of mass frame of the interaction (i.e. the nucleon frame):

$$\vec{v}_{\chi_1} = \frac{\mu_N}{m_{\chi_1}}\vec{v}, \quad \vec{v}_{N_{in}} = -\frac{\mu_N}{m_N}\vec{v}, \tag{2.4.3}$$

where μ_N still retains its previous definition of being the reduced mass of the WIMP-nucleon system, and m_N is still taken as the nucleon's mass. For the inelastic interaction, the WIMP mass will always be attributed to the incoming WIMP (m_{χ_1}).

With these orthogonal basis vectors, it is now possible to expand the initial energy (E_{in}) for the interaction to second order:

$$E_{in} \approx m_{\chi_1} + m_N + \frac{1}{2}\mu_N v^2. \tag{2.4.4}$$

To perform the expansion to retrieve the final energy of the interaction, the following momentum exchanges are required: $\vec{p}' = \vec{p} + \vec{q}$ and $\vec{k}' = \vec{k} - \vec{q}$. Giving:

$$E_{out} = m_{\chi_2} + m_N + \frac{1}{2m_{\chi_2}}|\vec{p}+\vec{q}|^2 + \frac{1}{2m_N}|\vec{k}-\vec{q}|^2 \approx E_{in} + \delta_m + \vec{v}\cdot\vec{q} + \frac{|\vec{q}|^2}{2\mu_N},$$

where momenta have been treated in orders of v and δ_m in v^2. Applying conservation of energy constraints enforces the requirement of:

$$\delta_m + \vec{v}\cdot\vec{q} + \frac{|\vec{q}|^2}{2\mu_N} = 0. \tag{2.4.5}$$

Placing this into the inelastic velocity gives:

$$\vec{v}^{\perp}_{\text{inel}} \equiv \vec{v} + \frac{\vec{q}}{2\mu_N} + \frac{\delta_m}{|\vec{q}|^2}\vec{q} = \vec{v}^{\perp}_{\text{el}} + \frac{\delta_m}{|\vec{q}|^2}\vec{q}. \tag{2.4.6}$$

Here, $\vec{v}^{\perp}_{\text{inel}}$ is perpendicular to $\vec{q}$, and the alterations from the elastic scenario ($\vec{v}^{\perp}_{\text{el}} = \vec{v} + \frac{\vec{q}}{2\mu_N}$) are all captured by δ_m. Therefore, the final Galilean and Hermitian invariant quantities are:

$$i(\vec{q}), \quad \vec{v}^{\perp}_{\text{inel}}, \quad \vec{S}_{\chi}, \quad \vec{S}_N. \tag{2.4.7}$$

Using these quantities, defined using the inelastic kinematics, it is possible to produce

[10] Vectors where the dot product between the two is zero, indicating they are perpendicular to one another.

all valid operators for both an elastic and inelastic non-relativistic WIMP-nucleon scatter:

$$
\begin{aligned}
&\mathcal{O}_1 = \mathbf{1}_\chi \mathbf{1}_N, \quad \mathcal{O}_2 = (v_{\text{inel}}^\perp)^2, \quad \mathcal{O}_3 = i\vec{S}_N \cdot \left(\frac{\vec{q}}{m_N} \times \vec{v}_{\text{inel}}^\perp \right), \\
&\mathcal{O}_4 = \vec{S}_\chi \cdot \vec{S}_N, \quad \mathcal{O}_5 = i\vec{S}_\chi \cdot \left(\frac{\vec{q}}{m_N} \times \vec{v}_{\text{inel}}^\perp \right), \\
&\mathcal{O}_6 = \left(\vec{S}_\chi \cdot \frac{\vec{q}}{m_N} \right) \left(\vec{S}_N \cdot \frac{\vec{q}}{m_N} \right), \\
&\mathcal{O}_7 = \vec{S}_N \cdot \vec{v}_{\text{inel}}^\perp, \quad \mathcal{O}_8 = \vec{S}_\chi \cdot \vec{v}_{\text{inel}}^\perp, \\
&\mathcal{O}_9 = i\vec{S}_\chi \cdot \left(\vec{S}_N \times \frac{\vec{q}}{m_N} \right), \quad \mathcal{O}_{10} = i\vec{S}_N \cdot \frac{\vec{q}}{m_N}, \\
&\mathcal{O}_{11} = i\vec{S}_\chi \cdot \frac{\vec{q}}{m_N}, \quad \mathcal{O}_{12} = \vec{S}_\chi \cdot \left(\vec{S}_N \times \vec{v}_{\text{inel}}^\perp \right), \\
&\mathcal{O}_{13} = i \left(\vec{S}_\chi \cdot \vec{v}_{\text{inel}}^\perp \right) \left(\vec{S}_N \cdot \frac{\vec{q}}{m_N} \right), \\
&\mathcal{O}_{14} = i \left(\vec{S}_\chi \cdot \frac{\vec{q}}{m_N} \right) \left(\vec{S}_N \cdot \vec{v}_{\text{inel}}^\perp \right), \\
&\mathcal{O}_{15} = - \left(\vec{S}_\chi \cdot \frac{\vec{q}}{m_N} \right) \left((\vec{S}_N \times \vec{v}_{\text{inel}}^\perp) \cdot \frac{\vec{q}}{m_N} \right),
\end{aligned}
\tag{2.4.8}
$$

which, when compared to the elastic operators in [126], have only altered by the replacement of $\vec{v}_{\text{el}}^\perp$ with $\vec{v}_{\text{inel}}^\perp$. As with the elastic derivation, $\mathcal{O}_2$ has been excluded due to it being relativistic. Additionally, the same operators derived for the elastic scenario can be used in the inelastic, and as shown in [128] this allows for the use of the same form factors implemented within the Anand et al. Mathematica package [127].

One major difference between the inelastic and elastic cases is the need to have the complex conjugate of q for the elastic case. This is because the initial and final states are identical. However, in the inelastic case, this is no longer true. The Hermiticity required within the elastic operators leads to them having real coefficients. However, in the inelastic scenario, the initial and final states are not the same, and the interaction no longer needs to be Hermitian. There is no longer a combination of $\vec{q}$ and $i\vec{q}$. Instead, the inelastic operators (Eq. 2.4.8), when placed into a Hamiltonian of Hermitian conjugate pairs produce arbitrary complex coefficients.

Within the derivation contained in [126], they highlight that the WIMP-proton coupling is not necessarily implicitly the same as the WIMP-neutron coupling; this is also true between the WIMP-isoscalar and WIMP-isovector couplings. Altering the interaction Lagrangian in Eq. (2.4.1) to account for the difference in couplings gives:

$$
\mathcal{L}_{\text{int}} = \sum_{N=(n,p),(\tau)} \sum_i c_i^{(N)} \mathcal{O}_i \chi^+ \chi^- N^+ N^-, \tag{2.4.9}
$$

where the coupling constant $c_i^{(N)}$ of each operator $\mathcal{O}_i$ is introduced, and τ refers to the isospin basis.

2.4.2 From Nucleon to Nucleus

To assess the size of the WIMP-nucleon scatter in a manner suitable for use in experimentation, the matrix element of the nucleon level operators needs to be evaluated inside the target nucleus [126]; which is achieved by representing the nucleus as a heavy many bodied system of nucleons. This requires the separation of $\vec{v}_{\rm el}^{\perp}$ to a component that acts on the center-of-mass of the nucleus ($\vec{v}_{\rm el\,T}^{\perp}$) and a component that depends on the relative velocity of the nucleons within the nucleus ($\vec{v}_{\rm nuc}^{\perp}$):

$$\begin{aligned}
\vec{v}_{\rm el}^{\perp} &= \vec{v} + \frac{\vec{q}}{2\mu_N} \\
&= \left(\frac{\vec{p}}{m_{\chi_1}} - \frac{\vec{k}}{m_N}\right) + \frac{1}{2m_{\chi_1}}\left(\vec{p}' - \vec{p}\right) + \frac{1}{2m_N}\left(\vec{k} - \vec{k}'\right) \\
&\approx \frac{1}{2}(\vec{v}_{\chi_1} + \vec{v}_{\chi_2} - \vec{v}_{N_{in}} - \vec{v}_{N_{out}}) \\
&= \frac{1}{2}(\vec{v}_{\chi_1} + \vec{v}_{\chi_2} - \vec{v}_{T_{in}} - \vec{v}_{T_{out}}) \\
&\quad + \frac{1}{2}\left[(\vec{v}_{T_{in}} - \vec{v}_{N_{in}}) + (\vec{v}_{T_{out}} - \vec{v}_{N_{out}})\right] \\
&\equiv \vec{v}_{{\rm el}\,T}^{\perp} + \vec{v}_{\rm nuc}.
\end{aligned} \tag{2.4.10}$$

The equivalent for the inelastic case is given by:

$$\begin{aligned}
\vec{v}_{\rm inel}^{\perp} &= \vec{v}_{{\rm inel}\,T}^{\perp} + \vec{v}_{\rm nuc} \\
&= \frac{1}{2}(\vec{v}_{\chi_1} + \vec{v}_{\chi_2} - \vec{v}_{T_{in}} - \vec{v}_{T_{out}}) + \frac{\delta}{|\vec{q}|^2}\vec{q} + \vec{v}_{\rm nuc},
\end{aligned} \tag{2.4.11}$$

which allows for the interpretation of q being the momentum transfer from the WIMP to the nucleus. For both the inelastic and elastic interactions, each nucleon has a perpendicular velocity that is equal to the sum of the target nucleus' velocity and of its own relative motion in the bound system. By separating these components, it is possible to reconstruct

the interaction Lagrangian in the centre of mass frame of the nucleus:

$$\begin{aligned}
\mathcal{L}_{\text{int}} &= c_1 \\
&+ ic_3\vec{S}_N \cdot \left(\vec{q} \times \vec{v}_A^{\perp}\right) + ic_3\vec{S}_N \cdot \left(\vec{q} \times \vec{v}_N^{\perp}\right) \\
&+ c_4\vec{S}_\chi \cdot \vec{S}_N \\
&+ ic_5\vec{S}_\chi \cdot \left(\vec{q} \times \vec{v}_A^{\perp}\right) + ic_5\vec{S}_\chi \cdot \left(\vec{q} \times \vec{v}_N^{\perp}\right) \\
&+ c_6 \left(\vec{S}_\chi \cdot \vec{q}\right)\left(\vec{S}_N \cdot \vec{q}\right) \\
&+ c_7\vec{S}_N \cdot \vec{v}_A^{\perp} + c_7\vec{S}_N \cdot \vec{v}_N^{\perp} \\
&+ c_8\vec{S}_\chi \cdot \vec{v}_A^{\perp} + c_8\vec{S}_\chi \cdot \vec{v}_N^{\perp} \\
&+ ic_9\vec{S}_\chi \cdot \left(\vec{S}_N \times \vec{q}\right) \\
&+ ic_{10}\vec{S}_N \cdot \vec{q} \\
&+ ic_{11}\vec{S}_\chi \cdot \vec{q} \\
&+ c_{12}\vec{S}_\chi \cdot \left(\vec{S}_N \times \vec{v}_A^{\perp}\right) + c_{12}\vec{S}_\chi \cdot \left(\vec{S}_N \times \vec{v}_N^{\perp}\right) \\
&+ ic_{13}\left(\vec{S}_\chi \cdot \vec{v}_A^{\perp}\right)\left(\vec{S}_N \cdot \vec{q}\right) + ic_{13}\left(\vec{S}_\chi \cdot \vec{v}_N^{\perp}\right)\left(\vec{S}_N \cdot \vec{q}\right) \\
&+ ic_{14}\left(\vec{S}_\chi \cdot \vec{q}\right)\left(\vec{S}_N \cdot \vec{v}_A^{\perp}\right) + ic_{14}\left(\vec{S}_\chi \cdot \vec{q}\right)\left(\vec{S}_N \cdot \vec{v}_N^{\perp}\right) \\
&+ \quad -c_{15}\left(\vec{S}_\chi \cdot \vec{q}\right)\left(\left(\vec{S}_N \times \vec{v}_A^{\perp}\right) \cdot \vec{q}\right) - c_{15}\left(\vec{S}_\chi \cdot \vec{q}\right)\left(\left(\vec{S}_N \times \vec{v}_N^{\perp}\right) \cdot \vec{q}\right).
\end{aligned} \tag{2.4.12}$$

Now that the Lagrangian is only in terms of the degrees of freedom associated with the nucleus ($\vec{S}_N$, $\vec{v}_N^{\perp}$), it can be simplified into six different nuclear charges and currents. The charges are scalar quantities that are dependent on the nucleus:

$$1, \vec{v}_N^{\perp} \cdot \vec{v}_N^{\perp}, \text{and } \vec{S}_N \cdot \vec{v}_N^{\perp}, \tag{2.4.13}$$

while the currents are for the nucleus dependent vector quantities:

$$\vec{S}_N, \vec{v}_N^{\perp}, \text{ and } \vec{S}_N \times \vec{v}_N^{\perp}. \tag{2.4.14}$$

As only leading order interactions are considered in this derivation, the $\vec{v}_N^{\perp} \cdot \vec{v}_N^{\perp}$ term is ignored, reducing the total number of unique nuclear charges and currents that can couple with a WIMP to five. The interaction Lagrangian can hence be expressed as a

linear combination of these nuclear responses:

$$\begin{aligned}\mathcal{L}_{\text{int}} =& \left\{c_1 + ic_5\vec{S}_\chi \cdot \left(\vec{q}\times\vec{v}_A^{\perp}\right) + c_8\left(\vec{S}_\chi\cdot\vec{v}_A^{\perp}\right) + ic_{11}\left(\vec{S}_\chi\cdot\vec{q}\right)\right\}\\ &+\left\{c_7 + ic_{14}\left(\vec{S}_\chi\cdot\vec{q}\right)\right\}\left[\vec{S}_N\cdot\vec{v}_N^{\perp}\right]\\ &+\left\{ic_3\left(\vec{q}\times\vec{v}_A^{\perp}\right) + c_4\vec{S}_\chi + c_6\left(\vec{S}_\chi\cdot\vec{q}\right)\vec{q} + c_7\vec{v}_A^{\perp} + ic_9\left(\vec{q}\times\vec{S}_\chi\right) + ic_{10}\vec{q}\right.\\ &\quad\left. + c_{12}\left(\vec{v}_A^{\perp}\times\vec{S}_\chi\right) + ic_{13}\left(\vec{v}_A^{\perp}\cdot\vec{S}_\chi\right)\vec{q} + ic_{14}\left(\vec{q}\cdot\vec{S}_\chi\right)\vec{v}_A^{\perp} - c_{15}\left(\vec{S}_\chi\cdot\vec{q}\right)\vec{q}\right\}\cdot\left[\vec{S}_N\right]\\ &+\left\{ic_5\left(\vec{S}_\chi\times\vec{q}\right) + c_8\vec{S}_\chi\right\}\cdot\left[\vec{v}_N^{\perp}\right]\\ &+\left\{ic_3\vec{q} + c_{12}\vec{S}_\chi - ic_{13}\left(\vec{q}\times\vec{S}_\chi\right) - c_{15}\left(\vec{q}\cdot\vec{S}_\chi\right)\vec{q}\right\}\cdot\left[\vec{S}_N\times\vec{v}_N^{\perp}\right].\end{aligned} \tag{2.4.15}$$

As each of the bracketed lines in Eq. (2.4.15) represents a different nuclear response, the Lagrangian can be further simplified by giving each response a name:

$$\begin{aligned} l_0 &= c_1 - ic_5\vec{v}_A^{\perp}\cdot\left(\vec{q}\times\vec{S}_\chi\right) + c_8\vec{S}_\chi\cdot\vec{v}_A^{\perp} + ic_{11}\vec{S}_\chi\cdot\vec{q}\\ l_0^A &= c_7 + ic_{14}\left(\vec{S}_\chi\cdot\vec{q}\right)\\ \vec{l}_5 &= \frac{1}{2}\left[ic_3\left(\vec{q}\times\vec{v}_A^{\perp}\right) + c_4\vec{S}_\chi + c_6\left(\vec{S}_\chi\cdot\vec{q}\right)\vec{q} + c_7\vec{v}_A^{\perp} + ic_9\left(\vec{q}\times\vec{S}_\chi\right) + ic_{10}\vec{q}\right.\\ &\qquad\left. + c_{12}\left(\vec{v}_A^{\perp}\times\vec{S}_\chi\right) + ic_{13}\left(\vec{v}_A^{\perp}\cdot\vec{S}_\chi\right)\vec{q} + ic_{14}\left(\vec{q}\cdot\vec{S}_\chi\right)\vec{v}_A^{\perp} - c_{15}\left(\vec{S}_\chi\cdot\vec{q}\right)\vec{q}\right]\\ \vec{l}_M &= ic_5\left(\vec{S}_\chi\times\vec{q}\right) - c_8\vec{S}_\chi\\ \vec{l}_E &= -\frac{1}{2}\left[c_3 + ic_{12}\vec{S}_\chi - c_{13}\left(\vec{q}\times\vec{S}_\chi\right) - ic_{15}\left(\vec{q}\cdot\vec{S}_\chi\right)\vec{q}\right]\vec{q}. \end{aligned} \tag{2.4.16}$$

The Lagrangian now becomes:

$$\mathcal{L}_{\text{int}} = l_0 1 - 2l_0^A[\vec{v}_N^{\perp}\cdot\vec{v}_N^{\perp}] + 2\vec{l}_5\cdot[\vec{S}_N] - \vec{l}_M\cdot[\vec{v}_N^{\perp}] + 2i\vec{l}_E\cdot[\vec{v}_N^{\perp}\times\vec{S}_N]. \tag{2.4.17}$$

One final modification needs to be performed prior to writing the WIMP-nucleon Hamiltonian required to calculate the scattering amplitude. This being a transfer from momentum to coordinate space, which [126] performs using:

$$\begin{aligned} -\vec{v}_{N_i}^{\perp} &= \frac{\vec{p}_{N_i} + \vec{p}'_{N_i}}{2m_N} \rightarrow \frac{1}{2m_N} i\left(\overleftarrow{\nabla}\delta\left(\vec{r}-\vec{r}_i\right) - \delta\left(\vec{r}-\vec{r}_i\right)\overrightarrow{\nabla}\right)\\ \vec{S}_{N_i} &= \vec{\sigma}(i), \text{ and}\\ 1 &\rightarrow \delta\left(\vec{r}-\vec{r}_i\right), \end{aligned} \tag{2.4.18}$$

where the initial and final momenta of the i^{th}-nucleon are given by $\vec{p}_{N_i}$ and $\vec{p}'_{N_i}$ respectively. The i^{th}-nucleons position in the center-of-mass frame of that nucleon is given by $\vec{r}_i$, the WIMP position in this frame is given by $\vec{r}$, and the Pauli spin matrix associated to the i^{th}-nucleon is given by $\sigma(i)$. A Dirac delta function ($\delta\left(\vec{r}-\vec{r}_i\right)$) is introduced to allow convolution of the relative positions of the WIMP and nucleons. The location of each

nucleon is considered by the inclusion of a plane wave ($e^{-i\vec{q}\cdot\vec{r}}$) to each term. By considering the contribution of all the nucleons in the nucleus, the Hamiltonian density for the WIMP-nucleus interaction can be written:

$$\begin{aligned}\mathcal{H}(\vec{r}) = &\sum_{i=1}^{A} l_0^{(N)}(i)\delta\left(\vec{r}-\vec{r}_i\right)e^{-i\vec{q}\cdot\vec{r}} \\ &+\sum_{i=1}^{A} l_0^{A(N)}(i)\frac{1}{2m_N}i\left[\overleftarrow{\nabla}\cdot\vec{\sigma}(i)\delta\left(\vec{r}-\vec{r}_i\right)e^{i\vec{q}\cdot\vec{r}} - e^{-i\vec{q}\cdot\vec{r}}\delta\left(\vec{r}-\vec{r}_i\right)\vec{\sigma}(i)\cdot\vec{\nabla}\right] \\ &+\sum_{i=1}^{A} \vec{l}_5^{(N)}(i)\cdot\vec{\sigma}(i)\delta\left(\vec{r}-\vec{r}_i\right)e^{-i\vec{q}\cdot\vec{r}} \\ &+\sum_{i=1}^{A} \vec{l}_M^{(N)}(i)\cdot\frac{1}{2m_N}i\left[\overleftarrow{\nabla}\delta\left(\vec{r}-\vec{r}_i\right)e^{-i\vec{q}\cdot\vec{r}} - e^{-i\vec{q}\cdot\vec{r}}\delta\left(\vec{r}-\vec{r}_i\right)\vec{\nabla}\right] \\ &+\sum_{i=1}^{A} \vec{l}_E^{(N)}(i)\cdot\frac{1}{2m_N}\left[\overleftarrow{\nabla}\times\vec{\sigma}(i)\delta\left(\vec{r}-\vec{r}_i\right)e^{-i\vec{q}\cdot\vec{r}} + e^{-i\vec{q}\cdot\vec{r}}\delta\left(\vec{r}-\vec{r}_i\right)\vec{\sigma}(i)\times\vec{\nabla}\right].\end{aligned} \tag{2.4.19}$$

As the WIMP-response operators shown in Eq. (2.4.2) could differ if the *ith*-nucleon is a proton or a neutron, the superscript N has been introduced; therefore, this is also applicable to isospin dependent WIMP-nucleon interactions as the coefficients can also be presented in terms of the i^{th}-nucleon.

It is now possible to extract the Hamiltonian from the Hamiltonian density by integrating over the position of the nucleons and the WIMP (i.e. contracting the delta functions[124]):

$$\begin{aligned}H = &\sum_{i=1}^{A} l_0^{(N)}(i)e^{-i\vec{q}\cdot\vec{r}_i} \\ &+\sum_{i=1}^{A} l_0^{A(N)}(i)\frac{1}{2m_N}i\left[\overleftarrow{\nabla}\cdot\vec{\sigma}(i)e^{i\vec{q}\cdot\vec{r}_i} - e^{-i\vec{q}\cdot\vec{r}_i}\vec{\sigma}(i)\cdot\vec{\nabla}\right] \\ &+\sum_{i=1}^{A} \vec{l}_5^{(N)}(i)\cdot\vec{\sigma}(i)e^{-i\vec{q}\cdot\vec{r}_i} \\ &+\sum_{i=1}^{A} \vec{l}_M^{(N)}(i)\cdot\frac{1}{2m_N}i\left[\overleftarrow{\nabla}e^{-i\vec{q}\cdot\vec{r}_i} - e^{-i\vec{q}\cdot\vec{r}_i}\vec{\nabla}\right] \\ &+\sum_{i=1}^{A} \vec{l}_E^{(N)}(i)\cdot\frac{1}{2m_N}\left[\overleftarrow{\nabla}\times\vec{\sigma}(i)e^{-i\vec{q}\cdot\vec{r}_i} + e^{-i\vec{q}\cdot\vec{r}_i}\vec{\sigma}(i)\times\vec{\nabla}\right].\end{aligned} \tag{2.4.20}$$

Which leads to a scattering amplitude of:

$$
\begin{aligned}
|\mathcal{M}|^2 &= |\langle j_\chi, M_\chi; j_N M_N | H | j_\chi, M_\chi; j_N M_N \rangle|^2 \\
&= | \sum_{i=1}^{A} \langle j_\chi, M_\chi; j_N M_N | \, l_0^{(N)} e^{-i\vec{q}\cdot\vec{r}_i} \\
&+ l_0^{A(N)} \frac{1}{2m_N} \left[-\frac{1}{i} \overleftarrow{\nabla} \cdot \vec{\sigma}(i) e^{-i\vec{q}\cdot\vec{r}_i} + e^{-i\vec{q}\cdot\vec{r}_i} \vec{\sigma}(i) \cdot \frac{1}{i} \vec{\nabla} \right] \\
&+ \vec{l}_5^{(N)} \cdot \vec{\sigma}(i) e^{-i\vec{q}\cdot\vec{r}_i} \\
&+ \vec{l}_M^{(N)} \cdot \frac{1}{2m_N} \left[-\frac{1}{i} \overleftarrow{\nabla} e^{-i\vec{q}\cdot\vec{r}} + e^{-i\vec{q}\cdot\vec{r}} \frac{1}{i} \vec{\nabla} \right] \\
&+ \vec{l}_E^{(N)} \cdot \frac{1}{2M_N} \left[\xi \bar{\nabla} \times \vec{\sigma}(i) e^{-i\vec{q}\cdot\vec{r}_i} + e^{-i\vec{q}\cdot\vec{r}_i} \vec{\sigma}(i) \times \vec{\nabla} \right] | j_\chi, M_\chi j_N, M_N \rangle \Big|^2 .
\end{aligned}
\tag{2.4.21}
$$

At this point, Fitzpatrick et al. [126] perform a multipole decomposition. Assuming the parity and CP of the nucleus is good, these multipoles vanish as well as the majority of off-diagonal terms. Finally, by explicitly summing over all the nucleons, the WIMP-nucleon scatter amplitude in the context of direct detection experiments can be given in a reduced form:

$$
\begin{aligned}
|\mathcal{M}|^2 &= |\langle j_\chi, M_\chi; j_N M_N | H | j_\chi, M_\chi; j_N M_N \rangle|^2 \\
&= 4\pi \sum_{i=1}^{A} \left[\sum_{J=1,3,\ldots}^{\infty} \left| \left\langle J_i || \vec{l}_5 \cdot \hat{q} \Sigma''_J(q) \| J_i \right\rangle \right|^2 \right. \\
&+ \sum_{J=0,2,\ldots}^{\infty} \left\{ |\langle J_i \| l_0 M_J(q) \| J_i \rangle|^2 + \left| \left\langle J_i \left\| \vec{l}_E \cdot \hat{q} \frac{q}{m_N} \Phi''_J(q) \right\| J_i \right\rangle \right|^2 \right. \\
&+ 2\,\mathrm{Re} \left[\left\langle J_i \left\| \vec{l}_E \cdot \hat{q} \frac{q}{m_N} \Phi''_J(q) \right\| J_i \right\rangle \langle J_i || l_0 M_J(q) || J_i \rangle^* \right] \Big\} \\
&+ 2\,\mathrm{Re} \left[\left\langle J_i \left\| \vec{l}_E \cdot \hat{q} \frac{q}{m_N} \Phi''_J(q) \right\| J_i \right\rangle \langle J_i || l_0 M_J(q) || J_i \rangle^* \right] \Big\} \\
&+ \frac{q^2}{2m_N^2} \sum_{J=2,4,\ldots}^{\infty} \left(\left\langle J_i \left\| \vec{l}_E \bar{\Phi}'_J(q) \right\| J_i \right\rangle \cdot \left\langle J_i || \vec{l}_E \bar{\Phi}'_J(q) \| J_i \right\rangle^* - \left| \left\langle J_i \left\| \vec{l}_E \cdot \hat{q} \bar{\Phi}'_J(q) \right\| J_i \right\rangle \right|^2 \right) \\
&+ \sum_{J=1,3,\ldots}^{\infty} \left\{ \frac{q^2}{2m_N^2} \left(\left\langle J_i || \vec{l}_M \Delta_J(q) \| J_i \right\rangle \cdot \left\langle J_i \left\| \vec{l}_M \Delta_J(q) \right\| J_i \right\rangle^* - \left| \left\langle J_i \mid \vec{l}_m \cdot \hat{q} \Delta_J(q) \| J_i \right\rangle \right|^2 \right) \right. \\
&+ \frac{1}{2} \left(\left\langle J_i || \vec{l}_5 \Sigma'_J(q) \| J_i \right\rangle \cdot \left\langle J_i \left\| \vec{l}_5 \Sigma'_J(q) \right\| J_i \right\rangle^* - \left| \left\langle J_i || \vec{l}_5 \cdot \hat{q} \Sigma'_J(q) || J_i \right\rangle \right|^2 \right) \\
&\left. \left. + 2\,\mathrm{Re} \left[i\hat{q} \cdot \left\langle J_i \left\| \vec{l}_M \frac{q}{m_N} \Delta_J(q) \right\| J_i \right\rangle \times \left\langle J_i \left\| \vec{l}_5 \Sigma'_J(q) \right\| J_i \right\rangle^* \right] \right\} \right] ,
\end{aligned}
\tag{2.4.22}
$$

where six nuclear responses ($\mathrm{M}, \Sigma'', \Sigma'', \Delta, \bar{\Phi}'$ and Φ'') have been introduced. These can

be simplified by constructing them in terms of scalar and vector spherical harmonics:

$$\begin{aligned}
\Delta_{JM}(q\vec{x}) &\equiv \vec{M}^{M}_{JJ}(q\vec{x}) \cdot \frac{1}{q}\vec{\nabla} \\
\Sigma'_{JM}(q\vec{x}) &\equiv -i\left\{\frac{1}{q}\vec{\nabla} \times \vec{M}^{M}_{JJ}(q\vec{x})\right\} \cdot \vec{\sigma} \\
&= \sqrt{J(J+1)}^{-1}\left\{-\sqrt{J}\vec{M}^{M}_{JJ+1}(q\vec{x}) + \sqrt{J+1}\vec{M}^{M}_{JJ-1}(q\vec{x})\right\} \cdot \vec{\sigma} \\
\Sigma''_{JM}(q\vec{x}) &\equiv \left\{\frac{1}{q}\vec{\nabla} M_{JM}(q\vec{x})\right\} \cdot \vec{\sigma} \\
&= \sqrt{J(J+1)}^{-1}\left\{\sqrt{J+1}\vec{M}^{M}_{JJ+1}(q\vec{x}) + \sqrt{J}\vec{M}^{M}_{JJ-1}(q\vec{x})\right\} \cdot \vec{\sigma} \\
\tilde{\Phi}'_{JM}(q\vec{x}) &\equiv \left(\frac{1}{q}\vec{\nabla} \times \vec{M}^{M}_{JJ}(q\vec{x})\right) \cdot \left(\vec{\sigma} \times \frac{1}{q}\vec{\nabla}\right) + \frac{1}{2}\vec{M}^{M}_{JJ}(q\vec{x}) \cdot \vec{\sigma} \\
\Phi''_{JM}(q\vec{x}) &\equiv i\left(\frac{1}{q}\vec{\nabla} M_{JM}(q\vec{x})\right) \cdot \left(\vec{\sigma} \times \frac{1}{q}\vec{\nabla}\right).
\end{aligned} \tag{2.4.23}$$

All of which can be explained directly or with a simple modification by electroweak physics. The interpretations of these nuclear response functions will not be discussed here, the reader is directed to [126]; which includes a comparison of these responses in different target nuclei. For the inelastic interaction, Barrelo et al. [128] show that the scattering amplitudes and nuclear response functions are the same as those in elastic interactions; and hence the same form factors as in the Anand et al. Mathematica package can be used with a simple modification to include $\frac{\delta_m}{|\vec{q}|^2}\vec{q}$ in the velocity.

The next stage is to relate these nuclear responses ($k = \mathrm{M}, \Sigma'', \Sigma', \Delta, \Phi'', \tilde{\Phi}'$) to the operator form factor ($F^{(N,N')}_{i,j}$). This is done through a linear combination of the nuclear form factors ($F^{(N,N')}_{k}$):

$$F^{(N,N')}_{ij}(q^2) = \sum_{k=M,\Sigma'',\Sigma',\Delta,\Phi'',\widetilde{\Phi}'} a_{ijk}\left(j_\chi, v^2, q^2\right) F^{(N,N')}_{k}(q^2), \tag{2.4.24}$$

where all the parameters dependent on the WIMP (mass, spin, relative velocity, mass-splitting) are built into the coefficients $a_{ijk}(j_\chi, v^2, q^2)$. The nuclear form factors themselves can be given for two cases. The first of which are for the case where there are no interference terms ($k = \mathrm{M}, \Sigma^m, \Sigma', \Delta, \Phi''$, and $\widetilde{\Phi}'$), and the nuclear form factor is described by:

$$F^{(N,N')}_{k}\left(q^2\right) = \frac{4\pi}{2j_A+1}\sum_{J=0}^{2j_A+1}\left\langle j_A \left\| k^{(N)}_J \right\| j_A \right\rangle \left\langle j_A \left\| k^{(N')}_J \right\| j_A \right\rangle. \tag{2.4.25}$$

The second is for the case where the interference between M and Φ'' or between Σ' and Δ is considered[11]:

$$F^{(N,N')}_{k_1,k_2}\left(q^2\right) = \frac{4\pi}{2j_A+1}\sum_{J=0}^{2j_A+1}\left\langle j_A \left\| k^{(N)}_{1J} \right\| j_A \right\rangle \left\langle j_A \left\| k^{(N')}_{2J} \right\| j_A \right\rangle. \tag{2.4.26}$$

[11] These being the only terms that produce a non-zero interference.

Explicit combinations of the nuclear form factor are given by Haxton et al. [127], which have been included in Table 2.1. Approximations of the nuclear form factors of various isotopes have been produced by Fitzpatrick et al. [126].

2.4.3 Model Independent Differential Rate

To construct a WIMP-nucleon scatter rate from the nuclear responses (Eq. 2.4.23), the relationship between them needs to be established. The generalised form of the WIMP-nucleus differential rate (Eq. 1.3.2) can be related to the differential cross-section as shown in Eq. (2.1.5). From here, Fermi's Golden Rule is applied to relate the differential cross-section to the spin averaged scatter amplitude (which encodes the particle physics of the interaction):

$$\frac{d\sigma}{dE_R} = \frac{1}{32\pi v^2 m_\chi^2 m_A} \frac{1}{(2j_A+1)} \frac{1}{(2j_\chi+1)} \sum_{\text{spins}} |\mathcal{M}|^2(q^2) dv, \tag{2.4.27}$$

where the spin contributions of the initial states are averaged, and of the final states are summed. This is the Haxton et al. [127] derivation, which contains an extra factor of $1/(4m_\chi m_A)^2$ to account for the normalisation required to match the relativistic WIMP-nucleon interaction operators to the corresponding non-relativistic terms.

Using the generalised Lagrangian in Eq. (2.4.1), the scatter amplitude can be rewritten in terms of the operator form factor:

$$\frac{1}{(2j_A+1)} \frac{1}{(2_\chi j+1)} \sum_{\text{spins}} |\mathcal{M}|^2 \equiv \frac{m_A^2}{m_N^2} \sum_{i,j=1}^{15} \sum_{N,N'=p,n} c_i^{(N)} c_j^{(N')} F_{ij}^{(N,N')} \left(v^2, q^2\right). \tag{2.4.28}$$

Here, the proton-neutron basis has been shown; this summation can also be just as easily performed in the isospin basis. As discussed, the form factors that appear in the WIMP-nucleon recoil spectrum (F_k) can be defined by the nuclear response operators k; leading to the substitution of Eq. (2.4.24) into Eq. (2.4.28); which when placed back into Eq. (1.3.2) retrieved the WIMP-nucleon differential rate:

$$\frac{dR}{dE_R} = \frac{\rho_0}{32\pi m_x^3 m_N^2} \int_{v>v_{min}} \frac{f(\vec{v})}{v} \sum_{i,j} \sum_{N,N'=n,p} c_i^N c_j^{N'} \sum_{k=\mathrm{M},\Sigma'',\Sigma',\Delta,\psi'',\bar{\psi}'} a_{ijk} F_k^{(N,N')} \left(v^2, q^2\right) dv. \tag{2.4.29}$$

$$
\begin{array}{lcl}
F_{1,1}^{(N,N')} & = & F_{\mathrm{M}}^{(N,N')} \\
F_{3,3}^{(N,N')} & = & \left(\frac{q^4}{4m_N^2}F_{\Phi''}^{(N,N')} + q^2\left(v^2 - \frac{q^2}{4\mu_A^2}\right)F_{\Sigma'}^{(N,N')}\right) \\
F_{4,4}^{(N,N')} & = & C\left(j_\chi\right)\frac{1}{16}\left(F_{\Sigma''}^{(N,N')} + F_{\Sigma'}^{(N,N')}\right) \\
F_{5,5}^{(N,N')} & = & C\left(j_\chi\right)\frac{1}{4}\left(q^2\left(v^2 - \frac{q^2}{4\mu_A^2}\right)F_{\mathrm{M}}^{(N,N')} + \frac{q^4}{m_n^2}F_{\Delta}^{(N,N')}\right) \\
F_{6,6}^{(N,N')} & = & C\left(j_\chi\right)\frac{q^4}{16}F_{\Sigma''}^{(N,N')} \\
F_{7,7}^{(N,N')} & = & \frac{1}{8}\left(v^2 - \frac{q^2}{4\mu_A^2}\right)F_{\Sigma'}^{(N,N')} \\
F_{8,8}^{(N,N')} & = & C\left(j_\chi\right)\frac{1}{4}\left(\left(v^2 - \frac{q^2}{4\mu_A^2}\right)F_{\mathrm{M}}^{(N,N')} + \frac{q^2}{m_N^2}F_{\Delta}^{(N,N')}\right) \\
F_{9,9}^{(N,N')} & = & C\left(j_\chi\right)\frac{q^2}{16}F_{\Sigma'}^{(N,N')} \\
F_{10,10}^{(N,N')} & = & \frac{q^2}{4}F_{\Sigma''}^{(N,N')} \\
F_{11,11}^{(N,N')} & = & C\left(j_\chi\right)\frac{q^2}{4}F_{\mathrm{M}}^{(N,N')} \\
F_{12,12}^{(N,N')} & = & C\left(j_\chi\right)\left[\frac{q^2}{m_N^2}\left(F_{\widetilde{\Phi}'}^{(N,N')} + F_{\Phi''}^{(N,N')}\right) + \left(v^2 - \frac{q^2}{4\mu_A^2}\right)\left(F_{\Sigma''}^{(N,N')} + \frac{1}{2}F_{\Sigma'}^{(N,N')}\right)\right] \\
F_{13,13}^{(N,N')} & = & \frac{C(j_\chi)}{16}\left[\frac{q^4}{m_N^2}F_{\widetilde{\Phi}'}^{(N,N')} + q^2\left(v^2 - \frac{q^2}{4\mu_A^2}\right)F_{\Sigma''}^{(N,N')}\right] \\
F_{14,14}^{(N,N')} & = & \frac{C(j_\chi)}{32}\left[q^2\left(v^2 - \frac{q^2}{4\mu_A^2}\right)F_{\Sigma'}^{(N,N')}\right] \\
F_{15,15}^{(N,N')} & = & C\left(j_\chi\right)\left[\frac{q^6}{m_N^2}F_{\Phi''}^{(N,N')} + \frac{q^4}{2}\left(v^2 - \frac{q^2}{4\mu_A^2}\right)F_{\Sigma'}^{(N,N')}\right] \\
F_{1,3}^{(N,N')} & = & \frac{q^2}{2m_N}F_{\mathrm{M}\Phi''}^{(N,N')} \\
F_{4,5}^{(N,N')} & = & -C\left(j_\chi\right)\frac{q^2}{8m_N}F_{\Sigma'\Delta}^{(N,N')} \\
F_{4,6}^{(N,N')} & = & C\left(j_\chi\right)\frac{q^2}{16}F_{\Sigma''}^{(N,N')} \\
F_{8,9}^{(N,N')} & = & C\left(j_\chi\right)\frac{q^2}{8m_N}F_{\Sigma'\Delta}^{(N,N')} \\
F_{11,12}^{(N,N')} & = & C\left(j_\chi\right)\frac{q^2}{8m_N}F_{\mathrm{M}\Phi''}^{(N,N')} \\
F_{11,15}^{(N,N')} & = & -C\left(j_\chi\right)\frac{q^4}{8m_N}F_{\mathrm{M}\Phi''}^{(N,N')} \\
F_{12,15}^{(N,N')} & = & \frac{-C(j_\chi)}{16}\left[\frac{q^4}{m_N^2}F_{\Phi''}^{(N,N')} + \frac{q^2}{2}\left(v^2 - \frac{q^2}{4\mu_A^2}\right)F_{\Sigma'}^{(N,N')}\right]
\end{array}
$$

Table 2.1: Relationship of specific operator form factors($F_{i,j}^{(N,N')}$) to the independent nuclear form factors ($F_k^{(N,N')}$) and the interference nuclear form factors ($F_{k_1,k_2}^{(N,N')}$); where the $C\left(j_\chi\right) = 4j_\chi\left(j_\chi+1\right)/3$. Collated by Larsen in [131] from [126] and [127].

Summary

This chapter started with the derivation of the WIMP-nucleus interaction rate before describing the relevant astrophysical parameters for DM, showing the influence of each of the different velocity components' uncertainties on the limits of a direct detection search. Following this, the derivation for the two simplest forms of WIMP-nucleon interaction was given; the SI and SD interactions are the only two present in the zero-momentum transfer limit and are the main models studied for the vast majority of direct detection searches. Furthering this, an overview of a model-independent EFT developed by Haxton et al. and the modifications required for the inelastic case by Barello et al. were given. It was shown that with a simple modification to the perpendicular velocity term, the inelastic scenario could be considered using the same operators. The EFT indicates that there are many possible forms of interactions that could occur between WIMPs and nucleons. Therefore, it is essential to start considering a model-independent approach that encompasses all possible interactions, especially as the limits for SI and SD interactions are about to reach a point where they will be encroaching into the irreducible neutrino background. In the final chapter of this thesis, limits on the strengths of all 14 of the non-relativistic EFT operators for the inelastic scenario will be calculated using the LUX WIMP Search (WS) data collected between 2014 and 2016.

Chapter 3

Detecting WIMPs with Xenon Time Projection Chambers

A multitude of different disciplines have greatly benefited from the use of gaseous and LXe as a detection or contrast medium. Medical applications of Xe extend beyond its use as an anaesthetic or for hypoxic-ischemic treatment [132]. With minimal risk of side effects, Xe serves as an ideal contrast material; inhalation of the gas has proven a valuable tool to indicate areas with high and low blood flow when combined with CT imaging of the brain [133, 134]; Xe is also used as the primary detection medium in PET scanners [135]. More recently the feasibility of using LXe as the detection medium within a Compton-camera to image radionuclide tracers within a patient has been investigated, with aims of reducing the dosage of the tracer while still achieving a similar precision to current methods [136]. Laser activation of Xe was first demonstrated in 1971. Falling into the category of excimer based lasers; they produce light in the ultraviolet range [137]. These lasers have seen use in a range of tasks from the photolithography of microelectronic devices, to laser enhanced NMR spectroscopy. Within particle physics, LXe and LAr have proven invaluable in the detection and study of particles interacting on the weak scale. In general, noble liquid detectors are categorised by the type of energy deposit they are instrumented to observe:

- **Ionisation detectors** only observe the charge, generally by the use of an instrumented anode.
- **Scintillation chambers** are those only instrumented with optical sensors.
- **Time projection chambers** are electronic proportional counters that observe both the ionisation and scintillation signals; through means of prompt and proportional scintillations.

Hereon only LXe detectors will be discussed, with specific focus on the TPC.

Part of the reason for such an extensive range of applications is a unique feature exhibited by only LXe and LAr. For both elements, incident ionising radiation can induce the production of both charge carriers and scintillation photons (which happen to be both complementary and anti-correlated [138]). Therefore, simultaneous observation of these signals allows for a determination of the energy of the interaction vertices and the distribution of interaction points within space and time; giving means to make precision measurements of a particles' properties. Hence, LXe and LAr are both ideal materials for large scale detectors employed in weak-scale physics searches. Further information behind the relevant microphysics for LXe is given in the first section of this Chapter.

With the inability to generate a controlled flux of DM, direct detection experiments rely on disentangling DM events from all possible backgrounds; especially those which induce a nuclear recoil. For this reason, it is imperative that the detectors and environment used to conduct such rare event searches use radiopure materials and have minimal cosmogenic and terrestrial radioactivity. The last section in this Chapter will describe the LZ experiment's: key detector components, experimental strategy and known sources of backgrounds. To truly understand the background, and indeed the signal itself, the read-out devices must be precisely calibrated across a range of energies.

Over recent years, utilisation of the Migdal effect has allowed for LXe TPCs to extend to lower recoil energies without the need for modifications to the detector. In essence, as a nucleus recoils after a scattering event, it's electron cloud does not displace at the same rate as the nucleus itself. Effectively a boost in the nucleus frame is then experienced by the electrons, where some electrons may be left behind and liberated, hence ionising the atom. This will not be discussed in this body of work; the reader is referred to [139, 84] for further information on the physics and utilisation of the phenomena within DM searches, and to Ref. [140] and [141] for experimental limits on sub-GeV DM obtained by the LUX and XENON collaborations respectively.

3.1 Properties of Liquid Xenon

LXe has many properties that make it a prime candidate medium for the direct detection of DM interactions. With a high atomic mass, Xe benefits greatly in terms of SI WIMP-nucleon interaction from the A^2 coherence effect; see section §2.3. SD interactions also gain a benefit from a Xe target due to the mix of naturally abundant Xe isotopes with

Property	Symbol	Value
Atomic number	Z	54
Isotopes	X	^{124}Xe(0.09%), ^{126}Xe(0.09%),
(Natural abundance)		^{128}Xe(0.1.92%), ^{129}Xe(26.44%),
		^{130}Xe(4.08%), ^{131}Xe(21.18%),
		^{132}Xe(26.89%), ^{134}Xe(10.44%),
		^{136}Xe(8.87%)
Mean molar mass	M	131.293 g/mol
Boiling point (at 1 atm.)	T_b	165.02 K
Density	ρ_b	3.057 cm^{-3}
Ionization potential	I	13.84 eV
W-value for ionization	W_i	23.6(3) eV/pair
W-value for scintillation	W_s	13.8 ± 0.9 eV/photon
Gap Energy	E_g	9.28 eV
Radiation length	X_0	2.87 cm
Attenuation length	λ_I	29-50 cm
Energy loss	$< dE/dx >$	3.89 MeV/cm
(Minimum ionising particle)		
Scintillation emission peak	λ_s	177.6 nm
Saturated e^- drift velocity	ν_e	2.6×10^5 ± 10% cm/s
(Electric field of 3-10 kV/cm)		
e^- mobility	μ_0^e	2000 ± 200 cm^2/V s
Xe$^+$ mobility	μ_0^i	2.6×10^{-3} cm^2/V s

Table 3.1: Summary of key properties of LXe including those key to use as direct detection target. Information collated from [142, 143, 144, 145, 146, 147].

differing spins[1], given in Table 3.1. A high density at boiling point, 3 g/cm^3, makes LXe highly effective at stopping penetrating radiation [2]; resulting in a mean interaction length of only a few centimetres for both neutrons and MeV energy gammas. Suffice to say, LXe is an excellent self-shielding material, where only a few cm^3 of the outermost volume are required to produce an ultra-low background inner fiducial volume. In addition, when compared with Ar, Xe has no long-lived radioisotopes. Cosmogenic Xe raises only a slight

[1]For Xe, the isotopes vary the number of un-paired neutrons that contribute to the total spin.

[2]Being able to do so over a sizeable homogeneous volume is not as easily achieved with Ge or NaI.

concern; but with a half-life of the order of days, early procurement can give sufficient time for most of the cosmogenic Xe to have decayed. In Table 3.1 attenuation length refers to that of the Rayleigh scatter of electrons as they traverse the Xe. The range of values are derived from experiments and has a corresponding theoretical value of 30 cm[146].

Ionisation Process

Before discussing the ionisation process in LXe, its right to mention its electronic band structure. As a solid[3], Xe has a face-centred cubic structure; and despite the influence of inter nuclear forces, the top of the valence band and the bottom of the conduction band have a separable band gap, E_g. As a result, energy deposited by ionising particles produce a number of electron-ion pairs (N_i), excited atoms (N_{ex}) and free electrons (with kinetic energy lower than that of the first excited state). For a given transfer energy (E_0) the number of electron-ion pairs at average energy E_i and the number of excited atoms at average energy of E_{ex}, is given by the Platzman equation [148]:

$$E_0 = N_i E_i + N_{ex} E_{ex} + N_i \epsilon, \tag{3.1.1}$$

where ϵ is the sub-excitation electrons' average kinetic energy. It is more convenient to use the average energy required to produce an electron-ion pair (W):

$$W = E_0/N_i = E_i + (N_{ex}/N_i)E_{ex} + \epsilon. \tag{3.1.2}$$

For solid and liquid phase rare gases, the ionisation potential can be replaced with the band gap:

$$W/E_g = E_i/E_g + (N_{ex}/N_i)(E_{ex}/E_g) + \epsilon/E_g. \tag{3.1.3}$$

Early calculations of W/E_g for LXe were pieced together from the ratios E_{ex}/E_g and N_{ex}/N_i approximated in [142], E_i from [149] and ϵ obtained through the Shockley method [150, 151]. W/E_g was found to be around 1.65 in LXe, with a W of 15.6 $\pm$ 0.3 eV/photon and E_g of 9.28 eV [142].

Electron and Photon Multiplication

An interesting feature of LXe is that when a field of greater than 10^6 V/cm is applied, the liberated electrons multiply in an avalanche process [152, 153]. By doing so, a gain of

[3] Xe, along with Kr and Ar, still have clear excitation peaks when liquid.

several hundred is achievable; however, this is at the cost of decreased energy resolution. The gain in the produced detectable signal is a function of this multiplicity. With a field strength marginally below the avalanche threshold, it is possible to induce proportional scintillation, i.e. photon multiplication [154].

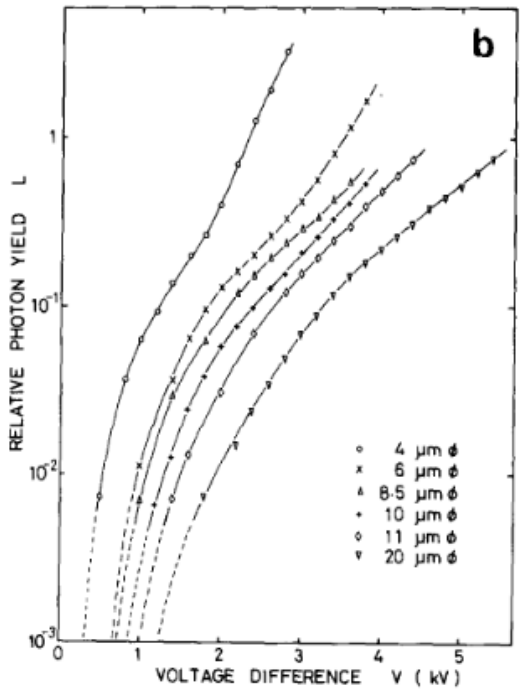

Figure 3.1: Relative light yield as a function of the applied voltage across wires of differing diameters [155].

A distinct advantage to photon multiplication is that it does not exhibit the same deterioration in the energy resolution as electron multiplication; this was first determined for LXe in 1982 and is shown in Figure 3.1. As shown, when using 4 μm wires held at 5 kV potential a maximum gain of 5 photons per electron was achieved [155]. By introducing a dopant with an ionisation energy lower than that of the LXe scintillation photons, it is possible to create additional charge carriers; hence allowing for even high levels of gain, as demonstrated in [156, 157].

Scintillation Process

Along with the liberating electrons from the ionisation process, the exchange energy to the LXe can produce scintillation photons. The emissions of photons from rare liquid gases originates from the decay of excited dimers (excimer) back to the atomic ground state. These excimers form either through the excitation of the atom (Xe^*), Eq. (3.1.4), or by

recombination of electrons with ions (Xe^+), Eq. (3.1.5); for LXe the relevant excimer is Xe_2^*. The two lowest electronic excited states of Xe_2^* form either a singlet $\left({}^1\Sigma_{ex}^+\right)$ or triplet $\left({}^3\Sigma_{ex}^+\right)$ state. De-excitation of either state to the ground state is accompanied by the emission of a Vacuum UltraViolet (VUV) photon with wavelength centred about $\lambda = 177.6nm$ [143, 158]. As there are no Xe_2 present, and the emitted photon's energy does not match a bandgap in Xe, the photon is not reabsorbed, and the medium scintillates.

$$\begin{aligned} Xe^* + Xe + Xe &\rightarrow Xe_2^* + Xe \\ Xe_2^* &\rightarrow 2Xe + h\nu \text{ (VUV)}. \end{aligned} \tag{3.1.4}$$

The difference between the decay constants of the eximer, 2.2 ns for the singlet and 27 ns for the triplet [146], is too short to allow for particle identification by pulse shape discrimination as seen in LAr detectors[4] [159]. The VUV photons emitted via recombination have a further delay of 45 ns, due to more stages in the process:

$$\begin{aligned} Xe^+ + Xe &\rightarrow Xe_2^+ \\ Xe_2^+ + e^- &\rightarrow Xe^{**} + Xe \\ Xe^{**} &\rightarrow Xe^* + \text{ heat} \\ Xe^* + Xe + Xe &\rightarrow Xe_2^* + Xe \\ Xe_2^* &\rightarrow 2Xe + h\nu \text{ (VUV)}. \end{aligned} \tag{3.1.5}$$

As the final stages of emission through recombination (Eq. 3.1.5) are the same as the excitation process (Eq. 3.1.4), the emitted photons from both will have similar wavelengths and decay constants from the excimer states. The electrons liberated by the ionisation process will either be recaptured by a Xe_2^+ ion (recombination), or escape the interaction point as free charge.

Nuclear and Electronic Recoils

An incident particle when interacting with an atom can induce two types of recoil: interactions with a bound electron produce an Electronic Recoil (ER), those with a nucleus produce a Nuclear Recoil (NR). The ratio of scintillation to ionisation differs between ER and NR, and as the predominant background in liquid noble TPC based DM searches is from ER events, and a WIMP induces NR, these distinctions serve as an important form of particle identification. For a given energy transfer to the atom, a different number of N_i and N_{ex} are produced, the ratio[5] of which differs for ER and NR, $N_{ex}/N_i = 0.06$ and

[4] LAr has a noticeably longer triplet lifetime of $\sim 1\mu$s.

[5] The recoil energy and field applied across the detection volume influence this ratio and hence also influence the ability to discriminate between the types of recoil.

1, respectively [145].

This difference affects the ratio of free charge carriers, n_e, compared to prompt scintillation photons, n_γ; which can be related to N_i and N_{ex} through the recombination probability r:

$$\begin{aligned} n_\gamma &= N_{ex} + rN_i \\ n_e &= (1-r)N_i, \end{aligned} \tag{3.1.6}$$

which implies that when an ionised atom recombines, a single photon can be emitted through a process independent of r:

$$N_{ex} + N_i = n_e + n_\gamma. \tag{3.1.7}$$

Simultaneous measurement of both n_e and n_γ can give an estimate of the recoil energy in ER events:

$$E_R = W(n_e + n_\gamma), \tag{3.1.8}$$

which, due to the anti-correlation between these two channels, is linear in energy and independent of the applied electric field. Here W is the average energy to produce either an electron or a photon, and weak dependencies on the applied field and exact recoil energy have been neglected. When considering NR events, the energy loss due to atomic motion needs to be accounted for by the introduction of a quenching factor $\mathcal{L}$ [160].

$$E_R = (W/\mathcal{L})/(n_e + n_\gamma). \tag{3.1.9}$$

Originally postulated by Lindhard (hence its colloquial name, the Lindhard factor), this quenching factor increases monotonically as a function of recoil energy from 0.15 to 1 for $E_R = 0.30$ to 100 keV [145]. .

Ionisation and Scintillation Yields

The ionisation yield quantifies the number of electron-ion pairs produced per unit of absorbed energy by the target medium. It has become colloquial in physics to use the previously defined W-value. The W-value is considered as being near-constant down to very low energies, where a weak dependence on the type and energy of the radiation begins to become significant. As a result of this constant relationship, it is possible to determine the energy of a deposition within the medium by observation of the produced ionisation signal. To correctly count the number of generated electron-ion pairs from an interaction in LXe several factors must be considered:

- **The purity of the liquid** is important in order to minimise the loss of charge carriers due to attachment to impurities.

- **The strength of the applied field** required across the detection volume must be sufficiently high to minimise the recombination of electron-ion pairs.
- **The calibration of readouts** is imperative to the precision and accuracy of the estimated energy deposition.

For a given energy deposition, E, the maximum scintillation yield is given by E/W_{ph}; with W_{ph} being the average energy to produce a single photon. When considered in the limit of no quenching processes, it is given by [144]:

$$W_{ph} = W/(1 + N_{ex}/N_i). \tag{3.1.10}$$

The scintillation yield itself is dependent on the linear energy transfer and the electron-ion pair density produced along the track of the incident particle.

3.2 The Time Projection Chamber

Initially conceived in the mid-70s by D. R Nygren, the TPC offers the unique combination of a bubble chamber, offering large amounts of topological information, and an electronic counter experiment, which gives flexibility in the active detection mass, timing and geometry choices of the detector [161]. The generalised operating principle of the TPC, shown in Figure 3.2, is to observe the electrons liberated from an ionisation medium after interactions with a traversing ionising particle; through the mechanisms discussed in §3.1. The medium itself can be liquid, gas or both and immerses a pair of parallel electrodes, forming a drift region of several millimeters to meters dependent on the intended detector application [162]. By holding one of the electrodes at a high negative potential, creating a cathode,

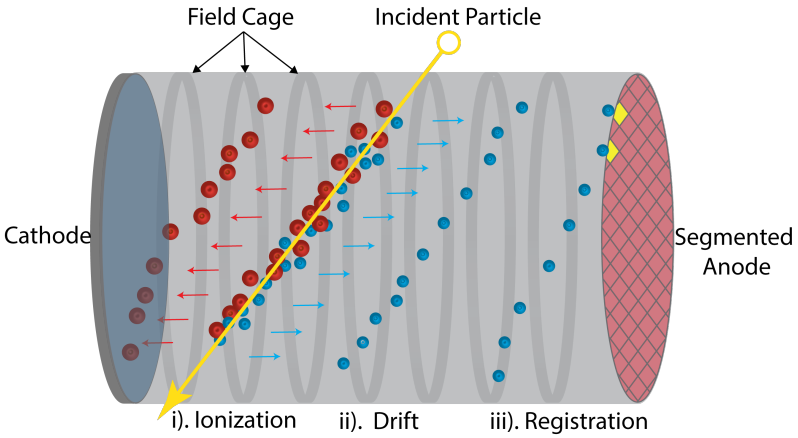

Figure 3.2: Diagram of the operating principle of a TPC, showing the drift of ionised electrons towards a segmented anode.

and the other at either ground or slightly positive, serving as an anode, a homogeneous electric field can be established across the detection volume. The typical strength of this electric field can range from 100 V/cm to 10 kV/cm [162]. In order to maintain a uniform field across the detection volume, field-shaping electrodes are placed at regular intervals. Establishing such a field compels any liberated electrons to drift towards the anode; which in many TPCs is segmented into a wireplane array consisting of a regularised structure of thin conductive wires each serving as an independent readout [163]. By imaging the received charge on the segmented anode and applying the centre of gravity method, $x-y$ spacial reconstruction of the interaction is possible [164]. To determine the z-coordinate (i.e. the depth) of the interaction, information on the arrival time of the drift electrons is required. The initial time (t_0) of the interaction can be determined by observation of the prompt scintillation signal (S1). Taking both of these times into account, the drift time of the electrons (t_d) can be determined [162]. Finally, with knowledge of the exact strength of the drift field, the full spatial properties of the interaction can be retrieved. Hence the TPC technique allows for the observation of highly resolved spatial tracks [163].

Single and Dual Phase TPCs

Originally TPCs were designed as single gas phase detectors, offering a system that is easy to operate and has flexibility on the orientation and geometry of the system. In order to apply the TPC technique to rare event searches where the interaction cross-section becomes ever smaller, the necessity to use targets with higher densities (i.e. more massive detectors in the same volume) became apparent. Moving to a liquid target medium was seen as the logical step forward as this gave both the required increase in density and a reduced diffusion of the ionisation electrons. However, this introduced the new issue that any electronic components that are required within the TPC will now have to be suitable to operate in a cryogenic environment. If suitable electronics are not selected, there is a risk that their effectiveness will be diminished. One means to overcome this was to use a dual phase detector; where the sensitive electronic components could be situated in the gas phase. Some clear consequences of using a dual phase system are: the orientation of the electrodes must now be vertical, the phase boundary must be finely tuned to create the extraction region at the desired location; and additional systems are required to maintain the cryogenic environment (which significantly increase the cost and complexity of the system). Another critical issue introduced by the transition to a liquid medium is the increased dependency of the amplitude of the produced signals on the purity of the liquid.

Even a small quantity ($\approx$ 1 part per million) of an electronegative substance, such as O_2, can lead to signal loss through the excitation of rotational and vibrational molecular states capturing the ionisation electrons [165].

Within DM searches, which typically employ the dual phase concept, the anode is no longer used as a segmented readout. Instead, an additional wireplane situated below the anode, referred to as the gate, is positioned near the phase boundary and held at a very high potential. This drives electroluminescence of the drifting electrons, producing a delayed proportionate scintillation signal (S2); which is typically detected using arrays of PhotoMultiplier Tubes (PMTs) situated at the top and bottom of the detector.

Energy Reconstruction in Dual Phase TPCs

The energy of the interaction of a traversing particle is split between the production of charge, heat and light, as explained in §3.1. Dual phase TPCs detect the light, S1, and the charge through the induced electroluminescent process, S2. Here, S1 is directly related to the previously defined number of photons produced in the interaction (n_γ) and S2 to the previously defined number of electrons (n_e) by the average number of photons (g_1 and g_2) detected per creation of each of these particle. Substituting this into Eq. (3.1.9), which relates the energy of an NR event to the number of photons and electrons created, gives:

$$E_R = \frac{W}{\mathcal{L}} \left(\frac{\mathrm{S1}}{g_1} + \frac{\mathrm{S2}}{g_2} \right), \tag{3.2.1}$$

allowing for the energy of the event to be determined directly from the observed quantities. For ER events, the equivalent equation is retrieved by making the same substitutions into Eq. (3.1.8):

$$E_R = W \left(\frac{\mathrm{S1}}{g_1} + \frac{\mathrm{S2}}{g_2} \right). \tag{3.2.2}$$

In most TPC experiments, the values of g_1 and g_2 are each fixed to a single measured parameter, however, the actual values of g_1 and g_2 will have some dependence on the location of the event in the detector. For this reason, each event requires a position dependent correction applied to the observed S1 and S2 quantities; referred to as $\mathrm{S1_c}$ and $\mathrm{S2_c}$ respectively.

Additionally, the presence of the Linhard factor in Eq. (3.2.1) compared to Eq. (3.2.2), causes a difference in the reconstructed energy of an event for a given number of observed electrons and photons between an ER response and an NR. Therefore, three different units can be associated with a recoil. When it is indiscriminate of the type of recoil, keV is

most often used[6], keV_{ee} is used when talking about the reconstructed energy for ER, and keV_{NR} for reconstructed NR.

Position Reconstruction in Dual Phase TPCs

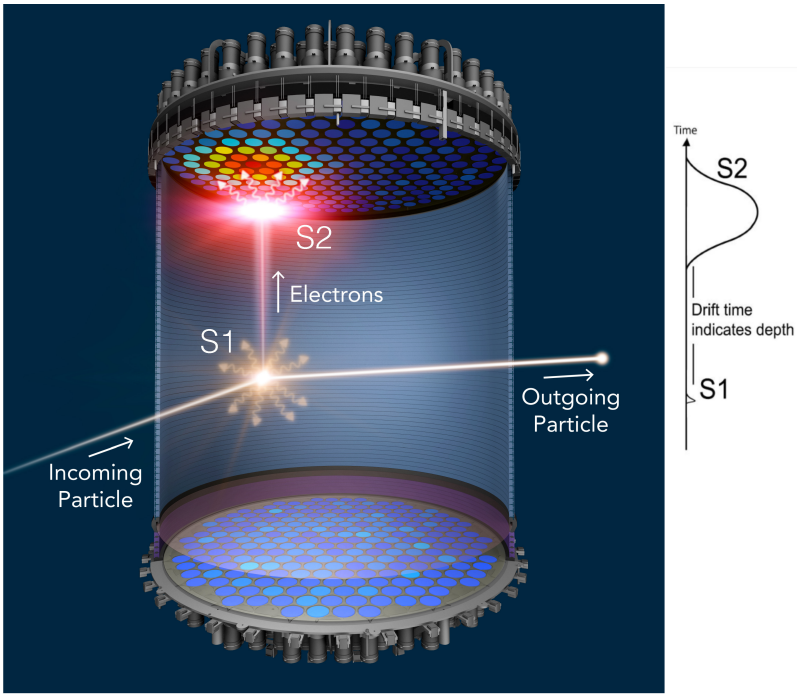

Figure 3.3: A particle traversing a dual phase TPC. On interacting with the target medium, a prompt S1 signal is emitted along with ionisation electrons; which are compelled by the electric field to drift to the extraction region where they undergo electroluminescence to produce the delayed S2 signal. The light of both is detected by the array of sensors at the top and bottom of the TPC [166].

The position of an interaction in the $x-y$ plane of a dual phase TPC is reconstructed from the resultant hit pattern of the ionisation electrons, either directly or through the induced S2 response on an array of sensors situated near the anode. This array could either be a segmented anode plane, a series of PMTs, silicon photomultipliers or charge-coupled devices. Figure 3.3 gives a graphic representation of an interaction with the LZ detector, and the resultant S2 hit pattern; the intensity of the observed signal in each PMT is scaled from blue to red.

As will be shown in §5.2.2 distortion in the electric field applied across the interaction volume can alter the ionisation electrons' path to such an extent that the hit pattern is either no longer directly correlated to the interaction site, or has become too diffuse to

[6]This is sometimes also expressed as "true" recoil energy.

accurately identify an interaction site. This is not limited to $x-y$ position reconstruction, any deviation in path, other than the known diffusion, will result in an inaccurate determination of the depth of the interaction in the detector, z. The inaccuracies in z arise from its calculation from the ionisation electrons' perceived path and uniform drift velocity (i.e. the time delay between the S1 and S2 signals); if this path is extended (i.e. the electric field compels the electrons to no longer directly drift on a vertical trajectory from the interaction site to the extraction region), or there are significant variations in the velocity of the electrons, any estimation of z would be biased. Fortunately, through a detailed study of the electric fields, it is possible to create a map of the deviations throughout the detector and map corrections to the ionisation electrons' $x-y$ hit pattern and drift velocity. Distortion of the hit pattern can also arise for interactions which occur near the edge of the TPC. The diffusion of the ionisation electrons will be compressed on the side closest to the field cage, and the photons in the S2 signal have an increased likelihood of reflecting off the edge of the detector smearing the response across neighbouring PMTs.

Discrimination of Electron and Nuclear Recoil

As explained in §3.1, interactions in LXe can be divided into whether or not they induce an NR or ER response within the target. ERs tend to be from particles which can interact electromagnetically: charged leptons, alphas, protons and photons. NR events such as those from neutrons, neutrinos and potentially WIMPs are caused by particles which do not interact electromagnetically. By comparing Eq. (3.2.1) and Eq. (3.2.2), it is clear that for a given E_R, the total number of photons and electrons produced will be less for NR interactions than ER. This difference, as previously stated, is primarily due to the atomic quenching that occurs in NR interactions reducing the number of free charge carriers. Additionally, there is some contribution to due to the differing recombination models used for ER and NR above $\approx$10 keV$_{\text{ee}}$. In general, a Thomas-Imel model [167] is used for both interactions where the tracks of the particles are smeared out by thermal effects and diffusion, and the recombination takes place in a box of 0 μm in dimensions. For ER events with recoil energies higher than 10 keV$_{\text{ee}}$, the ionisation density is used to determine the recombination following the Doke-Birks model [168]. A consequence of using different recombination is the inability to compare the initial ratio of excited to ionised atoms and the fraction of energy lost to heat at low energies between the two types of interaction. At energies where the same model is applied, the exact difference in recombination between NR and ER interactions will depend on the applied electric field

and the charge density of the interacting particle. Due to the higher ionisation density from NR compared to ER events, the recombination fraction is expected to be higher, reducing the number of free charge carriers. This results in a differing ratio of n_e to n_γ between the two types of interactions and giving the range of N_{ex}/N_i of 0.06 to 1 as previously stated (§3.1). The exact ratio for a given detector is determined through calibration using both neutron and gamma sources at a range of energies. Therefore, the ratio of S2 to S1 for a given interaction provides a powerful discriminator between the types of particles that induced the recoils in the target. Additionally, discrimination can be introduced by imposing an event selection that requires only a single scatter to be present in the event as the probability of an event of interest interacting more than once in the detection volume is vanishingly small.

3.3 The LZ Experiment

The LZ collaboration consists of over 250 people from more than 35 institutes based primarily in the US, UK, Portugal, and Korea. The collaboration is working towards the deployment and operation of a dual phase TPC containing 7 tonnes of LXe. The LZ detector has been constructed in the Davis Cavern[7], on the 4850 ft level of SURF in Lead, South Dakota, USA. SURF was formerly the site of the Homestake Goldmine, which was decommissioned in 2000 [170]. A standard means of reducing the influence of atmospheric backgrounds in rare event searches is to place them deep underground. The Davis Cavern is situated at a depth of 4300 m water equivalent. At such a depth, the muon intensity is reduced by a factor of 10^7 [171], see Figure 3.4, making the site ideal for rare event searches. With the backing of a generous donation from T. Denny Sanford, the Homestake mine was reestablished as a science facility in 2006. Continued funding from the US Department of Energy has seen multiple other experiments being conducted at SURF[8]; such as CASPAR [172], LUX [173] and Majorana [174]. The LZ collaboration is currently in the final stages of commissioning their TPC in the Davis Cavern, utilising some of the infrastructure used for LUX. Once commissioning has been completed, the detector will begin taking first data in early 2021.

[7] Previously used for the Ray Davis's solar neutrino experiment [169].

[8] SURF has also been selected for the site of the far detector part of the DUNE program/experiment.

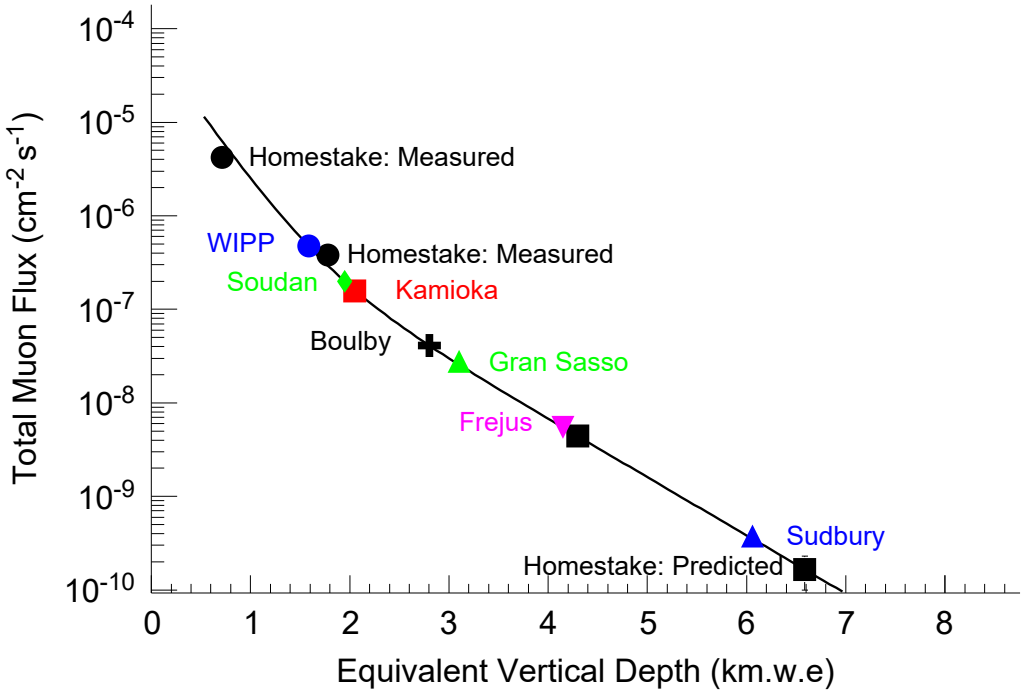

Figure 3.4: Muon flux for various different underground research facilities. Edited from [171]

3.3.1 Overview of the LZ Detector

The LZ detector consists of several different instrumented layers, as shown in Figure 3.5. The TPC's main housing is composed of two layers, the Inner Cryostat Vessel (ICV) and the Outer Cryostat Vessel (OCV); both of which have been fabricated from ultra-pure titanium [175]. The TPC is hermetically encapsulated by acrylic tanks containing $\sim$ 17 tonnes of Gadolinium-loaded Liquid Scintillator (GdLS) as shown in Figure 3.5, which in turn is housed within a 228 tonne water tank. The dimensions and masses of each of the LZ detector layers are given in Table 3.2. For a full description of the LZ detector and all of the required subsystems, the reader is referred to the LZ Technical Design Report [166].

The ICV is a cylinder with both a 1.6 m radius and height and defines the active region of the TPC, containing a total of 7 tonnes of LXe. The cathode grid location defines the lower bound of the active region and the upper is defined by the gate grid, positioned below the LXe surface. A further grid is situated above the LXe surface and used as the anode. A total of 58 uniformly placed titanium rings with a height of 25 mm are connected via a resistor ladder and produce a vertical electric field across the active region. These rings are implanted into PolyTetraFluoroEthylene (PTFE) panels,

and any exposed material is covered with extra PTFE; to minimise light escapes from the active volume. PTFE has demonstrated good reflective properties in LXe environments, $\approx$ 97.3% [176]. The gate is situated 13 mm below the anode, with the phase boundary between the liquid and gas phase Xe 5 mm above the gate (Figure 3.6). The electric field in that region, which is used for the extraction of electrons, is held at 10 kV/cm by biasing the cathode at -50 kV. A further grid is positioned just above the bottom array, and 14 cm below the cathode, to shield the PMTs at the bottom of the detector from the induced field (Figure 3.6). In this reverse field region, held at 2.9 kV/cm, any interaction will not produce a detectable ionisation signal and hence only produce S1 light [166]. To observe the produced scintillation light from an interaction, 494 PMTs are employed in a set of two arrays with optical windows facing inwards to the active region. Hamamatsu R11410-23 3-inch diameter ultra-low background PMTs ($\sim$ 1 mBq in U and Th) have been chosen due to their low radioactivity and sufficiently high quantum efficiency of $\approx$ 35% at 175 nm [177], corresponding to the Xe scintillation wavelength [178]. The array situated at the bottom contains 241 of the PMTs in an arrangement that allows for optimising the collection of S1 light. The remaining 253 PMTs are at the top of the detector in the Gaseous Xenon (GXe) region, and have been arranged to optimise the $x - y$ position

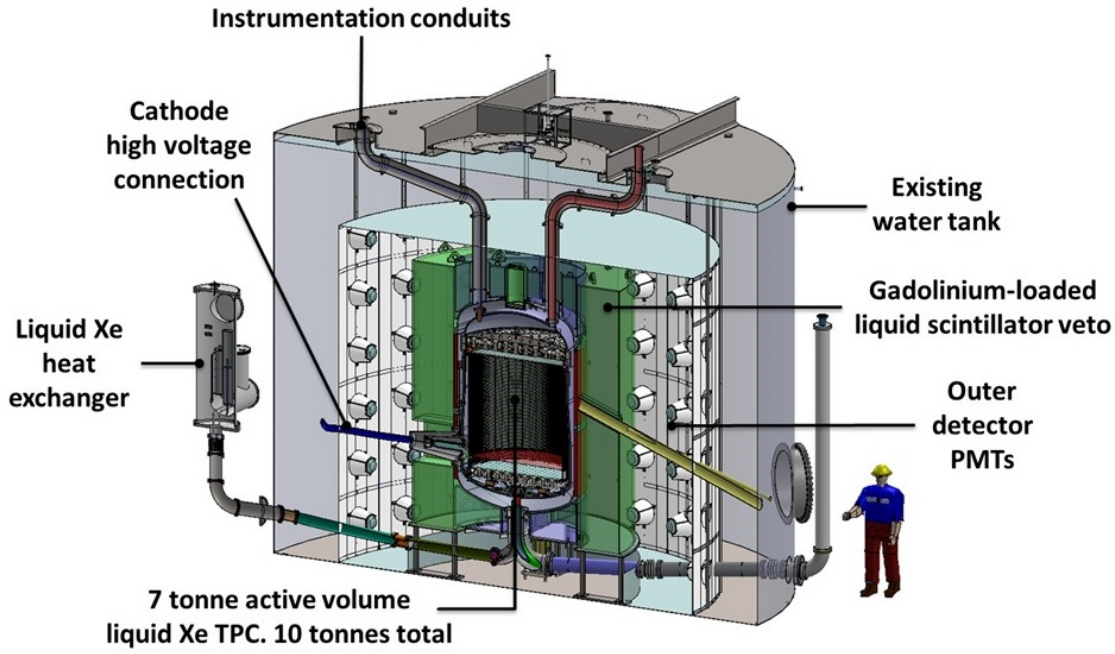

Figure 3.5: Rendered cut-through showing the layered structure of the LZ detector. The LXe TPC in the centre is surrounded by the scintillator tanks (green), all housed in the water tank (blue-grey). Annotations indicate some of the key subsystems within LZ [166].

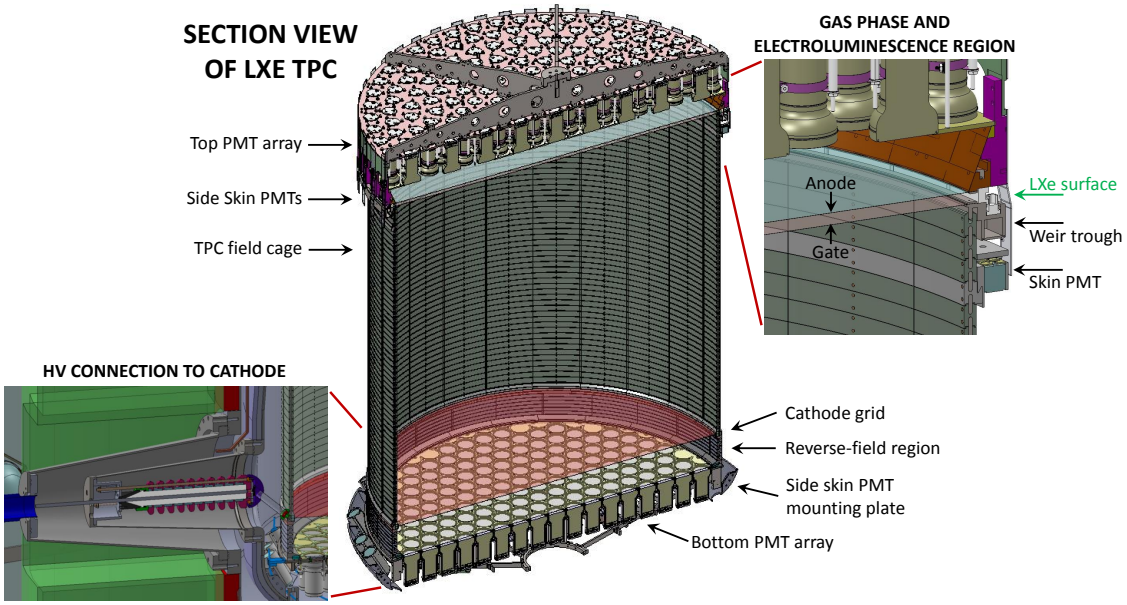

Figure 3.6: Rendered cut-throughs of the high voltage connection to the cathode, the LXe TPC, and the gas phase and the electroluminescence region. Annotations indicate the location of the top and bottom PMT arrays, the TPC field cage, the cathode grid, the reverse field region, the anode grid, gate and LXe surface [166].

reconstruction.

Control of the majority of the different subsystems required to operate and calibrate LZ will be handled by one centralized Slow Control (SC) system. LZ has opted to use Ignition, a commercial supervisory and data acquisition control system architecture supplied by Inductive Automation. The SC will use Ignition to control and monitor LZ subsystems via network connections, and for the cataloging of sensor readouts and commands in a historian database.

Veto Systems

The first-order approach to background reduction within a LXe TPC is to take advantage of the self-shielding properties of LXe, as described in §3.1. However, doing so leads to a reduction in the detector's attainable sensitivity, as reducing the fiducial mass reduces the exposure and consequently the sensitivity. To recover as much of this volume as possible, LZ implements a layered structure of specialised gamma and neutron veto systems. Figure 3.7 shows the difference in the expected rates of events which only scatter once within the TPC for the scenario of using self-shielding with and without a veto system. The first of these two systems, the LXe-Skin, is a LXe volume between the fiducial region of the TPC

Parameter [units]	Value
TPC active height [m]	1.46
TPC inner diameter [m]	1.46
active LXe mass [kg]	7000
xenon skin thickness, side [cm]	4.0 - 8.0
inner cryostat diameter [m]	1.58 - 1.66
inner cryostat height [m]	2.59
outer cryostat inside diameter [m]	1.83
outer cryostat height [m]	3.04
GdLS tanks outer radius [m]	1.64
GdLS thickness, side [cm]	61
GdLS thickness, top [cm]	40 - 62
GdLS thickness, bottom [cm]	34.5 - 57
GdLS mass [ton]	17.3
GdLS tanks, acrylic wall thickness [cm]	2.54
water thickness, GdLS vessels to PMTs [cm]	84
water tank diameter [m]	7.62
water tank height [m]	5.92
water mass [ton]	228

Table 3.2: Key dimensions and masses for the separate volumes within the LZ detector [179].

and the walls of the ICV. This near two tonnes of LXe is fitted with 93 Hamamatsu R8320 1-inch PMTs at the top and 38 Hamamatsu R8778 2-inch PMTs at the bottom. The primary purpose of the LXe-Skin is to identify events which scatter in the skin, especially neutron capture by materials within the TPC and gammas emitted from radionuclides in the material of the detector. Placing a threshold of 3 detectable photons on signals from the LXe-Skin results in a threshold of ∼100 keV across 95% of its volume and doubles the fraction of the fiducial region considered to be low background.

Neutrons will constitute the main NR background in LZ, and due to the robust discrimination between ER and NR events in LXe TPCs, will be the main background of concern. If a neutron-induced NR occurred near the edge of the ROI in the TPC, the secondary scatter might occur outside of the active volume, and the signature of the event

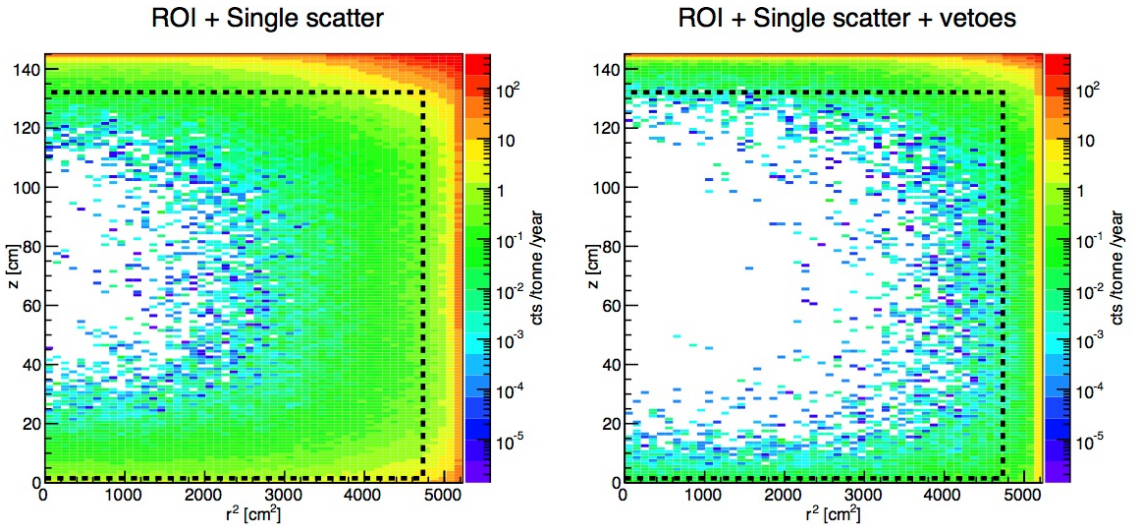

Figure 3.7: Simulated total NR and ER of single scatter background events in the LZ ROI, in a 6 keV to 30 keV energy window, for the cases of no applied veto (**left**) and with both the skin and OD vetoes applied (**right**). The dashed black line on both indicates the 5.6 tonne fiducial mass [179].

would be indistinguishable from that produced by a WIMP. A composite Outer Detector (OD) encompasses the TPC to observe a potential scatter external to the TPC. The first component is ten segmented acrylic tanks encapsulating the TPC which contain 17.3 tonnes of GdLS (the green layer in Figure 3.5). Neutrons scattering off proton-rich materials in the detector are moderated by the hydrogen in the GdLS before being captured by the gadolinium. This process produces an 8 MeV cascade of gamma rays [180]. The delay between a neutron inducing an S1 signal in the TPC and its resultant capture is $\approx$ 21 μs [181]. It is common for neutrons to drift out of the GdLS and then back in again where they are recaptured; resulting in an elongation in the capture process time to 200 μs. Therefore, to allow for an efficient vetoing of neutrons based on the coincidence signals between the TPC and OD, a period of 500 μs needs to be considered for neutron veto tagging.

120 Hamamatsu R5911 8-inch PMTs uniformly distributed about the circumference of the OD (6 PMTs in each column and 20 in each row) are used to capture light produced in the OD. Tyvek sheets will be used to cover the structural supports of the PMTs and create a curtain around the OD. With a reflectivity of at least 95%, the Tyvek should confine any light to within the instrumented volume [166]. The OD itself will be filled with ultra-pure deionised water, acting as a further shield for the TPC by suppressing backgrounds emitted from the surrounding cavern and cosmic rays. Additionally, this allows the OD to

act as a Cherenkov detector for these types of background, aiding efficient vetoing of these events. Simulations estimate the light collection efficiency within the OD at ≈7%. To act as an effective gamma veto, the PMTs would require a threshold of 100 keV. However, due to the presence of decaying ^{14}C, ^{147}Sm and ^{152}Gd, a higher threshold of 200 keV will be used for analysis. A 200 keV threshold results in a 95% efficiency for the detection of single-scatter neutron interactions in the TPC while only introducing a 5% deadtime. When conducting the analysis, a cut will be made on any signal in the LXe skin above three photons with an observed coincidence signal in the TPC (within an 800 μs time window of an observed S1 signal). Additionally, an event with a greater than 200 keV deposition in the OD within 500 μs of the TPC signal will also be removed. Due to the presence of these aforementioned radioisotopes, no simulations were conducted to determine reliable numbers for the neutron efficiency and dead time for a 100 keV threshold; which itself was an early stage optimistic assumptions.

To characterise the performance of the PMTs in all three detection layers (TPC, LXe-Skin and OD) regular calibration across a broad range of energies is required. To allow for the vetoing of events in the TPC accompanied by a signal in the OD, correct calibration of the time response across the readout channels for both detector layers is needed to high precision.

3.3.2 Backgrounds

The following section will outline the dominant backgrounds within LZ relevant to a WIMP-search, focusing on the 6 - 30 keV$_{NR}$ energy region, equivalent to 1.5 to 6.5 keV$_{ee}$, corresponding to the expected signal region of a 40 GeV/c^2 WIMP. Table 3.3 lists these backgrounds, and their resultant number of expected events for the full 5600 tonne-day exposure of LZ [179].

Radionuclides within the materials of the detector itself present a known background within LZ. A comprehensive screening campaign, consisting of nearly 2000 individual assays, was conducted during the fabrication to assess the radionuclides' exact quantities. Additionally, the self-shielding of the LXe further suppresses this form of background to the point where it is not considered a dominant background. Backgrounds that fall into this category, *detector components*, are generally from impurities in materials of naturally occurring gamma emitters: ^{49}K, ^{137}Cs and ^{60}Co as well as the ^{238}U, ^{235}U and ^{232}Th chains.

Of more concern is the plating of ^{222}Rn on surfaces during the manufacturing and detector assembly stages; falling into the category of *surface contaminants*. The decay of

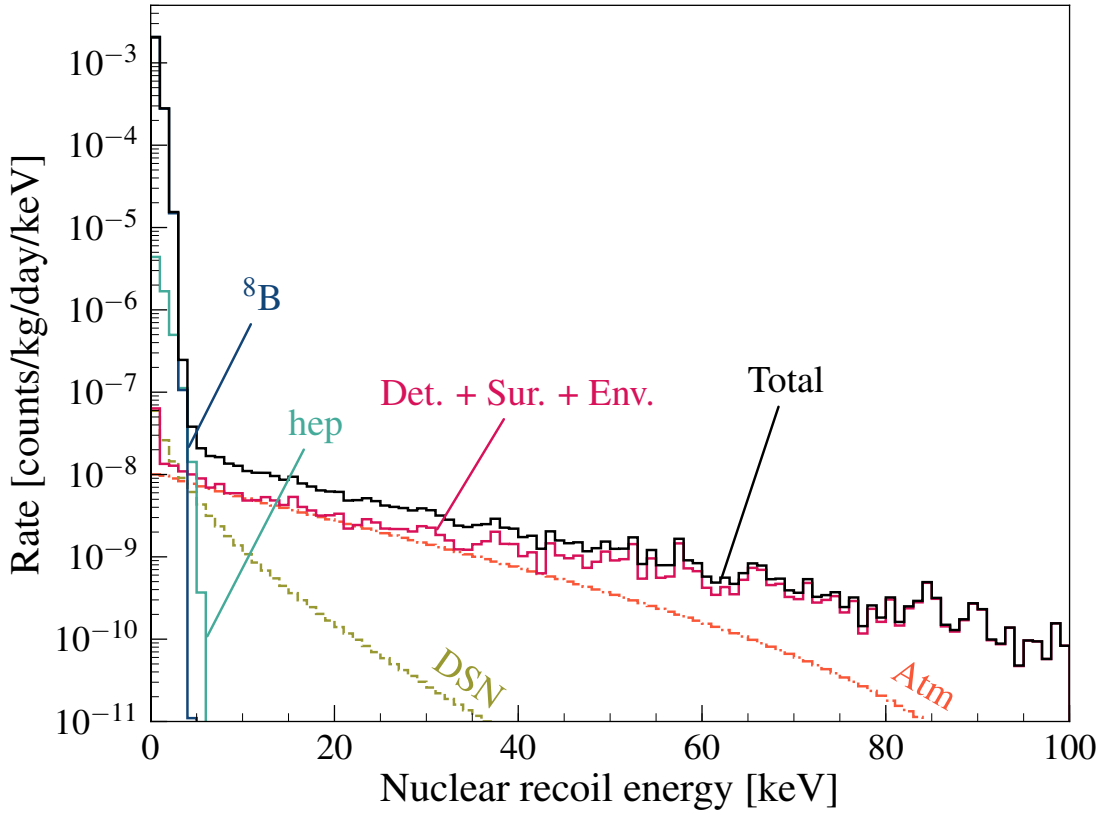

Figure 3.8: Differential rate spectra for ER backgrounds within LZ with a single-scatter within the 5.6-tonne fiducial volume and no coincidence signal in either the LXe-Skin or OD. Detector efficiencies and ROI cuts have not been included [179].

^{222}Rn can produce a NR background in the TPC through two channels: an (α,n) process where the neutron is emitted directly into the Xe, and through the ^{210}Pb sub-chain where the decay of ions in the sub-chain occurs near the detector's wall. The latter, through a suitable fiducial cut, can generally be rejected. One of the primary sources of radionuclide contaminants on surfaces is dust. By imposing a meticulous cleanliness regime during the detector's assembly, it is possible to minimise dust plating onto surfaces. The LZ TPC was assembled in a class 1000 cleanroom at SURF, utilising air ionisers to prevent static build-up on surfaces to further reduce the plate-out. Additionally, to monitor the degree of surface contamination, tape-lifting was conducted throughout, witness coupons were analysed and a full UV inspection conducted.

Another category of background of concern are the *environmental backgrounds*, the most significant of which are radioisotopes and their progeny produced from a material's exposure to a cosmic ray. Activation of the Xe can result in the presence of ^{127}Xe [182]; while activation of the titanium can lead to the presence of ^{46}Sc. The expected rates are

given in Table 3.3. The NR differential rate for the sum of environmental, detector and surface backgrounds is given in Figure 3.8 and the equivalent rates for ER backgrounds in Figure 3.9.

Dispersed radioisotopes are likely to still be in the LXe; most notably ^{220}Rn, ^{222}Rn, ^{85}Kr and ^{39}Ar. The last two are beta emitters and would induce an ER signal that should be discernible from a WIMP signature. The progeny of the first can produce a NR-like signal through "naked" beta emission. Within the ^{222}Rn sub-chain, there is a decay from ^{214}Pb to ^{214}Bi via the emission of a β. The ^{214}Bi then beta decays to an excited ^{214}Po, with a 90.2% branching ratio, releasing a high energy gamma on deexcitation. The signature of a beta followed by a gamma can easily be identified within the LXe even if it leaves the active region, where it is tagged by either the LXe-Skin or OD PMTs. There is also a chance the ^{214}Pb does not emit this gamma; generating a "naked" beta, which mimics a viable ER event within the TPC. The ^{220}Rn sub-chain also has a similar process.

LZ has conducted gas charcoal chromatography to purify the Xe to contain 450 ppt (parts per trillion) of ^{39}Ar and 0.015 ppt of ^{85}Kr [183]. For ^{222}Rn, the emanation from activated components is 1.53 μBq/kg [166]. Estimations on the number of events from these dispersed radioisotopes are given in Table 3.3 and their expected ER differential rate can be seen in Figure 3.9. From this, it can be seen that the dispersed ^{222}Rn is the dominant contributor to the observed number of ER events. The lack of available information on Rn emanation as a function of temperature from materials contributes to the uncertainty of these values. Additionally, there is no guarantee on the detector's outgassing levels or leaks introducing further Kr into the Xe.

Astrophysical neutrinos produce both ER and NR events via Coherent Elastic Neutrino-Nucleus Scattering (CEνNS) [184] and electric neutrino-electron scattering [185]; both being irreducible backgrounds. For high WIMP masses, neutrinos produced from muon and pion decays in the atmosphere, and those from supernovae are of greatest concern [105]. In contrast, those from solar processes:

$$^{8}\mathrm{B} \rightarrow ^{7}\mathrm{Be} + \mathrm{e}^{+} + \nu_{\mathrm{e}} \qquad (^{8}\text{B neutrinos}), \tag{3.3.1}$$

$$^{3}\mathrm{He} + \mathrm{p} \rightarrow ^{4}\mathrm{He} + \mathrm{e}^{+} + \nu_{\mathrm{e}} \qquad (\text{hep neutrinos}), \tag{3.3.2}$$

are only problematic for sub 20 GeV/c^2 WIMP masses; however, below this energy neutrinos emitted from ^{8}B produce a viable WIMP signature when scattering with the Xe for WIMP masses <6 GeV/c^2 [105], as can be seen in Figure 3.8 by the NR differential rate rapidly decreasing at ~6 keV. An additional ER background arises from the elastic

scattering of neutrinos produced from the *pp* solar chain; the rate of which is shown in Figure 3.9.

When considering the full exposure of LZ[9] the total expected background is 1131 ER and 1.03 NR events, as shown in Table 3.3. Therefore, when considering a search for a 40 GeV/c^2 mass WIMP, with a 99.5% ER discrimination below the NR median, a total of 6.18 events are expected in the signal region when considering the full exposure of LZ.

Background Source	ER	NR
Detector Components	9	0.07
Surface Contamination	40	0.39
Environmental	5	0.06
Dispersed radioisotopes	819	0
Physics	258	0.51
Total	1131	1.03
Sum of ER and NR in LZ for 1000 days, 5.6 tonne fiducial volume, with all analysis cuts = **6.18**		

Table 3.3: The estimated total contribution from all background sources in LZ relevant to a 1000 day WIMP search, with a 5.6-tonne fiducial volume. Numbers were determined from a cut and count analysis of the expected energy ROI for a 40 GeV/c^2 WIMP signal (1.5 to 6.5 keV for ERs and 6 to 30 keV for NRs). Analysis cuts applied: to single-scatter selection, LXe-Skin and OD veto, and the fiducial volume cut. Summarised from the table presented in [179].

[9]Full exposure being the total number of expected kilogram days of search data. For LZ this is 5600 kg of fiducial by 1000 days of live data collection.

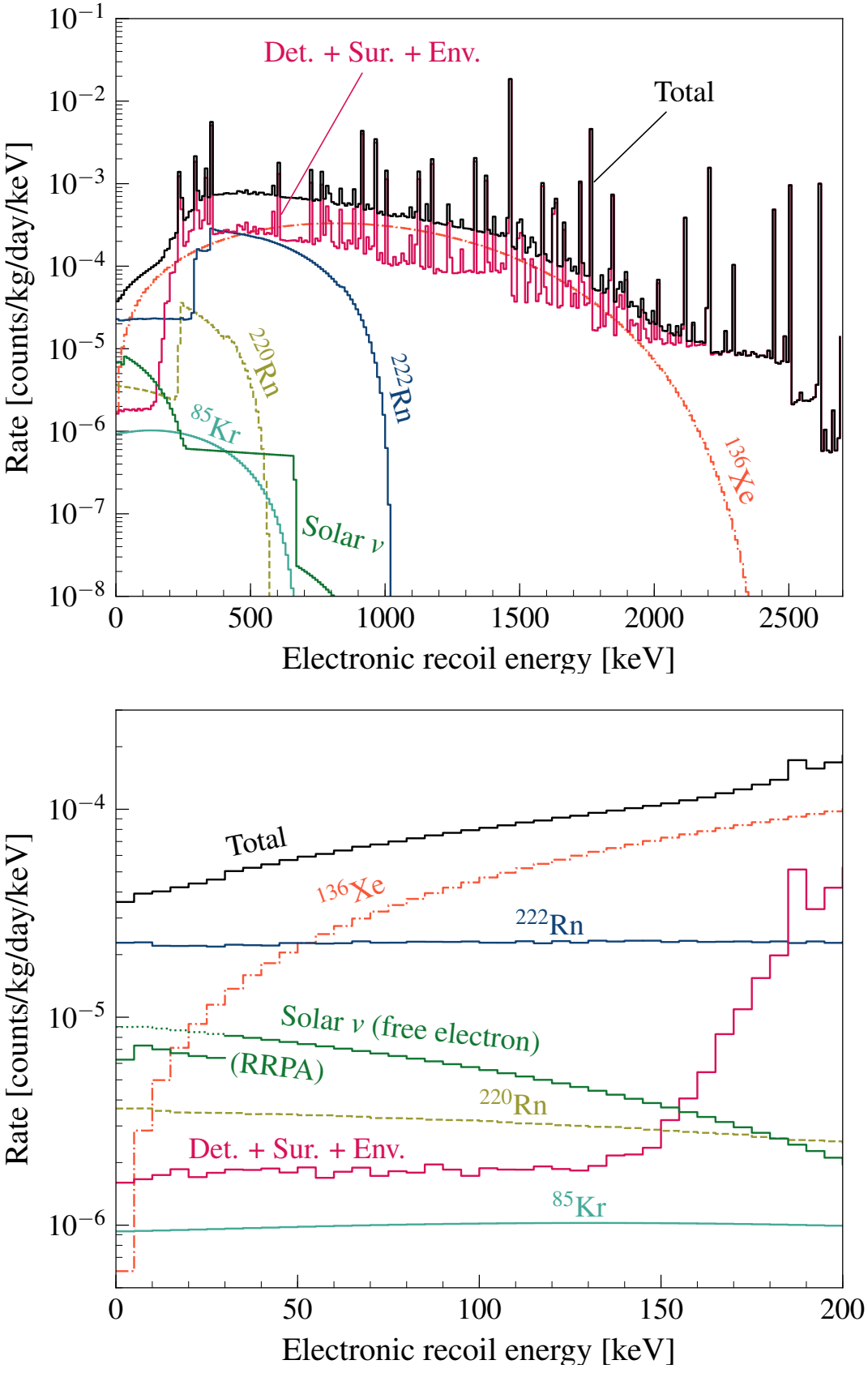

Figure 3.9: Differential rate spectra for ER backgrounds with a single-scatter within the 5.6 tonne fiducial volume and no coincidence signal in either the LXe-Skin or OD. Detector efficiencies and ROI cuts have not been included. **Lower** panel is the 0-200 keV region of the **upper** panel [179].

3.3.3 Calibrations

LZ will conduct intensive calibrations to ensure the correct identification of the energies and type of interactions in the TPC and veto systems. Accurate determination of these two properties are vital in LXe TPC experiments as this is the only viable means of particle identification, as explained in §3.1. Primary calibrations of the TPC will focus on determination of the S1 response to variations in (x, y, z) and the S2 response in (x, y, z, t), both of which are influenced by the exact geometry of the detector and the light collection efficiency. Additionally, these primary calibrations will assess the variations in the (z, t) response of S2. The S2 (z, t) response is sensitive to the ionisation electrons combining with electro-negative impurities in the LXe. Producing an inaccurate determination of the S2 associated to the event leading to an inaccurate determination of the recoil energy. Once these primary calibrations are addressed, further calibrations will be conducted to determine the event energy reconstruction within the TPC and to identify the ratio of S2/S1 used to classify the interaction type. Calibrations within LZ can be broken down into five different methodologies:

- The injection of radioisotopes directly into the LXe.
- The use of a bespoke deployment system to position commercial gamma and neutron sources at various heights within the vacuum space between the ICV and OCV.
- The generation of neutrons by a Deuterium-Deuterium (DD) generator attached to conduits to direct the neutrons into the TPC.
- The lowering of a photo-neutron source directly on top of the cryostat.
- The use of separate optical calibrations for the TPC and OD.

Internal Radioisotopes

The self-shielding properties of LXe makes it challenging to perform a NR calibration within the central volume of the LXe and nearly impossible to perform low energy ER calibrations via the use of external sources. One means to circumvent this is to perform a high exposure calibration (on the order of days) with a high rate, high energy source. However, this approach introduces significant dead-time to the data collection and could potentially lead to the activation of materials within the detector. Due to the reduction in data taking and potential introduction of secondary emissions from activated material, LZ will adopt the approach of mixing radioisotopes directly into the LXe to perform its

primary calibrations. In general, these radioisotopes decay with a short enough half-life to not impair data collection. Lower energy sources can be used to make an equivalent interaction energy in the TPC compared to an external source. A detailed description of LZ's systems to inject various sources into the LXe is given in [166].

^{83m}Kr will be injected into the LXe weekly in order to determine the influence of spatially varying parameters (g_1, g_2 and electron drift efficiency) within the TPC. ^{83m}Kr has a monoenergetic 41 keV decay (1.8 h half-life) which will be used to calibrate a combined S2 spatial response[10]. ^{83m}Kr decays in a two-step process, where the short decay half-life is 145 ns. This two-step process results in a time variation from decay to decay and in turn causes variations in the electron-ion recombination on an event to event basis; limiting the effectiveness of ^{83m}Kr for the calibration of the response of the PMTs to an ER interaction in the TPC [186].

Calibrations of the (x, y) position reconstruction of S2 signals could also be performed using ^{83m}Kr. These calibrations are significantly improved when using a homogeneously distributed source in the LXe. With the size of LZ and the intended recirculation system [166], ^{83m}Kr does not have a significantly long half-life to ensure it is homogenous in the LXe before it has decayed to the point where the rate of events is no longer statistically viable to use as a reliable calibration. LZ will instead use ^{131m}Xe, a long-lived Xe radioisotope with a half-life of 11.9 days; more than adequate to ensure homogeneity. Calibrations with ^{131m}Xe will also be used to help define the exact fiducial volume of the LXe.

To calibrate the low energy ER response and the discrimination ratio of S2/S1 at these energies, tritium-labelled methane will be injected into the LXe. The decay of the ^{3}H component (12.3 year half-life) generates betas with a spectrum of energy ending at 18.6 keV. Due to the long half-life the ^{3}H needs to be actively removed from the LXe. The CH_4 component of the tritium-labelled methane has a lower absorption rate into the PTFE than ^{3}H and can be effectively extracted by the getter.

The last of the injected sources, ^{220}Rn, will calibrate the large S1 signal response of the LXe-Skin. Unlike ^{222}Rn, ^{220}Rn does not have long-lived progeny and hence would not impact the experiment's sensitivity. ^{220}Rn decay produces a 6.3 MeV alpha followed by a secondary 6.8 MeV alpha. Calibrations of the light and charge yield at the boundaries between the LXe and surrounding material are possible by observing the decay of ^{220}Rn progeny, which are expected to plate-out on to these surfaces.

[10] This parameter can alter over time based on the purity of the LXe.

External Gamma and Neutron Sources

LZ will utilise a Calibration Source Deployment (CSD) system to position neutron and gamma sources at various heights between the ICV and the OCV. A full description of the CSD will be given in §4.1. Table 3.4 lists the calibration sources to be deployed by the CSD, the calibration they are used for and their activities. For those where the CSD run scheme is known, information on this is included.

Source	Calibration	Activity	Run Positions
^{133}Ba	OD/skin/TPC (energy)	3 kBq	NA
^{228}Th	OD (energy scale)	6.6 kBq	3 positions in z
^{57}Co	TPC (liquid level scan)	6 kBq	10 positions in z (small spacing)
^{22}Na	TPC/OD (timing)	0.5 kBq	2 positions in z (bi-weekly)
AmLi	TPC-NR band/OD (energy)	130 Bq (185 MBq Am)	NA
AmLi	TPC (45 keV endpoint)	130 Bq (185 MBq Am)	NA
^{252}Cf	TPC NR band/OD (energy)	120 Bq	NA
AmBe	TPC NR band and high energy	100 Bq (185 MBq Am)	NA

Table 3.4: List of CSD based sources with the calibration they perform and run positioning (if known).

The deployed neutron sources used for the NR band calibration (AmLi, AmBe, ^{252}Cf) were selected to give a wide range of different endpoint energies to cover as much of the NR band as possible. Figure 3.10 shows each of the deployed neutron sources' expected rate along with the expected rate from the DD and photoneutron sources. Both the AmLi (α,n) and the ^{252}Cf (a spontaneous fission source) are pivotal in calibrating the response in the OD generated by the interaction of a neutron with the GdLS. AmBe and AmLi (α,n) are excellent sources for calibrating the NR response in the TPC and OD. The broad range of the emitted neutron energies from AmBe makes it ideal for calibrations from threshold recoil energies to 300 keV; whilst AmLi with a maximum neutron energy of 1.5 MeV gives an endpoint recoil energy of 40 keV.

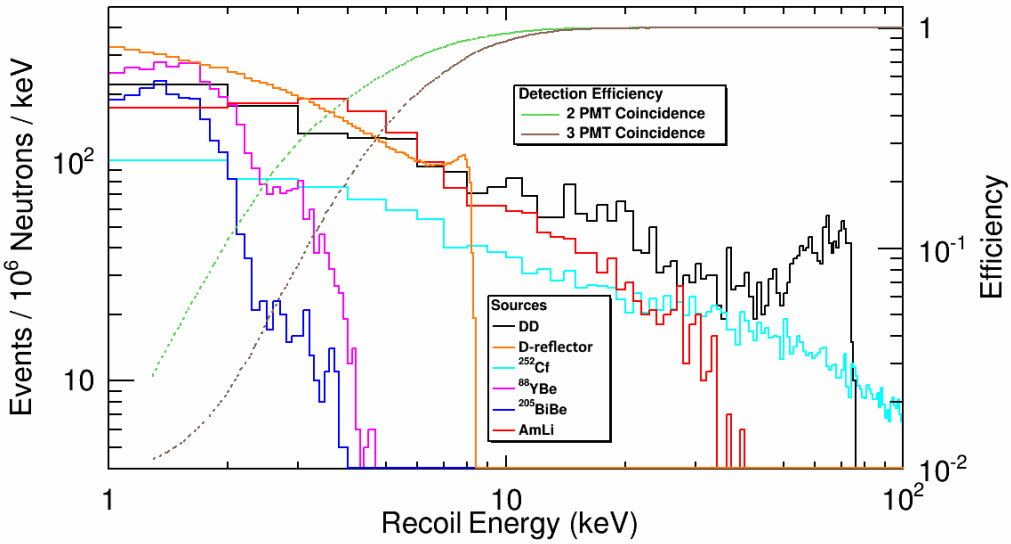

Figure 3.10: Expected rate as a function of recoil energy for the various neutron sources used to calibrate LZ: DD (black), D-reflector[11](orange), ^{252}Cf (cyan), ^{88}YBe (red), ^{205}BiBe (blue) and AmLi (magenta). The right axis gives the NR efficiency at these energies for the 2-fold (green dashed) and 3-fold (grey dashed) PMT coincidence levels[12][166].

The deployed gamma sources will serve little use in calibrating the energy response of the TPC PMTs. However, they will play a vital role in the calibration of the veto system's energy response and to synchronise the time response between the TPC, LXe-Skin and OD. Calibrations for high energy backgrounds and the efficiency of observing signals near the TPC's edge will utilise a ^{228}Th source; which emits a 2.615 MeV gamma (and many other smaller energy gammas and X-rays). ^{228}Th will also be the primary radioisotope based calibration of the OD PMTs' response across a wide range of energies; as well as to provide useful information on the time synchronisation of coincident signals in LZ's different detection volumes. The influence on the height of the interaction in the OD response to the ^{228}Th source is given in the left panel of Figure 3.11. Shown in the right panel of Figure 3.11 is the LXe-Skin response as a function of the interaction height to the 164 keV gammas emitted from the decay of ^{57}Co; a dedicated calibration for the 200 keV threshold required by the LXe-Skin. To sufficiently calibrate the energy response as

[11] A process to reduce the neutron flux in the TPC from the DD generator, the reader is directed to [187] for a complete explanation of the DD generator hardware and calibrations.

[12] During data collection LZ will operate with the 3-fold coincidence; however it may be beneficial during calibrations to adopt a 2-fold coincidence. This is due to the limited time in which they are performed and to aid in the calibration of the low energy response of the TPC.

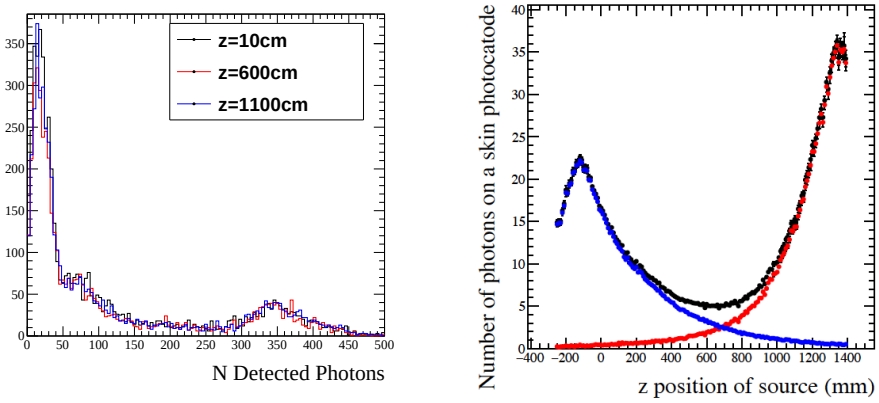

Figure 3.11: The estimated number of photons as a function of source height, using ^{228}Th for the OD (**left**) and ^{57}Co for the LXe-Skin (**right**). The **left** panel shows the number of photons detected by the PMTs at the top (red) and bottom (blue) of the LXe-Skin as well as the combined value (black) [166].

a function of source height in the LXe-Skin requires the capability to position a source with a 5 mm precision. Further calibrations of the timing of synchronisation between the TPC and the OD will be performed using a deployed ^{22}Na source. The decay of ^{22}Na is characterised by the emission of two back-to-back 511 keV gammas; this distinct behaviour of the decay makes it ideal for this calibration.

^{133}Ba was not initially included in the calibration procedure outlined in the LZ technical design report [166]. ^{133}Ba will be the only calibration that undergoes electron capture and will be used to cross-calibrate the energy response in the TPC, LXe-Skin and OD.

Deuterium-Deuterium Generator

Additional to deploying external sources using the CSD, LZ will also use an external DD generator[13]; procured from Adelphi Technologies [188]. This generator produces, through DD fusion, monoenergetic neutrons (2.45 MeV) at a rate of 10^9 per second. These neutrons can interact in the TPC with a range of recoil energies, making them pivotal in calibrating the NR response of the TPC. The generator itself is housed externally to the entire detector. The generated neutron beam will be directed on the TPC via two conduits running through the OD to the TPC[14]. DD calibrations were conducted on the LUX

[13] This calibration will not be discussed in detail; the reader is directed to [166] for a complete description.

[14] By directing the neutrons through this dedicated conduit, they will not have to pass through the water or GdLS in the OD which have been designed to moderate and capture neutrons.

experiment and showed the validity of this form of NR calibration down to 1.1 keV_{nr} for light yield, and to 0.7 keV_{nr} for charge yield [189].

Photoneutron Sources

^{88}YBe and ^{205}BiBe sources will be lowered through an opening in the OD and positioned such that the source sits central to the top array of the TPC. Being photoneutron sources, these will be used to calibrate the detector's response to NR events with energies at a few keV_{nr}; where the interaction is equivalent to that of a low mass WIMP. This calibration will aid in the separation of low mass WIMP interactions from interactions induced by the coherent scattering of ^{8}B neutrinos; which as mentioned in §3.3.2 are a significant background of concern in DM experiments.

Optical Calibrations

LZ will also utilise an Optical Calibration System (OCS) for the OD, details given in §4.2, and another optical system within the TPC. The optical system within the TPC consists of multiple 470 nm LEDs mounted on the top and bottom PMT arrays. These LEDs will be extensively used during the detector's commissioning stages; such as to determine the optimal PMT gain to produce a high single photoelectron detection efficiency of the PMTs within the TPC; which is pivotal in determining a suitable threshold for the PMTs during data collection. The OCS will be responsible for the single photoelectron detection efficiency of the PMTs within the OD, regular cross-checking of the OD PMTs response across their full required dynamic range and to validate the simulated optical model of the OD.

3.3.4 WIMP Search Strategy

With the implementation of the LXe-Skin and OD veto systems, LZ will be capable of monitoring a 5.6 tonne fiducial volume throughout its intended operational period of 1000 live-days. Searches for single-scatter NR events will occur in a predefined ROI in the recoil energy spectra for WIMP-nucleon interaction. When considering an SI or SD WIMP-nucleon interaction for a WIMP with a 40 GeV/c^2 mass, the ROI is between 1.65−6.5 keV for ER events and 6−30 keV for NR.

As stated in §3.2, g_1 is the observed fraction of the produced S1 light from an interaction. For LZ the optical simulations place g_1 at 0.12 photons detected[15] per photon

[15]The measure of photons detected (phd) accounts for the double photoelectron emission probability

produced (phd/ph) by an S1 and $g_{1,\mathrm{gas}} = 0.1$ phd/ph for S2 electroluminescence photons produced in the extraction region. The value of g_1 and $g_{1,\mathrm{gas}}$ were derived from optical simulations that include the 97.7% reflectivity of the PTFE when in LXe [176] and 85% when in GXe [191]. These simulations incorporated the measured 27% quantum efficiency of the TPC PMTs to 175 nm wavelengths[16] and the probability for two photoelectrons to be emitted by a single photon [192] as well as the literature value of 100 m (500 m) for the photon absorption length in LXe (GXe) [193]. For the S2 signals, a single ionisation electron is expected to produce 83 phd. The ionisation electrons are extracted with an efficiency of 95%, which is not included in $g_{1,\mathrm{gas}}$ [194], and results in a g_2 of 79 phd/electron. A nominal drift field of 210 V·cm^{-1} will be used during data collection with an estimated 850 μs electron lifetime [166]. To reduce the noise being recorded during data collection,

from a PMT photocathode at 175 nm wavelengths [190].

[16] This includes the first dynode collection efficiency.

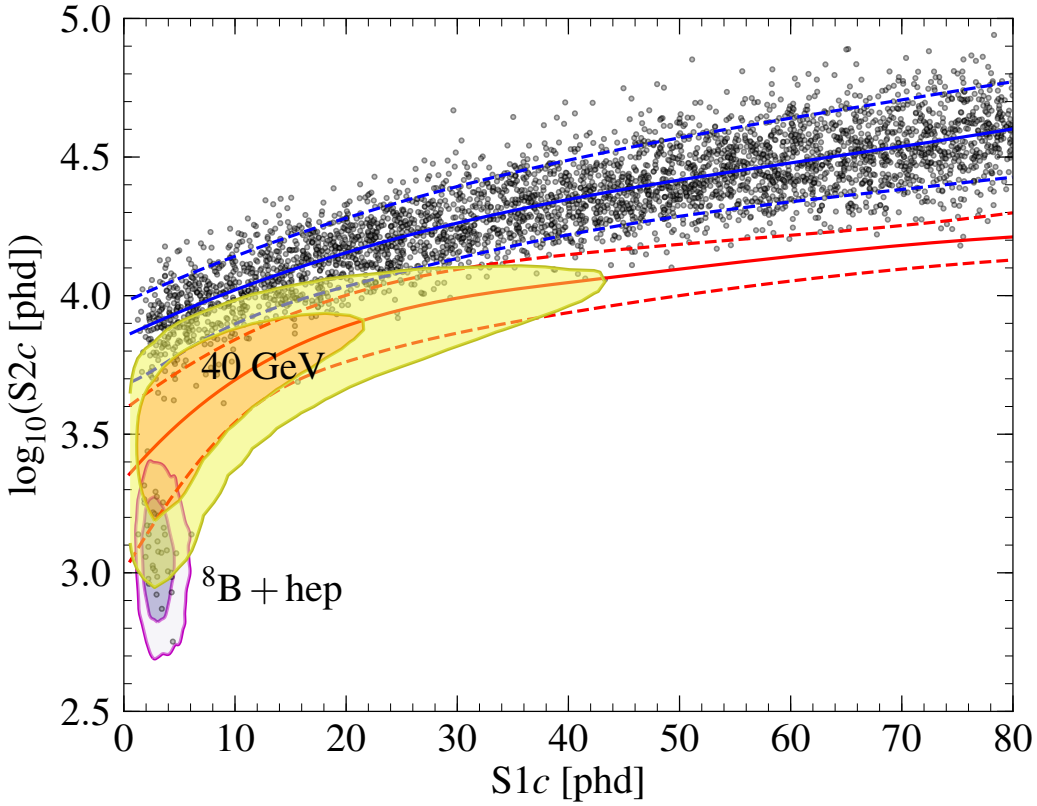

Figure 3.12: Simulated background data for 1000 live-days of exposure using the full 5.6 tonne fiducial mass. Red solid (mean value) and dashed (10% and 90%) lines indicate the NR band, while blue indicates the ER band. The shaded regions represent the 1σ and 2σ contours of the expected NR background (^{8}B and hep) and a 40 GeV/c^2 WIMP signals [179].

a 3 fold-coincidence is required to identify S1 signal.

During operation, the primary backgrounds (as given in §3.3.2) produce an NR or ER signal within the fiducial volume. The LZ collaboration intends to run a two dimensional (S1, S2) Profile Likelihood Ratio[17] (PLR) fit to distinguish ER and NR events; which as given in §3.2 is possible by discrimination based on the differing ratios of ionisation to scintillation yields produced by ER and NR events.

The LZ collaboration has conducted in-depth simulation using these detector parameters to determine the expected background signals within the complete exposure of LZ [179]. Figure 3.12 shows the distribution of these background events in S1-S2 space, as can be seen, most of the events resides within the region bound by the blue dashed lines, the ER band. As previously stated, the ^{8}B and hep neutrino backgrounds are of more significant concern for low mass WIMPs, which is highlighted by the region bound by their 1σ and 2σ contours. Also included in this figure are the expected 1σ and 2σ contours in S1-S2 space for a 40 GeV/c^2 WIMP. By performing a PLR analysis on these full exposure (5.6 tonne active mass over 1000 live-days) simulations, the LZ collaboration project an exclusion on the SI WIMP-nucleon interaction, with a 90% confidence, at a cross-section of 1.4×10^{-48} cm^2 for a WIMP mass of 40 GeV/c^2 (Figure 3.13) [179] . For the same WIMP mass, the projected 90% exclusion limit of the SD WIMP-neutron (WIMP-proton) interaction is at a cross section of 2.3×10^{-43} cm^2 (7.1×10^{-42} cm^2).

[17] For an in-depth description of the LZ PLR the reader is directed to [108].

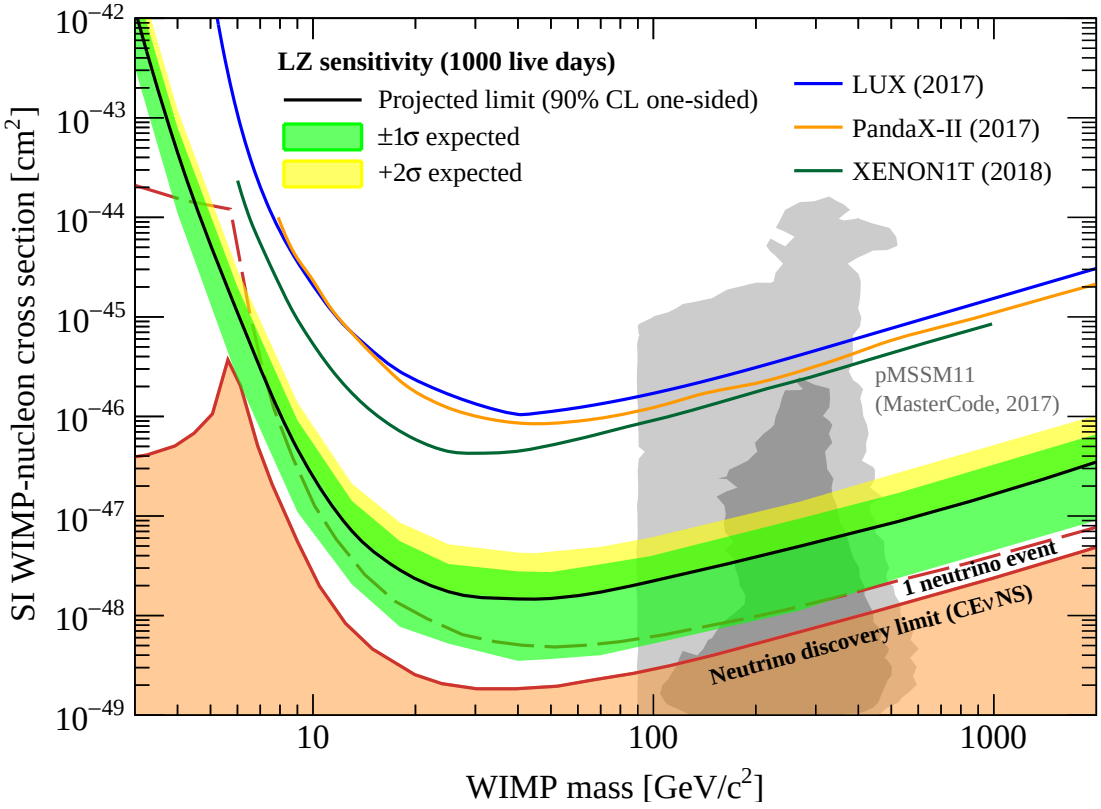

Figure 3.13: Projected sensitivity of LZ to SI WIMP-nucleon interactions over a period of 1000 live-days using a 5.6 tonne fiducial mass. The minimal cross-section obtained was 1.4×10^{-48} cm^2 for a WIMP mass of 40 GeV/c^2. Power constraints on the -2σ region lead to its omission from the plot [195]. Included are the results from other DM searches utilising LXe TPCs [90, 89, 88]. The background arising from coherent scattering of neutrinos with the target are included in the shaded region [105, 106]. Additionally the favoured regions from the pMSSM11 model scans have been included[107]. Image from [179].

Chapter 4

LZ Calibration Systems: Calibrated Source Deployment and Optical Calibration System

The following chapter will outline two of the key calibration systems used within LZ: the Calibrated Source Deployment (CSD) system and the Optical Calibration System (OCS). Each section will contain a summary of the systems design and Quality Assurance (QA) procedures.

4.1 Calibration Source Deployment System

LZ will utilise both internal and external sources to calibrate energy, position and timing in the TPC, LXe-Skin and OD, as covered in §3.3.3. A dedicated subsystem is required to position external neutron and gamma sources; the CSD. A total of three calibration tubes allow access for the CSD sources into the detector. Each calibration tube is fitted with its own individual CSD system. The geometrical arrangement of three calibrations tubes optimise the reach of the calibration. These tubes are in the vacuum space between the ICV and OCV, as shown in Figure 4.1 and their radial positioning relative to the TPC shown in Figure 4.2. The three CSD units were designed and manufactured by members of the LZ collaboration at the Rutherford Appleton Laboratory (RAL). The system has now been shipped and installed on-site at SURF and is ready to perform initial calibrations of the TPC in early 2021. The main requirements of the CSD are:

- To accurately position the source to within ± 5 mm.

- To have the capability to perform greater than 1000 operations.
- To have a radioactive rate lower than that of the cryostat.
- To be able to operate at a slight over pressure in the calibration tubes to prevent leakage of air or Rn into the system.

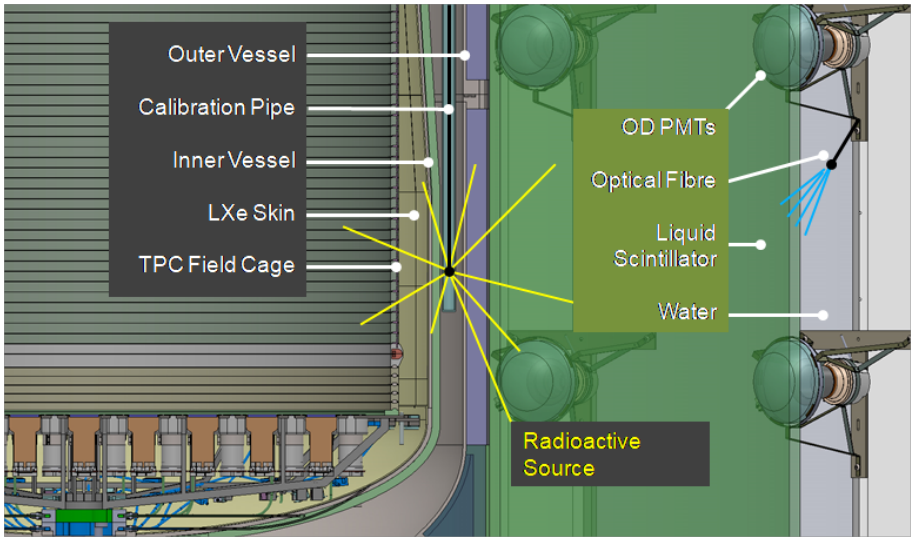

Figure 4.1: CAD rendering of LZ, showing the location of a calibration tube between ICV and OCV, Figure from [166].

4.1.1 Design

To ensure complete coverage during the main TPC calibration, a set of three 2.36 cm diameter calibration tubes run the 6 m length from the top of the water tank to below the cathode grid. The tubes were manufactured from the same titanium as used in the manufacturing of the cryostats; minimising the radioactive background contribution to the TPC. To position a source at a specific distance in the calibration tube, a 2 phase stepper motor[1] with a 1.8° resolution controls the deployment of a filament. The filament is reeled around a drum, and is driven by the motor via a 19:1 reduction planetary gear-head[2]. A $\sim$ 0.15 mm diameter braided composite filament was chosen due to its high max load of 12 kg; §4.1.2 includes a comparison of different filaments. All of this is housed in a K50 tee-piece, coupled to the calibration tube via a connection chamber, Figure 4.3. A wheel lever feeds the filament from the drum into the calibration tube, preventing snagging of the filament. An end switch is attached to the pinwheel to prevent over retraction of the

[1]Motor model: SH2141-5511 by SANYO DENKI Co.
[2]Gear-head model: GP 22A by MAXON.

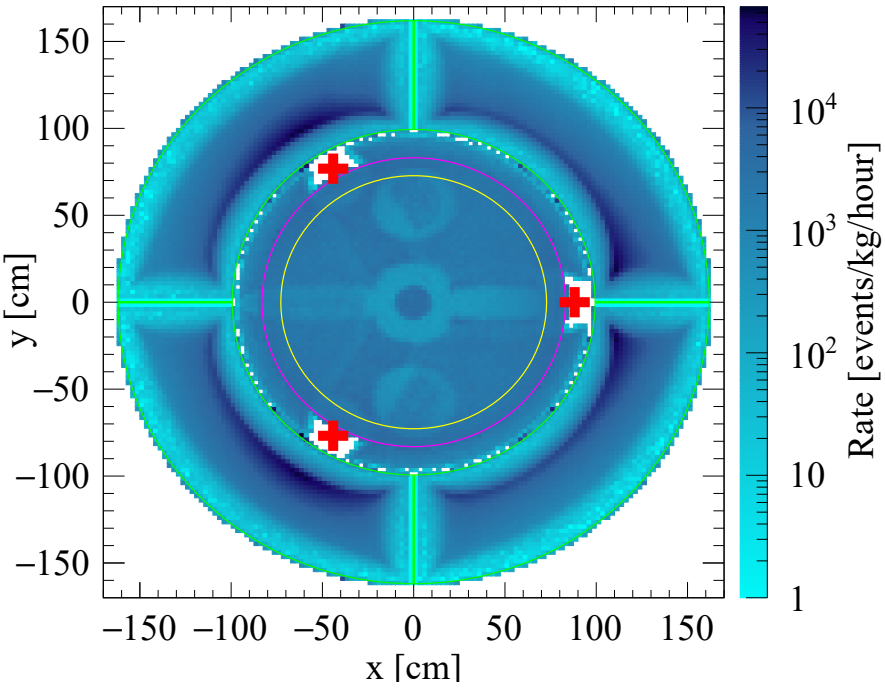

Figure 4.2: Simulation of deployed AmLi source, heat map shows the expected NR rate. Red crosses indicate radial locations of the CSD source tubes, the TPC border is shown in yellow, the LXe skin in pink and the edge of the acrylic tanks containing the GdLS in green [196].

source into the tee-piece.

Commercial sources[3] have been selected for all gamma sources, whilst for the neutron sources a bespoke AmLi source was developed. Each source will be encapsulated into one end of a 127 mm long, ∼16 mm diameter acrylic cylinder. An M4 hole is tapped into the opposite end of the cylinder, allowing for a vented screw to be securely attached to a ring collar[4]. The filament is attached to the capsule via a hole bored through the top of the screw and secured with a cap topped with a reflector, as shown in the left of Figure 4.4. A potential serious risk would be posed by the detachment of the source from the deployment filament, which would drop freely down the calibration tube. To mitigate against this, a shock absorber has been placed at the bottom of each calibration tube to ensure the sources remain intact in such eventuality. Furthermore the source capsule holder screw is made from a ferromagnetic material that would allow for the retrieval using a magnet attached to a retrieval filament. For attenuation of the gamma flux the AmLi source capsule[5] required a much larger capsule, shown in the right of Figure 4.4; the 105

[3] Eckert and Ziegler type R sources.

[4] Marensic stainless steel (410SS) was chosen due to its good corrosion resistance.

[5] Produced by the University of Alabama from (inner to outer) W, W, SS.

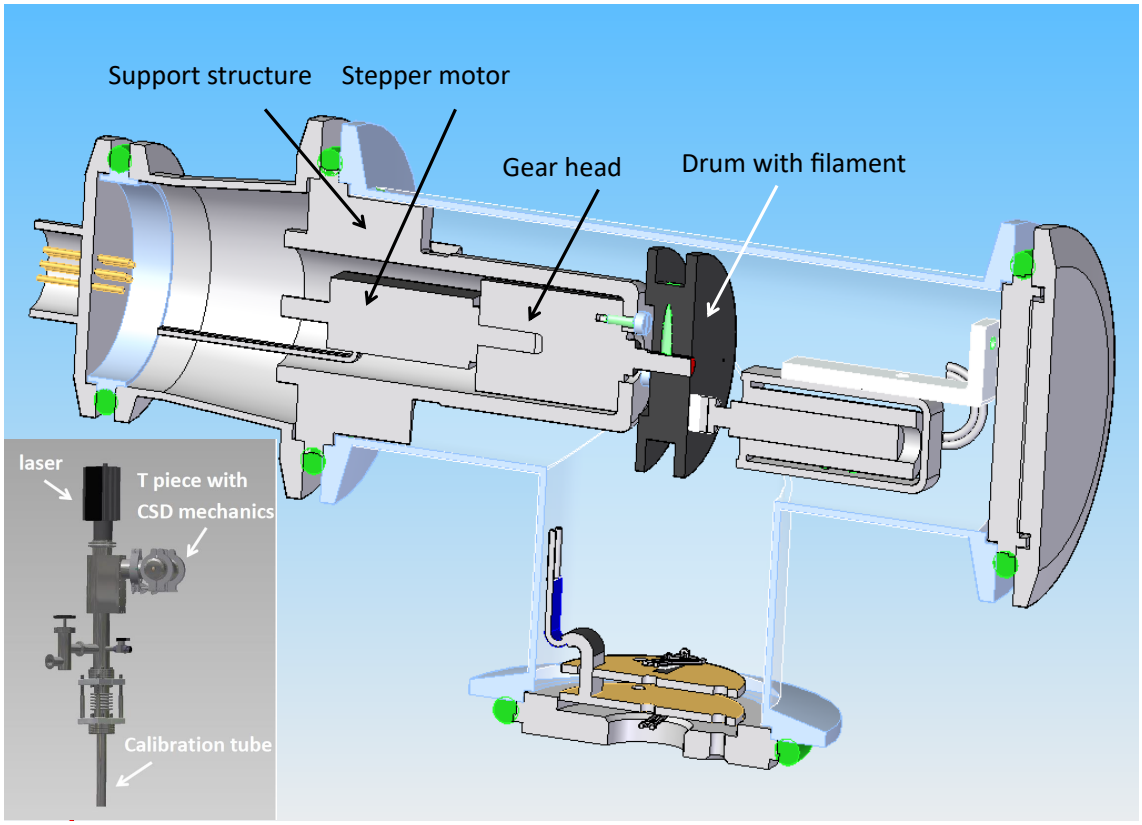

Figure 4.3: CAD showing the breakdown of the CSD components housed in the tee-piece. The insert shows the mounting of the tee-piece to the connection chamber [166].

g AmLi source will be the heaviest load on the system.

An ILR1181-30 Micro-Epsilon, Class II laser ranger, with a 2 mm precision, is attached to the top of the connection chamber; the light is incident on the top of the source capsule onto which a reflective paper is attached. By establishing a feedback between the stepper and the laser ranger, the requirement of accurate positioning within ± 5 mm was met. §4.1.2 shows these stability tests.

Nitrogen purging of the CSD and source tubes will occur after any access has happened to the connection chamber (i.e. opening and closing the chamber to attach a source). A six-way piece connects the CSD chamber to the calibration tube providing a pumping port, pressure relief port and pressure gauge port (Figure 4.5). The remaining ports are populated with a gas inlet, outlet, pressure relief and vacuum valve. To absorb the mechanical stresses on the system upon cooling, the six-way piece has a set of bellows between its connection to the calibration tubes.

Figure 4.4: The **left** image shows the dummy source capsule used for testing and the insert shows a finalised Cf^{252} encapsulated. The **right** of the image shows the Russian-doll capsules used for the AmLi source.

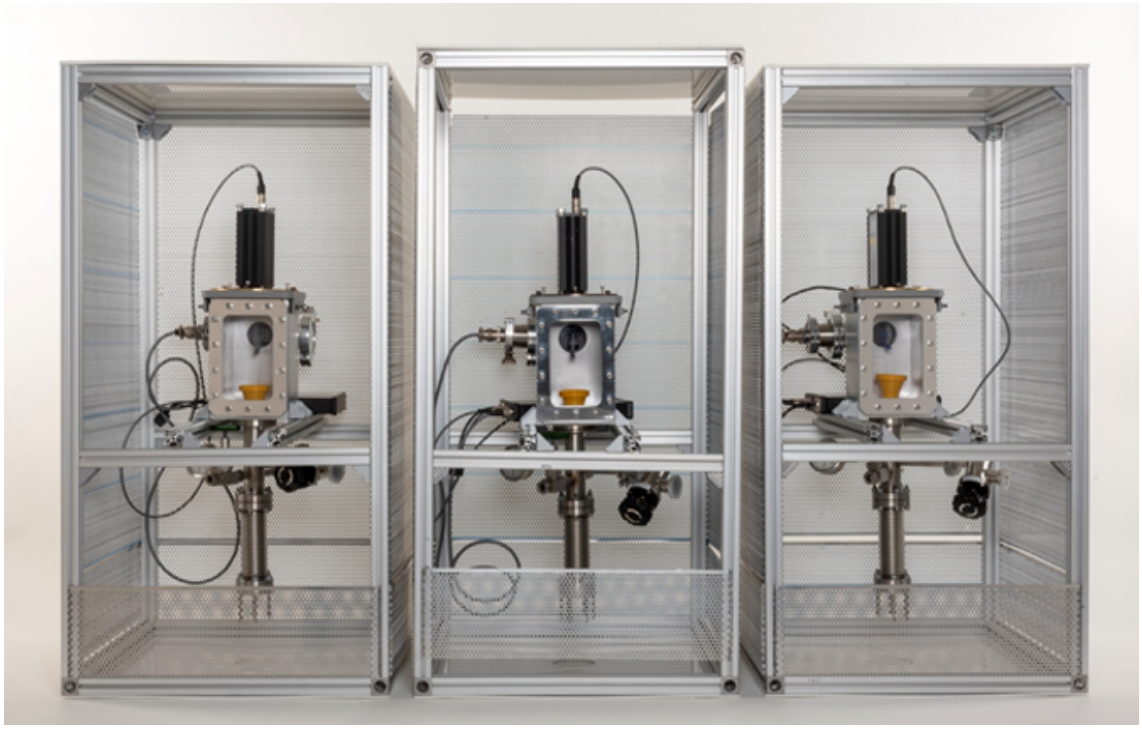

Figure 4.5: Photo of the three complete CSD units prior to shipment for installation at SURF.

Electronics

Each of the CSD units is operated via a Xilinx 7 series Zynq Field Programmable Gate Array (FPGA) chip on a Zybo board with a PMODSTEP daughter board[6], shown in Figure 4.6. Configuration data and the boot file are contained on a Micro SD card inserted into the board. The three identical channels connect to a single Ethernet switch, which connects to LZ's SC. IP and MAC addresses are set within the code and require compilation to change.

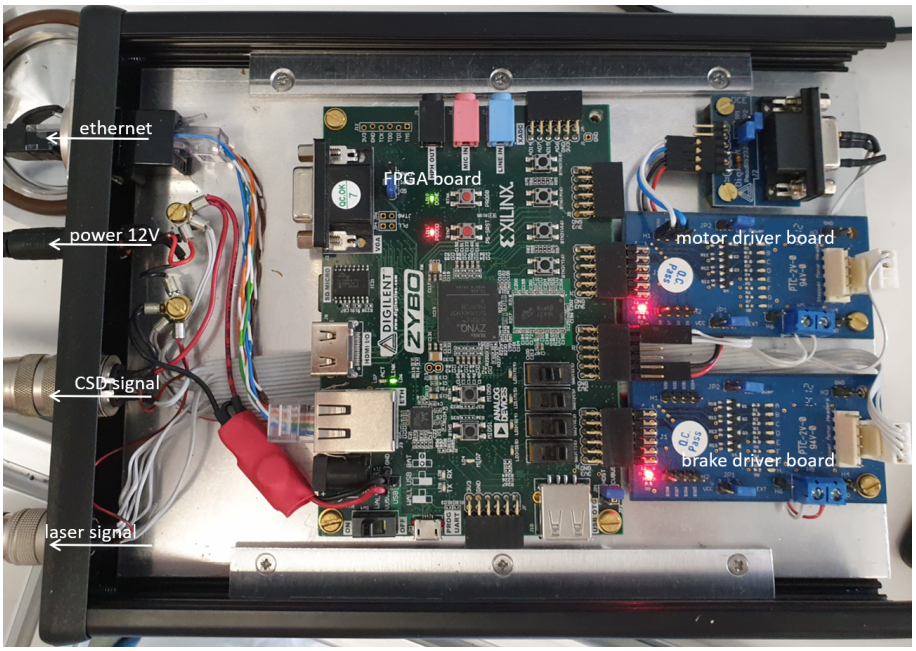

Figure 4.6: Image of board, key components annotated.

The FPGA was programmed using the default Zynq processing system. Each board also possesses two analogue input timers, two unidirectional GPIO ports and a serial port connection. A standalone interrupt-driven application, developed in SDK with Vivado 2017.3 WebPack, gives easy control to update the current operation immediately. An echo server with Xilinx modified processes in Modbus commands was established with DCHP mechanism disabled. Modbus is limited to a single 32-bit register, where the function code is ignored. The following is the structure of the Modbus commands:

00 00 00 00 00 08 01 XX XX AA dd dd dd dd

Here XX is any number, AA has the register address in the lower byte (upper ignored) and dd is any data byte. Table 4.1 contains a list of the available registers, the data needed to be sent and what action the command performs.

[6]Both boards were produced by Diglent.

Register	Data	Action	Description
02	Any	Immediate stop	Power off motor coil and apply breaks
04	Any	Retract filament till end switch is hit	Reference point for operation without laser
05	Position	Move to position with feedback	Actively holds the source at set position with adjustment from laser
06	Position	Move to position without feedback	Moves source to set position
08	Any	Read input port state	Returns 14 bits, where last two indicate state of end switches
09	Solenoid	Toggles state of breaks	Uses only two least significant bits. 1 = turn on breaks. 2 = turn off breaks

Table 4.1: ModBus registers used to operate the CSD.

4.1.2 Quality Assurance of the CSD Systems

Throughout the CSD's development, QA tests were performed, with focus directed towards attainment of the system's requirements. These tests were vital in achieving system readiness before instalment. The following tests were conducted with a single CSD unit at RAL, using a 1:1 scale of the calibration tube (6 m tube with CSD situated at top), as shown in Figure 4.7. During these tests, a Delphi Code[7] was used to set the Modbus commands for the CSD unit with a 50 g dummy source. This dummy source was made from the same materials and with the same dimensions as the commercial source encapsulating capsules. Before operating the system, a sanity check was performed by taking a laser reading of a source at a known distance. For the initial tests, the source pipe was not sealed on the bottom (the source tubes that will be implemented into LZ will be closed as they are placed within the vacuum layer between the ICV and the OCV). The dummy source capsule was extended to the full 6 m tube length; allowing for the laser's calibration to the source's distance at the bottom of the source tube. Calibration of the final installed system occurred along similar lines by taking the readings from the empty calibration tube with only the shock absorber (which has a reflector on it) in place.

[7]Developed by A. Khazov, STFC RAL.

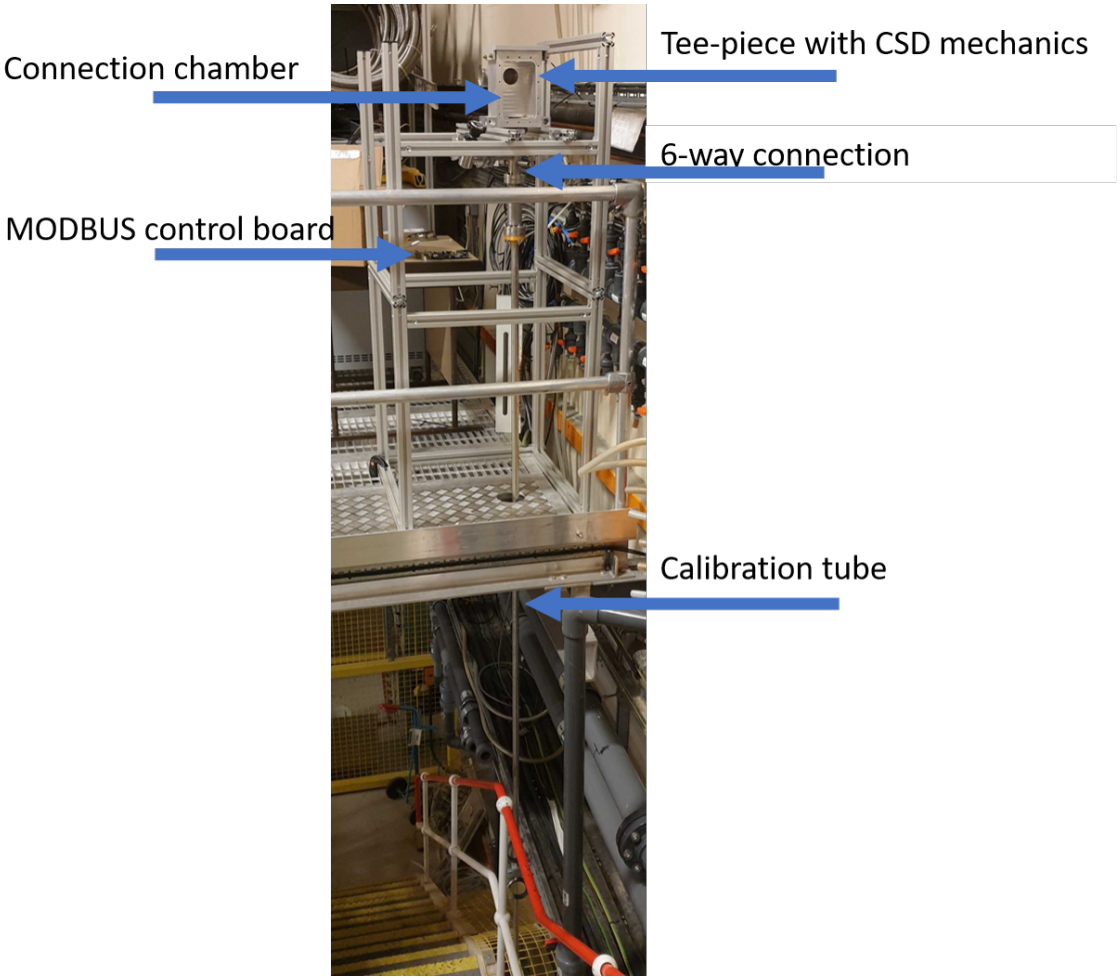

Figure 4.7: Annotated photo of the 1:1 scale CSD test set-up at RAL.

When entering a distance to position the source, the code controlling the motor converts the distance into an estimated number of steps. With the chosen stepper motor and gear head, this gives 52.36 steps/mm. As the filament is unreeled the amount of filament around the drum decreases. This results in a correlation between the amount the source travels with each step to the current extended distance. Therefore, it is important to understand whether this variation is significant enough to cause discrepancies between the stepper set and the laser read distances. Any differences will be corrected by the feedback loop with the laser ranger. It is important to note that the further off the initial positioning is, the longer the time needed for adjustment; increasing the deadtime between positioning and data recording. By setting a range of steps which is then converted into distances by the above ratio, sending the source to this position with no feedback adjustments, and then comparing this to the laser read distance, it is possible to identify the degree to which this influences the accuracy of the initial placement. The results in Figure 4.8 give a gradient of 0.019 mm/step. Inverting the gradient retrieves

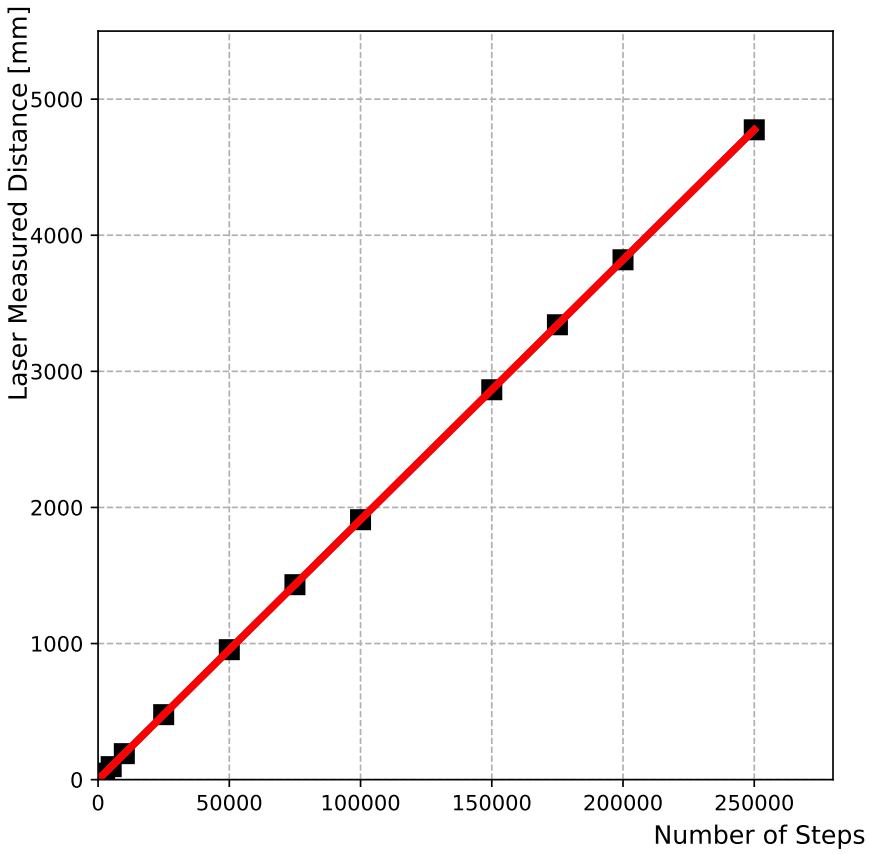

Figure 4.8: CSD laser read distances as function of number of steps, with no feedback adjustments. Straight line fit is shown in red, with gradient of 0.0191 mm/steps and an intercept of 0.0001 mm.

52.63 ± 0.38 steps/mm, which is consistent with the estimated number of 52.36 steps/mm.

Filament Elongation

Elasticity of the filament material should be minimal; additionally the filament should be strong enough to withstand sufficient force to not break under the load of the heavier AmLi source capsules. The laser feedback would adjust the position of the source to compensate for any deviation from the set distance; however, this would increase the system's settle time, and the ratio of steps to mm would now become a function of the extended length. Measurement of the required force as a function of the extended length are given in Figure 4.9. The 0.15 mm diameter braided microfilament[8] was selected as it displayed the least elongation across all applied forces, whilst still being able to withstand loads of 100 N.

[8] 100% spectra fibre by Innovative Textiles Inc.

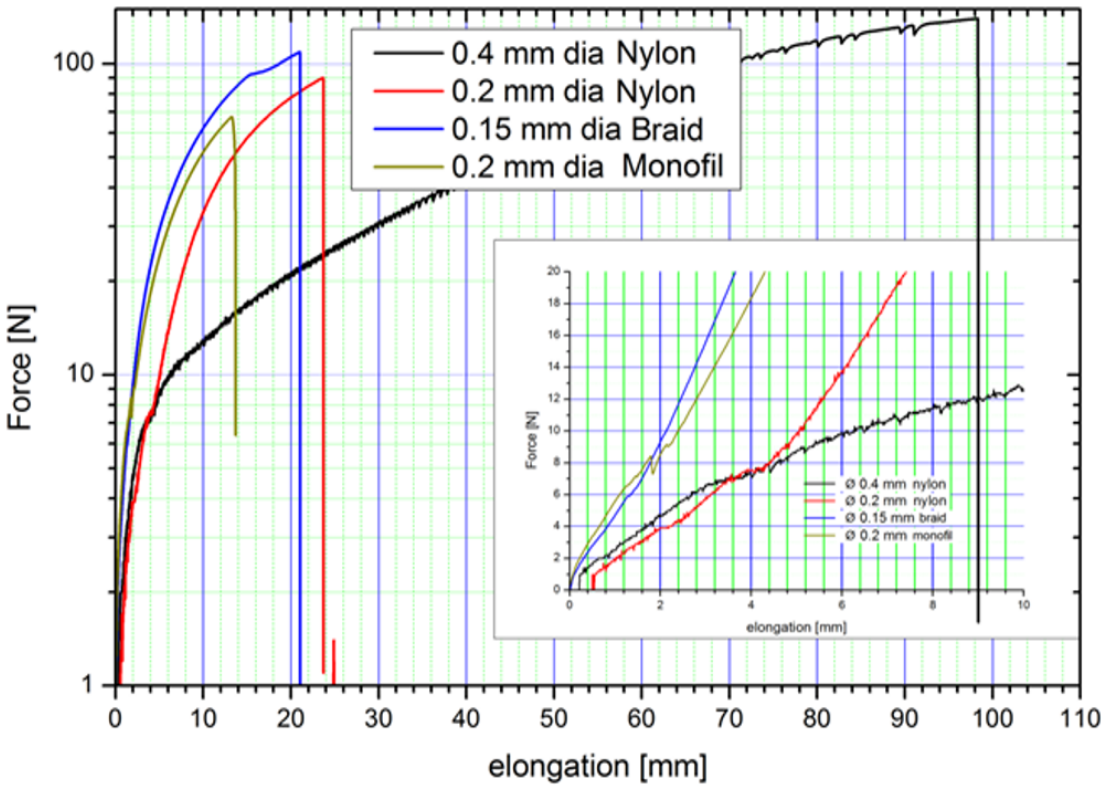

Figure 4.9: Amount of elongation experienced by several different filaments for a given force. Sub-panel plot is a zoom in of the 0 to 10 mm elongation region.

Variance in Travel Distance

A second test with no feedback adjustments was conducted to determine the average number of extra/fewer steps made by the motor per mm. The source was moved in increments of 25 mm, 100 mm, 200 mm, 500 mm and 1000 mm recording the initial and final positions read by the laser each time. Multiple measurements for each increment were made with the average of each result shown in Figure 4.10. Converting these distances back into steps and dividing by the distance travelled gives the deviation from the expected number of steps per mm. The results show that the variance in steps per mm was near consistent for all travelled distances, ≈ 0.52 steps/mm. The small adjustment was fed back into the script handling the conversion of input distance to number of steps performed. It should be noted that as the laser of the test CSD unit was calibrated to the entire length of the calibration tube, it is expected that larger deviations from the true position are expected at shorter set deployment distances. This is due to the change in the effective diameter of the spool; i.e. on average, more length is extended per revolution of the spool during the initial stages of casting the filament and will show the most significant divergence from a distance per step established from the whole length.

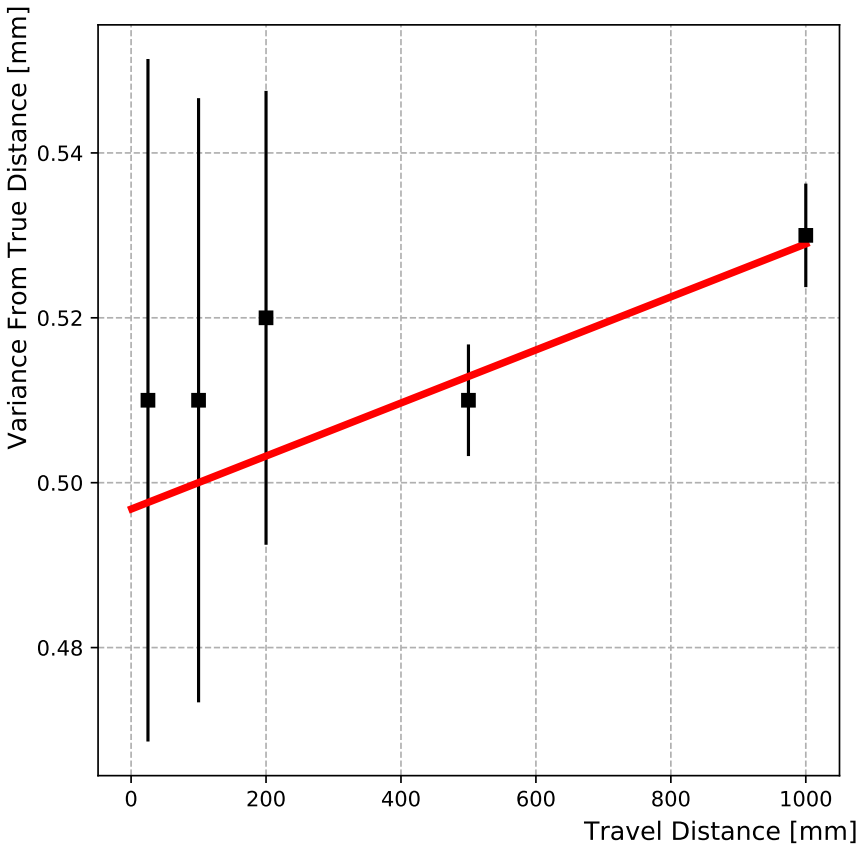

Figure 4.10: Variance from true distance set as a function of set travel distance. Points shown are averaged over each of the collected data sets and errors on y are their related standard deviations.

Long Term Stability

To verify the long term stability of the system, a 14 hr test was conducted. A source was extended to a distance of 5 m overnight in a non-temperature regulated environment. From Figure 4.11 it can be seen that over this time, both feedback enabled and disabled measurements varied by no more than 1 mm. This small variation helped confirm that: the filament has very little elasticity, and variations in length due to temperature changes will be negligible. Additionally, the feedback enabled curve does show more micro adjustments as it continuously seeks to reach the set distance; which can be considered as a very low level "noise" on the position. During actual operation, the system will only ever be holding a source at a given position for a matter of seconds to minutes. With this in mind, the stability is more than sufficient to ensure the required ±5 mm precision needed for the LXe-Skin calibration (§3.3.3).

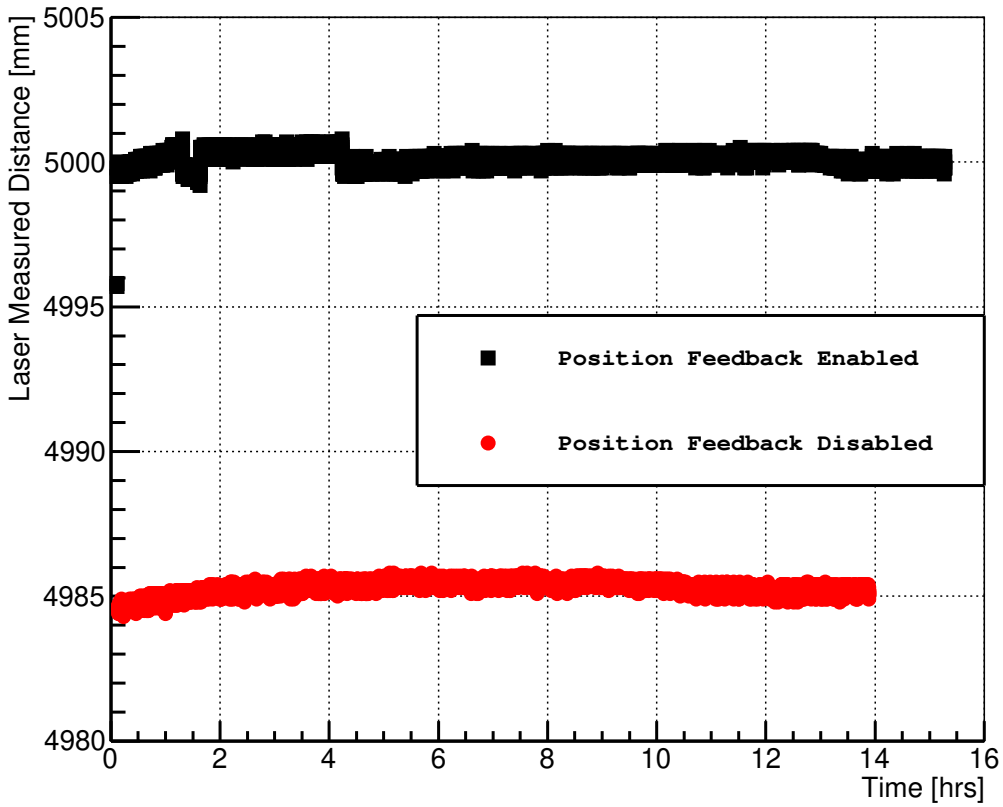

Figure 4.11: CSD long term stability test, set distance of 5 m over a period of ≈14 hrs. Shown are measurements with feedback adjustment enabled (black) and disabled (red).

Velocity

To determine the system's approximate velocity, the source was positioned at 2.4 m and then retracted to 0.4 m, as shown in Figure 4.12. The gradient gives the retraction velocity (working against gravity) to be 9.35 mm/s ≡ 0.1777 steps/s. This translates into requiring ≈ 10 minutes to retract the system from its full extended length of 6 m.

Burn-In

During testing, the duty cycle of the device far exceeded that of actual operation (continuous operation for ∼ 5 hours), this served as a thorough burn-in test of the device. Only two issues arose: warping of the 3D printed drum due to heating; and self snagging of the filament. The first was addressed by replacing the drum with one made from aluminium. The second is preventable by ensuring even initial spooling of the filament and that a sufficient load is placed onto the filament during operation. By making these changes, each CSD unit will operate beyond the 1000 cycles set out in the system's requirements.

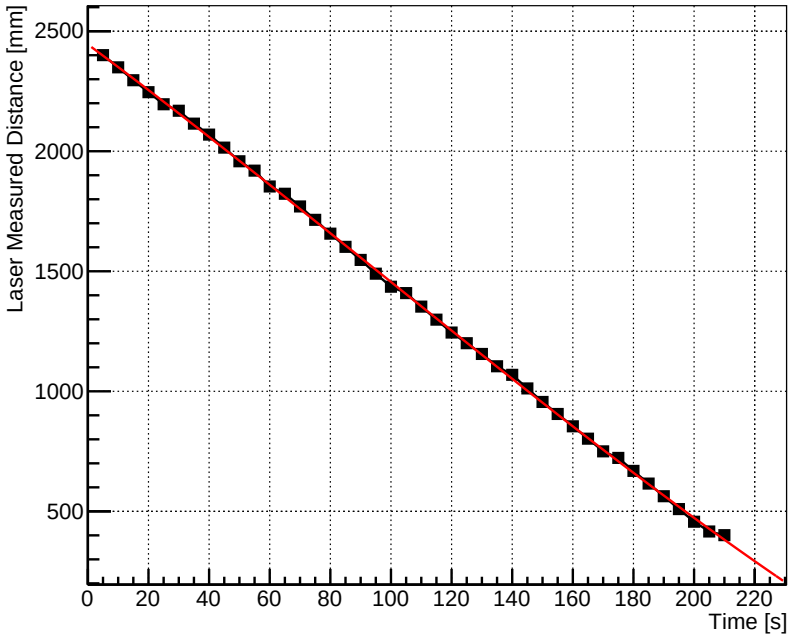

Figure 4.12: CSD retraction from set distance to determine velocity. Straight line fit applied with a gradient of -9.35 ± 0.13 mm/s and an intercept of 2445 ± 3. mm

System Commissioning Test

All three CSD units have now been installed on-site at SURF; Figure 4.13 shows one of the units installed on top of the water tank in the Davis Cavern. Initial tests of the system have been conducted; this being the laser measured distance as a function of the number of steps the motor has performed for each unit and is given in Figure 4.14. It should be noted that the deviation from the straight-line fit observed in all three units is due to the variation in the amount of filament unravelled per step. As the filament is spooled on a drum, the equivalent circumference decreases proportionately to the amount of filament that has been unravelled. It is the likely cause for the deviation of the data from the fit at high steps.

All three units were simultaneously pumped down to $\sim 10^{-4}$ mbar. All connecting pieces were leak checked; the leak rate was found to be 10^{-6} to 10^{-7} mbar l/s; far surpassing the minimum requirement of pressures within the tube of 1 mbar.

Calibration of the total length of the source tube and hence of the laser feedback system was conducted at SURF. The estimated lengths with associated uncertainties for all components that contribute to the distance between the CSD connection chamber and the bottom of the source tube are given in Table 4.2. Without any source in the system, a measure of the distance to the bottom of the tube was obtained by observing the response

of the laser light reflecting off the shock absorber (which was coated in a reflective material) at the bottom. This process was conducted on all three units, the results of which are given in Table 4.3. This table shows that all 3 units produced a laser read consistent with the determined length of the source tube.

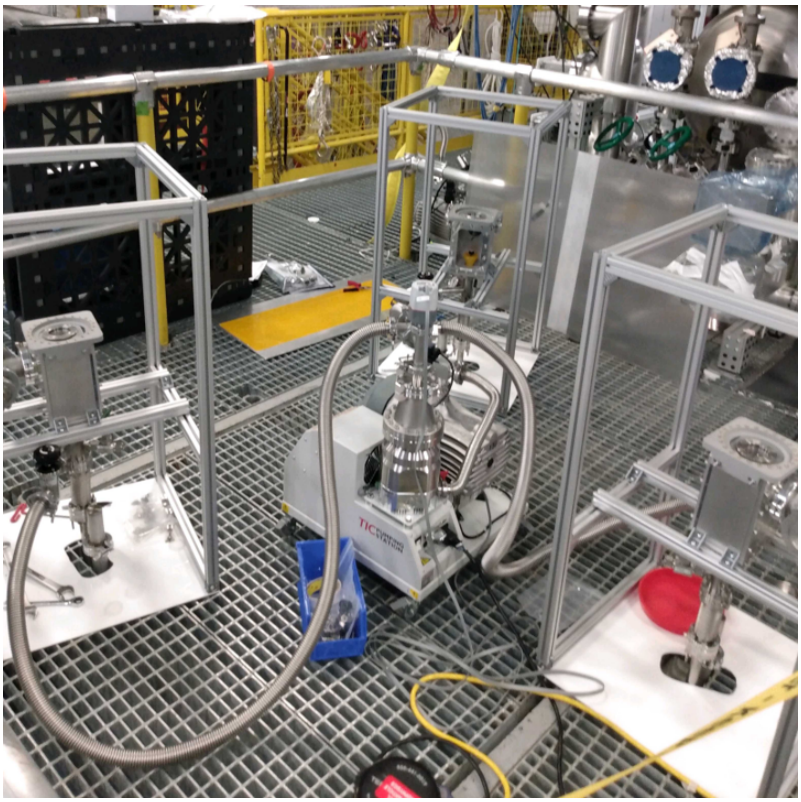

Figure 4.13: Photo of the three CSD units installed at SURF and coupled to the source tube during initial pump down tests. Photo accredited to Dr A. Kamaha.

Item	Length/Adjustment [mm]	Range/Uncertainty [mm]
CSD bottom flange to laser bottom distance	544	defined by 3 following items
Adjustment screws		2
Bellows		10
Position of CSD support		2
Upper calibration tube	3359	2
Lower calibration tube	2363	2
Disk in bottom tube end weld	-4	1
Shock absorber	-23	1
Reflections of laser light	3	1
Total	**6252**	**21**

Table 4.2: Determination of the calibration source tube length and error. Adjustment screws refers to the total action in the screws used to adjust the positioning of the laser.

CSD Unit	Laser Read [mm]
CSD1	6232
CSD2	6254
CSD3	6248

Table 4.3: Laser read distance of the calibration tube for all 3 CSD units.

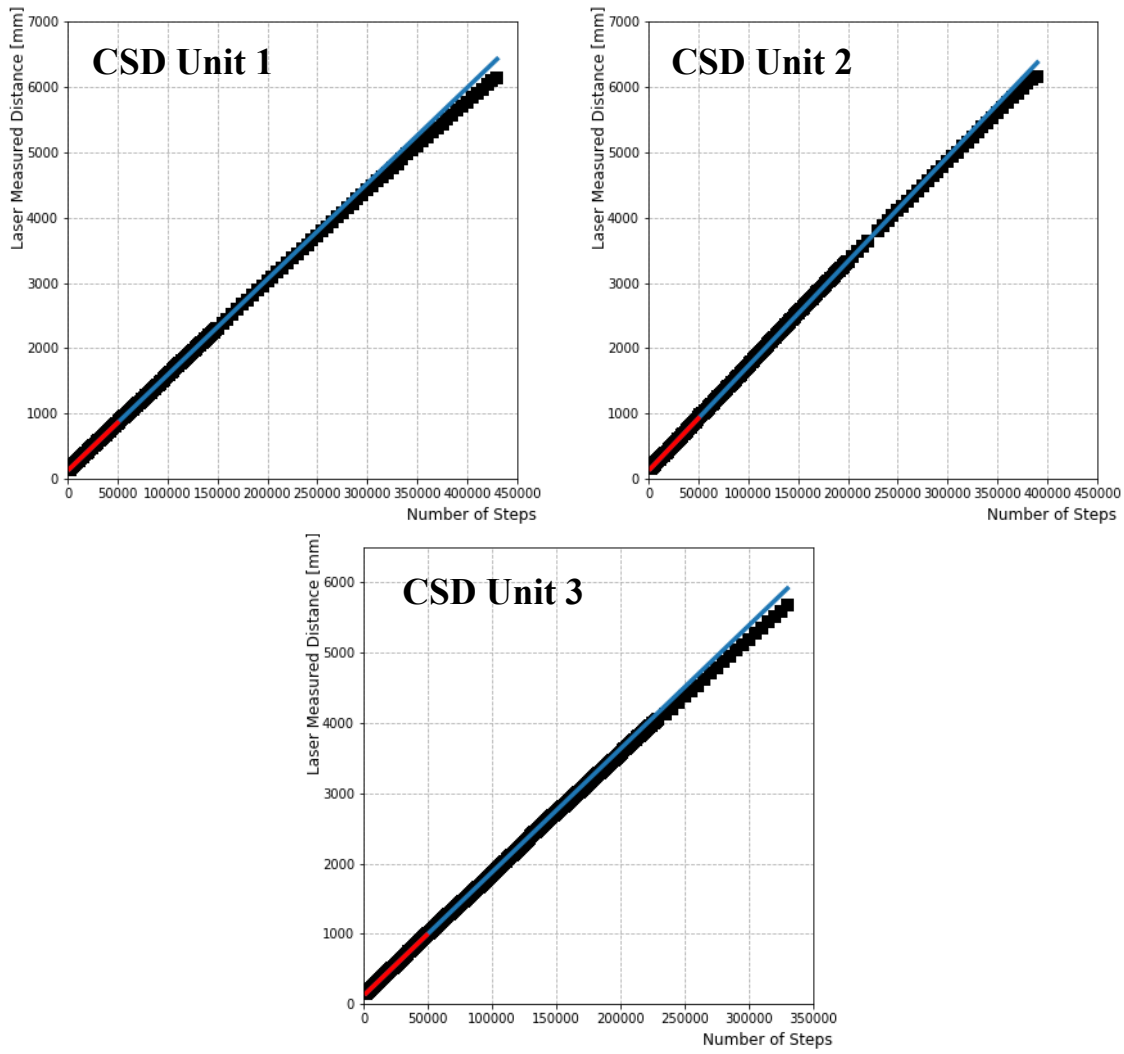

Figure 4.14: Commissioning data for all three CSD units at SURF. Shows the laser read distances as function of number of steps. Due to the uneven spooling of the filament, on the deployment of the source, a slight divergence from the linear relationship between steps and distance is observed, which, as previously stated, is more problematic at shorter distances. For this reason, the linear fit to the data is separated in two: a fit to the first 50000 steps (red line) and a fit after the first 50000 steps shown (blue line).

4.1.3 Integration of the CSD into the LZ Control System

Within LZ, the control of detector systems will be handled by the SC system, as explained in §3.3. To allow for the control of the CSD system, the Modbus command protocols had to be established within the Ignition software used by the SC; this was initially done on a standalone version of the Ignition at RAL. To facilitate ease of control of the CSD systems a bespoke GUI has been made and along with the command protocols has been integrated into the main LZ SC systems. The GUI consists of two modes of operation:

- Shifter mode - for general calibration procedures. It allows for the deployment of a source from each of the CSD units following a fixed calibration plan.
- Expert mode - for debugging and system checks. It allows for greater freedom of inputs and control of the system.

The shifter mode GUI is shown in Figure 4.15. The key components are the selection of the calibration procedure through drop down lists. Once a user selects the CSD unit to deploy and the source type in use, a python script then handles the process of passing the relevant Modbus commands to the unit: move to desired distance; retract; and update the readout from the laser. For each source, the position of each calibration procedure are set within a JSON file. By using a JSON file external to the Ignition software it is easier to make amendments to any of the deployment positions for a given source without the user needing knowledge on how to code within Ignition. Additionally, the use of JSON files allows for ease of archiving the set procedures used at any given time. To prevent a CSD unit from being deployed without an attached source, a shifter must alter the state of the radio buttons (which default to 'Source not in'); if this is not done, the calibration procedure will not be executed. An emergency stop is included in addition to a button to force the unit to retract the filament. A series of indicators positioned at the top of the GUI give instant feedback to the user on the current status of the system and communication status with the data acquisition system, SC and the overall Run Control of LZ. An additional set of indicators are provided on the GUI itself to give instant feedback on the current state of the CSD unit (idle, moving or waiting for DAQ), and the DAQ state (idle or recording). Each unit has a visualised output showing the current laser read position, allowing for instant feedback to the user on the position of the capsule during deployment.

The expert GUI, shown in Figure 4.16, has means to input a specific distance to deploy the source to; this can be done with or without the laser feedback enabled. The lower

half of the expert GUI allows for the incremental deployment of a source capsule; this gives the functionality to check the laser alignment has not drifted during the lifetime of the system. This is important as movement of the calibration tubes due to vibrations of thermal contraction could result in the laser no longer being incident on the reflector.

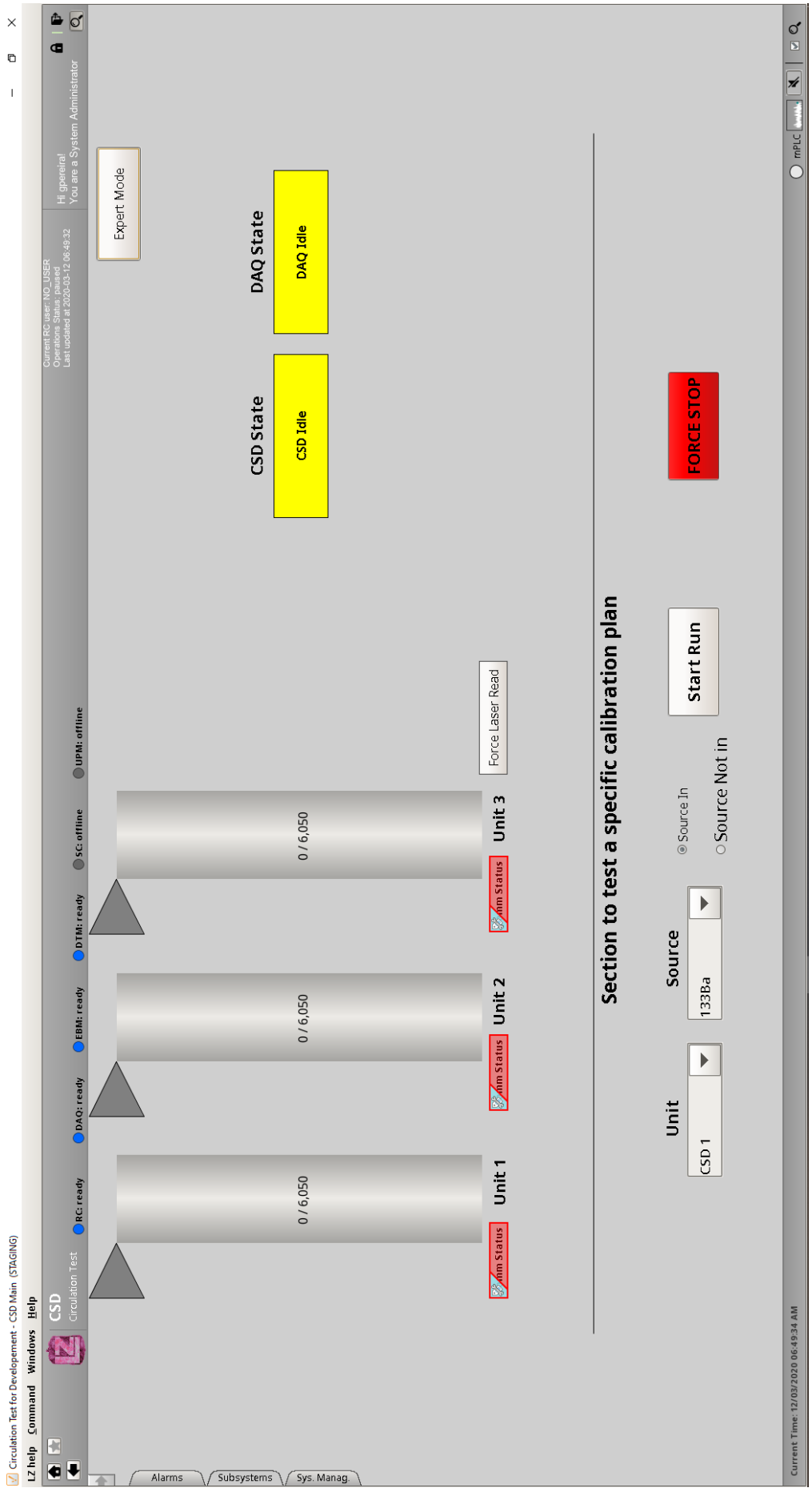

Figure 4.15: Ignition GUI for use by a shifter to conduct a calibration procedure using one of the CSD units.

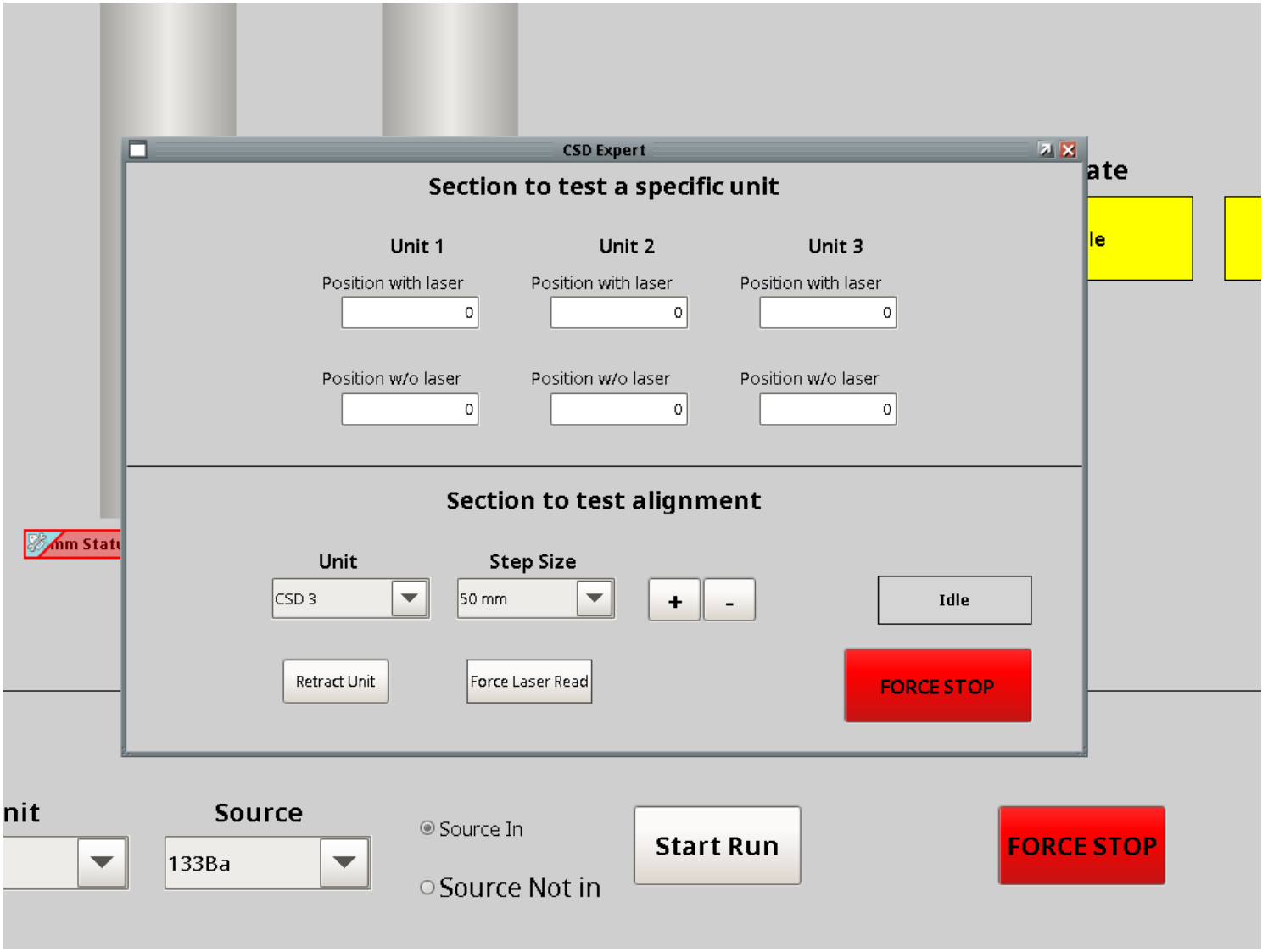

Figure 4.16: Ignition GUI for use by an expert to deploy a CSD unit to a specific distance (with or without the laser feedback) and to increment the position of a source capsule by a given number of steps.

4.2 Optical Calibration System

To conduct calibrations specific to the OD, LZ will utilise an OCS consisting of 40 LED-driven optical fibres. The main function of the OCS is to cross-calibrate the responses of the veto PMTs with the response observed from sources deployed by the CSD. Due to the reduced downtime offered by an optical-based calibration, the OCS will regularly check the gain of these PMTs to ensure they are stable over the life of the experiment. The OCS will also check the optical properties of the acrylic tanks containing the GdLS and the GdLS itself and confirm the accuracy of the optical model of the OD. By calibrating over the expected energy range of events that originate from neutron or gamma interactions, it can be ensured that neutron background events producing signals in the TPC could be efficiently vetoed. An efficient and well-modelled veto for such events is imperative to prevent a reduction of the fiducial volume of the internal LXe TPC; which could lead to an almost two-fold decrease in the overall sensitivity of the experiment. As the overall sensitivity of a TPC is directly proportionate to the fiducial volume, any reduction would decrease discovery potential. The OCS was developed by the University of Liverpool and is currently in the final stage of installation into the LZ OD at SURF. The requirements for the OCS are as follows:

- To be able to inject between 500 and 50000 photons per channel to check the veto PMT threshold energy of 150 keV and match the energy deposition of sources deployed by the CSD.
- To be able to inject 1 million photons via simultaneous use of all channels to mimic the expected muon signal.
- To maintain a pulse to pulse variation of $\leq 10\%$, within statistical variation.
- To maintain variations between calibrations of $\lesssim 100$ photons at 150 keV to provide a stable threshold calibration.
- To achieve a precision of 100 photons for injections of 700-2000 photons and a precision of 1000 photons for injections between 5000-10000 photons, to reduce the uncertainty when matching to expected background signals.
- To achieve an injected pulse width of < 20 ns, to be within the LZ data acquisition system's shaping time.

- To inject light with wavelength of 365 - 390 nm, 430 - 450 nm and 450 - 460 nm. The first band of wavelengths to monitor the acrylic tanks for degradation, the second matches the GdLS scintillation light, and the final band is far enough from the end of the absorption spectrum of GdLS and, therefore, will be used to monitor the stability of the attenuation length in GdLS.
- To achieve up to a 10 kHz pulse frequency, utilising the available 4 kHz bandwidth of the readout systems.
- To contribute $< 5\%$ to the overall limit on the OD radioactivity rate.

4.2.1 Design and Functionality

To achieve the requirements mentioned earlier, the OCS utilises 5 Optical Calibration Cards (OCCs). The OCCs consist of a bespoke FPGA motherboard that allows for the mounting of 8 pulser boards (four per side and each with a chosen LED wavelength) and two photodiode boards (one per side). The emitted light from each pulser board is routed to a patch panel outside the water tank using a 15 m optical fibre. At the patch panel, each 15 m fibre is attached to a 21 m fibre by an SMA-SMA connector, and is patched into the water tank via an air and light-tight feedthrough before having its optical face routed to the desired injection location.

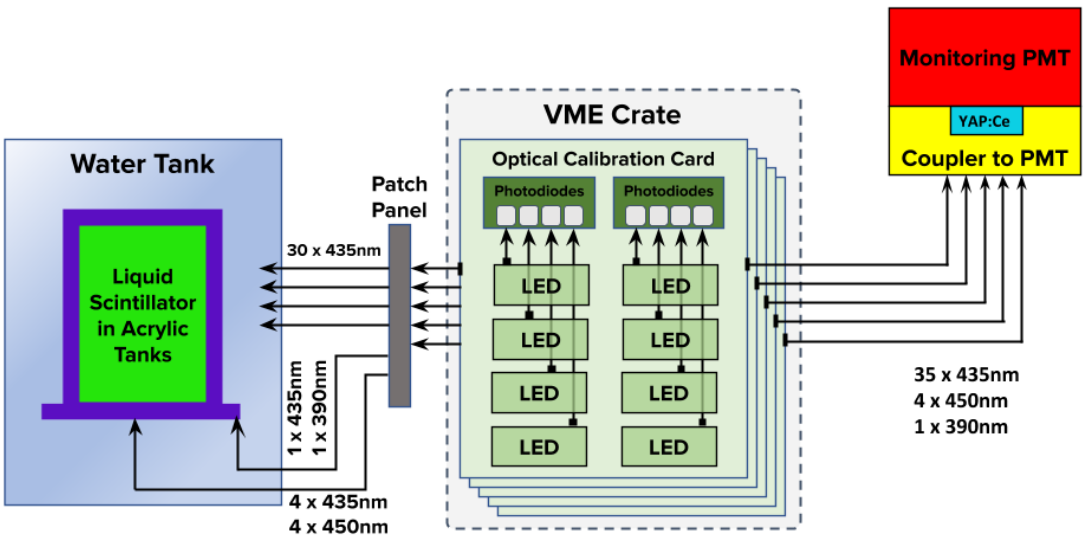

Figure 4.17: General design of the optical calibration system. Stated distances are the length of fibre used in that section [197].

One of the key features of the OCS is its ability to self-monitor the light level of each injection made to the OD. Figure 4.17 shows the overall scheme of the OCS. The output from each of the LEDs is split three ways: one as an input to the OD, one incident on a photodiode and the final one incident on the monitoring PMT (the same 8-inch Hamamatsu R5912 PMT as used in the OD). The photodiodes observe each LED's output, while the monitoring PMT observes the entire light level input to the detector across all channels. A YAP:Ce pulser[9], with a $\sim$ 20 Hz rate and an energy deposition of $\sim$ 5k photoelectrons[10], is affixed to the monitoring PMT to create a known fixed signal that can be used to determine if the PMT properties have drifted. The self-monitoring helps to quickly determine whether any deviations from expected signals from the OD PMTs are due to problems with the control conditions of the PMTs or they are due to an issue with the injected light from the OCS itself.

Injecting the desired light pulses from each channel at an intended intensity requires a unique set of calibration parameters. These values were mapped for each channel during the QA procedures. When performing a calibration with the OCS, this mapping will be retrieved from a database linked to the LZ SC system; which is also the system that will handle the user interface for controlling the OCS. The OCS controller serves as a bridge between the FPGA motherboard and LZ's SC by translating SC's commands into the relevant FPGA register values. Additionally, this controller handles the return of measurements of the boards' temperatures and photodiode outputs to SC.

[9] A yttrium aluminium perovskite scintillator coupled to a weak ^{241}Am source; manufactured by Scionix.
[10] When coupled directly using optical grease.

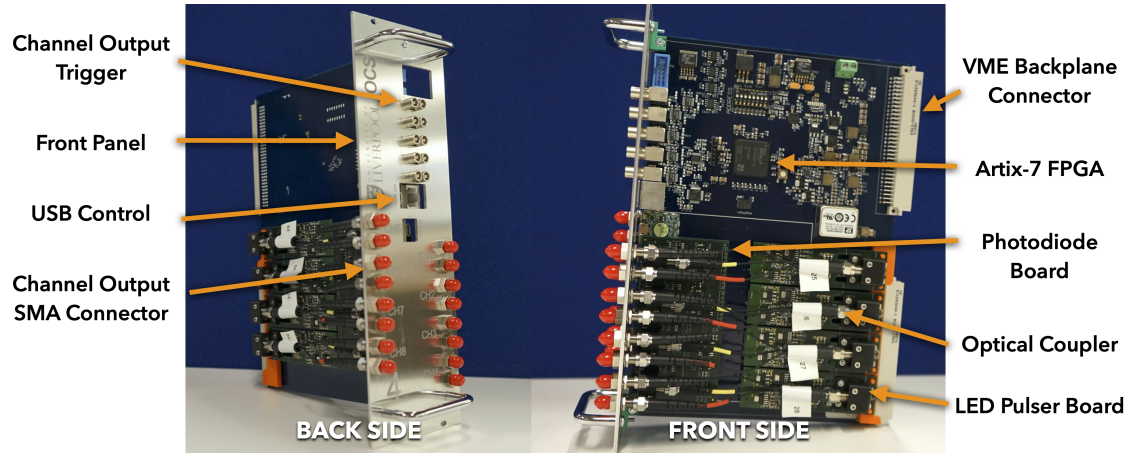

Figure 4.18: Annotated photo of the front and back of an OCC outfitted with 8 pulser boards and two photodiode boards [197].

Optical Calibration Card

The OCS's key electronic components are primarily housed on the OCCs; with each OCC controlling the operations of 8 LED pulser boards and two photodiode boards. Additionally, the OCC handles the relevant communication protocols with the SC. It was decided early to develop the OCCs to be modular, separating the pulser boards from the main FPGA motherboard[11], with intent to dramatically reduce downtime if a single channel needs to be repaired, replaced or upgraded. A photo of an OCC is given in Figure 4.18; annotated to show the FPGA motherboard, pulser boards and photodiode boards. Control of an LED's pulsing happens by the FPGA sending a low voltage digital signal to the pulser board, which is then converted to a transistor-to-transistor logic signal. Figure 4.19 gives a circuit schematic showing that the transistor current draw across the LED is prohibited by a reverse bias of -1 V when not in operation. When pulsing the LED, this signal is turned off, and the cathode returns to a nominal voltage allowing the LED to be forward biased. The number of emitted photons per pulse is controlled by the width of the supplied low voltage digital signal. The primary calibration of the OD PMTs will be performed using 435 nm wavelength LEDs[12]. 435 nm LEDs were selected due to this being the expected wavelength of scintillation light produced by GdLS [199]; beneficially, the OD PMT's quantum efficiency is near-optimal at this wavelength.

As was described previously, the light output from a given pulser board is split three ways: to the relevant injection point in the OD, to the monitoring PMT and to an in-

[11] An Artix-7 FPGA using VHDL firmware and programmed by electronic technicians at the University of Liverpool.

[12] BL-LBVB5N15C model by BRITE-LED Optoelectronics [198].

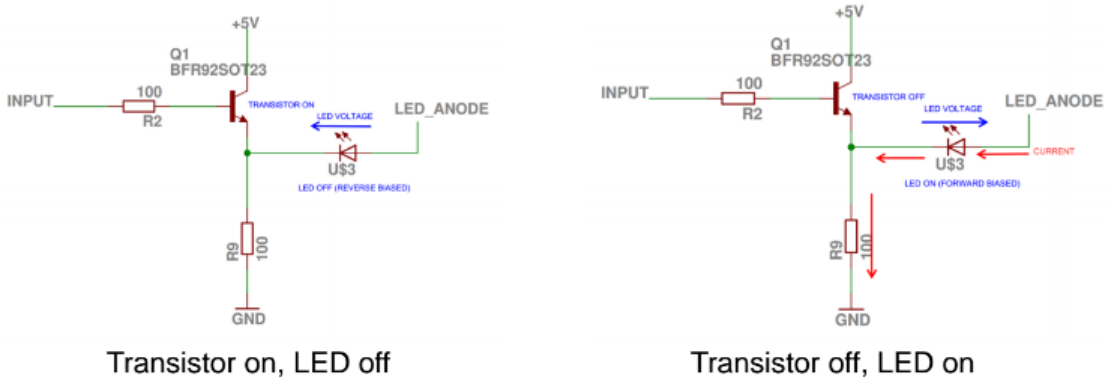

Figure 4.19: Circuit diagram of the transistor to transistor logic used to control output from the LED. Annotated to show the direction of voltage applied across the LED when turned off (**left**) and on (**right**).

dividual photodiode[13]. For the latter, both sides of the motherboard have a pin set to mount a four-channel photodiode board, sufficient to monitor the channels on that side of the motherboard. Each of the four photodiode board channels has its output voltage passed into a precision switched integrator trans-impedance amplifier[14]. This particular op-amp was selected to allow for continuous integration using a switch-input measuring technique; two voltage-controlled switches toggle the op-amp between hold (no reading), integrate (continuously accumulate the input charge) and rest states. To ascertain the correct period for each of these states the photodiode board was designed with a pin set that allowed it to be mounted to an Arduino Uno; the resultant code was then used as the framework for the FPGA control of this board.

Optical Fibres and Couplers

Super ESKA SH4002 duplex fibres[15] with two 980 μm polymethyl-methacrylate resin cores have been selected as the main routing fibres for the OCS. These duplex fibres have a refractive index of 1.49 and a width of 4.4 mm when including the polythene protective layer [202]. Based on measurements of light transmissibility and radioactivity performed on these fibres by SNO+, they were determined as the most suited to meet the requirements of the OCS [203]. The fibres were sourced with one end bare and the other with an SMA connector affixed to the duplex fibre's two strands. To increase each fibre's light profiles' uniformity, the bare fibre ends' optical face have undergone ice polishing at

[13] A S5971 high response speed Si PIN photodiode by Hamamatsu [200].
[14] An IVC102 by Burr-Brown [201].
[15] Manufactured by Mitsubishi.

Fermi National Accelerator Laboratory. Figure 4.20 shows the visual inspection of the fibres with both a uEye camera and a microscope. By using liquid nitrogen to flash freeze one end of the fibre, a constant lubricant is supplied during polishing. Additionally, the ice acts to prevent the cladding around the fibre cores from experiencing sufficient force to induce splitting of the cladding from the core.

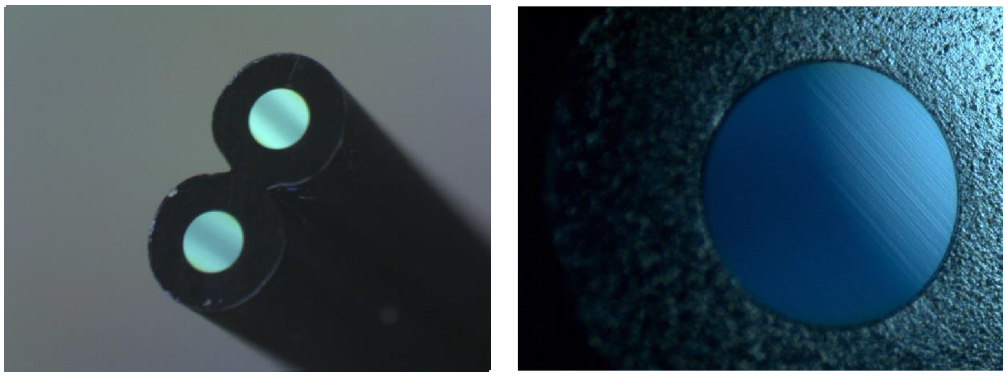

Figure 4.20: Ice polished Super ESKA SH4002 duplex fibre from an imaging camera (**left**) and a microscope (**right**).

The length of one of the fibres was measured to be 21.07 ± 0.5 m, and its weight to be 163.3 g. A 1.14 m bare section of duplex fibre weighed 8.2 g, giving a mass per length of 7.19 g/m. Figure 4.21 shows the distribution of all of the fibre lengths. The majority of fibres had a length of ≈ 21.05 m and will route the light generated by the OCCs to the side installation positions. The eight with a length of ≈ 21.3 m will be used to direct light under the liquid scintillator tanks.

To ensure the system is light tight from the pulser board to the intended output (injection point, monitoring PMT or photodiode board), a bespoke multichannel coupler and two different housing types were developed (Figure 4.22). The first of the housings were for the LED, where a 3D printed structure was designed to encapsulate a commercially available metal-bodied SMA fibre optic connector. After the electronics boards had arrived at the University of Liverpool, the precision 3D printed LED housing had to be added to the board along with the pre-tested LEDs. The LED legs were soldered to the board, and black epoxy was applied around the LED legs on the back of the housing to ensure light tightness. After construction, each board was tested for light leaks by connecting the LED housing SMA connector to a power meter and recording the observed light level with and without an intense external light applied to the board. The board then was tested to ensure the required dynamic range of pulse intensity could be met.

The construction of the photodiode boards entailed attaching the photodiode into the

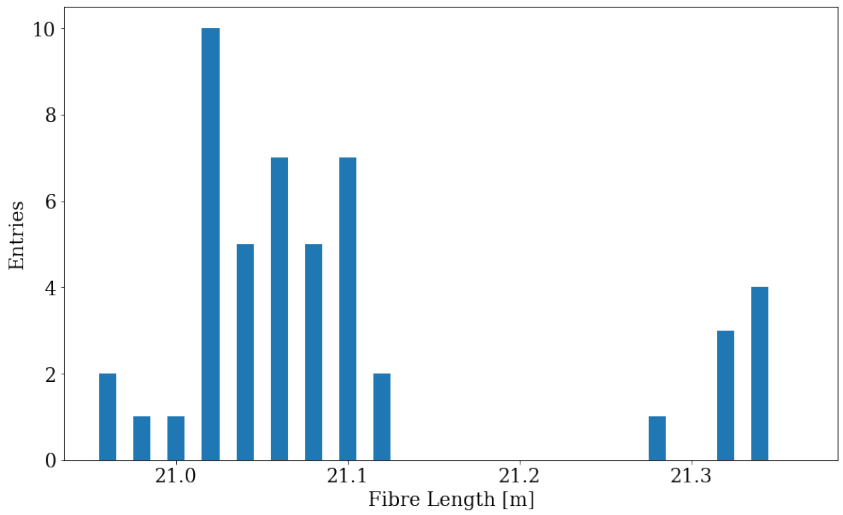

Figure 4.21: Distribution of OCS duplex fibre lengths.

housing (Figure 4.22), attaching this to the board and soldering the photodiode legs to the board. After testing to see if the photodiodes were operational, light tightness tests[16] were carried out in addition to a short pass/fail test to ensure that the photodiode gave a sensible response to a calibrated light source when applied from a fixed distance. Figure 4.23 shows the distribution of power meter readings for a background (light off) and light on. The uncertainty on the means of the distribution is approximately 0.0025 nW (to be compared with 400 nW when the channel is open and the light is on). The differences of the means with light on/off are consistent with 0 within this uncertainty for all measured channels. With only two channels having the difference larger than 3 σ (-3.5 σ and -3.7σ). However, the difference is negative ("light on" mean is smaller than the "light off" one) showing that this is a systematic uncertainty of the measurements (stability of the power

[16]Similar tests were performed on the pulser boards after assembly.

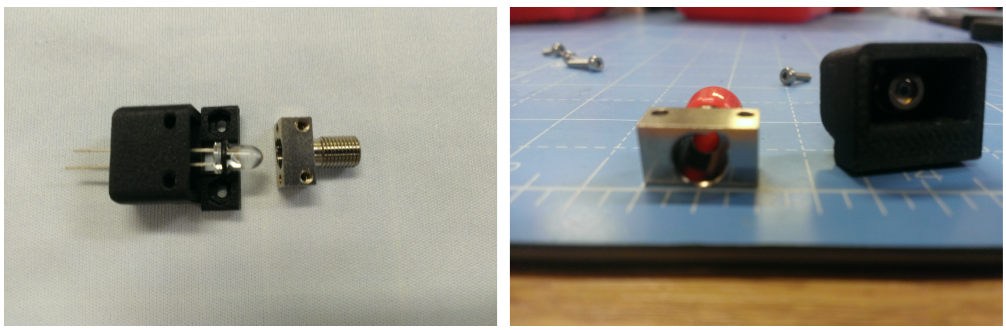

Figure 4.22: 3D printed housings for the LED (**left**) and photodiode (**right**).

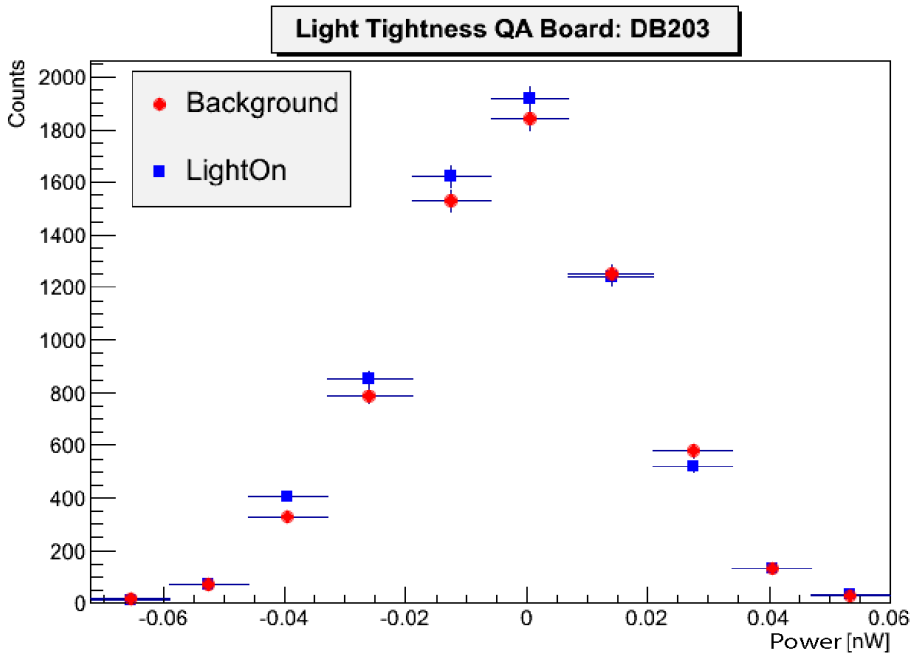

Figure 4.23: Example of the light tightness test conducted on a photodiode board channel.

meter itself).

The bespoke multichannel coupler was required to attach all channels to the monitoring PMT using 2 m long ESKA SH4001-1.3 single core fibres. These fibres had an SMA connector on one end and bare fibre on the other[17]. This coupler was developed to have a hex pattern centred directly above the PMT's photocathode to optimise coverage; there are a total of 54 channels attached to the coupler[18] (Figure 4.24). The centre of the PMT facing side of this coupler has a rectangular slot to seat the YAP:Ce pulser. A secure fit between the source and the PMT is maintained by attaching the source to a spring-loaded bolt that runs through the coupler's length and is attached to the source's back. The light transmission of each fibre was measured before glueing them into the multichannel coupler (Figure 4.25). There are no outliers in the low light transmission region, confirming that all fibres could be used in the assembly. Both the multichannel coupler and the housings were 3D printed[19] using a composite of carbon fibre and engineering nylon, which offers increased strength in small features and is a near-black material.

As previously mentioned, to route the light emitted by an LED from a pulser board to the three intended channels (photodiode, monitoring PMT and injection point), a bespoke

[17]Supplied by FibreFin with both ends polished.

[18]Redundancy has been built in to allow for the potential of fibres breaking or to allow for an extension of the OCS.

[19]Fabrication by AMW at the University of Liverpool.

Figure 4.24: Images of the OCS multichannel coupler used to route light from each pulser board onto the monitoring PMT. **Top left** shows the fabrication stage, **top right** shows the monitoring PMT facing edge, **bottom left** shows the bundling of the fibres for shipment to SURF, and **bottom right** shows light being emitted from all channels.

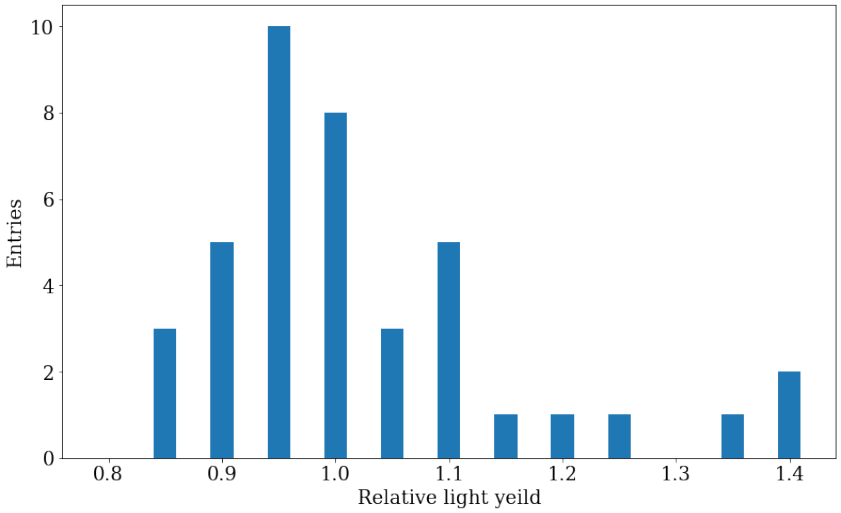

Figure 4.25: Relative light yield of the fibres used in the multichannel coupler.

three-way coupler (Figure 4.26) was produced. The locations of pulser and photodiode boards on the OCC determine the lengths of the coupler legs. Positions of the LED and photodiode on the boards are adjustable with 5 mm tolerance, allowing connections of the coupler without strong bending. The three-way couplers were made with short fibre tails (Mitsubishi ESKA SH4001-1.3), which were supplied with an SMA-connector on one end and the other left bare. The fibre to the photodiode was cut to 11.5 cm, and two other fibres have a length of 14.5 cm. The SMA connectors used to combine the bare fibre ends were also bought in the FiberFin. Initially, they had a ferrule with an inner diameter of 2 mm, but to fit three 1 mm fibres, this inner diameter was increased to 2.2 mm. Also, 2 mm has been cut from the ferrule to ensure a 0.5 mm gap between the LED and the end of the ferrule. 42 couplers have been produced with redundancy to allow for the fabrication of 14 more.

The fibres were preliminarily polished, and the light transmission has been measured (Figure 4.27) using a calibrated light source. The light source uses a lens to focus the light on the fibre; therefore, the light output depends strongly on the angular position of the fibre (with an increase in the spread of the light output distribution with increasing

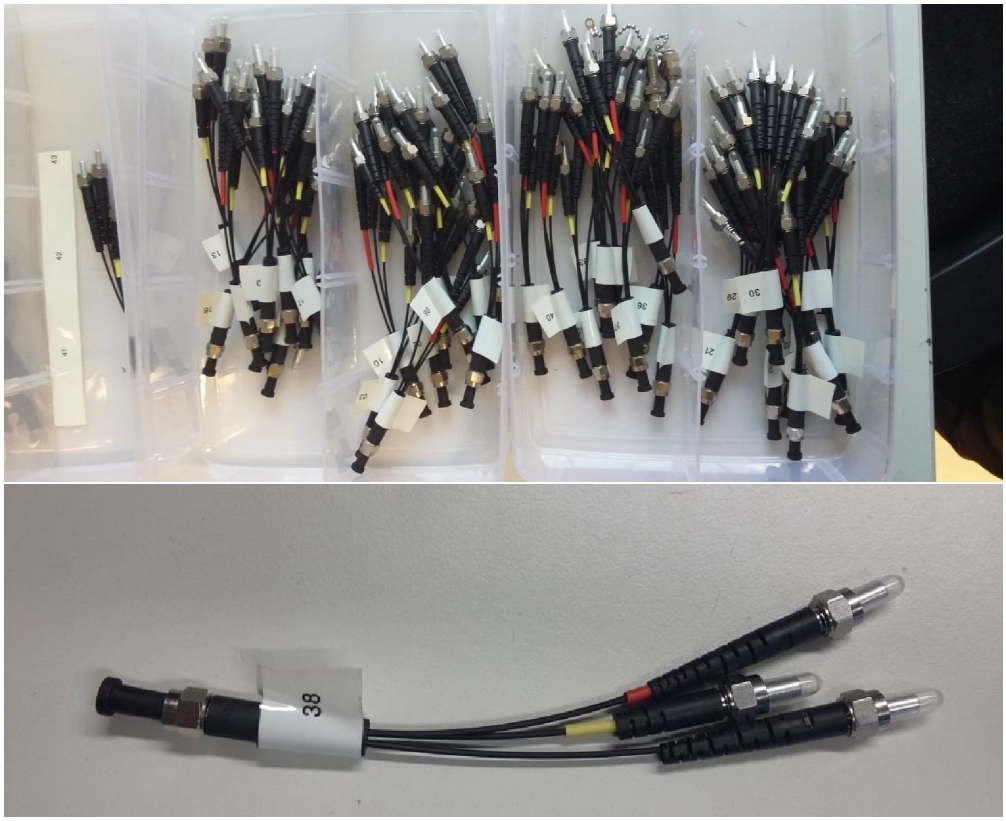

Figure 4.26: **Top** shows all couplers post manufacturing. **Bottom** is a photo of a single three-way coupler.

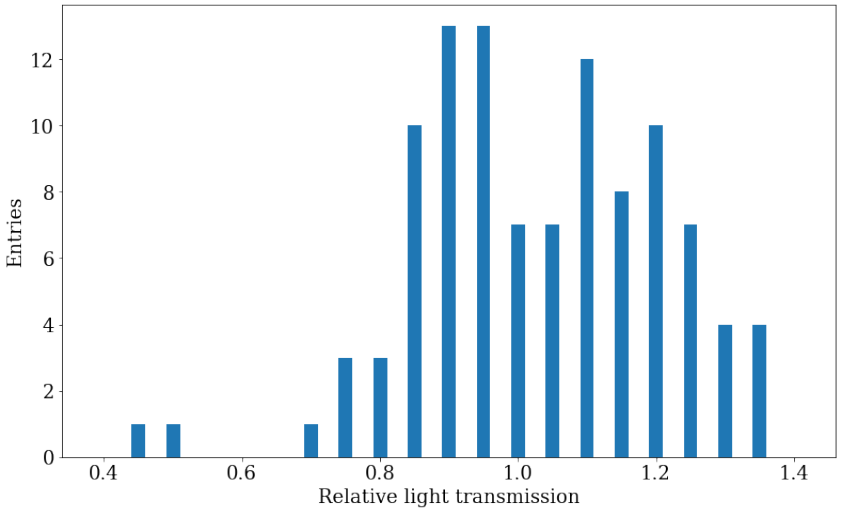

Figure 4.27: Relative light transmission of the three-way couplers.

distance). These measurements allowed for the identification of two couplers with broken fibres (their relative light yield was around 0.5 in Figure 4.27).

The connectors with the three fibres were polished with added water, leading to a much better visible quality of the polishing (Figure 4.28), but the light transmission increased only by 15%. This shows that the light transmission is not too sensitive to scratches on the fibre faces, though of course all the precautions will be taken to avoid them. The couplers were given ID numbers, and their legs were marked with different colour sleeves (Figure 4.26), allowing easy identification, measurements and storage of the parameters in a database.

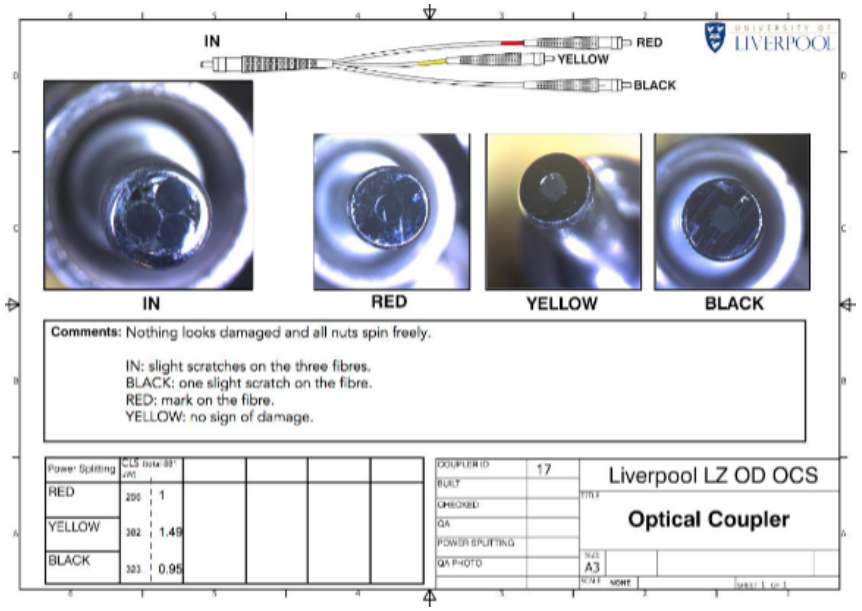

Figure 4.28: Example of the three-way coupler QA.

Fibre Support Structure

To perform the initial alignment of the OCS injection points and to maintain this alignment throughout the operational lifetime of the detector, the 30 fibres used to perform calibration tasks on the main OD PMTs are fixed onto the PMT support ladders by a Fibre Support Structure (FSS). The FSS has been designed to allow for adjustments on all three rotational axes and enforces a 50 mm curvature on the fibre; this is done to prevent damage to the fibre core and reduce the potential attenuation of the signal. The FSS comprises 26 parts that have either been sourced from low radioactivity materials or have been passivated: 7 PTFE components (machined using a five-axis CNC), two PTFE inserts, seven bolts, and a further nine inserts. The GdLS and acrylic monitoring fibre outputs are affixed into place using a stainless-steel bracket and a PTFE fibre holder (light through holes in tank base support structure).

The optical face from each injection point needs to be inward-facing, perpendicular to the water tank wall and parallel to the tank's radius (such that the centre of the beam profile is incident on the central origin perpendicular to the base of the water tank). Precise alignment of each fibre is achieved using two self-levelling cross patterned lasers, adjusted such that their projection is incident on the acrylic tanks. A further green laser is attached to the back of the FSS. Adjustments to the FSS are made until the green laser light is incident on the two levelling lasers' crossing point. After alignment, the FSS position can be fixed to prevent drift in alignment. The FSS is key to ensuring the fibres' alignment

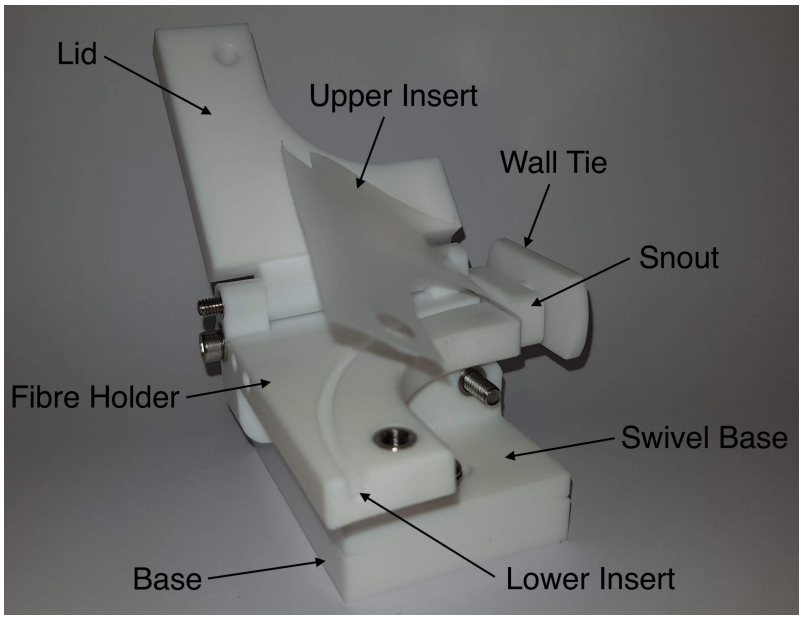

Figure 4.29: Annotated photo of a FFS [197].

during the filling of the water tank, and throughout the system's operation. A precise and accurate alignment is imperative to verify the OD optical model, which has been used to estimate the neutron rates and expected neutron veto efficiencies of the OD.

Self-Monitoring Systems

As previously mentioned, the OCS has incorporated self-monitoring systems to ensure the level of light being injected into the OD is precisely known. First, the monitoring PMT, using a bespoke multichannel coupler, monitors the light output from all 435 nm channels. This PMT is monitored for any variation, allowing for a better understanding of the threshold of the OD PMTs.

The coupling of the YAP:Ce pulser allows for the monitoring of any drift in the monitoring PMT's time response and gain by consistent application of a baseline signal with a sufficiently different frequency from that of an LED pulse. The YAP:Ce pulser produces a peak at $\sim$ 2000 photons with a resolution of 8%. By performing a $\sim$ 2 minute gain calibration of the monitoring PMT before injecting light into the OD, a precision of 2% can be reached on the known number of photons injected into the OD.

The second check is performed on each channel individually; this has been achieved through implementing a four-channel photodiode board to both sides of each of the OCCs. The selection process for appropriate photodiodes and optimisation of the signal will be discussed later in §4.2.3. If an LED were to emit light other than when intended, the photodiode would detect this emission and send an alarm to the SC. Also, any light leakage into any of the channels could be quickly identified by viewing which photodiode channel gives a non-nominal response. The photodiode board went through several incarnations during development, with the data format interchange layout of the final design given in Figure 4.30. During the design phase, the objectives were to monitor pulses across the full dynamic range of the OCS and have an individual channel to monitor each LED channel.

By cross-checking the outputs across all injected channels from the corresponding photodiode channel, the monitoring PMT and the OD PMTs it is possible to determine whether or not an observed deviation from a sourced based calibration is due to either an issue with the number of photons generated by the OCC, a drift in the monitoring PMT parameters or a drift in the OD PMT parameters.

As many semiconductor devices are used in the OCC, including the LEDs themselves; there is the potential for a strong dependency between the operating temperature and the emitted light level. QA testing of the earlier iterations of the pulser board led to

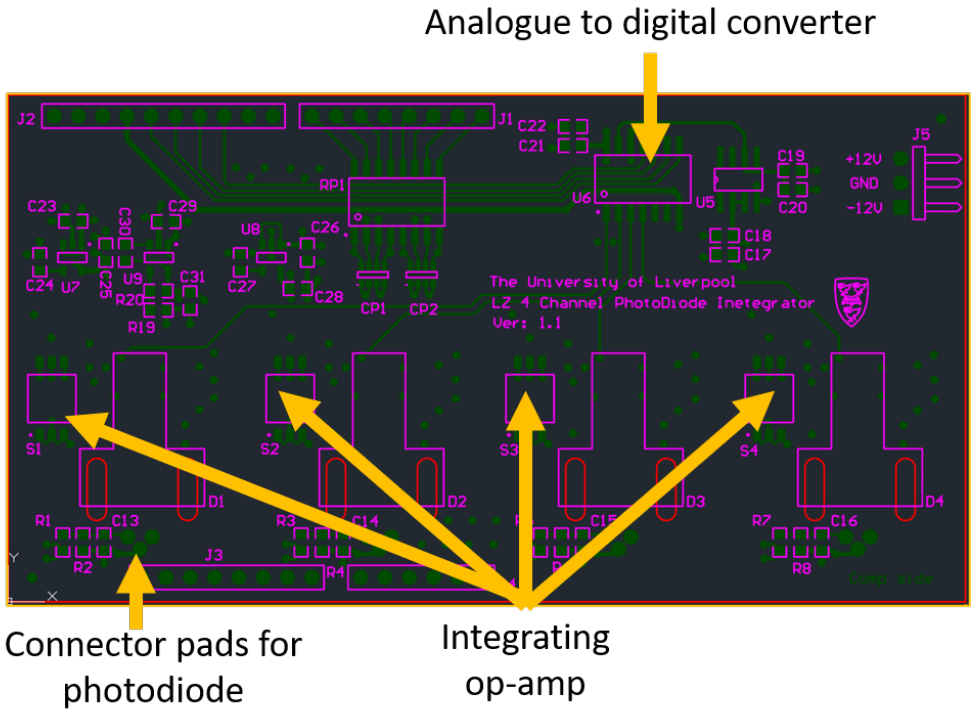

Figure 4.30: Drawing interchange format of the OCS photodiode board.

revisions in the choice of specific electronic components. Each OCC has a temperature readout on-board to allow for adjustments to be made as necessary. By understanding the temperature dependence of the OCS electronics, it will be possible to make adjustments to the electrical pulse width to maintain the intended number of photons per pulse.

Scintillator and Acrylic Tank Monitoring

For the task of monitoring the GdLS, the OCS will have a duplex fibre positioned underneath each of the four acrylic tanks, such that the emitted light travels vertically through the tank. One core of each fibre will be coupled to a 435 nm LED and the other to a 450 nm LED. As the GdLS has a sharp end to its absorption spectrum at 420 nm (Figure 4.31), it is possible to monitor for degradation by determining the ratio of the 435 nm and 450 nm light detected by the OD PMTs. Degradation in quality would be noticed by a change in this ratio as the absorption spectrum is shifted by impurities; where a reduction in intensity would be observed for the 435 nm light. Similarly, to monitor the acrylic tanks housing the GdLS both a 435 nm and a 390 nm LED will be pulsed independently with light incident on one of the tanks' bottom lips. The ratio of light emitted into the OD to the light observed by the OD PMTs for each LED can then be monitored for variations over the course of the experiment. When combining these two measurements, it will be

possible to determine whether degradation has occurred within the acrylic, the GdLS or both. Depending on the deviation from the nominal signal, it may be possible to make adjustments such that the validity of the signal generated by the scintillator is still upheld; pivotal in neutron and gamma event discrimination. The monitoring of the GdLS and the acrylic tanks requires 10 LED-driven fibres: five 435 nm, four 450 nm and one 390 nm.

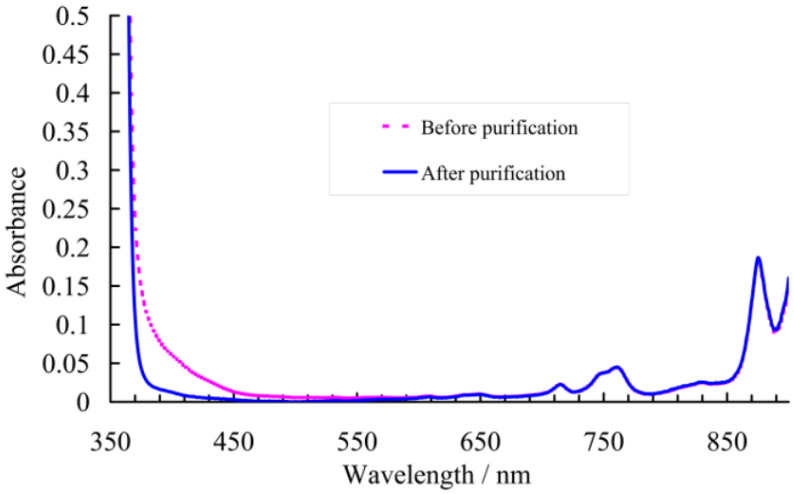

Figure 4.31: Daya Bay LAB absorption spectra before and after purification [199].

4.2.2 R&D of the OCS Pulser Board

This section will outline some of the tests conducted during the development of the OCS. The majority of these tests were conducted to determine whether the component choices for the OCS would produce a system that operates within the requirements. The OCC's first iteration was used for most of the tests outlined in this section; Figure 4.32 shows an annotated picture of this prototyping board. At this point, the FPGA was being powered by a power supply unit and was not placed in a VME create; allowing it to be easily placed into an environmental chamber. Additionally, as previously stated, the photodiode board was designed in a way that allowed it to also be controlled by an Arduino Uno during the R&D stages.

Prior to fabrication of the first pulser board the LEDs themselves underwent a selection process. Several hundred 435 nm LEDs were capacitance checked both using an LRC circuit and a multimeter. The capacitance of the LEDs were separated into two subsets: those distributed around 51 pF and those distributed about 72 pF. Both subsets were used in the initial stages of testing to assess which would best match the requirements of threshold calibration, coverage of the required dynamic range and stability between

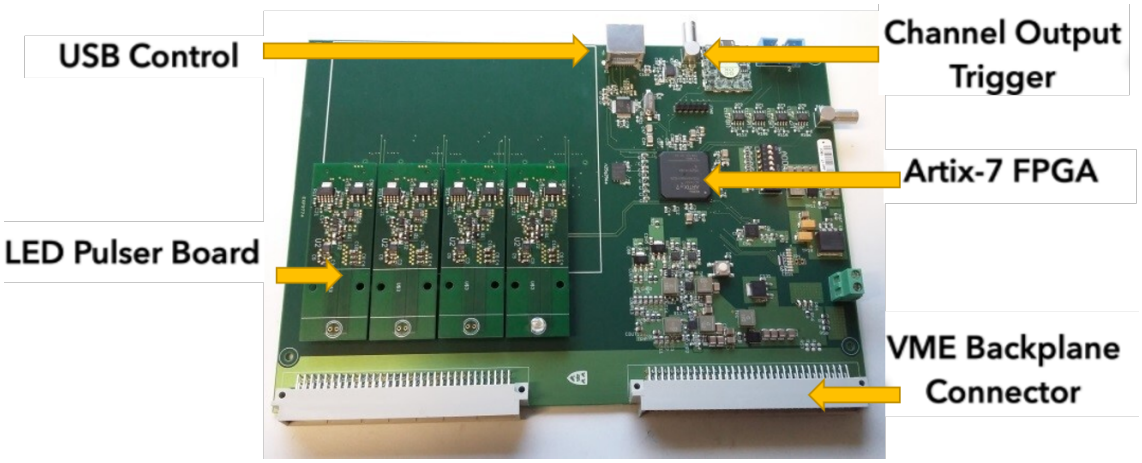

Figure 4.32: Annotated photo of the prototyping OCC with key components indicated.

generated pulses.

Threshold Calibration Photons per Pulse Equivalence

Two of the most critical requirements of the OCS are to perform and maintain accurate calibrations of the OD PMT threshold of 150 keV, and to monitor for deviations from calibration at energies equivalent to both terrestrial and cosmological background source. Therefore, before finalising the LEDs' selection to be used in final production, both capacitance subsets of LEDs were tested against these requirements.

An external pulse generator was used to control the width, frequency and amplitude of the electrical signal delivered to an LED housed within a dark box. The resultant pulse of light from the LED was split between a Hamamatsu H10721-20 photosensor[20] and a power meter by a 2-way optical fibre splitter. Figure 4.33 shows the number of detected photons by the power meter per pulse ($n = Pt/h\nu$, where n is the number of photons, P is the power, t is time, h is Planck's constant and ν is the speed of light over the wavelength) as a function of the electric pulse width delivered to the LED; annotated to show the regions equivalent to the threshold energy and energies of other calibration sources.

It was estimated using the detector simulation that the OCS needs to produce between 700 and 1200 photons per pulse to calibrate the 150 keV threshold required in the OD. Figure 4.33 shows that this is achievable with the 51 pF (72 pF) subset when a pulse of 1 (0.5) photons per picosecond is incident on the PMT. It is also apparent that both subsets of LEDs could deliver pulses containing numbers of photons across the full dynamic range. Further to this, both subsets were able to produce pulses in steps of 1 thousand photons

[20] An 8 mm diameter PMT with in-built power supply circuit.

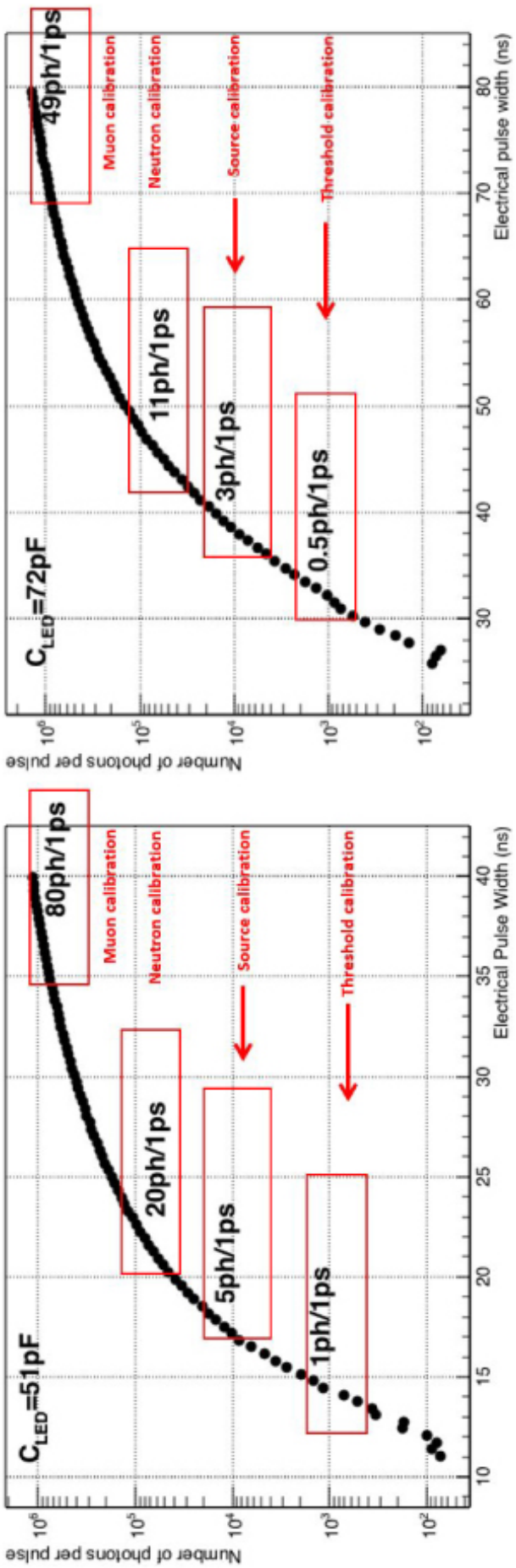

Figure 4.33: Number of photons per pulse detected by the power meter as a function of electrical pulse width supplied. Shows number of photons per second energy equivalence for threshold as well as other planned calibration sources.

for energies equivalent to source-based calibrations, 1 MeV to 3 MeV (5k to 15k photons per pulse).

Pulse to Pulse Variations

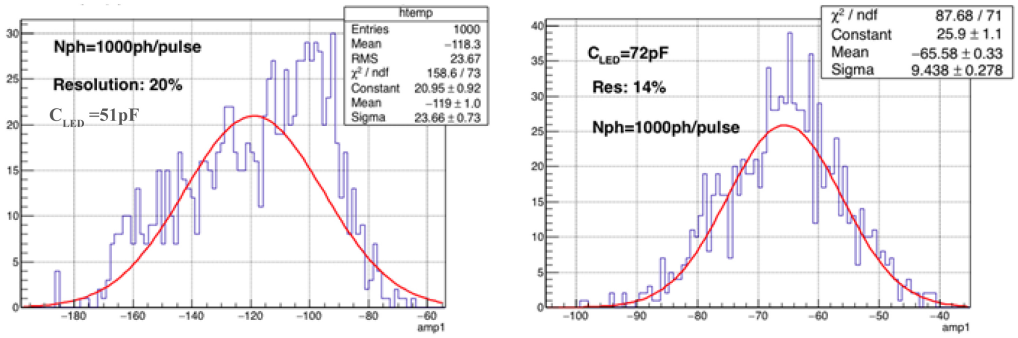

Figure 4.34: Histogram of binned PMT amplitude, using an average of 1k photons per pulse with both a 51 pF (**left**) and a 72 pF (**right**) LED. Gaussian fit has been applied to both data sets.

For both LED subsets, the pulse to pulse variations was investigated. The supplied electrical pulse width was set to produce an average of 10k photons per pulse; obtained from Figure 4.33. By comparing the left and right plots in Figure 4.34 the variations between pulses for the 72 pF subset appear more uniformly distributed than those of the 51 pF subset; this was attributed to issues in guaranteeing fibre alignment in the early test set-up. Despite having a less uniform distribution, the 51 pF LEDs should have offered better resolution than the 72 pF; in the final section of this chapter it will be shown that the resolution for 51 pF LEDs was 10%, §4.2.4. Additionally, the vast majority of LEDs were in the 51 pF subset, which require a smaller electric pulse width to induce emission from the LEDs than the 72 pF subset. For these reasons, it was decided that the 51 pF LEDs would be used in final production. Advantageously, the 51 pF LEDs have a faster response to a supplied signal due to having a sharper rising edge than the 72 pF LEDs.

Temperature Dependency

Several of the pulser board components, including the LED, are semiconductor-based; potentially leading to a device which is strongly susceptible to variations in temperature. To identify the extent to which this would affect the number of photons generated for a given electrical pulse width, measurements were taken in a temperature variable environ-

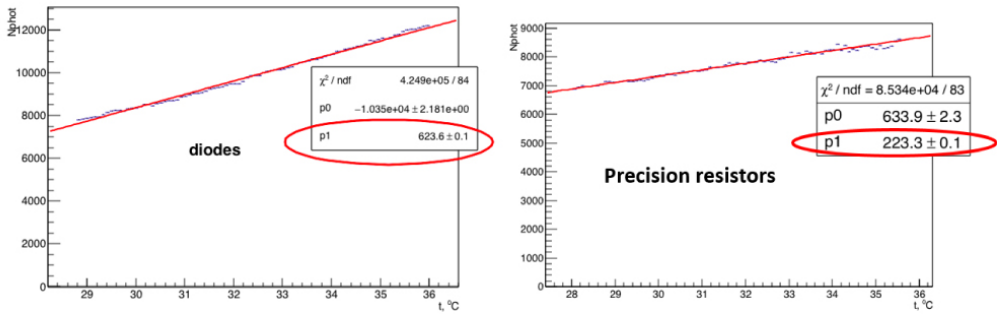

Figure 4.35: Number of photons detected by the power meter as a function of LED environmental temperature after replacing diodes with linear regulator and implementing precision resistors.

mental chamber. The temperature in the environmental chamber was raised from room temperature up to 36° C, before being allowed to cool back down. Measurements of the exact temperature at the pulser board were obtained using an Adafruit driven temperature sensor affixed to the board. The number of photons per pulse was again determined using the power meter; situated external to the chamber. The initial variations due to temperature, given in the left of Figure 4.35, were found to be 623 photons per degree. Talks with the boards' developers led to replacing the power diode with a linear regulator, the former being a semiconductor device, which reduced the variations to 349 photons detected per degree. Finally by swapping the resistor for a precision resistor, which are less susceptible to temperature variations due to having a higher power density, the final temperature variations from the pulser board were 223 photons per degree, as given by the right of Figure 4.35. It is expected that the local temperature variations around the OCS electronics will be ± 1 K; which will be monitored by on-board temperature sensors. Even with such a significant deviation in the number of photons being emitted due to temperature, the cross-checking procedure using the monitoring PMT allows for adjustments to the correct set point before injection of light in to the OD.

Long Term Stability

The OCS is not intended to be used for long periods of time during actual operation at SURF. However, it is still important to understand the long term stability of the system. Measurements of the light emitted from a single 435 nm, 51 pF LED pulser board (attached to the development FPGA board) were collected using both the power meter and the PMT. An initial pulse width was set to produce pulses in the range of 8k photons detected and during the 7 hours of data collection a 6% drift was observed in the power readings and

a 2.4% in the PMT; as shown in the top two panels of Figure 4.36. The bottom panel of Figure 4.36 shows a less than 1% variation in environmental temperature during this time. The process was repeated for ≈ 1600 photons per pulse; this time the number of detected photons by the PMT was normalised against the temperature variations and the fluctuations observed in the power meter measurements. The timing resolution of the power meter was insufficient to observe signal pulse information; additionally, the power meter performs integrated measurements of the signal. In contrast, the PMT was recording single pulse information, which allowed for the spread in the amplitudes of the pulses to be determined. Also, the power meter being a calibrated device, made it possible to determine the average number of photons per pulse trivially. This would not have been as easy to achieve with the PMT as the signal is strongly dependant on the gain and would have required thorough calibration.The observed drift in the power meter in Figure 4.36 was attributed to ambient light leakage and natural fluctuations due to the ∼5% accuracy of the device. A light leakage would not have caused deviations in the PMT measurements. This is because the PMT was only observing pulse to pulse information, which was externally triggered by the same signal used to induce the pulse from the LED. These tests were left to run overnight and would explain the decrease in observed ambient light throughout data taking. Figure 4.37 shows that the normalised PMT measurements had a maximum variation of 3.5%; the required stability of the OCS.

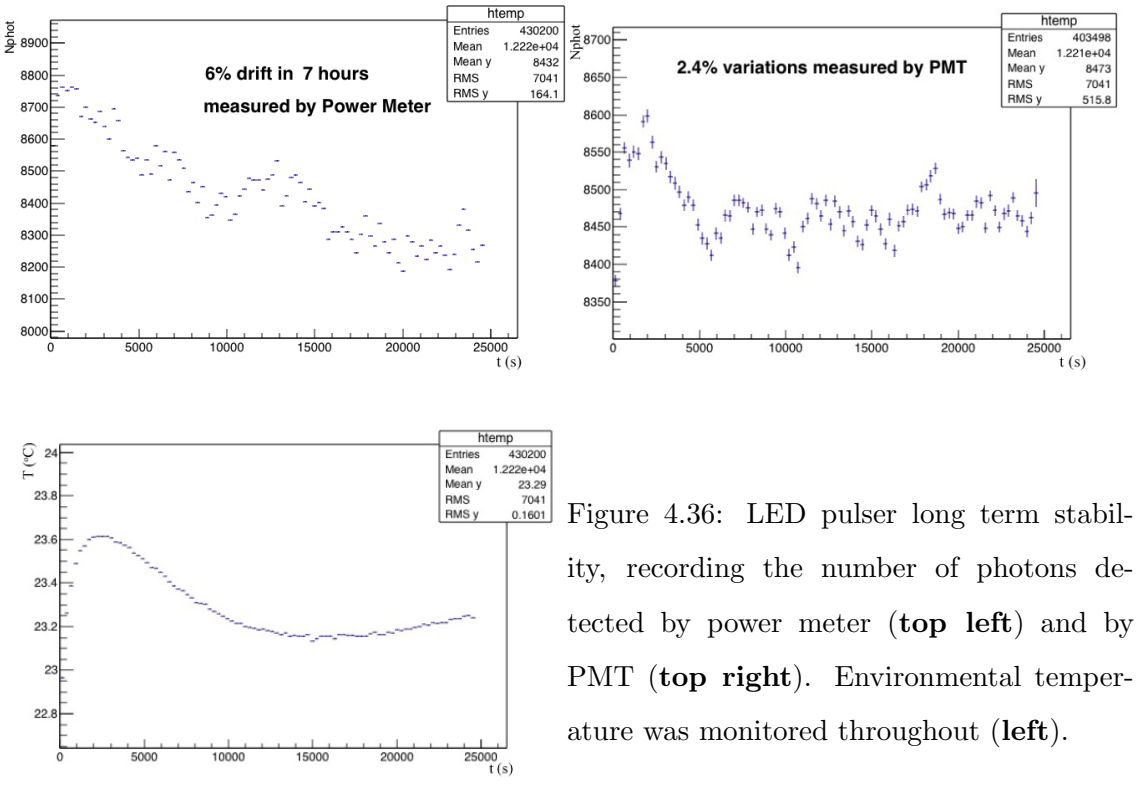

Figure 4.36: LED pulser long term stability, recording the number of photons detected by power meter (**top left**) and by PMT (**top right**). Environmental temperature was monitored throughout (**left**).

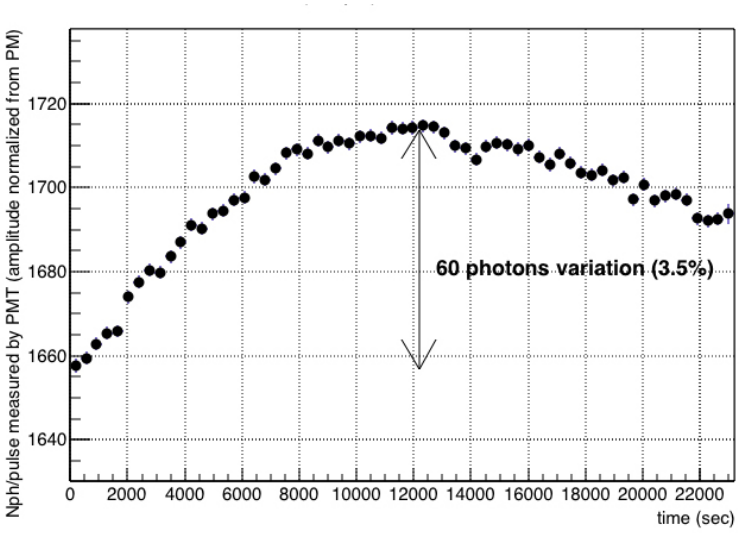

Figure 4.37: Number of photons per pulse detected by PMT, normalised against variations observed by the power meter.

Summary

This section outlined some of the tests conducted during the development stages of FPGA and pulser boards used in the OCS. It was found that the 435 nm LEDs could be initially categorised into two subsets based on their capacitance (51 pF and 72 pF). Both subsets displayed the ability to produce pulsed outputs of photons covering the full required dynamic range of the OCS with an increment size of ∼1000 photons. The pulse to pulse stability for both subsets was also found to be within the OCS requirements. A significant difference is observed between the number of photons per pulse for a given electric pulse width between the subsets. Those with a 51 pF capacitance were selected for use in the final system as the number of photons per picosecond was larger than that of the 72 pF LEDs; this being 1 photon/ps at threshold for the 51 pF subset compared to 0.5 photons/ps for the 71 pF subset.

Several components of the pulser boards were changed to reduce the temperature dependency of the generated light output; final measurements showed a variation of ≈ 300 photons/°C. Long term stability tests showed that for low light level (≈ 1500 photons/pulse) a maximum drift of 3.5% was observed over a 7 hr period, and a 1° C change in environmental temperature. A 3.5% variation is within the requirements set for the OCS; however, it highlights the need to monitor the OCC's environmental temperature during actual operation to allow for corrections if the temperature significantly alters.

4.2.3 R&D of The OCS Photodiode Board

To allow for the self monitoring of each LED channel, the OCS will have a dedicated photodiode readout for each channel. Prior to the design of the final photodiode board a series of developement tests were conducted.

Using the development FPGA board and a single 435 nm pulser channel, the supplied electrical pulse width to an LED pulser was varied, and the response of an individual photodiode channel was recorded. Estimate of the photons arriving at the photodiode was obtained by splitting the light incident onto the photodiode and a power meter. Figure 4.38 shows the results of these tests.

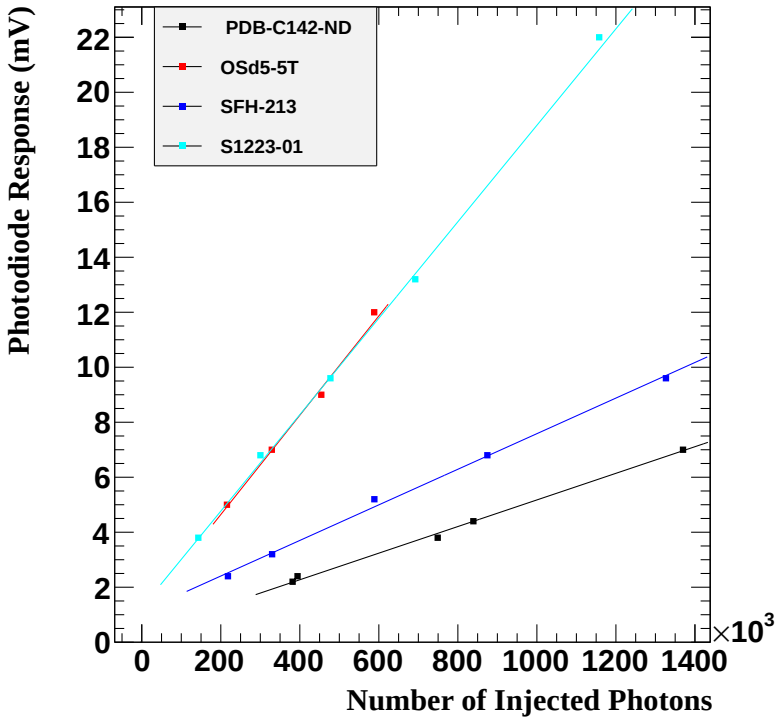

Figure 4.38: Output response of several different photodiodes as a function of average number of injected photons. Errors were attributed to both x and y variable but not visible.

Out of the photodiodes tested[21], the S1223-01 photodiode offered both the greatest range in output voltages (increasing the precision at each point) and the best coverage of the intended dynamic range of photons per pulse; despite not being optimised for these wavelengths. For these reasons, the S1223-01 photodiode was selected for use in further

[21] Additionally several other photodiodes were tested (AEPX65, BPX65 and BPW21) but were not included due to not showing a significant response below 200k photons per pulse.

Figure 4.39: Oscilloscope output signals of switch one and two, for two of the four photodiode board integrating op-amps. Green and magenta are switch one for each op-amp, yellow and blue are switch two for the first and second photodiode respectively. Both sets of signals are set to have a 100 μs integration time, 10 μs hold period, a 10 μs reset period and a 10 μs pre-integration hold.

tests; additionally, after this stage of testing another viable photodiode (an S5971 photodiode) was identified and used within the next stages of testing.

Control of the Integrating Op-amp

To accurately determine the number of photons incident on the photodiode, the output voltage is passed into a trans-impedance integrating chip (labelled as integrating op-amp in Figure 4.30); specifically an ICC102M [201]. As previously mentioned, this op-amp can operate in a continuous integration mode where two voltage-controlled switches can alter the state. During development, the control of these switches was performed through an Arduino Uno. The photodiode board was supplied with a ± 12 V from an external power supply while the Arduino was powered by a 5 V input from a connected computer. An oscilloscope was used to probe the two control switches to ensure they were being toggled correctly; the oscilloscope trace is shown in Figure 4.39. This Figure shows the switch control signals being passed for two of the four ICC102M op-amps required on each photodiode board; the script's processing delay created the offset between measurements.

It was shown that by selecting an appropriate integration window, it is possible to cover the entire dynamic range of injections from the OCS using a single capacitance

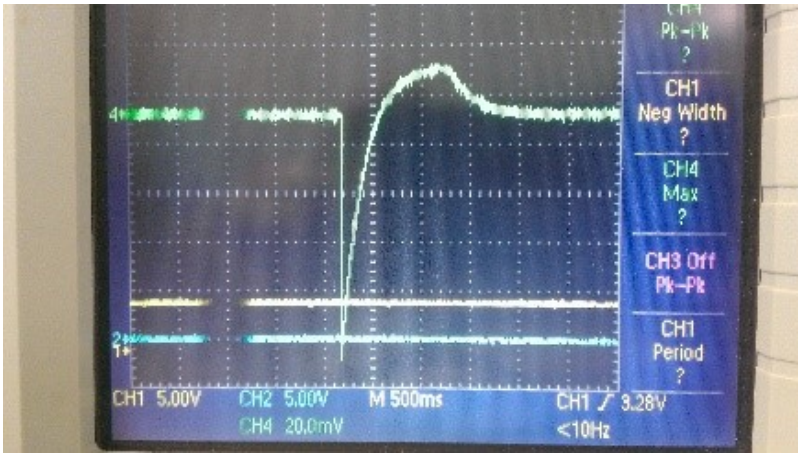

Figure 4.40: Oscilloscope output displaying saturation of the voltage in the integrating chip at approx. 125 mV. An arbitrarily long integration time was used, with natural light incident on the S5971 photodiode.

value across the op-amp. Another essential property to understand about the integrating chip is the maximum voltage that can build up before saturation occurs. Figure 4.40 shows the op-amp saturating output at $\approx$ 125 mV after being left to detect environmental light over an arbitrarily long integration period. The value of saturation was used to identify a suitable analogue to digital converter capable of high resolution over the op-amp's expected output range.

Op-Amp Feedback Capacitance Selection

The integrating op-amp selected has the means to toggle three inbuilt parallel capacitors and one that can be externally mounted. Ideally a single capacitance value that gives sensible readout across the full dynamic range of the OCS should be used on all photodiode channels on all photodiode boards. To identify the most appropriate capacitance, tests were performed using the FPGA motherboard and a single pulser board. The photodiode board was supplied with $\pm$ 12 V, and again the light was split from the pulser such that it was incident on a photodiode channel and a power meter. The op-amp output was again observed through an oscilloscope with probes across the output of the op-amp that would later feed into an Analog-to-Digital Converter (ADC). Initial measurements were taken of the photodiode's response as a function of the number of photons injected per pulse. The photodiode board had the options of setting three different feedback capacitors: 6.5 pF, 20 pF and 60 pF. A 10 ms integration time was used for all three sets of measurements.

For all three capacitances modes, the relationship between the photodiode's response

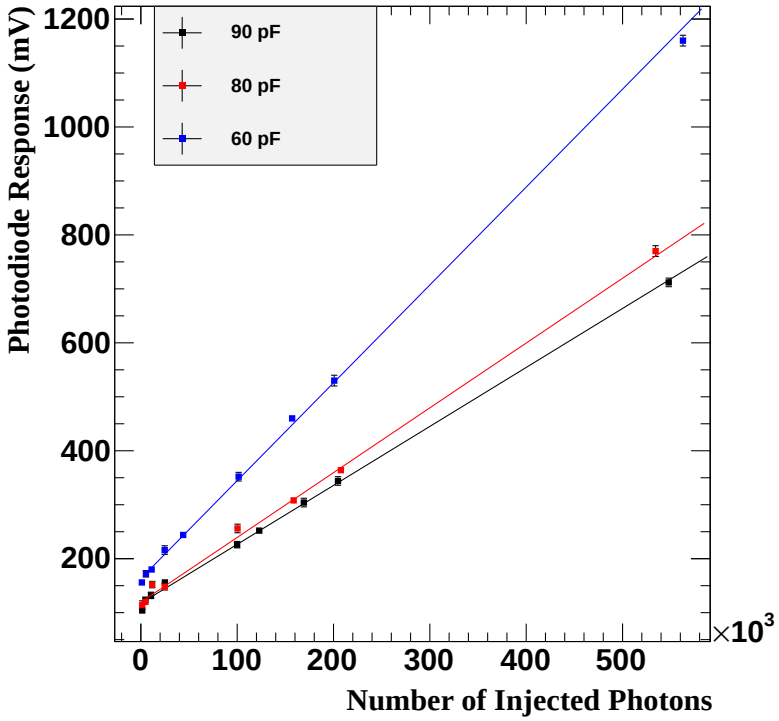

Figure 4.41: Integrated voltage from the op-amp as a function of average number of injected photons. An integration window of 10 ms was used, with 3 different board capacitance: 6.5 pF (black) with c = $1.17284{\cdot}10^{2}$, m = $1.09275{\cdot}10^{-3}$, and χ^2/NDF of 22.9363/7. 20 pF (red) with c = $1.19329{\cdot}10^{2}$, m = $1.20059{\cdot}10^{-3}$, and χ^2/NDF of 18.3887/ 6. 60 pF (blue) with c = $1.63177{\cdot}10^{2}$, m = $1.81360{\cdot}10^{-3}$, and χ^2/NDF of 22.0929/7. Errors attributed to y-values but not visible. An average of 1.5k photons were injected per pulse with a 10 ms integration period. All gradients are in units of mV/number of injected photons, and all intercepts in units of mV.

and the number of photons appears near linear (Figure 4.41). It is also clear that a greater response across the entire range was induced at the smallest capacitance. Also, the 500k pulses did not cause the op-amp to clip out. Therefore, to ensure the detection of signal levels significantly above the background and electronic jitter, at the lowest photon injection of 1k, the board should be operated with a 60 pF capacitance.

Op-amp Integration Window

A range of integration times between 10 and 200 ms were investigated to determine the most suited for the accurate determination of the light output from the pulser board across the full dynamic range. Again, the op-amp on the photodiode board was set to have a 60 pF

capacitance. Light was injected at the 12k photons per pulse level to limit the systematic error introduced by small variations at very low photons per pulse. A corresponding background measurement accompanied each measurement for a given integration period; with the mode taken as the background value and the variance as its associated error. For these tests a previously untested type of photodiode was also investigated, the S5971.

Each photodiode's response for each integration window could then be background subtracted and normalised against the number of photons per pulse detected by the power meter. As the integration period is several orders of magnitude greater than the electronic pulse width delivered to the LED by the FPGA, multiple pulses will be incident on the photodiode during each measurement. Therefore, it is viable to assume any measurements made with a mistiming between the pulses and the photodiode board acquisition will be averaged.

As can be seen from Figure 4.42, the S1223-01 gave meaningful outputs within this range and a more significant response for all integration periods. Considering both photodiodes' response at the 2500 ms integration point, the S5791's value is not in trend with the rest of the data; this is due to the output saturation whilst taking a background measurement. Hence, both the signal level and background are equal, and the background subtraction gives a near-zero response. This did not occur for the S1223-01; this was attributed to this photodiode having a more extensive range and a negative initial amplitude. Therefore it was determined that any integration period from 10 to 1000 ms would be suitable for either choice in photodiode.

Low Light Level Detection

To verify that both the selected capacitance mode and photodiode choice were viable to distinguish between the number of photons at the lower end of the required OCS dynamic range, an additional set of measurements were taken of the photodiode response to the number of injected photons.

Using the development FPGA the number of photons per pulse was varied from 500 to 5000 photons in increments of 500. The photodiode board was set to a 500 ms integration period and a 60 pF capacitance across the op-amp. The FPGA, pulser and photodiode board were placed into a light tight environment, and before pulsing of the LED, the background levels of each photodiode were recorded. Initial measurements of the low end were not detectable from noise. To overcome this, an external 2.5 pF capacitor was soldered to the op-amp. Consequently, the saturation of the integrated signal occurs for a

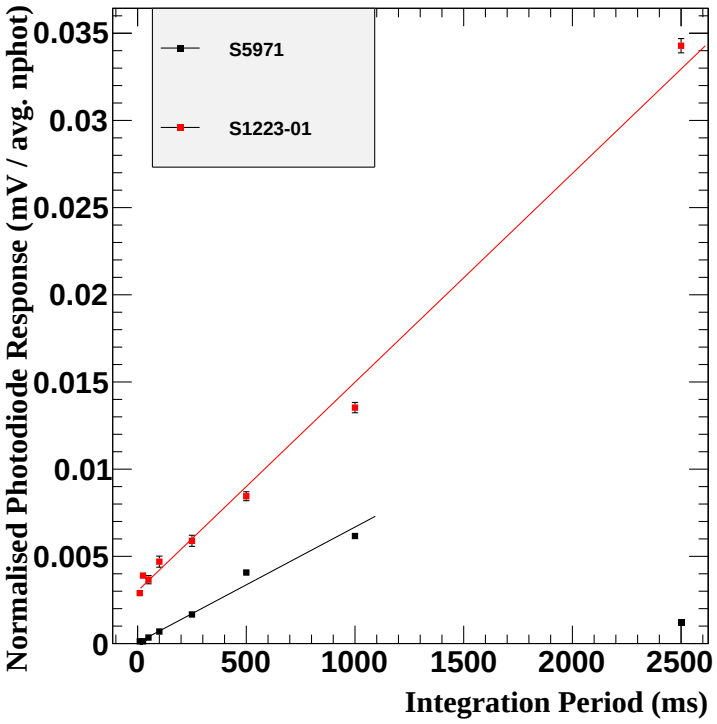

Figure 4.42: Normalised photodiode response as a function of integration period for both the S5791 (black) and S1223-01 (red) photodiode. The photodiode board was operated with a 60 pF capacitance and an average of 12k photons injected per pulse. Both follow a linear distribution: S5871 m = (6.624 ± 0.170)·10^{-6}, c = (5.359 ± 5.402)·10^{-5}, χ^2/NDF = 36.35/5. S1223-01, m = (1.197 ± 0.015)·10^{-5}, c = (3.015 ± 0.092)·10^{-5} and, χ^2/NDF =57/6. All gradients are in units of mV per average number of injected photons per second, and all intercepts in units of mV per average number of photons.

lower number of photons per pulse. To compensate, measures from the photodiode board were extrapolated from the gradient of the integration. With this feedback capacitance the S5791 had a background of (34 ± 2) mV, and the S1223-01 had -(42 ± 4) mV.

From Figure 4.43 it can be seen that the S1223-01 photodiode gave a larger voltage output for the same number of photons as the S5971; i.e. the S1233-01 has greater resolution across the range of photons per pulse investigated. Despite having an increased resolution, the measurements obtained for the S1223-01 photodiode have more significant deviation from the expected trend; hence offering less precision on any measurements made. It was later noted that some of the deviation observed for the S1223-01 photodiode was likely due to induced noise; the S1223-01 does not have a grounding pin whereas the S5971 does. The conclusion was drawn that the S5971 photodiode was most appropriate to

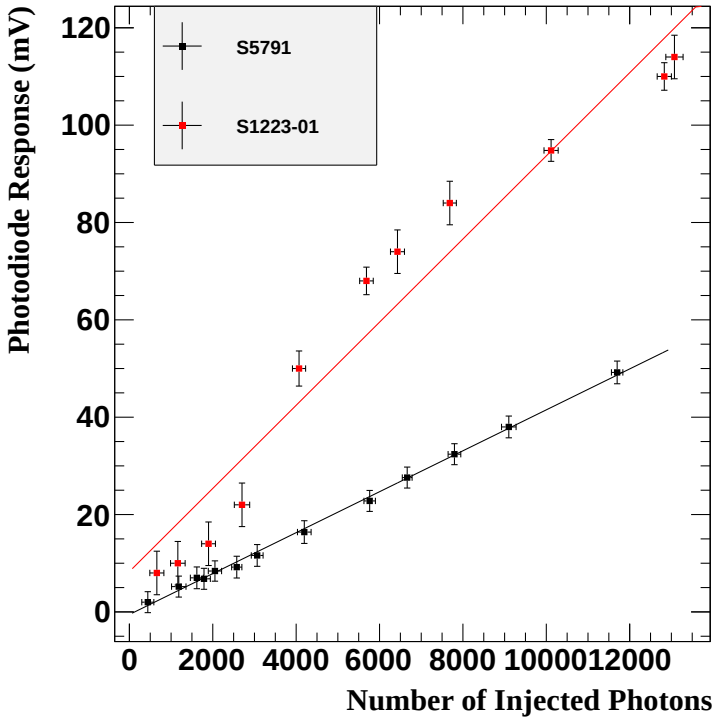

Figure 4.43: Output voltage of the S5791 (black) and S1223-01 (red) photodiodes as a function of average photons per pulse, using a 500 ms integration period. A linear fit was performed on both data sets were the S5791 data had: m = (4.204 ± 0.193)·10^{-3}, c = (-0.528 ± 1.057), and χ^2/NDF of 10.76/11. The fit for the S1223-01 data had: m = (8.540 ± 0.288)·10^{-3}, c = (8.286 ± 2.328) and χ^2/NDF of 517.68/11. The high χ^2/NDF for the S1223-01 is likely due to pick-up noise on the photodiode.

accurately monitor down to the 1000 photons per pulse required for the OCS to correctly match the energy of the threshold calibration for the OD PMTs.

Summary

Both the S1223-01 and the S5791 photodiodes were identified as being suitable for the purpose of monitoring light across the full dynamic range for the OCS. Due to the lack of a grounding pin the S1223-01 photodiode showed greater instability in its output, it was decided that the S5971 photodiode would be used in final production. It was identified that when using a 2.5 pF feedback capacitance for the trans-impedance op-amp, the integration period can be kept to a minimum whilst still giving responses distinguishable from background. For the lower end of the OCS dynamic range, this capacitance should be used with an integration time of ≈ 250 ms.

4.2.4 OCS Final QA and Commissioning

Ten photodiode boards are needed to monitor 40 OCS channels. From the tests conducted in §4.2.2 it was decided that each photodiode board will consist of four Hamamatsu S5971 photodiodes, each feeding into an individual IVC102M trans-impedance integrating op-amp, with a four-channel input MCP3204 12–bit ADC. This particular ADC has a maximum voltage of 2.048 V, giving a resolution of 0.488 mV. As previously stated, the photodiode boards need to give out reliable measurements for the full dynamic range of the OCS. To prevent the need to toggle physical switches between different light injection levels, it was decided not to measure the accumulated charge in a fixed time window but instead measure the dV/dt by sweeping the integration's width. Once the measured voltage reaches the saturation point of the integrating op-amp, the integration is stopped. All ten boards were produced and tested; with each channel showing a linear dependence on the light intensity in the range needed for the monitoring and calibration of the LZ OD[22].

Final validation tests of the photodiode boards were conducted using a 10 kHz light pulse from a 435 nm LED driven by an OCC. The light output from the LED was split down three channels; only two were used during the test. The first was incident on the Thorlab PM100USB power meter, the second on the channel's photodiode connected with flying cables to the DRS4 digitiser board. An Arduino Uno was used to control the photodiode board's logic, and ± 12 V was supplied. Sequential reading of the channels was controlled through the SPI protocol. Measurements of each channel were taken over the range 500 to 60000 photons per pulse (18 to 23 ns wide trigger pulse equivalence) which covers the threshold and source calibration ranges. The ratio of the light incident down each channel first measured using a power meter, found that the channel the photodiode is on receives 1.12 times the light received by the power meter during the measurements. Figure 4.44 shows the ADC readout for the photodiode response as a function of number of injected photons measured by the power meter. All four channels on each of the ten boards have been tested, all showing a consistent linear relationship. The gradient of each channel are given as a histogram in Figure 4.45, where it can bee seen that the majority of the channels have a dV/dt of $\approx$ 5.1 V/s, with outliers deviating from this by no more than 0.9.

The response of all four channels of a single photodiode board to light levels equivalent to the required threshold of the OD PMTs, and to the full dynamic range of injection levels was tested. The results of which are given in Figure 4.46. Where it can be seen in

[22]Spare boards will be produced together with the boards needed for Super-K and Hyper-K.

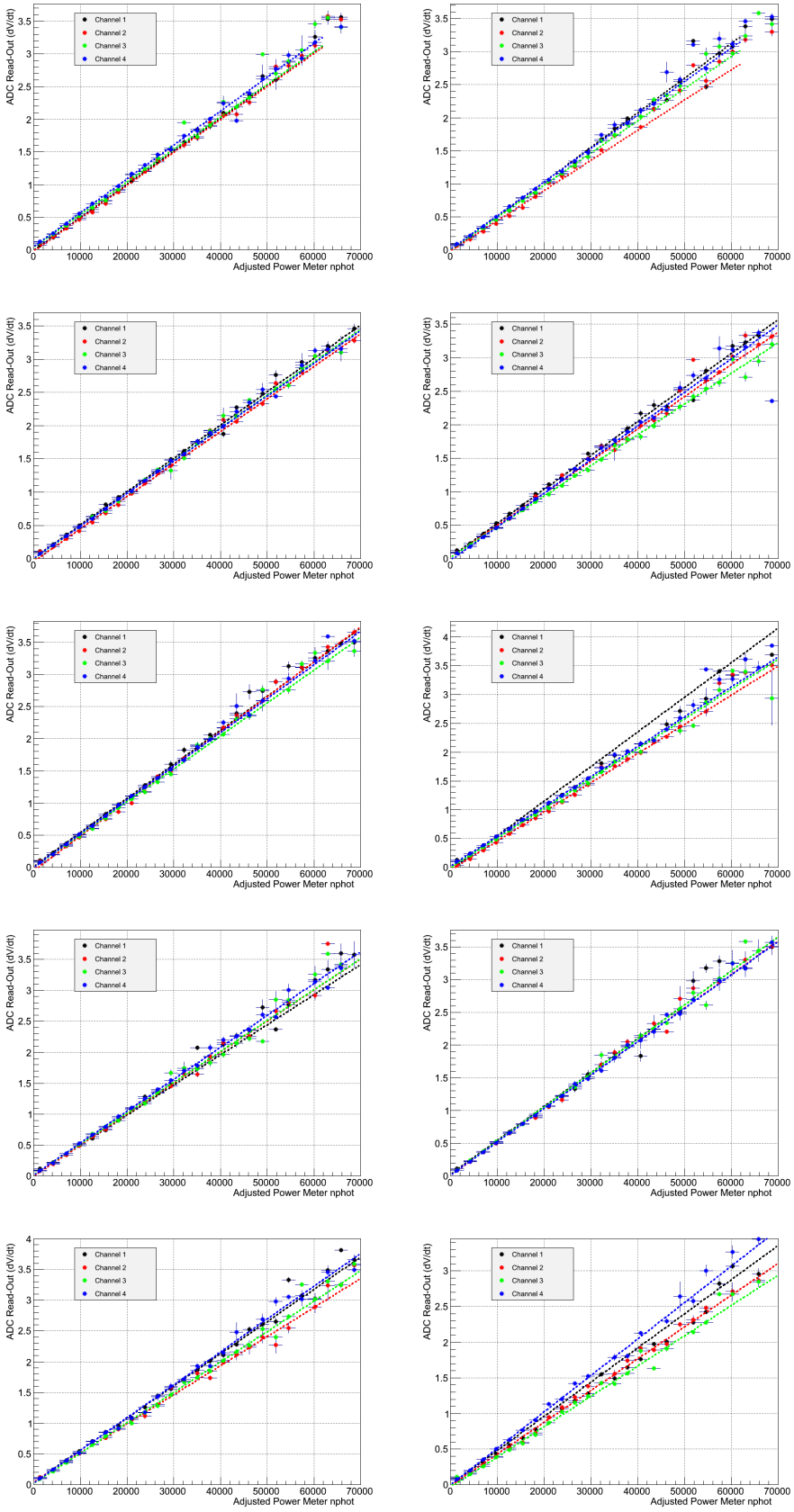

Figure 4.44: Differential voltage from photodiode as read by ADC as a function of average number of photons per pulse as read by the power meter. Shown are the four channels for each of the ten boards. Number of photons have energy range equivalent to other OD calibrations.

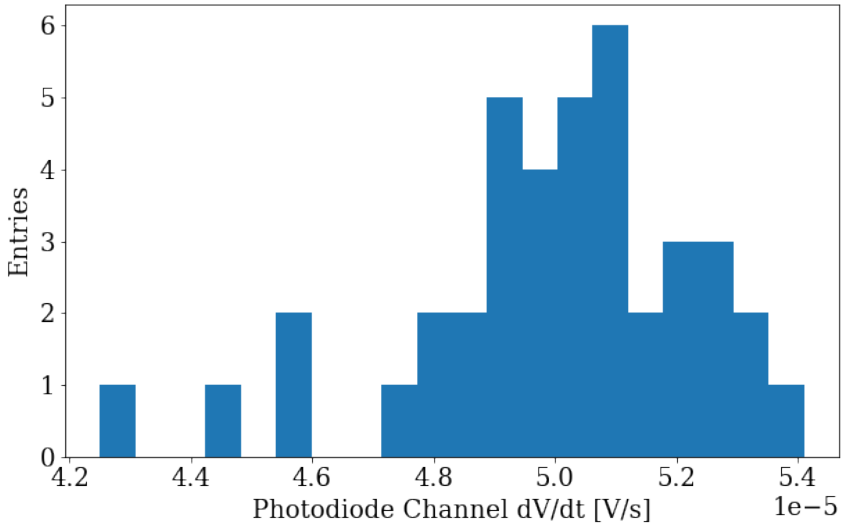

Figure 4.45: Histogram of the gradients of the differential voltage from all photodiode channels.

the left panel that all four channels gave a discernible readout at the 1000 photons per pulse, even though channel 1 appears to have a steeper gradient than the other three channels at these low levels of light injection. These deviations will not decrease its reliability in readout as each channel's response is considered when determining the photon numbers by the photodiode boards during operation. The right panel of Figure 4.46 shows the photodiode board response to the number of photons per pulse equivalent to the OD's extended energy range (10000 to 150000 photons per pulse). The same test procedure was conducted, just with a 90 pF feedback capacitance within the integrator. Again, a linear relation was found between the differential voltage and the number of photons; gradient of $(6.84 \pm 0.01) \cdot 10^{-5}$ V/s and an intercept of -0.004 ± 0.001 V.

After validation of the photodiode boards and construction of the OCCs, the OCS was shipped to SURF where final QA tests were conducted on each OCC channel. To validate the performance of the system after transport, a calibration check was performed. All pulser board channels were checked for their absolute light output over a range of injected photons by varying the supplied electrical pulse width to the pulser. Measurements were determined from a single sample from the Thorlab PM100USB power meter (giving the absolute number of photons) and 4000 samples from the Hamamatsu H10721 PMT (pulse width of the injected light). A DRS4 evaluation board was used to record the PMT pulses and the supplied electrical pulse width to the pulser board. Each measurement was repeated three times. The data was then histogrammed and fit with a Gaussian, taking

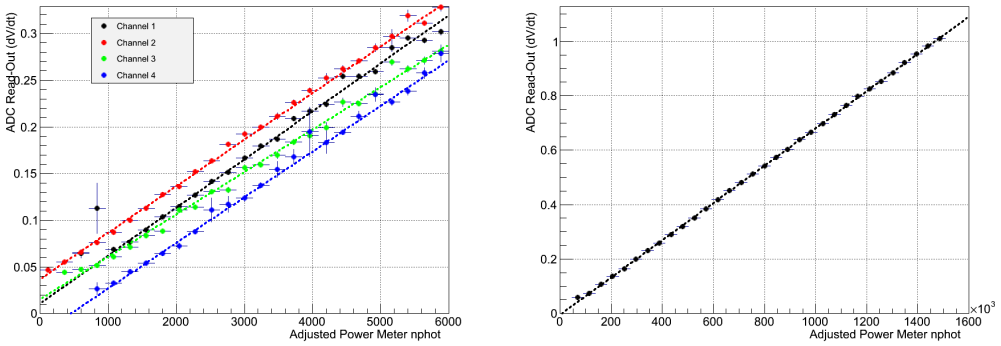

Figure 4.46: Differential voltage from photodiode as read by ADC as a function of average number of photons per pulse as read by the power meter. Shown are the four channels for one board. Number of photons have energy range equivalent to the OD thresholds (**left**) and across the full dynamic range (**right**).

the mean and the standard deviation as the light intensity measure for each supplied electrical pulse width (also referred to as the trigger width).

One of the key assessments is the calibration curve required for each channel to ensure that the correct electrical pulse width is delivered to the pulser to produce the desired number of photons per pulse. This pulse can be varied from 20 to 60 ns with 504 possible unique values, to generate a light output from 700 to 700000 photons per pulse. The fine step size is $\sim$ 40 ps, allowing for precise control of the number of photons injected, which will be vital in the threshold calibrations of the OD PMTs. The exact relationship between the electrical pulse width and the number of produced photons (Figure 4.47) is distinct for each channel and is given by:

$$\begin{aligned} TW &= A + e^{\lambda}, \\ \lambda &= B\ln(N_{ph}) + C\ln(N_{ph})^2 + D\ln(N_{ph})^3 \end{aligned} \tag{4.2.1}$$

where TW is the supplied electrical pulse width, N_{ph} is the intended number of photons to inject and A, B, C and D are channel specific calibration parameters.

As stated in §4.2, an essential requirement of the OCS is to produce pulses of light with a width less than 20 ns to match the expected pulse width of light emissions from the GdLS and water in the OD. For each supplied electrical pulse width, light was emitted at 4 kHz, the required operational rate of the OCS. The power meter reading was used to normalise the PMT waveforms to the absolute number of photons, and the full width at half maximum of these pulses was taken. Figure 4.48 shows the output from a single channel of the light pulse's width as observed by the PMT against the number of photons

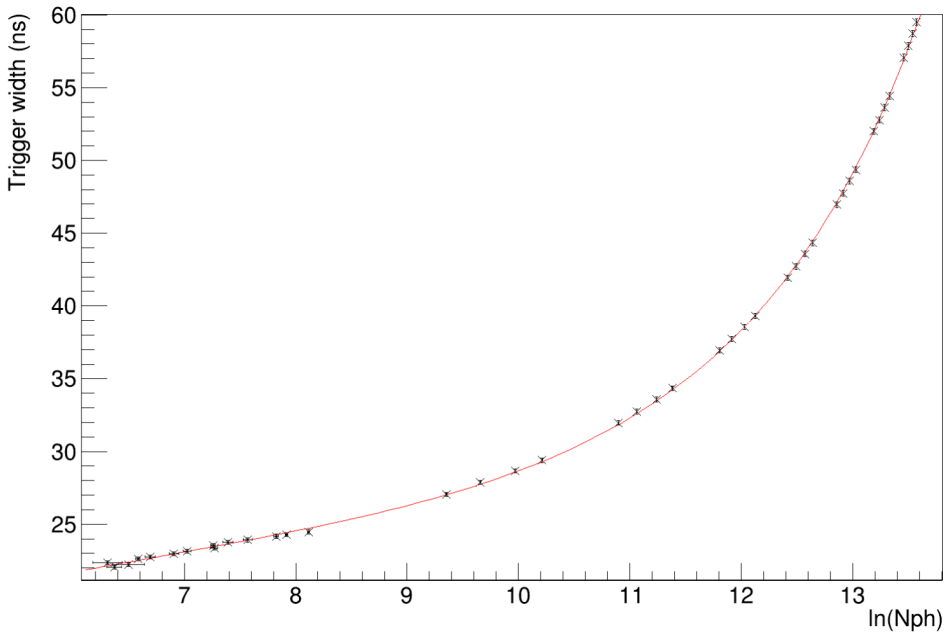

Figure 4.47: Trigger width supplied to the pulser board as a function of the number of photons per pulse. Each channel is fitted with the function given in Eq. (4.2.1) [197].

detected by the power meter.

Further validation testing was performed on each channel to verify that the calibration equivalent light injection levels (700 photons, 1000 photons, 20000 photons and 50000 photons) could be generated. Individual channel trigger widths were determined by placing their relevant calibration parameters individually into Eq. (4.2.1). If the trigger width was not accessible by the channel, the closest discretised increment was selected. Figure 4.49 shows that for each intended light injection level, all channels could produce the required number of photons with a minimum accuracy of 10%. This confirmed that the OCS calibration's internal precision allows for all channels to perform consistently between calibrations.

It was noted during testing that the initial distribution of photons per pulse for the 51 pF LEDs (Figure 4.34) was not Gaussian as expected. It was therefore important to verify whether or not these distortions were due to reflections in the intial test set-ups and not due to the profile of either the LED or final fibre optics. Using a single channel from a finalised OCC, the pulse to pulse variations for a single channel were measured using a PMT. As can be seen by the Gaussian distribution in Figure 4.50, it was confirmed that the initial variations were due to the test set up and not the LEDs.

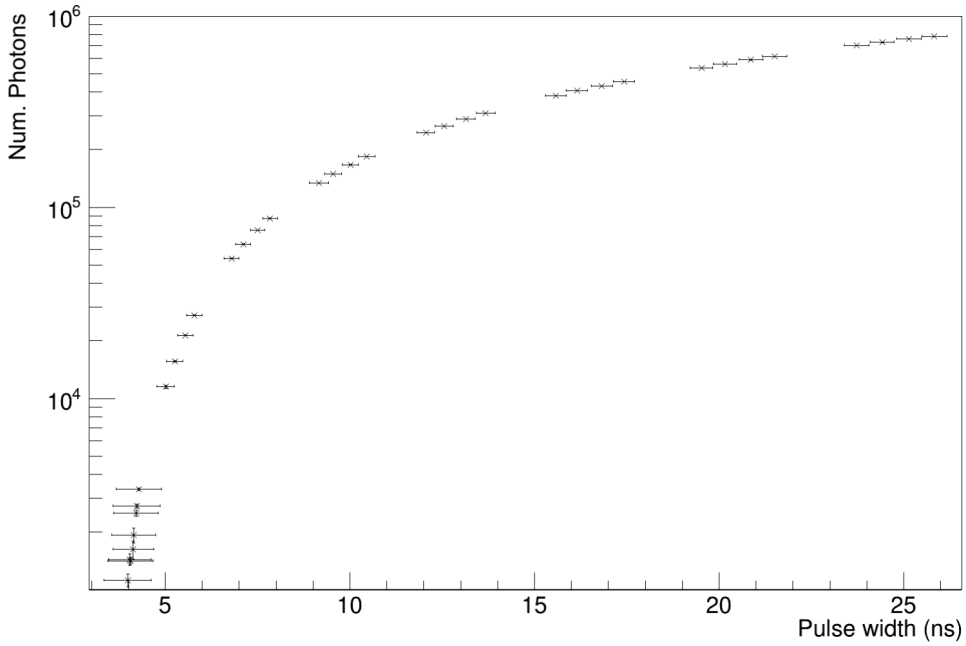

Figure 4.48: The number of photons per pulse as a function of the PMT measured pulse width. The pulse width can be seen to be less than 20 ns and therefore meeting the requirement set on the OCS [197].

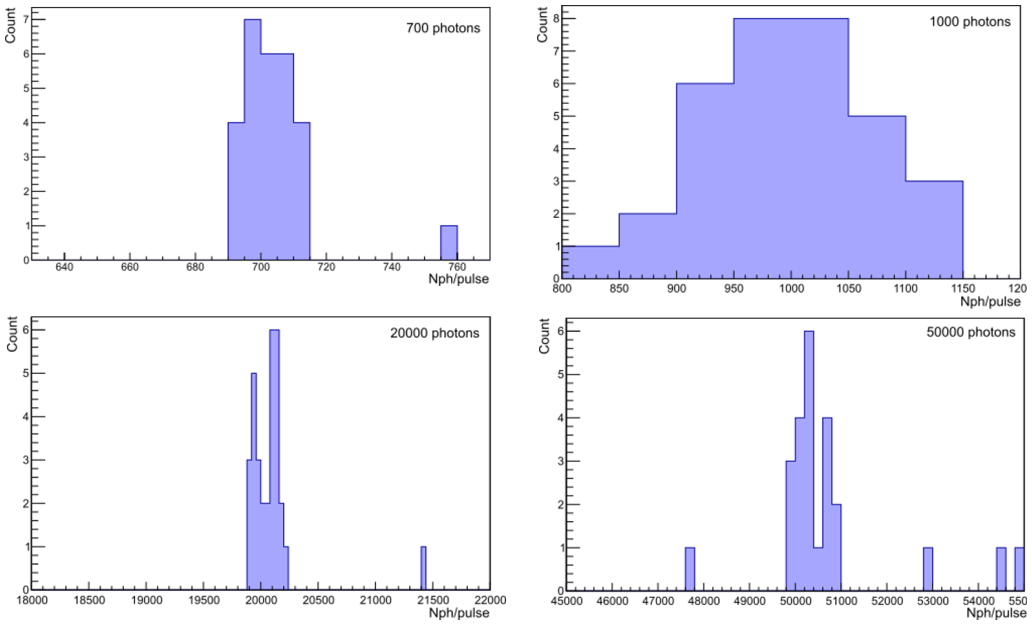

Figure 4.49: Number of photons per pulse generated by each of the OCS channels for a trigger width determined by Eq. (4.2.1) corresponding to: 700 photons per pulse (**top left**), 1000 photons per pulse (**top right**), 20000 photons per pulse (**bottom left**), and 50000 photons per pulse (**bottom right**) [197].

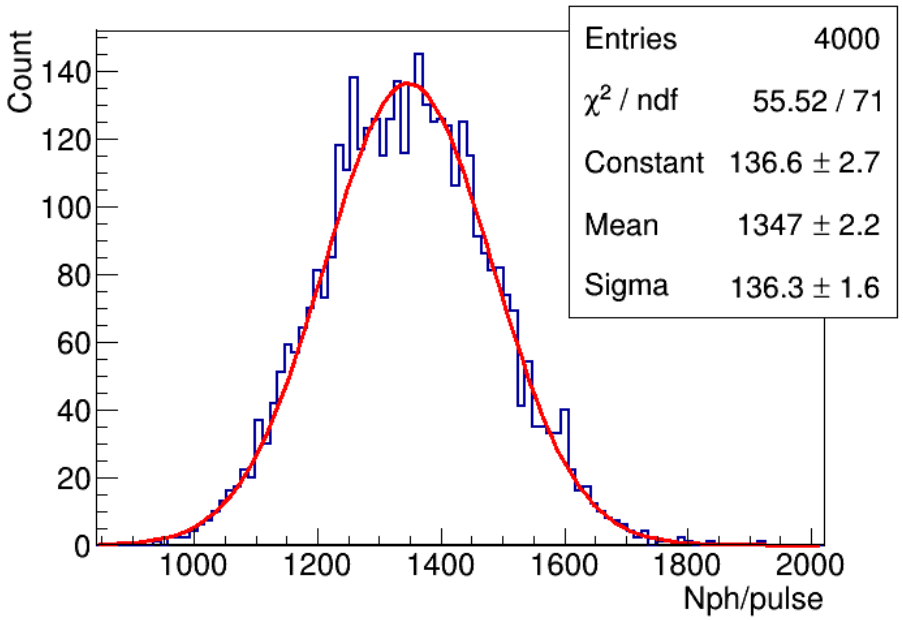

Figure 4.50: Distribution of numbers of injected photons per pulse at the level corresponding to 150 keV energy deposition in the OD. The resolution of 10%, which is not corrected for the spread due to the PMT measurement, shows that the system meets the pulse width requirement set by the experiment. The resolution is better for higher light intensities [197].

Summary

This chapter outlined two calibration systems vital to the operation and science reach of the LZ detector. It started with an overview of the CSD's mechanical and electronic components that allow it to conduct multiple energy and timing calibrations throughout all three layers of the LZ detector. Following this were the quality assurance tests performed on the CSD to ensure it met all the initial design and operational requirements. The second section of this chapter covered the OCS, a calibration system pivotal to the correct calibration of the OD veto systems and monitoring for degradation in the GdLS. Again a description of the critical components and operational premise of the system was given. It was shown that the OCS can produce signals with energies equivalent to the required OD PMT threshold and to energies comparable to other sources that will deposit energy in the OD. In addition, the OCS self-monitoring systems were validated to be sensitive enough to detect low light output levels to confirm the number of photons per pulse before injection into the OD.

Chapter 5

Effective Field Theory Searches with the LUX Time Projection Chamber

One of the final analyses performed by the LUX collaboration was the interpretation of WIMP search results using Effective Field Theory (EFT) [126]. The EFT principles have been outlined in §2.4. As discussed in that section, most WIMP-nucleon EFT operators have a significant rate in a wide range of NR energies, hence motivating the requirement to look out to higher recoil energies than previously investigated by LUX.

This high-NR analysis of the WS2014-16 data places limits on the inelastic EFT operators (Eq. 2.4.8) in the isoscalar basis by performing hypothesis testing with the use of a Profile Likelihood Ratio (PLR) developed specifically for this analysis. Within the PLR framework, hypothesis testing is performed to assess each event's likelihood in the data on whether or not it is more background or signal like. This analysis used 5-dimensional Probability Density Functions (PDFs) to assesses the data to the background and signal models.

This chapter will start with a description of the LUX experiment, the WS2014-16 data set (§5.2.2) and calibrations (§5.2.1), the relevant background models (§5.2.3), the process for developing the signal models (§5.2.4) and the exact methodology of the PLR in §5.2.5. Presented in the final section of this closing chapter are the resultant limits on the coupling to the inelastic WIMP-nucleon EFT operators[1] in the isoscalar basis.

[1] These inelastic limits have been published in tandem with limits on the coupling to the elastic WIMP-nucleon EFT operators [204].

5.1 The LUX Experiment

Over 100 people from 24 institutes, stemming from Portugal, the UK and the USA form the LUX Collaboration. LUX conducted DM searches between the 21^{st} of April 2013 and 2^{nd} of May 2016; using a 370 kg dual-phase LXe TPC.

LUX used ultra-radiopure titanium for the construction of their inner cryostat, and wrapped it with an insulating material before being housed in a larger cryostat, see Figure 5.1. Assaying of the titanium is outlined in [205]. The inner cryostat stood 101 cm tall and had a 62 cm diameter. The active volume of the detector was a 49 cm tall by 50 cm diameter dodecahedral cylinder; giving an active mass of 251 kg. To observe the primary and secondary scintillation light, 61 PMTs were positioned inward facing in the top array and a further 61 in the bottom array. Wire grids were used to establish the drift and extraction fields. Uniformity of these fields was maintained by a series of copper field rings. To increase the detectors light collection efficiency these copper rings were surrounded on the inside edge by 12 PTFE panels. The Xe temperature was maintained at condensation point, 165 K, by a set of thermosyphons coupled to the copper shield above and below the PMT arrays. Additionally, the copper shield aids in displacing the Xe within the

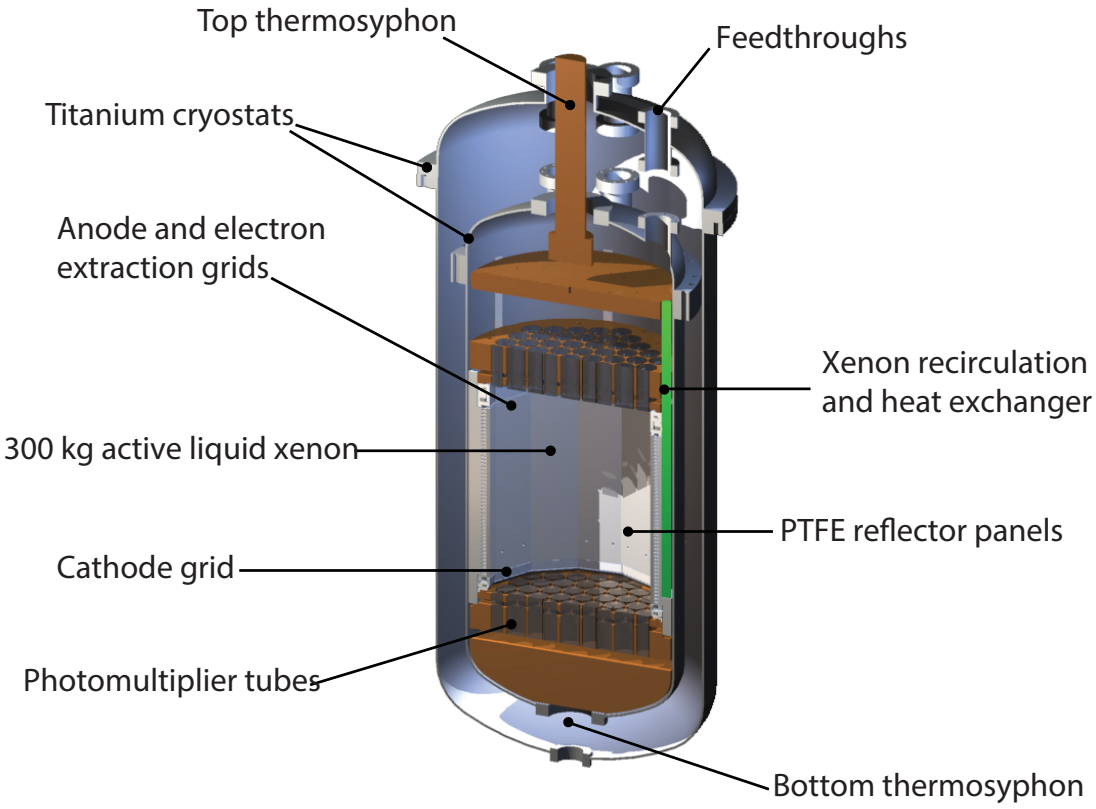

Figure 5.1: Annotated render of the cross-sectional view of the LUX detector [173].

inner cryostat and acts as a shield from gammas originating from the cavern walls. For a comprehensive overview of the LUX detector please see [173]. LUX was situated in the same water tank that now houses the LZ detector, and had a significantly reduced PMT coverage of the OD.

Five ultra-finished stainless-steel wire grids were spaced within the inner vessel to create the required drift and electric field. Figure 5.2 shows the layout of these grids. Grids were positioned 2 cm above and below the top and bottom arrays. Doing so shields the PMT photocathode by negating the electric field produced by the anode and cathode grids. The bottom grid was made with 206 μm wires with a 1 cm pitch (98% transparency). The top grid had the same pitching but with 50 μm wires; this variation in wire size was due to the two regions' having different field strengths. Positioned 4 cm above the shielding of the bottom array was the cathode grid. This defines the bounds on the bottom of the active layer. The maximum drift length distance in LUX was taken as the 49.5 cm distance from the cathode to liquid surface. Again 206 μm wires were used, this time with a 5 mm pitch

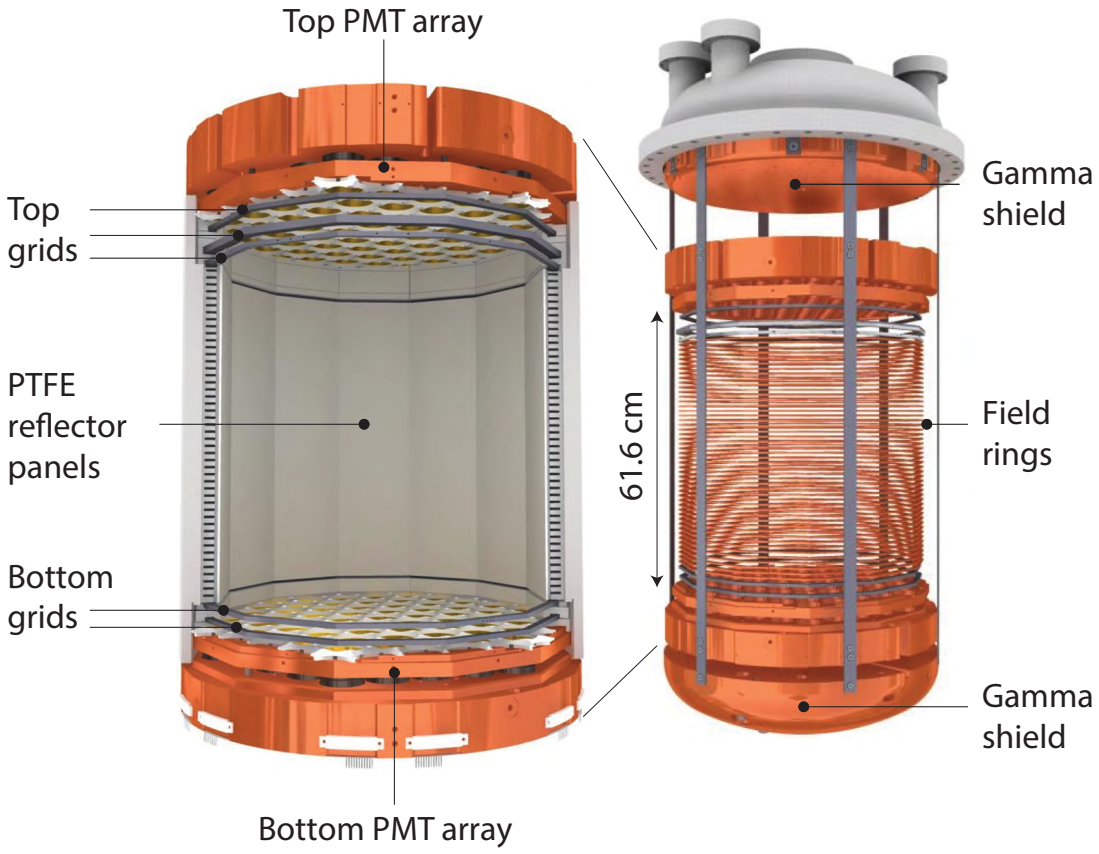

Figure 5.2: Rendered image showing high voltage grids, shaping rings and PTFE panels of the LUX detector [173].

(96% transparency). The gate grid was made of 50 μm wire with a 5 mm pitch (99% transparency). The drift field's resultant strength is proportional to the voltage difference between the gate and cathode grids. The anode grid was 1 cm above the gate and 4 cm below the top grid, this volume being the extraction region. It was made from a 30 μm stainless steel mesh, with 0.5 mm spacing (88% transparency).

The 47 copper field-shaping rings could be stepped in voltage between the anode and cathode grids using a resistor chain. A 1 cm spacing was used between each of these rings. This helped to ensure uniformity of the drift and electric fields throughout the active volume. During initial science data collection, a drift field of 181 V/cm and an electric field of 6.0 kV/cm (3.1 kV/cm) in the gas (liquid) phase was established for nominal operation[2]. To achieve this, the grids were held at: -1.0 kV top, 3.5 kV anode, -1.5 kV gate, -10.0 kV cathode, and -2.0 kV bottom.

Overview of Simulations

Monte Carlo simulations within LZ and LUX are performed using the same modelling software but differ in some parameters to tune the detectors' specificities. The code structure used for the LUX WS2014-16 high energy nuclear recoil analysis was as follows[3]:

- LUX_BACCARAT is a LUX specific version of the Geant4 simulation code developed by the LZ collaboration, validation of this code is given in [196]. This code allows for the calculation of the differential recoil spectra of each background component based on the detector materials' radio-assay measurements.

- LLAMA is a handler for the Noble Element Simulation Technique (NEST v2.1.0) [206] framework. to include the spatial and temporal changing detector parameters experienced in the LUX WS2014-16 data. LLAMA generates the spatial and energy parameters for each interaction based on the recoil energies and the expected rates determined from BACCARAT. For a complete description of the methods and techniques applied to accurately simulate the scintillation and ionisation using NEST within the LUX detector, the reader is directed to [207].

The NEST framework uses an empirical model based on all currently available light and charge yield data obtained within LXe experiments. Due to this, it is expected that there may be a slight deviation from this data when modelling a specific detector; this

[2]Designed to go to higher field strengths; limited by electroluminescence occurring on the cathode grid.

[3]For LZ the corresponding software packages are BACCARAT and LZLLAMA (again being a handler for NEST with detector parameters selected to match LZ).

was especially true in the case of the LUX WS2014-16 data as the ^{14}C and ^{3}H calibration obtained by LUX had not been incorporated into NEST's modelling. The inclusion of these calibration data sets allowed for the optimisation of NEST towards the reproduction of LUX data. For energies greater than the highest calibrated point, extrapolation was performed. In addition, LLAMA allowed the inclusion of the temporal and spatial pathologies that adversely affect the data. Figure ?? shows the resultant and accurate reproduction of the 14C band and the WS2014-16 ER data by LLAMA.

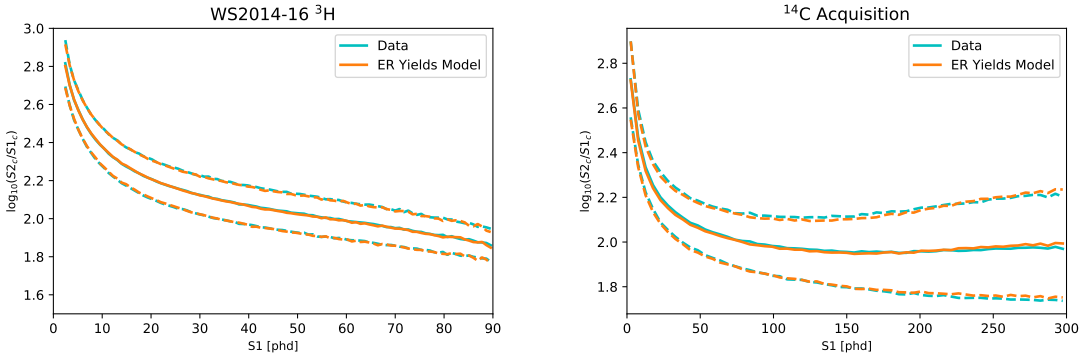

Figure 5.3: The final LUX ER yields model using LLAMA with the WS2014-16 ^{3}H data (**left**) and the 14C acquisitions (**right**). Temporal dependencies on g1 and g2 for each of the time bins were considered by LLAMA.

5.2 LUX WS2014-16 High-NR EFT Analysis

The following section outlines the inelastic EFT WIMP-Search (WS) analysis of the LUX WS2014-16 data for NR energies out to ∼180 keV. A description of the calibrations performed, the data quality selection process, and the background and signal models used in the applied statistical method is given. Due to extending the window out further than used in previous LUX analysis, the data quality cuts and backgrounds had to be reassessed and differ from those presented in [90]. The LUX collaboration have previously produced limits on the coupling to EFT operators in the isoscalar basis for elastic interaction using a much lower exposure data set [208]. Additionally, the limits on the couplings for elastic interaction in the proton-neutron basis of the EFT operators for this WS2014-16 analysis are presented in [204].

Before collecting the WS2014-16 data, the LUX TPC grids underwent a conditioning process to increase the strengths of the field at the extraction region and of the drift field. Unfortuantely a significant amount of charge accumulated on the TPC walls during

this process, resulting in localised distortions of the drift field that varied in strength during the WS2014-16 acquisition. The strength of the drift field became spatially and temporarily dependent with values from 50 to 550 V/cm. To correct for this effect, the LUX collaboration produced a detailed mapping of the detector's field strengths using in-depth 3D electrostatic models[4].

The aim of the 3D electrostatic mapping was to discretise the detector into four bins in time (each spanning a month to several months worth of data), each with four spatial bins (with a bin width equivalent to 65 μs drift time) to give a total of 16 separate "detectors" selected such that the field can be considered static and near-uniform in that bin. Figure 5.4 shows the separation of the WS2014-16 data into these 16 bins out to 300 phd in the

[4]This was achieved using the COMSOL Multiphysics software [209]. The process for which is covered in [210].

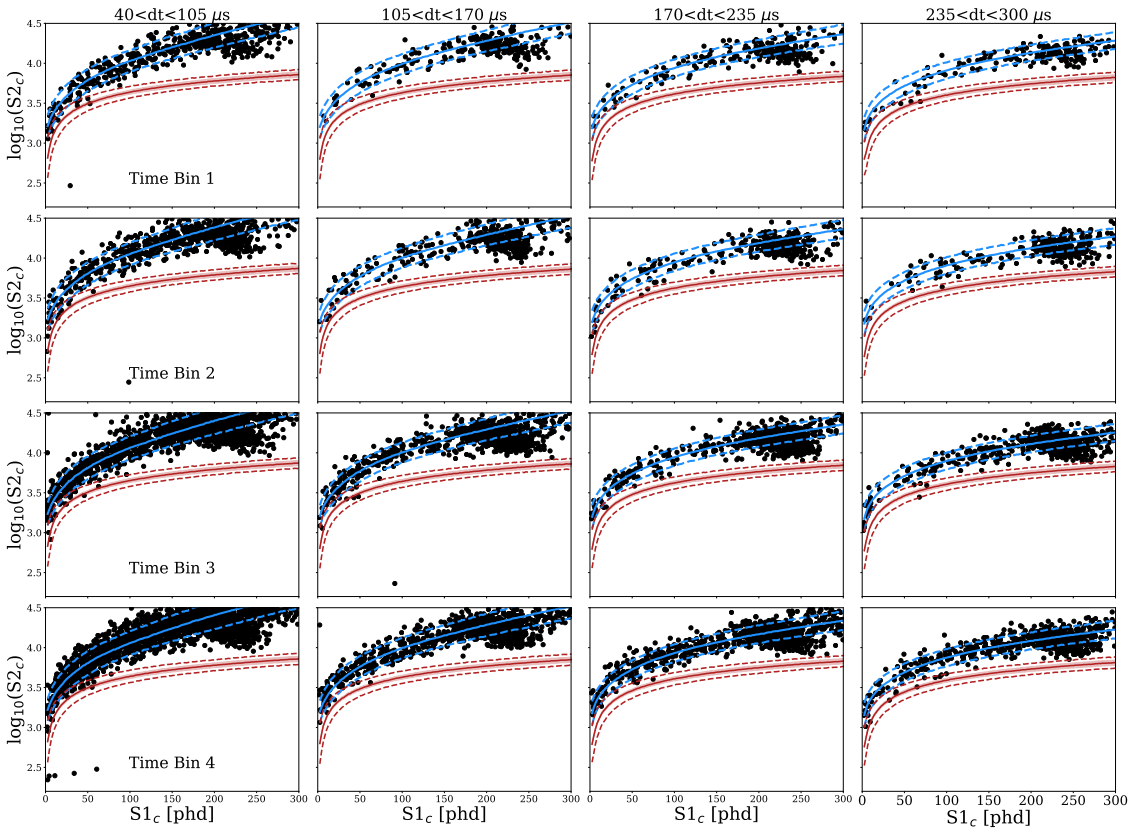

Figure 5.4: LUX WS2014-16 data divided into 4 spatial drift bins, each subdivided into four time bins containing varying proportions of the total livetime after removing periods with high ^{83m}Kr exposure. The mean (90% confidence interval) of the NR response is shown by the red solid (dash) line and the equivalent for the ER response in blue [204].

S1 signal ($\sim$ 180 keV). By constructing these uniform bins, it is possible to minimise the inaccuracies in g_1 and g_2; which both gradually decreased with time from 0.100 $\pm$ 0.002 to 0.097$\pm$ 0.001 phd/photon and from 18.9 $\pm$ 0.8 to 19.7 $\pm$ 0.2 phd/e^- respectively [90].

To quantify the sensitivity, or constrain the possibility, of the experiment to a WIMP-nucleon interaction, where the interaction dynamics are entirely attributed to a single operator, this analysis adopted a limit setting approach under a PLR methodology. PLRs are excellent for handling statistical analysis of high dimensional parameter space, as long as the models provided for the null and alternative hypothesis are accurate and cover all known potential influences. For the WS2014-16 high-NR analysis, 5-dimensional models were required ($S1_c$, $S2_c$, r, drift time[5] and the azimuth angle about the centre of the TPC) for the signal models investigated. The same 5-dimensional models were required for the prevalent backgrounds; backgrounds which remain even after data quality cuts (The general ER background, backgrounds from the wall, residual ^{83m}Kr decay, accidental coincident signals and γ-X events). One means of simplifying the analysis was to separate the energy ($S1_c$, $S2_c$) and spatial components (r, drift, azimuth angle) of an event into separate PDFs. This was done with the exception of the model describing the wall events; a full 5-dimensional PDF is required due to the direct correlation between the energy and spatial observables of these events.

5.2.1 Calibrations

During operation, a multitude of internal and external calibration sources were used. The majority of the external sources did not provide any meaningful calibration for the work contained within this Chapter. Therefore, these will not be discussed; this is with exception of the DD source. Table 5.1 gives the sources that were used, the means of placing them into the system and the intended calibration.

It is vital to note that only a single NR calibration was used. This was not of concern when performing analysis with a ROI bound under 74 keV; the DD generator can produce a wide range of energy depositions, with a well-tagged energy, in the TPC. However, for this high-NR analysis, the ROI extends to $\sim$180 keV. All of the injected sources were β emitters, where CH_3T and ^{14}C were used to calibrate the ER energy response over a wide range of S1 values. For a given energy of interaction in the TPC, the produced S1 and S2 light will not be consistent throughout the detector's volume. The injection of ^{83m}Kr was vital in mapping the position dependency of the produced S1 and S2 of an interaction;

[5] At points drift time will be referred to as drift.

Source	Method	Decay Type	Energy [keV]	Calibration	Ref.
			Electron Recoil		
CH_3T	Injected	β	0-18.6	Low energy S1	[211]
^{14}C	Injected	β	0-156	High energy S1	[212]
^{83m}Kr	Injected	β	41.5	S1 and S2 position dependence corrections	[213]
			Nuclear Recoil		
DD	External generator	Neutron	0.7-74	NR band	[189]

Table 5.1: Table of the ER and NR calibration sources used in the high-NR LUX WS2014-16 analysis. References are given to the relevant publication of each source.

due to its homogenous distribution in the LXe. The resultant maps are then used to correct the number of detected photons in the S1 ($S1_c$) and S2 ($S2_c$) signals of each event. Figure 5.6 shows the extent to which these different calibration sources covered the S1-S2 space used in this search, where it can be seen that the DD covers less than half of this parameter space within the NR band. The NR band beyond the DD calibration energies has been extrapolated using NEST [206].

NEST provides an accurate determination of the charge and light yields of an NR

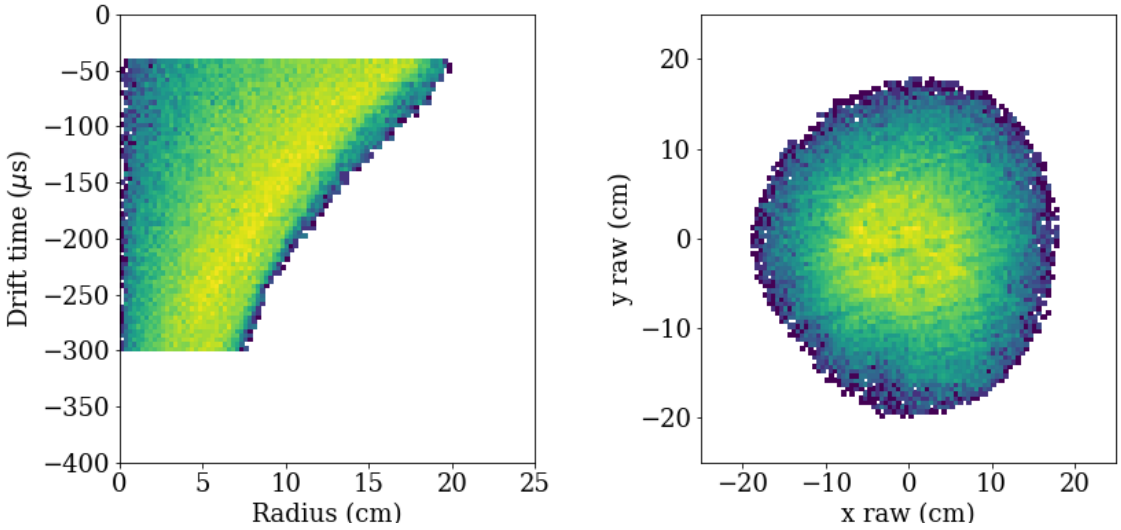

Figure 5.5: ^{83m}Kr spatial response, defining the edge of the fiducial volume in drift−radius (**left**) and $x-y$ (**right**).

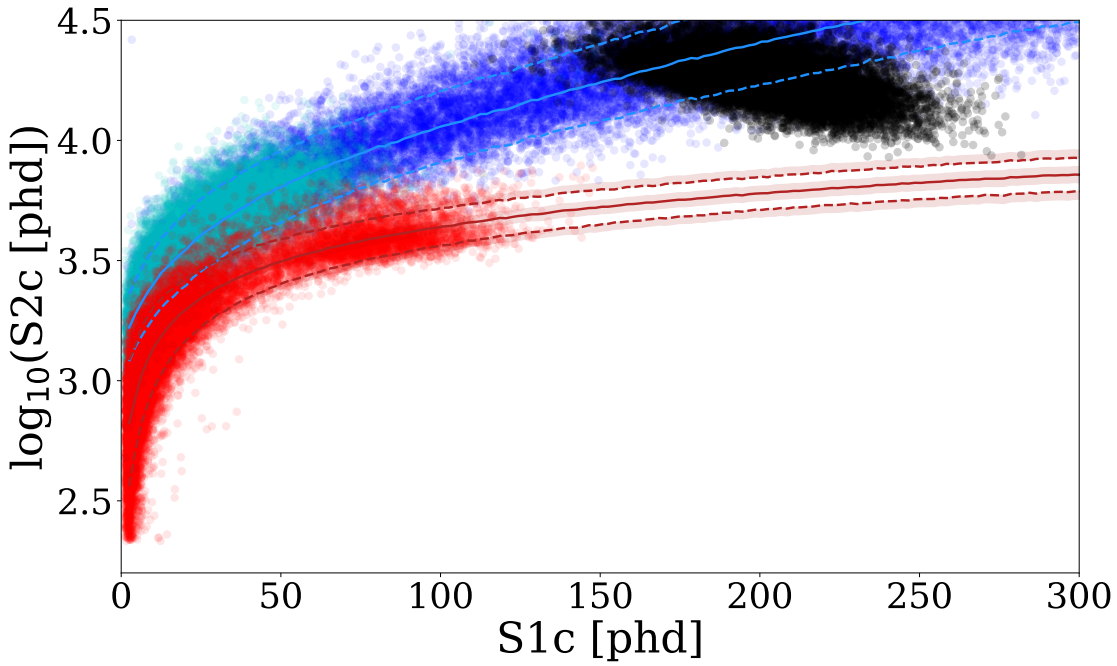

Figure 5.6: Sample of the $S1_c$-$S2_c$ response from different calibration sources in LUX: ^{14}C (blue), CH_3T (cyan), ^{83m}Kr (black) and DD neutrons (red). The mean (90% confidence interval) of the NR response is shown by the red solid (dash) line and the equivalent for the ER response in blue. The shaded red region about the NR response lines defines their uncertainties [204].

interaction based on an empirical fit to all known LXe recoil data [214]. The fit used within NEST is constrained at high energies by a 330 keV recoil from AmBe [215]; helping to increase the accuracy in the resultant charge and light yields at energies relevant to this analysis. As the NR region of this analysis involved extrapolating beyond the highest NR calibration energy, a $\sim$ 180 keV cut off was selected to ensure simulated light and charge yields did not carry too large of an uncertainty.

5.2.2 Data Selection

As previously mentioned, this analysis's energy ROI extends far above any previous LUX analysis performed on this data. It was therefore imperative to revisit the data quality cuts applied and the resultant overall efficiency. At these higher recoil energies, new complications can arise with: position reconstruction[6], previously unconsidered backgrounds, overpopulation of non S1 and S2 signals in and around the signals themselves[7], and events in the GXe region of the detector being classed as an S2 signal. To prevent any biasing during this high-NR analysis, the WS2014-16 data was salted[8] early on in the data pipeline.

A further issue was noted at high S1 values in the WS2014-16 data, leakage of ^{83m}Kr

[6]Most often, the result of the merger of the S2s from a multiple scatter event.

[7]I.e. noise from electrons and photons not associated to the event.

[8]The introduction of events mimicking a WIMP-nucleon signal that are removed after cuts have been finalised. A full description of the LUX salting process is given in [90].

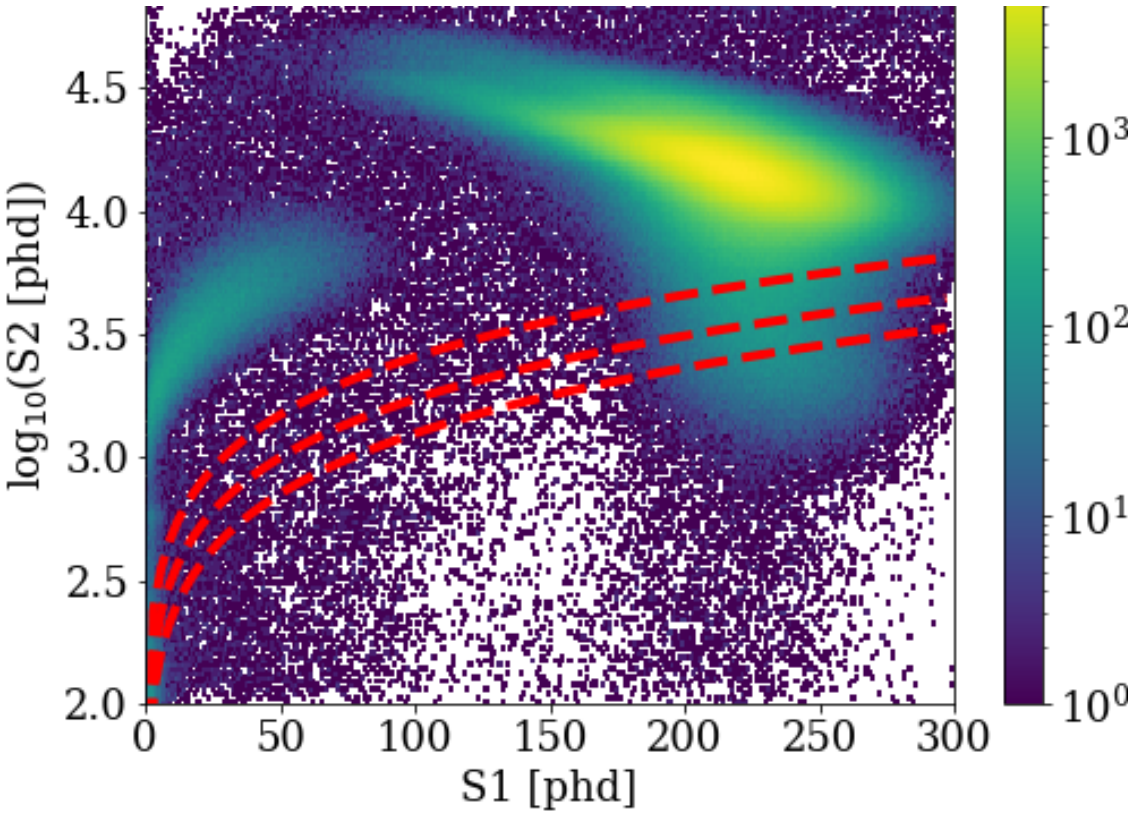

Figure 5.7: LUX high-NR WS2014-16 data showing the leakage of deposition from ^{83m}Kr decays into the the expected NR region; a rough mean and 90% CLs of which are given in red dashed lines are included to guide the eye and are not representative of the actual NR band.

events from the expected ER to NR band. Figure 5.7 shows all events prior to cuts in the WS2014-16 data. A rough estimate of the NR response mean and 90 % confidence limits have been added to this figure to help highlight the extent to which ^{83m}Kr were leaking into the expected signal region. To omit the data most at risk of being contaminated with ^{83m}Kr leakage, all data within 17 half-lives of ^{83m}Kr were excluded. This amounted to a reduction of 20.8 live-days, reducing the total live-days used for this analysis to 311.2 live-days. The total live-days are not split equally amongst the time bins (43.9, 43.8, 85.8 and 137.7 live-days); due to the variation in the drift field across the detector. The drift bins associated with the bottom of the detector have the weakest field (50-100 V/cm), whereas those at the top had the strongest (400-550 V/cm).

The variations in the drift field also impacted the fiducial volume. The fiducial volume for this analysis was taken as a central cylinder of the LXe between 40 and 400 μs in drift and with a radius set 3 cm in from the TPC's wall. The distorted drift field compelled ionisation electrons to curve away from the wall as they drift to the extraction region. This alteration to the electrons' path results in a dependency between the S2 hit pattern on the top array PMTs and the depth of the associated interaction (the deeper the interaction, the more centralised the hit pattern). As the exact strength of the fields were observed to alter throughout the data collection period, each time bin's fiducial volume is different. By applying a series of cuts and counting the remaining observable ^{83m}Kr-like events, each bin's exact radius was defined. The resultant fiducial volumes of each bin in this analysis were: 105.4±5.3, 107.2±5.4, 99.2±5.0, and 98.4±4.9 kg. When combined with the live-days for each bin, the total exposure used for this analysis was 3.14×10^4 kg·days.

Further cuts were performed to remove single scatter backgrounds (those that would mimic a WIMP signal). Events with an overabundance of pulse preceding or following the S1 or S2 were also removed; these are attributed to single photons and electrons originating from the grids or impurities in the LXe [140]. Cuts were also applied to remove misidentified S1s and S2s. A misidentified S1 was characterised by a distorted hit pattern (significant asymmetry between the number of events observed in the top and bottom array) or by a non-standard pulse shape[9]; which is expected to be a close approximate to a Landau distribution. S2s with large pulse width, and those with a non-standard pulse shape as a function of area and drift time[10] were removed. After the application of all of these cuts, the single scatter selection efficiency based on the ER and NR calibration (and

[9] Distortion in the shape of the S1 pulse is usually an identifier of light leakage in the detector.

[10] Bulk S2s tend to have a near-Gaussian shape.

extrapolation with NEST) was >96% for the majority of the energy ROI of this analysis (Figure 5.8).

As shown in Figure 5.6, the NR and ER bands diverge at greater energies, reducing the leakage of the ER backgrounds to the NR band at higher energies. However, as reported in [208], new signals can appear in and below the NR band at these energies which originate from the 5.6 cm gap between the cathode and the bottom PMT array. If a gamma-ray scatters in this Reverse Field Region (RFR) and then scatters again in the fiducial region, both interactions would contribute to the observed S1 signal. However, only the latter would produce an S2. The S2/S1 ratio of this γ-X would be abnormally low for an ER event. When combined with the reduced combination observed at the bottom of the LUX detector due to the weaker fields, there will be an increase in ER event leakage into the NR signal region. A γ-X model and cut have been developed to describe and suppress this background. The cut was trained on simulated γ-X events with a 89.2% rejection of

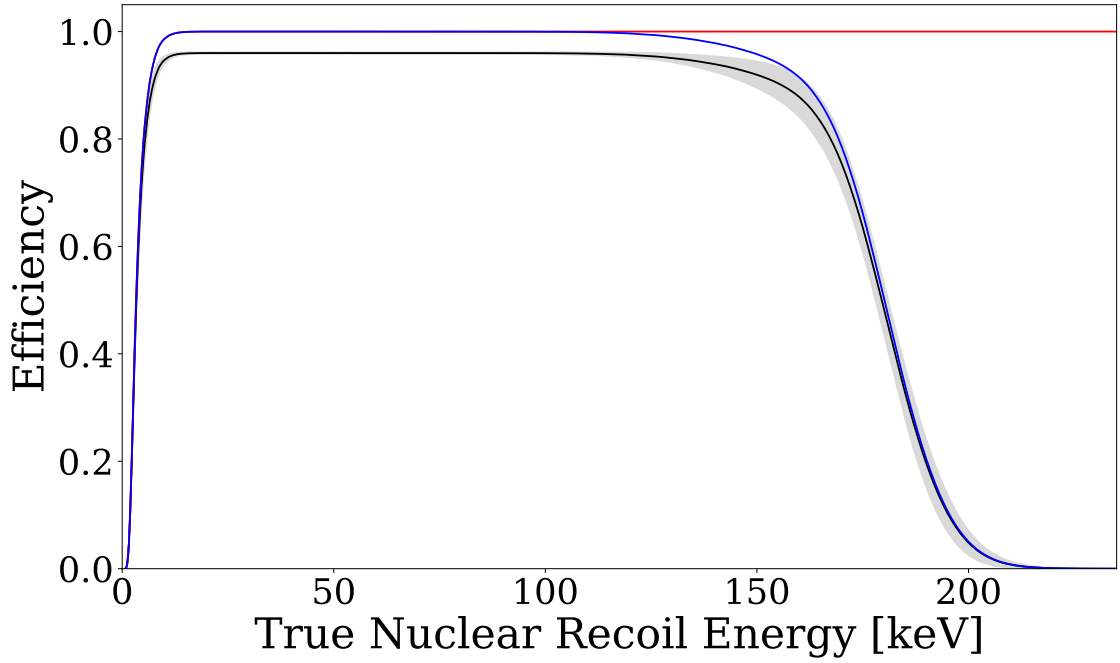

Figure 5.8: NR detection and selection efficiencies based on calibration data and simulations. The combined S1 and S2 detection efficiency in the fiducial volume, prior to the application of data quality cuts, is given in red. The blue line indicates the S1-S2 mean detection efficiency in the extended energy ROI. The mean overall efficiency is given in black, and the standard deviation of this due to the use of different time and drift bins is the grey band. [204].

γ-X and a 1.7% removal of single scatter events. This reduced the overall efficiency of this analysis to 94.4%. The efficiency as a function of the recoil of energy used for this analysis is given in Figure 5.8.

To reduce bias when analysing the WS2014-16 data, LUX implemented a salting procedure. Salting is the process of deliberately introducing events with signal like properties that are undisclosed to the analysers. The analysers then aim to produce all cuts and models based on the salted data in a manner that minimises the removal of the salt events. Salting, in comparison to the more standard methods of preventing bias, blinding, has the distinct advantage that rare background events are not "hidden" during the development of cuts and models [216]. Therefore, no assumption is required on how well characterised and understood the background is. Whereas when applying a blinded approach, this becomes a requirement to ensure that nothing unexpected will be present in the data when "opening" the blinded region [216]. One of the primary motivations for the selection of a salting procedure for the WS201-16 data set was that several previous direct detection WIMP searches that conducted a blinded analysis later discover un-modelled, pathological backgrounds after "opening" the region [217, 218, 219].

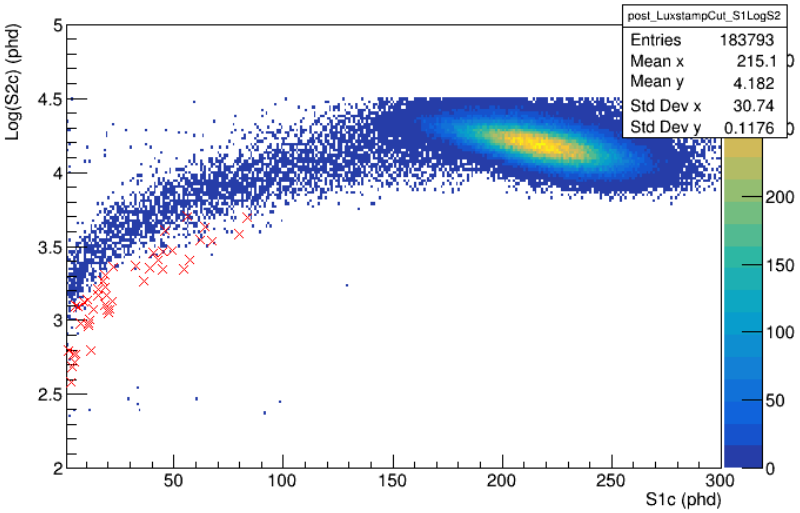

Figure 5.9: WS2014-16 data after after all data quality cuts and the removal of the salted events, which have been included as red crosses.

For the WS2014-16 data set, salting was conducted by introducing WIMP like signals constructed from uncorrelated S1 and S2 signals picked from a tritium calibration data set. To ensure the salting procedure actually prevented bias, the properties of the salted events are limited to only those who conducted the procedure. By stitching pairs of S1 and S2 pulses together, a distribution of events with unknown parameters is created within

the expected WIMP signal region. Full details of this procedure are given in [90]. Once all cuts and models had been finalised, the properties of the salted events were identified and removed from the data used to produce the final analysis. Figure 5.9 shows the WS2014-16 data after all cuts have been applied and the salted events removed, the salted events are also indicated within this figure.

5.2.3 Background Models

The majority of the background for the WS2014-26 data set is expected to be dominated by ER events, with a significant proportion attributed to ^{220}Rn, ^{222}Rn and their charged progeny (which plate-out on the surfaces of the TPC). The next largest contributors to the ER background are ^{40}K, ^{60}Co, ^{232}Th and ^{238}U; all of which were described in §3.3.2.

General Electronic Recoil Backgrounds

To construct the ER background model required for the PLR, accurate spatial and energy spectra for each background source were required. To obtain these spectra, simulations using LUX-BACCARAT[11] were performed based on the results of the radio-assay campaign of the detector materials. However, uncertainty in these assays and the exact geometry of the components cause discrepancies at higher energies. To improve the accuracy of the light and charge responses from these simulations at these energies, a fit is imposed on the simulations of each source above 80 keV (this fit included single and multiple scatter data); thus giving the effective rate of each of the considered background sources (Figure 5.10). These expected rates were then used within NEST to determine the $S1_c$ and $S2_c$ distributions of the expected ER backgrounds. Finally, all ER backgrounds, except ^{210}Pb were combined into a single PDF to be included in the PLR. The ^{210}Pb chain was included individually with a much higher uncertainty due to the lack of a clear assessment of its relative rate during WS2014-16.

^{83m}Kr

An omission from the combined ER model are events related to the interaction of gammas from the decay of ^{83m}Kr in the LXe[12]. As described in §3.3.2, ^{83m}Kr has a two-component decay with a near minimal separation in time between the two emissions, which themselves are detected as a single S1 and S2. In general, most LXe DM searches do not perform

[11] A Geant4 based code.

[12] LUX injected ^{83m}Kr into the LXe weekly.

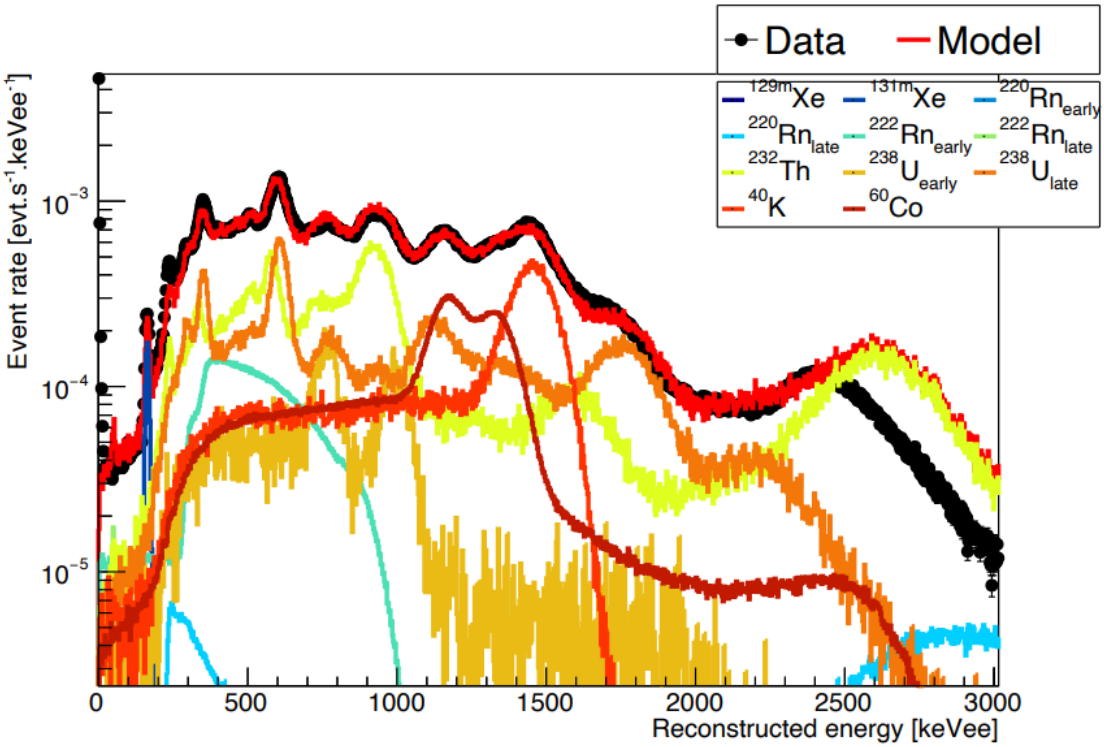

Figure 5.10: LUX WS2014-16 ER background data (black dots), showing the individual fit to each radioisotope (as given in the legend) and the sum of these fits (solid red line). To prevent bias, the fits were performed above the ROI of this analysis (> 50 keV$_{ee}$). The deviation in the data that can be seen at the lowest energies was attributed to the presence of ^{83m}Kr in the calibration data. Variations between the data and the model at the highest energies were attributed to the saturation of the PMTs; which was not accounted for in the model [LUX Collaboration].

analyses at high enough energies for this to become an issue. The whole spectrum can effectively be cut from the data (preventing a reduction in the experiment's total exposure) at the higher energies used in this analysis[13], ^{83m}Kr-like events have the potential to fall within the NR signal region. The mono-energetic ^{83m}Kr decays are observed to have a range of S2/S1 ratios, with some residing just above the NR band. The likelihood of ^{83m}Kr-like events in the NR band further increases with weakening field strengths in the TPC, due to the separation of the NR and ER being a function of these fields. Figure 5.11 shows the energy PDF for the ^{83m}Kr divided into the four drift and four time bins, where it can be seen that the ^{83m}Kr signal region moves closer to the NR band with increasing drift (i.e. the interaction was deeper in the detector, where LUX's drift fields were at their

[13]Other ER backgrounds become less of an issue at increasing recoil energies due to the divergence between the NR and ER band being more significant at higher energies.

weakest). As previously stated, 20.8 live-days were excluded from the WS2014-16 data set to reduce the amount of ^{83m}Kr contamination in the signal region (NR band). Despite this, some ^{83m}Kr-like events remain in the system, motivating the need to implement a data-driven model for this source into the PLR. The excluded ^{83m}Kr data was used to construct the required 5-dimensional model.

Exact numbers of the expected events were determined by calculating the remaining ^{83m}Kr events at the end of each exclusion period and the exact value extrapolated across the data collection period.

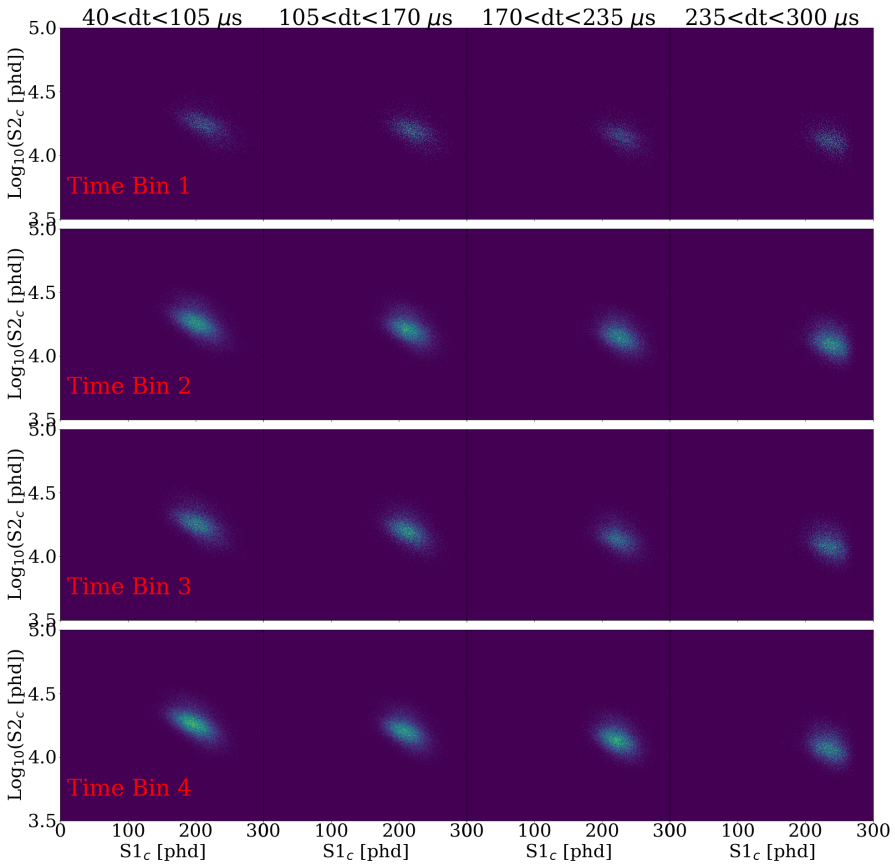

Figure 5.11: ^{83m}Kr energy PDF divided into the time bins (rows) and drift bins (columns). These are data driven models obtained from the WS2014-16 weekly ^{83m}Kr calibrations.

Wall Backgrounds

Wall backgrounds were introduced into the analysis to correctly model events originating from or near the TPC's wall, where the extraction efficiency is reduced[14] when compared to that of events originating from the bulk LXe. Details of a similar methodology have been reported in [140]. The main background of concern from the TPC walls is from ^{206}Pb, which produces a lower S2/S1 ratio than the other ER backgrounds, being low enough to cause events to populate the region under the NR band. Due to the radial field in LUX, the position reconstruction of events originating from the wall directly correlates to the drift field, the azimuth angle, and the acquisition time [210]. The combination of these effects results in the fluctuation of the position reconstruction for events near or at the wall[15]. The wall model carries the most significant uncertainty out of all the ER background sources (due to the reduction in the S2 size for an equivalent energy ER occurring in the bulk LXe). It is possible to minimise the number of wall events by reducing the radius used to define the fiducial volume; however, as the overall sensitivity is directly correlated to the fiducial volume, it is highly advantageous to minimise the reduction of the fiducial radius. Even after redefining the fiducial volume based on the above, a fraction of wall events will still be present in the fiducial volume, thus motivating the necessity of a wall model in the PLR.

The model was constructed by studying the position reconstruction for events occurring outside the defined TPC wall[16]. For each of the unique drift and time periods, the number of events within this radius was counted. Integrating the resultant distribution tail gave an estimate of the expected number of wall events that leak into the fiducial volume. From this, the 5-dimensional model required by the PLR was constructed. Since there is a direct correlation between the position, acquisition time and strength of the drift fields for wall events, this can be considered the only true 5-dimensional background model used in this analysis.

γ-X Events

γ-X events, as just described in the data selection section, are a previously unmodeled background that became more prevalent at higher recoil energies. The time between the scatter in the RFR and the scatter in the fiducial volume is negligible, leading to the

[14] Which results in a degradation of the S2 signal.

[15] These fluctuations are Gaussian with a width of $1/\sqrt{\text{S2}}$ [220].

[16] It is assumed that the number of events within a fixed radius out from the TPC wall is the same as the number with the same radius in from the TPC.

merger of the S1s whilst producing a single S2 signal from the scatter in the fiducial volume. Therefore, the S2 size only accounts for the energy deposition in the fiducial volume and can lead to the S2/S1 ratio of an ER event being shifted into the NR region. With the weakest drift field being at the bottom of the LUX detector, where these events occur, and the discrimination between ER and NR events is at its worst, an increase in the amount of leakage of ER events to the NR bands was expected in the LUX WS2014-16 data set. The most prevalent origins of the gamma-ray component of the γ-X events in LUX were from β and γ ER background sources in the materials that make up the cryostats and bottom PMT array. Additional contributions to γ-X events come from the backscatter of emissions from the cathode grid itself.

As previously mentioned, the likelihood of γ-X contamination in the single scatter data increases as the energy of the ROI is pushed higher. Typically direct detection experiments do not conduct analyses at these high energies, and as such, these events would be excluded by an energy ROI cut. However, due to this analysis's extended ROI, these events need to be considered, and a model included in the PLR. Due to the topology of a γ-X event, it is not easy to disentangle these events from actual single scatter events in the data; this limits the ability of using a purely data-driven model. For this analysis, the γ-X model was based on double scatter events occurring in the fiducial volume near the cathode. An S1 less than 300 phd and two interactions with a vertical separation of 3 cm (the distance between the bottom of the fiducial volume and the cathode grid) were required for these events. Further to this, only double scatter events with an S2 within 4 cm of the cathode and a second S2 in the upper part of the fiducial volume were considered. The size of the S2 from the uppermost scatter was taken as the size as the S2 of the γ-X event. Based on these criteria, 17 near miss double scatter events were identified in the WS2014-16 data. Using a LUX-specific NEST version, a model was generated based on these events' parameters; the interaction sites were transferred 4 cm down to ensure the first scatter occurred in the RFR. The previously mentioned γ-X cut was then applied to the model generated from the shifted double scatter parameters, giving an expectation of 1-10 γ-X events in the complete exposure of this analysis.

Accidental Coincidence

The last category of events that contribute to the backgrounds in this analysis, were events that produced an accidental coincidence between uncorrelated S1-only and S2-only single-scatter events [221]. Again, to incorporate these accidentals in the PLR, a 5-dimensional

model and the expected rates were required. The WS2014-16 data was filtered to obtain a data set consisting of events with a single S1 or a single S2. The rates of these events were then used within a Monte Carlo generator to create random pairings between the S1-only and S2-only signals. Generally, S1-only and S2-only events consist of a few photons and electrons in regions of the detector with poor scintillation and charge yields, which provide the most significant risk of mimicking a single scatter at recoil energies equivalent to the expected peak rate of WIMP-nucleon interactions. Using the S1-only and S2-only event rates, the number of expected accidental coincident events was determined for this extended energy ROI analysis to be less than one throughout the full exposure.

5.2.4 Signal Models

For this PLR analysis, the null hypothesis was represented by the signal PDFs of each operator-δ_m combination. The differential recoil spectra for each operator-δ_m combination was generated out to 210 keV using the modified Mathematica package[17] by Barello et al. [128], as outlined in §2.4.

To allow for ease of comparison to previous limit setting on the inelastic WIMP-nucleon EFT operators by the XENON collaboration [222], this analysis was conducted in the isoscalar basis. In the isoscalar basis, the charge densities of the nucleons are effectively averaged such that the interaction becomes indiscriminate to the type of nucleon involved, even though both the isoscalar and proton-neutron basis provide insight. For this WIMP-nucleon EFT, the UV scale governing the physics is far higher than the energies that are probed in the experiment. At these lower energies, the UV interactions have to be reduced to effective ones, which is done at the u, d and s quark level. The assumption is made that the couplings to each quark at these scales are roughly equivalent. Therefore the mass differences of these quarks are negligible at the high-energy scale of the underlying physics, and the interaction would be isoscalar. By performing this analysis in the isoscalar basis, it is possible to test this assumption's validity. Additionally, by using either an isoscalar or isovector basis, the target's nuclear state can be considered as isospin symmetric; a property of the strong force that can aid in simplifying the analysis.

To further facilitate comparison to the XENON100 results, this inelastic EFT analysis was conducted using the same fixed WIMP mass of 1 TeV/c^2. Five δ_m values were

[17] The signal PDFs used in the elastic WIMP-nucleon EFT analysis were developed in tandem using the same method as outlined here. The unaltered Anand et al. Mathematica package [127] was used to develop the elastic operator differential rates for operator-mass-nucleon combinations in the proton-neutron basis. The same high-level workbook was used to ensure consistency between the signals models in these analyses.

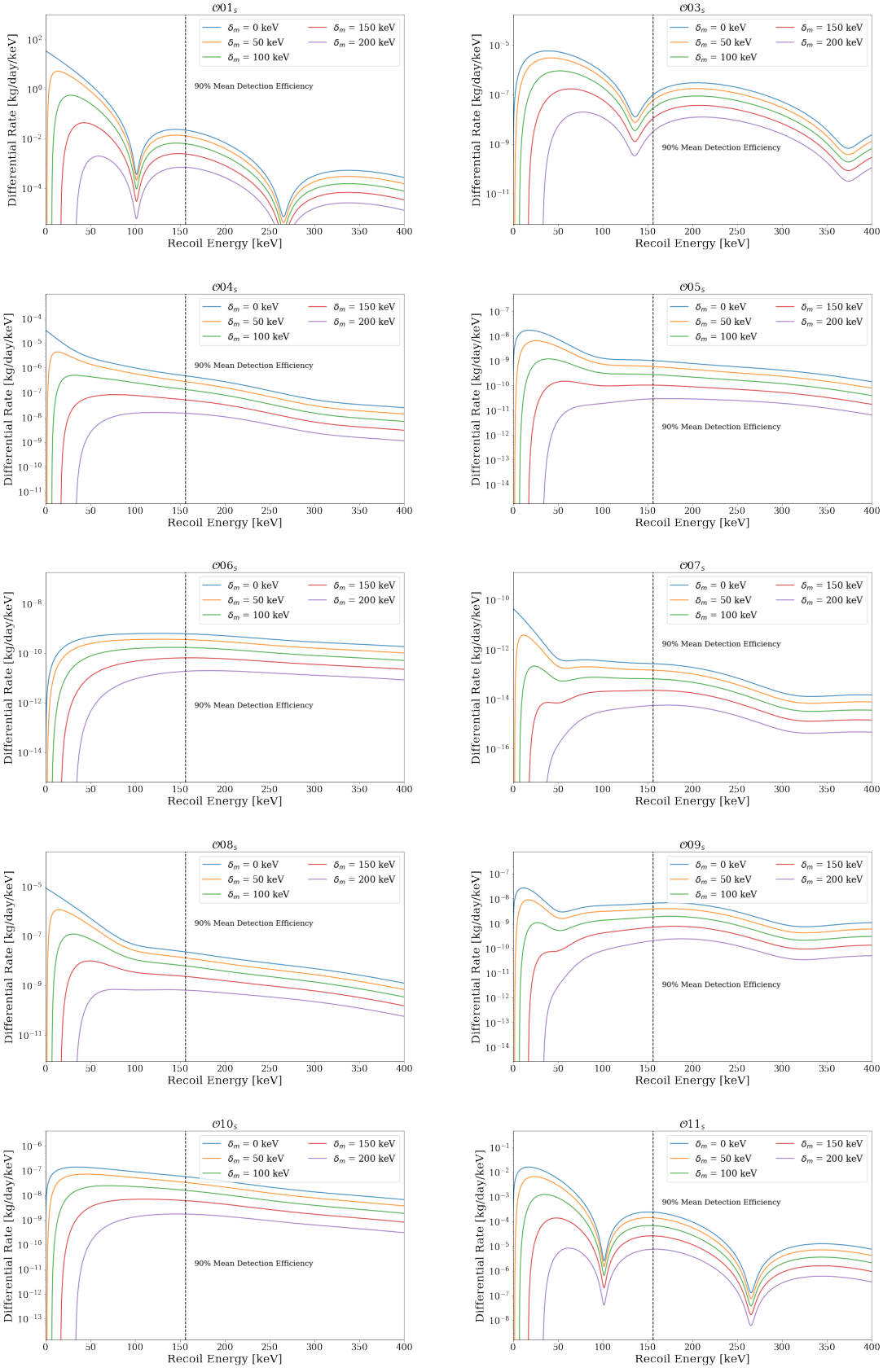
$\mathcal{O}1_S$
$\mathcal{O}3_S$
$\mathcal{O}4_S$
$\mathcal{O}5_S$
$\mathcal{O}6_S$
$\mathcal{O}7_S$
$\mathcal{O}8_S$
$\mathcal{O}9_S$
$\mathcal{O}10_S$
$\mathcal{O}11_S$
δ_m = 0 keV
δ_m = 50 keV
δ_m = 100 keV
δ_m = 150 keV
δ_m = 200 keV
90% Mean Detection Efficiency
Differential Rate [kg/day/keV]
Recoil Energy [keV]

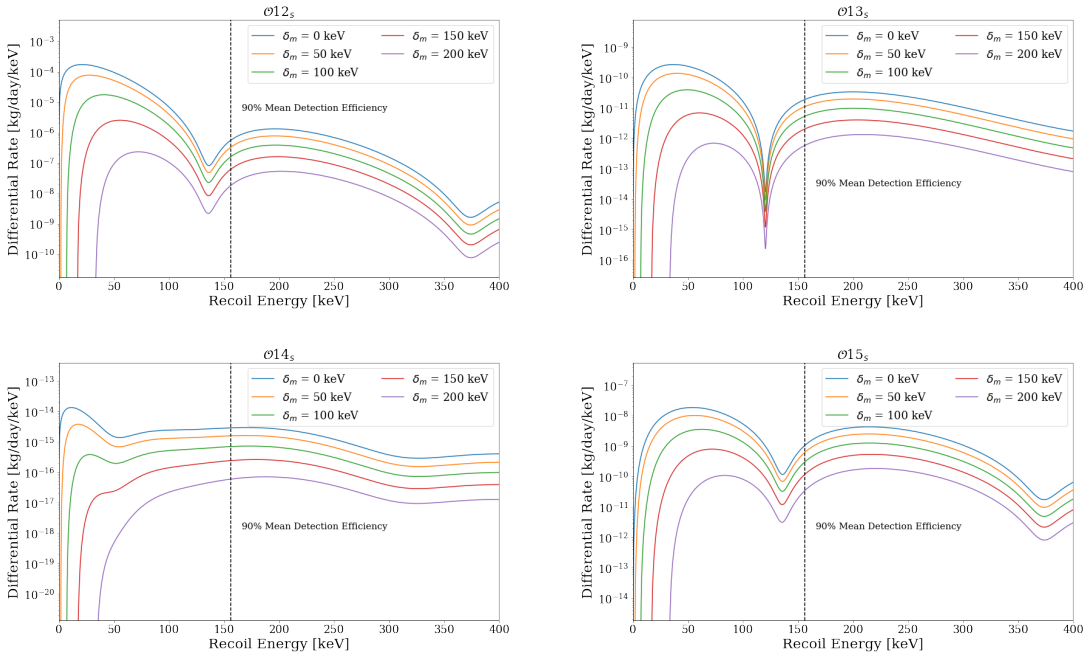

Figure 5.12: Differential recoil spectra for the fourteen non-relativistic EFT WIMP-nucleon operators for a 1 TeV/c^2 WIMP in the isoscalar basis. Each plot shows the recoil spectra for the operator over a range of δ_m values: 0, 50, 100, 150, 200 keV. The spectra were generated with a coupling strength of unity, and excluding the possibility of interference terms. The vertical line shows the energy at which the detection efficiency reduced below 90%.

considered[18] for each of the fourteen operators: 0, 50, 100, 150, 200 keV.

As noted in §2.4.1, the dependency on the target nucleus' spin component varies between the operators. To aid in the realism of the resultant recoil spectra, the natural abundance of Xe isotopes (as given in Table 3.1) was folded into a matrix to be considered as the target nuclei. The SHM (Eq. 2.2) was used to describe the velocity of the DM with: $|V_E|$= 245 km/s, v_0= 220 km/s and v_{esc} = 544 km/s. The local DM density was taken as 0.3 GeV/cm^3. For each operator, the coupling with nucleons was set to 1, and all others to 0; therefore this analysis only assesses the operators as a pure interaction; no mixing or interference between operators was considered. By considering the case of a single operator dominating the interaction, the differential recoil rate scales linearly with

[18] Due to the high dimensionality of the models used in the PLR, the computational time required to analyse a single model to produce a single point on the limit plot was ≈ 15,000 CPU-hrs. The elastic EFT analysis used ≈ 5 million CPU-hrs. To help reduce the additional resource and environmental impact of the inelastic analysis, only five δ_m values were processed for each operator. This resulted in ≈ 1 million CPU-hrs and still gave sufficient coverage of the parameter space.

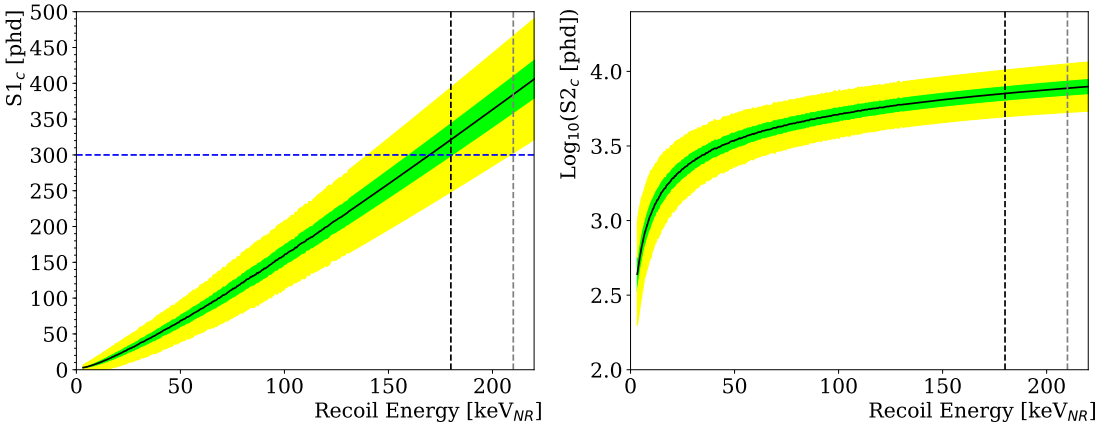

Figure 5.13: Expected S1 (**left**) and S2 (**right**) responses for a given recoil energy in the LUX detector. Values were extrapolated from flat NR spectra simulations using LUXLLAMA. Black solid line shows the expected mean signal response, with the related one and two sigma uncertainties indicated by the green and yellow shaded regions respectively. The blue dashed horizontal line is at 300 phd S1. The black dashed lines on both plots are at 180 keV$_{NR}$ and the grey is at the highest recoil energy able to produce an S1 of 300 phd.

$c_i^{(N)^2}$:

$$\frac{dR}{dE_R} = \frac{c_i^{(N)^2}\rho_0}{32\pi m_\chi^3 m_N^2}\int_{v>v_{min}} \frac{f(\vec{v})}{v} F_{i,i}^{(N,N)}\left(v^2, q^2\right) dv. \tag{5.2.1}$$

This is expressed in units of /kg/day/keV. No scaling to the LUX SI expected rate was conducted[19]. The final recoil spectra of the operator-δ_m combination used in this analysis are shown in Figure 5.12.

Figure 5.13 gives the mapping between the expected S1 and S2 responses to an NR interaction in the LUX detector[20]. To preserve at least 90% of the expected 300 phd S1 signals, this 0 to 180 keV energy window was required. When generating the signal PDFs, it was essential to include the upper limit of recoil energies capable of producing an S1 of 300 phd. Therefore, the generation of the PDFs for the signal models need to include the rate out to $\sim$ 210 keV$_{NR}$. Recoil spectra where the rate had significantly decreased

[19]It is often hard to construe the exact formalism used to develop the differential rates in other experimental WIMP-nucleon EFT analyses. Some experiments opt to scale to the expected SI WIMP-nucleon rate, while others opt not to.

[20]The S1 and S2 responses for recoil energies out to 300 keV$_{NR}$ were determined from simulations using LLAMA. 100000 events were simulated for each increment of 0.2 keV$_{NR}$ in recoil energy and the mean, one sigma and two sigma values were extrapolated.

by 210 keV were cut at a recoil energy that persevered 99.9% of the total expected rate. All other recoil spectra were cut at 210 keV$_{NR}$. For the S2 signals, a max recoil of 210 keV$_{NR}$ gives a 7.5% (540 phd) uncertainty in the size of the S2; however, the NR and ER bands are well separated at these energies. Thus, this would not affect the ability to discriminate NR and ER events based on their S2/S1 ratios.

The exact phd values for S1 and S2 from the Legacy Analysis Monte Carlo Application (LLAMA) do not account for all position dependent corrections; therefore, an additional script was required to conduct this mapping. After correction of the parameters describing the interaction's energy, a cut on the S1$_c$ size equivalent to the maximum recoil energy of the given spectra or at 300 phd (whichever was least) was made for each signal model. For the same $\mathcal{O}15_s$ signal model as shown previously, the generated energy PDF, overlayed on the final WS2014-16 high-NR data after all cuts, is given in Figure 5.14.

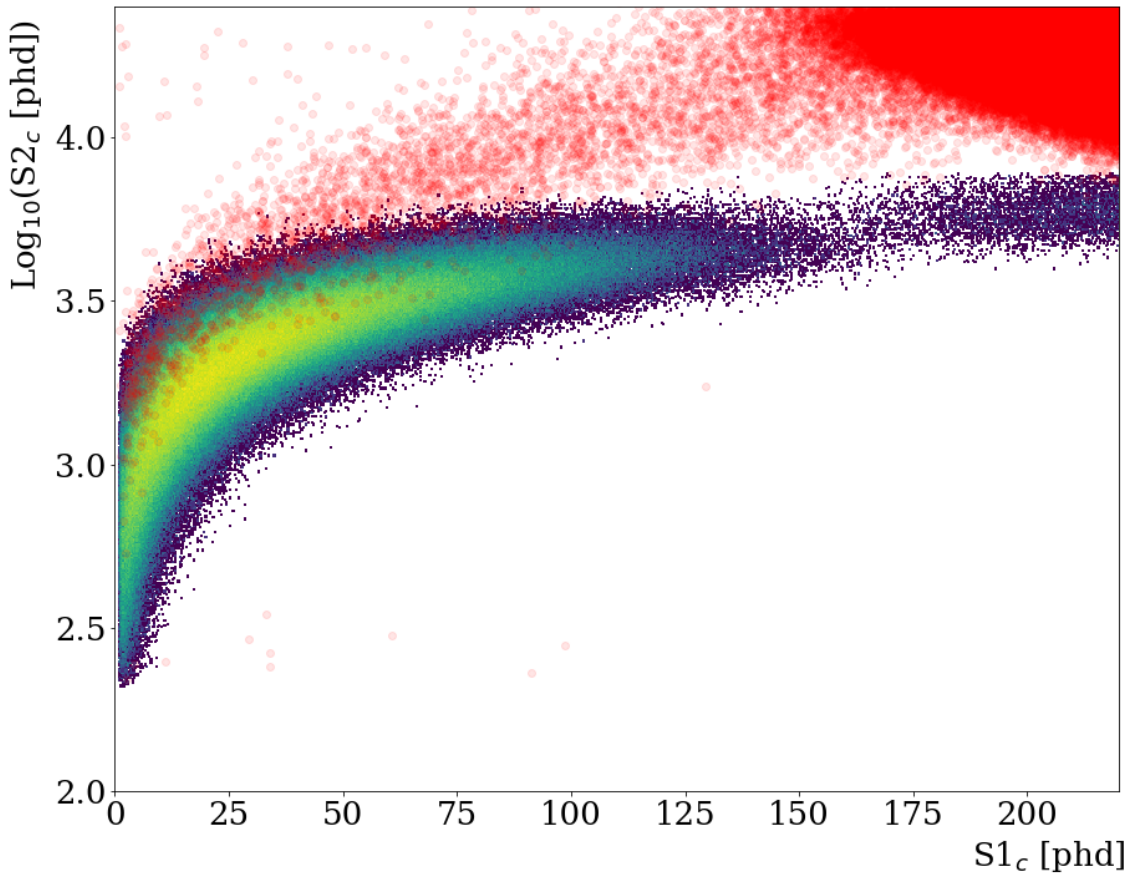

Figure 5.14: Energy (S1$_c$, S2$_c$) components PDF of the signal model. Signal model shown (colour-map) is for a $\mathcal{O}15_s$ elastic WIMP-nucleon interaction for a 1 TeV/c^2 WIMP. The red markers are the events from the final WS2014-16 data after all cuts had been performed.

As is be explained in §5.2.5, the PLR for this analysis is performed on 5-dimensional PDFs of the null and alternative hypotheses. Simulations were performed using LLAMA [207] to determine these five parameters for NR interactions based on the EFT WIMP-nucleon recoil spectra. LLAMA applies the spatial and energy corrections required for the 16 bins in the WS2014-16 data; the NR response itself is taken from NEST whilst considering the mapping of the variations in drift and extraction field strengths of the WS2014-16 data set [210]. Therefore, with LLAMA, it was possible to generate signal models with events homogeneously distributed in the fiducial volume's exact bounds within each of the 16 bins. An example of the resultant spatial PDF in each bin for a $\mathcal{O}15_s$ elastic ($\delta_m = 0$) WIMP-nucleon interaction, for a 1 TeV/c^2 WIMP, is given in Figure 5.15; validating the homogeneity of the signal model in all 16 bins.

For the PLR to be able to make a final determination on the number of detected signal

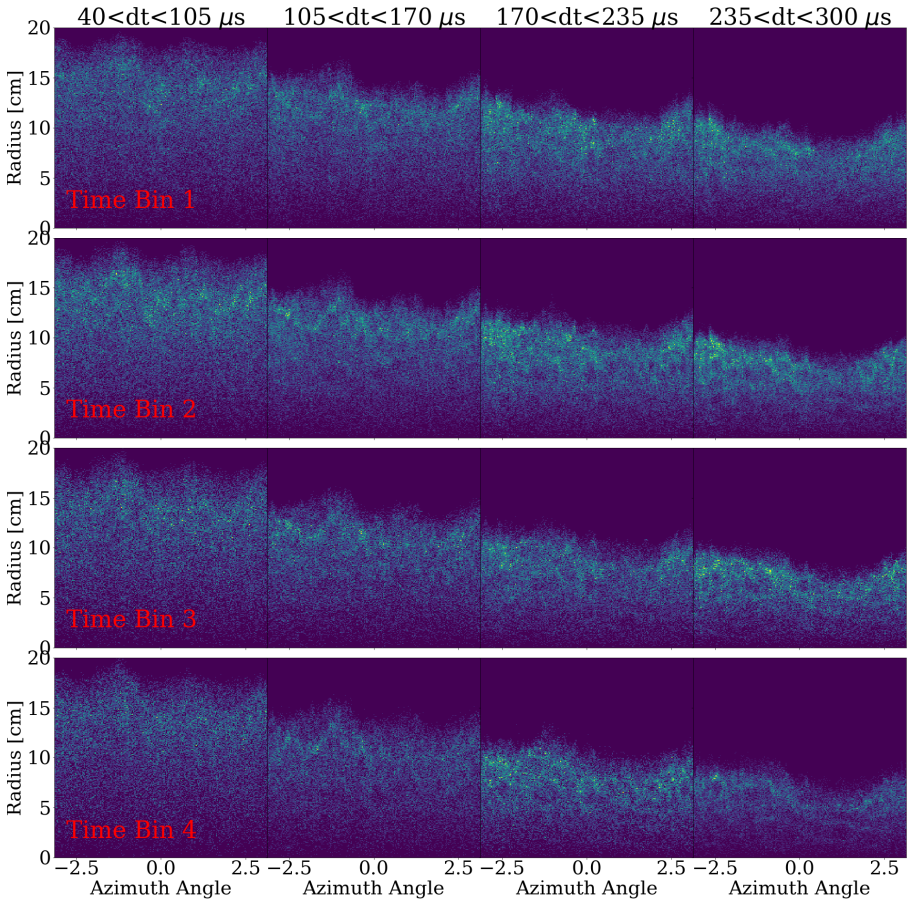

Figure 5.15: Radial and azimuth angle components of the spatial PDF broken up into time bins (rows) and drift bins (columns). Signal model shown is for a $\mathcal{O}15_s$ elastic WIMP-nucleon interaction for a 1 TeV/c^2 WIMP.

events in the WS2014-16 data set, each event required to be weighted by its likelihood to occur. This weight was taken as the efficiency (S1+S2 after all data quality cuts) adjusted rate of the respective recoil spectra complete exposure divided by the total number of events contained in the signal model after all cuts had been applied.

5.2.5 Statistical Method

It is commonplace in direct detection DM searches to use hypothesis testing to exclude a specific model or determine whether a particular observable is significant enough to claim a discovery. In general, a frequentist approach is adopted, in which two hypotheses are compared to see which is most compatible with the observables in the data: the null hypothesis (H_0) and the alternative hypothesis (H_1). By assuming that the null hypothesis is correct, an evaluation can be performed to determine whether the null hypothesis can be rejected. When applying hypothesis testing to make claims of a discovery, the background is the null hypothesis and the combined background and signal is the alternative. The outcome can be either: there is insufficient evidence to exclude the null hypothesis; or rejecting the null hypothesis in favour of the alternative, hence confirming the presence of a signal.

For the WS2014-16 high-NR analysis, a limit setting procedure was selected; more specifically, hypothesis test inversion was conducted to determine a 2-sided frequentist Confidence Interval (CI) via the Neyman Construction [223]. In limit setting, the parameters attributed to the null and alternative hypothesis are swapped. Therefore, the null hypothesis is attributed to the parameters from the signal and background models, while the alternative is now just the background. By doing so, it is possible to determine the upper limit on the Parameter Of Interest (POI), the threshold value which, when exceeded, would class a parameter as being incompatible with the observed data. A series of hypothesis tests are then performed over a range of POI values to find the value at which the null hypothesis can be excluded with some predetermined value of significance.

The POI to which the upper limit was set for this analysis was the expected number of WIMP-nucleon events (μ_0) in the WS2014-16 data. This means the hypotheses to be tested are: $H_0 : \mu = \mu_0$ and $H_1 : \mu \neq \mu_0$. Each signal model was hypothesis tested for a range of POI to determine the p-value was greater than the significance $\alpha = 0.1$ at the 90% CI of the POI. Values of μ that are rejected as they produced a p-value below the test size are found on either side of the not rejected values. This gives a two-sided confidence interval on μ and hence infers a two-sided test statistic. An upper limit is produced by

disfavouring μ if it predicts a signal rate significantly higher than the expected observed rate.

In order to assess the POI, a test statistic needs to be defined. For this analysis, the negative log-likelihood of a PLR was used:

$$q = -2\ln(\lambda), \tag{5.2.2}$$

here λ, the PLR, is constructed from the likelihood profile ($\mathcal{L}_P$) of the profile (P) in the data set ($\vec{X}$) given a set of POI and nuisance parameters (θ):

$$\lambda(\vec{X}) = \frac{\mathcal{L}_P\left((\mu_0, \hat{\hat{\theta}})\middle|\vec{X}\right)}{\mathcal{L}_P\left((\hat{\mu}, \hat{\theta})\middle|\vec{X}\right)}. \tag{5.2.3}$$

Here the terms with hats are allowed to float such that they maximise the profile likelihood. The double hat terms values account for the fact that the exact values which maximise the likelihood of a nuisance parameter when $\mu = \mu_0$ are not necessarily the same value when the POI is allowed to float.

The observables (data, signal and background) of this analysis are formed from 5-dimensional ($\{r, d, \phi, S1_c, \text{ and } S2_c\} \equiv \vec{\mathcal{O}}$) PDFs as described in §5.2.2. As mentioned in §5.2.3, the wall model was the only model out of all signals and backgrounds models that required a true 5-dimensional PDF as the spatial and energy observables were correlated. For all other models, the PDF could be split into the spatial and energy observables as they were considered independent:

$$\begin{aligned}\mathcal{P}_{\text{source},t_i,z_i}\left(\vec{\mathcal{O}}_i\right) \equiv\ & \mathcal{P}_{\text{source},t_i,z_i}\left(r_i, d_i, \phi_i\right) \\ & \cdot\mathcal{P}_{\text{source},t_i,z_i}\left(S1_{c,i}, S2_{c,i}\right),\end{aligned} \tag{5.2.4}$$

where $\mathcal{P}_{\text{source}}, t_i, z_i\left(\vec{\mathcal{O}}_i\right)$ is the PDF of each "source" (i) in a given drift (z) and time bin (t).

From this, an unbinned extended likelihood function was written which considered the number of events in the data set (n_{obs}) and the the number of events expected ($n_{\text{exp}} = n_{\text{sig}} + \sum_{b_i} n_{b_i} + n_{\text{wall}}$) from a background model (b_i):

$$\begin{aligned}\mathcal{L}\left(\left(\mu, \vec{\theta}\right)\middle|\vec{X}\right) = & \text{Pois}\left(n_{\text{obs}}; n_{\text{exp}}\right) \\ & \cdot \prod_{\vec{x}_i \in \vec{X}} \Big[n_{\text{sig}} R_{\text{sig},t_i,z_i} \mathcal{P}_{\text{sig},t_i,z_i}\left(\vec{\mathcal{O}}_i\right) \\ & + \sum_{b_j} n_{b_j} R_{b_j,t_i,z_i} \mathcal{P}_{b_j,t_i,z_i}\left(\vec{\mathcal{O}}_i\right) \\ & + n_{\text{wall}} R_{\text{wall},t_i,z_i} \mathcal{P}_{\text{wall},t_i,z_i}\left(\vec{\mathcal{O}}_i\right)\Big] \cdot \prod_{\theta_i \in \vec{\theta}} \mathcal{P}_i\left(\theta_i\right),\end{aligned} \tag{5.2.5}$$

where each data point ($\vec{x}$) contains the set of observables $\vec{\mathcal{O}}$ in the analysis bin in which it was measured (time bin (t), drift bin (z)). n_{b_i} is the number of expected events from background source b_i, and is taken as the nuisance parameter in this analysis. While the POI was n_{sig}, the expected number of signal events, and as no nuisance parameters associated to the threshold was included, n_{sig} can be considered as a pure function of $c_i^{(N)^2}$; the coefficients associated to each of the EFT operators are used in the generation of their signal models using Eq. (5.2.1). If the detector threshold changes, then the result from the velocity integral changes, which the expected rate depends on, thus placing a dependency on the velocity integral in the relationship between n_{sig} with $c_i^{(N)^2}$. The inclusion of threshold related nuisance parameters would have required recalculating the velocity integral considering the nuisance parameters, which would have been a time-consuming process. As the threshold behaviour of the detector was well-calibrated, it was deemed unnecessary to include such nuisance parameters. Additionally, the uncertainty on the efficiency was not included; this is because, as shown in Figure 5.8, the uncertainties resulting from the extrapolation using NEST to beyond the DD calibration gave an uncertainty on the mean of the NR band in S2 space of $\approx 7.5\%$. This corresponds to a variation in the S2 size by about 540 phd at these higher recoil energies. However, by these energies, the NR and ER bands have sufficiently diverged that this uncertainty would have a negligible impact. For each source, the expected rate in a given analysis bin is given by $R_{\text{source}}, t_i, z_i$ and $\mathcal{P}_i(\theta_i)$ is the PDF of the associated nuisance parameter. All terms with a subscript wall are the equivalent to those with the subscript source, but are applicable to the wall model alone.

It is possible to solve hypothesis testing in an analytical manner. However, the WS2014-16 data did not lie in the asymptotic regime and hence could not be reduced through this approach [224]. The asymptotic formulae are usually considered safe for data analysis with high background and high-signal-rate, such as in collider experiments. However, for a low-background rare event search, it is easy for problems to develop due to the quantised signal. It has already been seen within the direct DM detection community that a χ^2 distribution test statistic distribution is a good approximation for the test statistic distribution; however, it is often the case that the discreetness of the signal coupled with a low background leads to a quantisation of the true test statistic distribution and hence becomes poorly approximated by the asymptotic formulae. For example, the initial results produced by XENON1T utilised the asymptotic formulae [225]; these results were later corrected, citing a significant error contribution from the asymptotic approach producing

an almost two-fold worsening of the SI limit [88]. This meant the alternative of computing the test statistic against a collection of Monte-Carlo simulated pseudo-experiments based on the models had to be used. For each signal model a custom built PLR[21] pre-calculated a set of these pseudo-experiments based on the 5-dimensional PDFs. Hypothesis testing was then performed on these psuedo-experiments, the p-values of which are then plotted against the POI, allowing for linear interpolations to find the POI at which the p-value intercepted the significance of 0.1, giving the number of observed signal-like events.

PDF smoothing was conducted on the energy PDFs using the built-in *setInterpolationOrder(1)* function in Roostats [227]; this function can only be used on 1- and 2-D PDFs. For the spatial PDFs, a high-stats bootstrapping of events was performed to fill in any holes in the distribution. The bootstrapping process took the reconstructed 3D positions of the events and fed them back into NEST. This process was repeated for each model contributing to the ER model until all time and drift bin combinations contained approximately 3 million events, increasing the statistics by up to 500 times (dependent on the model/bin). Following this, the positions were smeared within a 3D Gaussian volume with a sigma of 1 cm in each direction to help fill in holes; this volume was arbitrary but deemed to be small enough to be physical whilst still large enough to be useful.

5.3 LUX WS2014-16 Inelastic Dark Matter Limits

Presented here are the limits on the 90% CI two-sided frequentist of $c_i^{(N)^2}$. Limits were obtained using the method discussed in §5.2.5 to determine the ratio of observed to expected signal events. The resultant limit on $c_i^{(N)^2}$ was calculated from the ratio of observed to expected signal events for a given model. Signal models were considered for all EFT operators (Eq. 2.4.8) in the isoscalar basis for a WIMP mass of 1 TeV/c^2 and δ_m values of 0, 50, 100, 150 and 200 keV. For each signal model, the maximum bound of the energy ROI was set to include >90% of the expected rate. The initial constraints and final fit values (obtained using a background-only hypothesis) of the nuisance parameters used in this analysis are given in Table 5.2.

As signal models were developed using the Anand et al. Mathematica package, the couplings used in this analysis ($c_i^{(N)}$) have dimensionality of mass^{-2}. This dimensionality results from Anand et al.'s decision to normalise the spinors and use a dimensionless representation of the operators in the code.

[21] Developed by Dr S. Alsum for the LUX Collaboration using RooFit [226].

Parameter	Constraint	Fit Value
Standard ER	1498.0±187.5	1495.1±51.2
Wall-based Backgrounds	11.3±2.8	12.8±2.2
$\gamma - X$	3.4±2.5	5.2±2.0
^{83m}Kr	5.2±1.5	4.8±1.3
Accidental Coincidence	$0.41^{+0.43}_{-0.41}$	0.51±0.39

Table 5.2: The nuisance parameters of the LUX WS2014-16 high-NR PLR [204].

Additionally, the Mathematica package scales the couplings by m_w^{-2} (m_w being the Higg's vacuum expectation value of 246.2 GeV/c^2). Therefore, the limits produced in this analysis are given without any dimensionality if a factor of m_w^2 scales them, meaning the resultant limits are set in $(c_i^N \cdot m_w^2)^2$. By presenting results in terms of $c_i^{(N)^2}$, only absolute values of the coupling constant can be retrieved. As this was also the dimensionality for the limits on the inelastic isoscalar EFT operators reported by XENON100 [222], a direct comparison between the results can be performed. This also motivated the choice of the 1 TeV/c^2 WIMP mass used in this analysis. Figure 5.16 shows the limits on $(c_i^N \cdot m_w^2)^2$ from this analysis as a function of the mass splitting (δ_m) for the fourteen non-relativistic EFT operators; for a 1 TeV/c^2 WIMP.

The upper limits for all operators bar $\mathcal{O}_{13}$ and $\mathcal{O}_{15}$ lay within 2σ of the expectation. When comparing these upper limits to those set by XENON100, at least a 2-fol improvement in the lower limit should be expected due to the differences in the exposures used in the two analyses. However, this is not the case. The majority of the limits produced in this analysis have an upper limit comparable to that of XENON100. An improvement to the limit in certain regions of the parameter space is seen for $\mathcal{O}_5$, $\mathcal{O}_7$, $\mathcal{O}_8$ and $\mathcal{O}_{11}$. Conversely $\mathcal{O}_3$, $\mathcal{O}_{13}$, $\mathcal{O}_{14}$ and $\mathcal{O}_{15}$ produced upper limits significantly worse than those by XENON100.

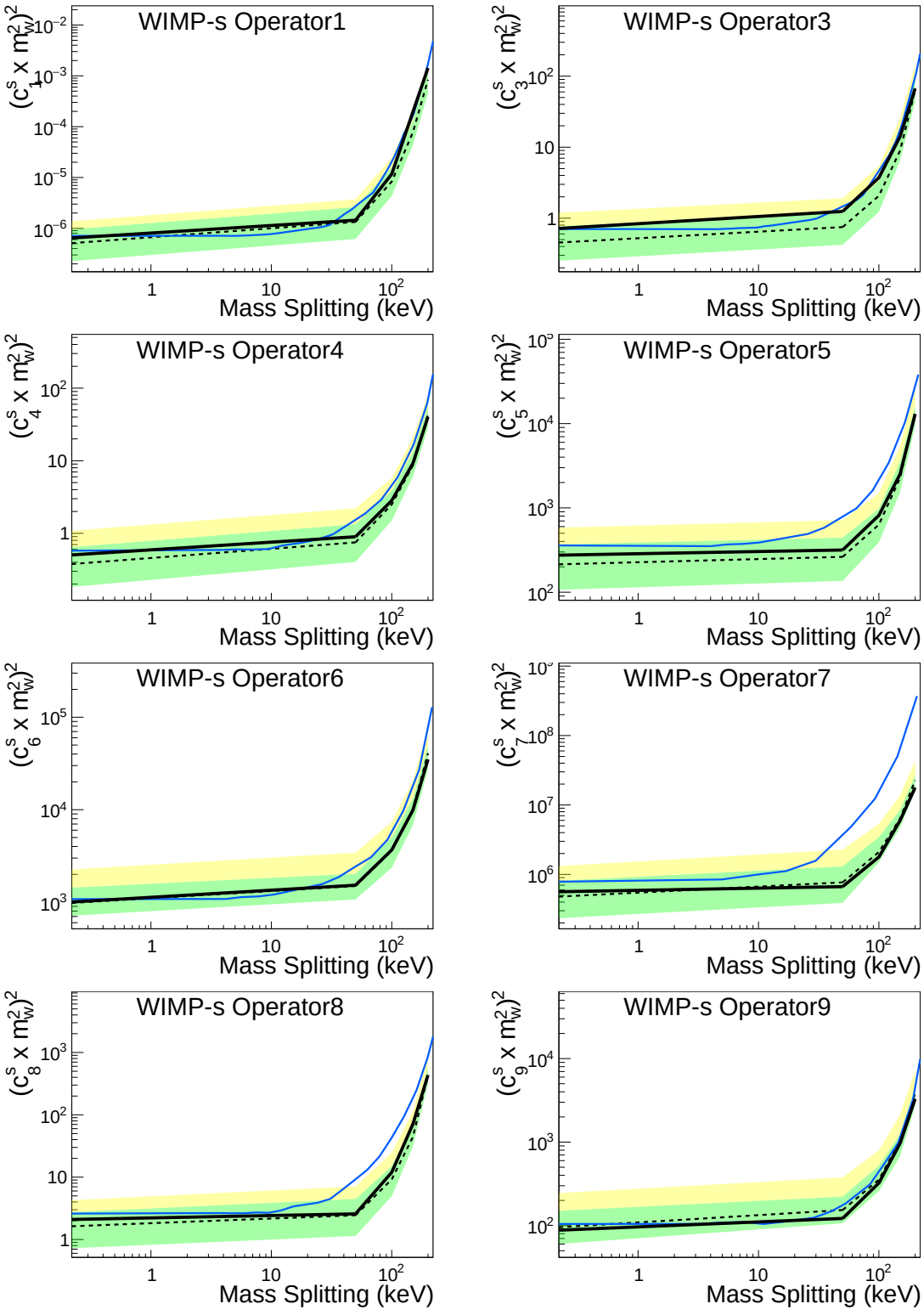

Figure 5.16: The LUX WS2014–16 90% CI sensitivity limits for isoscalar WIMP-nucleon dimensionless couplings for the non-relativistic EFT operators $\mathcal{O}_1$, $\mathcal{O}_3$ - $\mathcal{O}_9$ and a fixed WIMP mass of 1 TeV. Solid black lines show the limit produced by this analysis, while dashed black lines indicate the expectation, with green and yellow bands indicating the 1σ and 2σ sensitivity expectations, respectively. Previous limits from XENON100 [222] are shown with blue lines. Each plot uses δ_m values of 0, 50, 100, 150, and 200 keV [204].

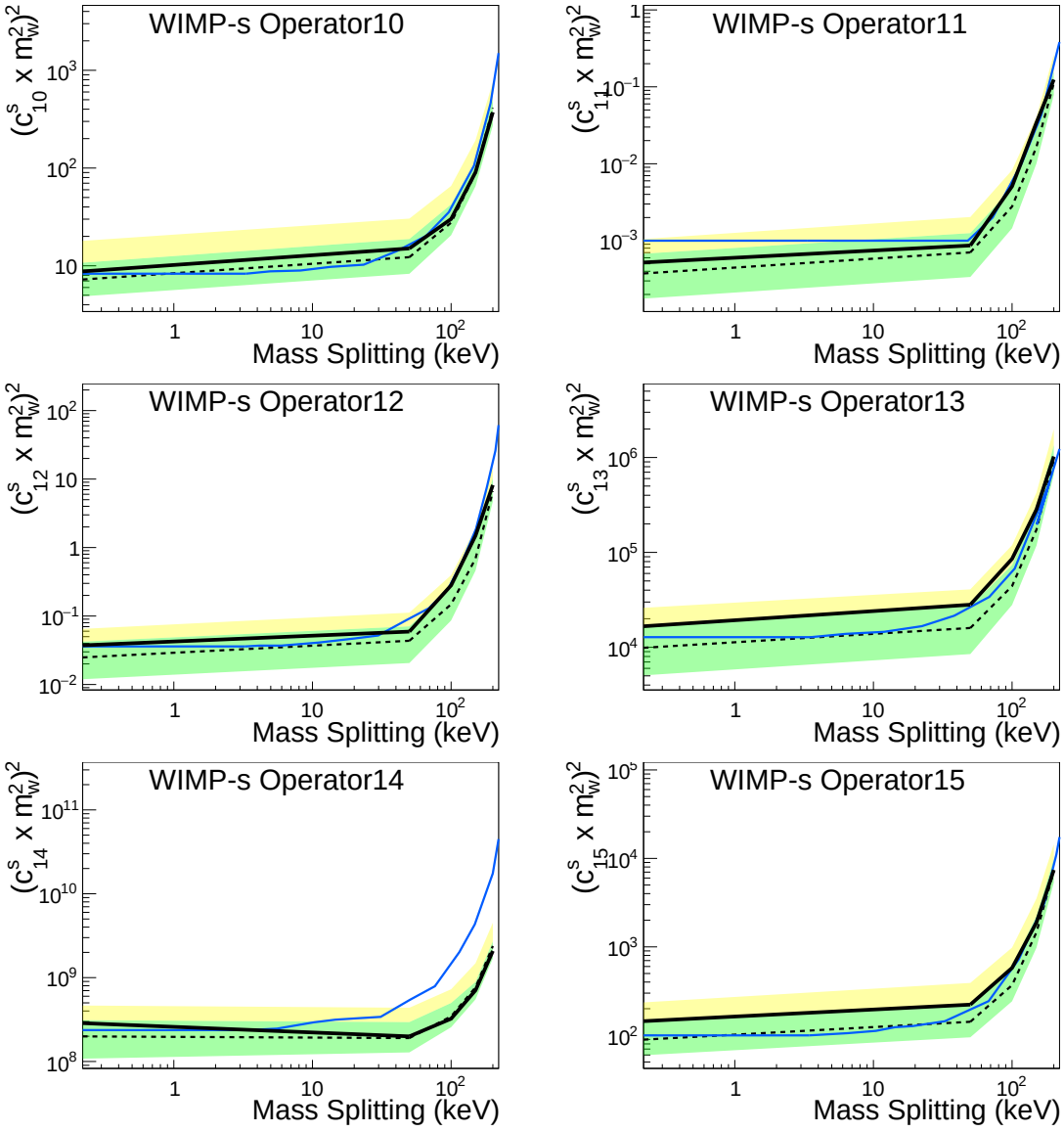

Figure 5.17: The LUX WS2014–16 90% CI sensitivity limits for isoscalar WIMP-nucleon dimensionless couplings for the non-relativistic EFT operators $\mathcal{O}_{10}$ - $\mathcal{O}_{15}$ and a fixed WIMP mass of 1 TeV. Solid black lines show the limit produced by this analysis, while dashed black lines indicate the expectation, with green and yellow bands indicating the 1σ and 2σ sensitivity expectations, respectively. Previous limits from XENON100 [222] are shown with blue lines. Each plot uses δ_m values of 0, 50, 100, 150, and 200 keV [204].

It was found that in some areas of the energy phase space, the signal models could overlap with the background models, which also happened to be populated with data. Figure 5.18 shows the final WS2014-16 data used in this analysis, showing the likelihood from the PLR of each event to be described by a particular model using the signal model for O15s with a WIMP mass of 1 TeV/c^2 and δ_m of 0 keV. Looking closely at Figure 5.18 it appears that some events produced a significant likelihood of being from the signal model, but still have a higher likelihood of being from one of the backgrounds. Studies performed by the LUX collaboration indicate that these are background events which have leaked into the NR region.

When the signal model overlaps a background model in regions where there is also data, the PLR will predict an increased number of observed events, which directly worsens the resultant limit. This increase in the number of observed events explains why many of the operators' upper limits are significantly higher than their expected limit. The most likely origins of the data in the region of phase space in which the models overlap are: low-energy accidental-like events, $\gamma - X$-like events, and ^{83m}Kr. These were included within the background models, but uncertainties on each of these backgrounds' exact rates can lead to fluctuations that produce an agreement with signal events. This effect was problematic for all signal models in the inelastic analysis. The decision to use a 1 TeV/c^2 WIMP mass means all signals will have a significant rate across the entire energy ROI and are highly likely to contain events that overlap with the background. Looking at the recoil spectra (Figure 5.12) of $\mathcal{O}_3$, $\mathcal{O}_{13}$, $\mathcal{O}_{14}$ and $\mathcal{O}_{15}$, it makes sense why these operators produced the largest deviation from the expected limit. These operators have the lowest expected rate for all values of δ_m used in this analysis and are therefore more sensitive to variations in the number of observed events.

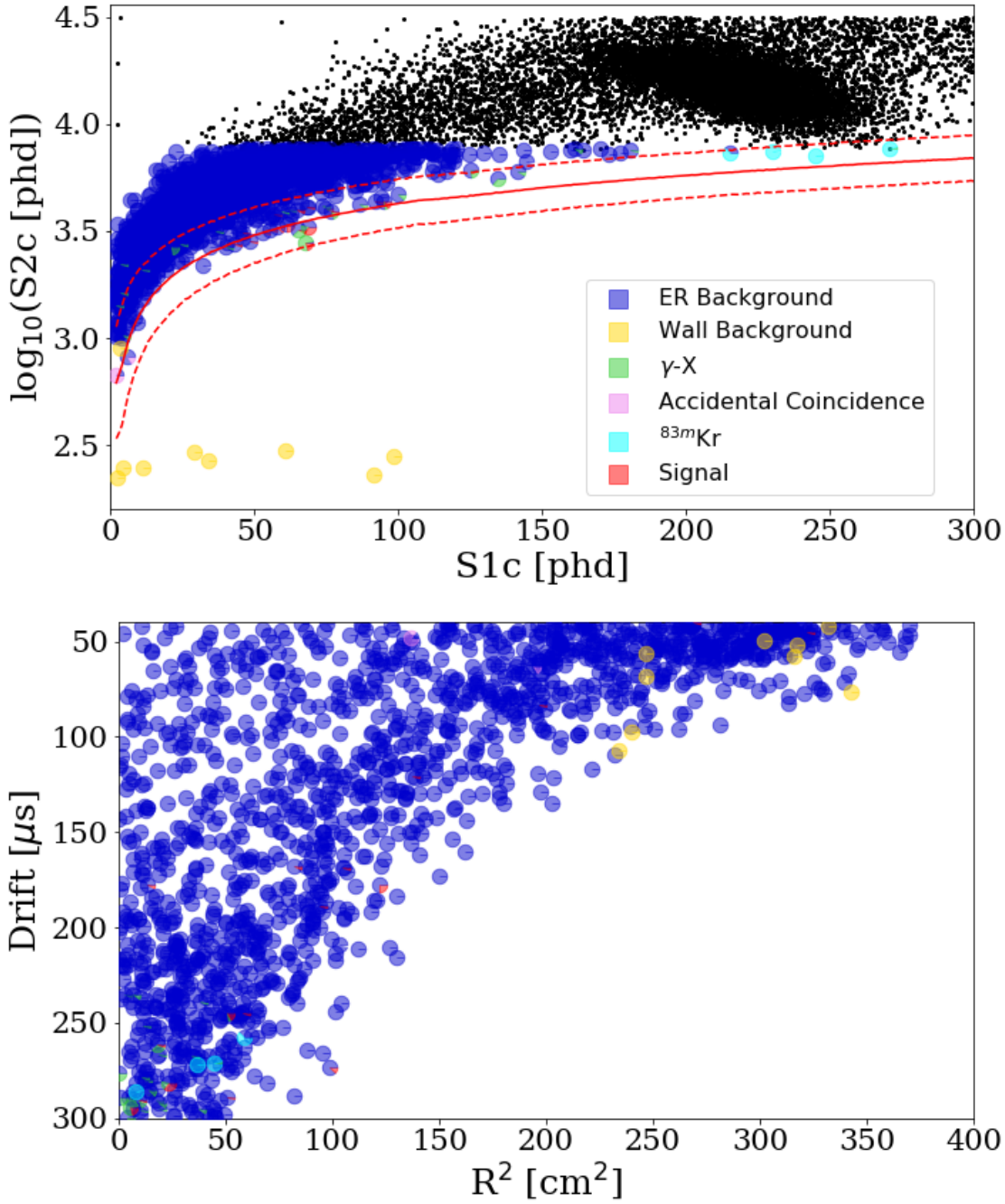

Figure 5.18: The unsalted WS2014–16 data. Given in black are the events which fell outside of the ROI of this analysis. The colours of the events within the ROI indicate the likelihood for that event to fall within a given model. The markers with multiple colours infer an overlap between the background models and the data at that region of parameter space. The mean and 90% CI of the expected NR response is given by the red solid and dashed lines, respectively. The **top** panel shows the distribution of events in terms of the energy parameters, and the **bottom** shows the distribution of events in terms of their radii as observed by the top PMTs and the drift time.

Summary

This chapter covered the WS2014-16 High-NR inelastic EFT limit-setting procedure. Starting with a description of the LUX detector, followed by an overview of the High-NR EFT analysis, where the temporal and spatially varying drift field issues were discussed. The relevant calibrations conducted for this analysis, both NR and ER, were covered. The data quality cuts, efficiencies and methodologies for preventing bias that allowed for the construction of the final WS2014-16 data set were discussed. This chapter then went on to describe the approach for modelling the relevant backgrounds and the signal models for each of the EFT operators, as described in §2.4, and the construction of the required PDFs for each. Following this, the statistical method was used to assess these PDFs to produce the final limits for each operator-delta combination. The final section of this chapter contained the limits for each of the 14 considered operators in the inelastic interaction model. These results were shown to be highly competitive with those produced by XENON100, and in some regions of parameter space for certain operators, world-leading limits were set.

Conclusion

Despite almost 100 years of cosmological and astronomical evidence indicating DM's presence in the Universe, the detection of an interaction involving a DM particle continues to elude generations of searches.

The LZ collaboration are in the final stages of commissioning their ultra-low background LXe TPC. To achieve the detector's greatest possible sensitivity to DM interactions, LXe-Skin and OD veto systems have been implemented. Both of which require comprehensive calibration of their energy and time responses. As indicated, the two systems presented in this thesis, the CSD and the OCS, are critical in characterising the PMTs in the LXe-Skin and OD, which are vital in the correct identification of neutron and gamma single-scatter events in the TPC.

The CSD will be pivotal to the calibration of the energy response of the PMTs in the TPC, LXe-Skin and OD, the cross timing calibration of the three detection layers, and determining the exact position of the liquid-gas phase barrier in the TPC. Additionally, the CSD will deploy neutron sources that will allow for the characterisation of their response in the OD PMTs, which is essential to correctly identify neutron events that produce a single scatter in the TPC. The tests outlined in this document show that the three CSD units meet the requirements to accurately place a source with a precision of several mm and maintain this position using a laser feedback system, which is vital to most of the calibration tasks that will be conducted using the CSD. The CSD has now been installed at SURF and is currently undergoing its final commissioning checks. Initial checks show all three are functioning correctly and are ready for deployment of sources for calibration purposes.

The OCS has successfully demonstrated the ability to inject a known number of photons across the equivalent energies of background sources from 700 to 50000 photons per pulse per channel with a high degree of precision. Implementing a self-monitoring system ensures exact knowledge of the number of photons per pulse injected through the implementation of the photodiode board and the monitoring PMT. The OCS will have 30

injection points situated between the arrays of OD PMTs; these will be used to characterise and monitor their performance throughout the LZ detector's operation. Additionally, five injection points situated under the acrylic tanks will be used to inject light to monitor the degradation of both the GdLS and the acrylic tanks housing it.

Direct detection searches for the favoured DM candidate, the WIMP, are on the precipice of reaching SI and SD cross-sections where the irreducible neutrino background will become problematic. For this reason, it has become necessary to start exploring models with a more complex interpretation of the interaction between DM and SM particles. It is even more interesting to set bounds on the underlying model-independent DM-nucleon EFT, which characterise all possible mechanisms by which DM can interact with the SM.

The final chapter of this thesis presented the LUX WS2014-16 high-NR analysis based on the EFT derived by Fitzpatrick et al. and modified for inelastic kinematics by Barello et al. Within this analysis, the energy ROI was extended far beyond that of a typical direct detection SI or SD analysis, necessitating a recharacterisation of the data and backgrounds at these energies. Most notable is the inclusion of background models for multiple-scatter $\gamma - X$ events (which can produce a single-scatter like event in the TPC), and ^{83m}Kr decays (as there is a high likelihood for these events to have leaked from the ER region to the NR region due to the issues with the fields in the WS2014-16 data). NEST was used to model the ER and NR responses independently for 16 time and drift bins and extrapolate the NR response to energies beyond LUX's calibration points.

Reported were the inelastic EFT WIMP-nucleon scattering results for isoscalar interactions with a 1 TeV/c^2 WIMP. These inelastic limits were comparable to those produced by XENON100. In some regions of the explored parameter space for individual operators a more sensitive limit was obtained, despite the resultant limit for many of the operators being poorer than the expectation. The weakening of the limits was attributed to the observed overlap of the signal model with a background event in the final data, which was more problematic for signals with a higher energy range (i.e. higher mass). As this inelastic analysis opted to use a WIMP mass of 1 TeV/c^2, all signal models were susceptible to this potential overlap. Even though a lower mass may retrieve more stringent limits, it would have been harder to perform a comparison with the previously produced limits. This analysis adds to the experimental data already available concerning WIMP-nucleon EFT. Hopefully, this analysis will aid in setting bounds within the low energy theory, which could then be used in the development of higher energy-scale theories.

Bibliography

[1] W. Thomson, Baron Kelvin, LECTURE I, Cambridge Library Collection - Physical Sciences, Cambridge University Press, 2010, p. 5–21. doi:10.1017/CBO9780511694523.005.

[2] H. Poincaré, The milky way and the theory of gases, Popular Astronomy 14 (1906) 475–488.
URL http://articles.adsabs.harvard.edu/pdf/1906PA.....14..475P

[3] E. J. Öpik, Bull. de la Soc. Astr. de Russie 21 (1906) 150.

[4] J. H. Oort, The force exerted by the stellar system in the direction perpendicular to the galactic plane and some related problems, Bulletin of the Astronomical Institutes of the Netherlands 6 (1932) 249.
URL https://ui.adsabs.harvard.edu/abs/1932BAN.....6..249O

[5] T. S. V. Albada, R. Sancisi, M. Petrou, R. J. Tayler, Dark matter in spiral galaxies [and discussion], Philosophical Transactions of the Royal Society of London. Series A, Mathematical and Physical Sciences 320 (1556) (1986) 447–464.
URL http://www.jstor.org/stable/37810

[6] D. Clowe, M. Bradač, A. H. Gonzalez, M. Markevitch, S. W. Randall, C. Jones, D. Zaritsky, A direct empirical proof of the existence of dark matter, The Astrophysical Journal 648 (2) (2006) L109–L113. doi:10.1086/508162.
URL http://dx.doi.org/10.1086/508162

[7] R. J. Cooke, M. Pettini, C. C. Steidel, One percent determination of the primordial deuterium abundance, The Astrophysical Journal 855 (2) (2018) 102. doi:10.3847/1538-4357/aaab53.
URL http://dx.doi.org/10.3847/1538-4357/aaab53

[8] P. Collaboration, Planck 2018 results. vi. cosmological parameters (2020). arXiv:1807.06209.

[9] M. Ackermann, A. Albert, B. Anderson, W. Atwood, L. Baldini, G. Barbiellini, D. Bastieri, K. Bechtol, R. Bellazzini, E. Bissaldi, et al., Searching for dark matter annihilation from milky way dwarf spheroidal galaxies with six years of fermi large area telescope data, Physical Review Letters 115 (23) (Nov 2015). doi:10.1103/physrevlett.115.231301.
URL http://dx.doi.org/10.1103/PhysRevLett.115.231301

[10] G. Giesen, M. Boudaud, Y. Génolini, V. Poulin, M. Cirelli, P. Salati, P. D. Serpico, Ams-02 antiprotons, at last! secondary astrophysical component and immediate implications for dark matter, Journal of Cosmology and Astroparticle Physics 2015 (09) (2015) 023–023. doi:10.1088/1475-7516/2015/09/023.
URL http://dx.doi.org/10.1088/1475-7516/2015/09/023

[11] A. Klypin, H. Zhao, R. S. Somerville, CDM-based models for the milky way and m31. i. dynamical models, The Astrophysical Journal 573 (2) (2002) 597–613. doi:10.1086/340656.
URL https://doi.org/10.1086/340656

[12] F. Zwicky, Die Rotverschiebung von extragalaktischen Nebeln, Helvetica Physica Acta 6 (1933) 110–127.
URL https://ui.adsabs.harvard.edu/abs/1933AcHPh...6..110Z

[13] V. C. Rubin, J. Ford, W. Kent, Rotation of the Andromeda Nebula from a Spectroscopic Survey of Emission Regions, ApJ159 (1970) 379. doi:10.1086/150317.

[14] V. C. Rubin, J. Ford, W. K., N. Thonnard, Extended rotation curves of high-luminosity spiral galaxies. IV. Systematic dynamical properties, Sa − > Sc., ApJL225 (1978) L107–L111. doi:10.1086/182804.
URL https://ui.adsabs.harvard.edu/abs/1978ApJ...225L.107R

[15] E. F. Eiroa, C. M. Sendra, Gravitational lensing by a regular black hole 28 (8) (2011) 085008. doi:10.1088/0264-9381/28/8/085008.
URL https://doi.org/10.1088/0264-9381/28/8/085008

[16] M. Markevitch, Chandra observation of the most interesting cluster in the universe, arXiv preprint astro-ph/0511345 (2005).

[17] R. B. Partridge, A measurement of excess antenna temperature at 4080 Mc/s, Cambridge Astrophysics, Cambridge University Press, 1995, p. 355–356. doi:10.1017/CBO9780511525070.010.

[18] D. J. Fixsen, E. S. Cheng, J. M. Gales, J. C. Mather, R. A. Shafer, E. L. Wright, The cosmic microwave background spectrum from the fullcobefiras data set, The Astrophysical Journal 473 (2) (1996) 576–587. doi:10.1086/178173.
URL http://dx.doi.org/10.1086/178173

[19] A. Boesgaard, G. Steigman, Big bang nucleosynthesis: Theories and observations, Annual Review of Astronomy and Astrophysics 23 (2003) 319–378. doi:10.1146/annurev.aa.23.090185.001535.

[20] C. L. Bennett, et al., NINE-YEAR WILKINSON MICROWAVE ANISOTROPY PROBE (WMAP) OBSERVATIONS: FINAL MAPS AND RESULTS, The Astrophysical Journal Supplement Series 208 (2) (2013) 20. doi:10.1088/0067-0049/208/2/20.
URL https://doi.org/10.1088/0067-0049/208/2/20

[21] N. Aghanim, et al., Planck 2018 results. I. Overview and the cosmological legacy of Planck, Astron. Astrophys. 641 (2020) A1. arXiv:1807.06205, doi:10.1051/0004-6361/201833880.

[22] R. K. Sachs, A. M. Wolfe, Perturbations of a Cosmological Model and Angular Variations of the Microwave Background, The Astrophysical Journal 147 (1967) 73. doi:10.1086/148982.
URL https://ui.adsabs.harvard.edu/abs/1967ApJ...147...73S

[23] E. Di Valentino, A. Melchiorri, J. Silk, Planck evidence for a closed universe and a possible crisis for cosmology, Nature Astronomy 4 (2) (2019) 196–203. doi:10.1038/s41550-019-0906-9.
URL http://dx.doi.org/10.1038/s41550-019-0906-9

[24] P. Ruiz-Lapuente, Dark energy: observational and theoretical approaches, Cambridge University Press, 2010.

[25] D. H. Weinberg, M. J. Mortonson, D. J. Eisenstein, C. Hirata, A. G. Riess, E. Rozo, Observational probes of cosmic acceleration, Physics Reports 530 (2) (2013) 87–255.

doi:10.1016/j.physrep.2013.05.001.
URL http://dx.doi.org/10.1016/j.physrep.2013.05.001

[26] R. H. Cyburt, B. D. Fields, K. A. Olive, T.-H. Yeh, Big bang nucleosynthesis: Present status, Reviews of Modern Physics 88 (1) (2016) 015004. arXiv:1505.01076, doi:10.1103/RevModPhys.88.015004.
URL https://ui.adsabs.harvard.edu/abs/2016RvMP...88a5004C

[27] B. D. Fields, K. A. Olive, T.-H. Yeh, C. Young, Big-bang nucleosynthesis after planck, Journal of Cosmology and Astroparticle Physics 2020 (03) (2020) 010–010. doi:10.1088/1475-7516/2020/03/010.
URL http://dx.doi.org/10.1088/1475-7516/2020/03/010

[28] S. W. Randall, M. Markevitch, D. Clowe, A. H. Gonzalez, M. Bradač, Constraints on the self-interaction cross section of dark matter from numerical simulations of the merging galaxy cluster 1e 065756, The Astrophysical Journal 679 (2) (2008) 1173–1180. doi:10.1086/587859.
URL http://dx.doi.org/10.1086/587859

[29] C. Kouvaris, Composite millicharged dark matter, Physical Review D 88 (1) (Jul 2013). doi:10.1103/physrevd.88.015001.
URL http://dx.doi.org/10.1103/PhysRevD.88.015001

[30] E. D. Nobile, M. Nardecchia, P. Panci, Millicharge or decay: a critical take on minimal dark matter, Journal of Cosmology and Astroparticle Physics 2016 (04) (2016) 048–048. doi:10.1088/1475-7516/2016/04/048.
URL http://dx.doi.org/10.1088/1475-7516/2016/04/048

[31] H. Baer, K.-Y. Choi, J. E. Kim, L. Roszkowski, Dark matter production in the early universe: Beyond the thermal wimp paradigm, Physics Reports 555 (2015) 1–60. doi:10.1016/j.physrep.2014.10.002.
URL http://dx.doi.org/10.1016/j.physrep.2014.10.002

[32] A. Del Popolo, M. Le Delliou, Small scale problems of the cdm model: A short review, Galaxies 5 (1) (2017) 17. doi:10.3390/galaxies5010017.
URL http://dx.doi.org/10.3390/galaxies5010017

[33] A. Klypin, A. V. Kravtsov, O. Valenzuela, F. Prada, Where are the missing galactic satellites?, The Astrophysical Journal 522 (1) (1999) 82–92. doi:10.1086/307643.
URL http://dx.doi.org/10.1086/307643

[34] M. R. Lovell, V. Eke, C. S. Frenk, L. Gao, A. Jenkins, T. Theuns, J. Wang, S. D. M. White, A. Boyarsky, O. Ruchayskiy, The haloes of bright satellite galaxies in a warm dark matter universe, Monthly Notices of the Royal Astronomical Society 420 (3) (2012) 2318–2324. doi:10.1111/j.1365-2966.2011.20200.x.
URL http://dx.doi.org/10.1111/j.1365-2966.2011.20200.x

[35] M. Milgrom, A modification of the Newtonian dynamics as a possible alternative to the hidden mass hypothesis., ApJ270 (1983) 365–370. doi:10.1086/161130.
URL https://ui.adsabs.harvard.edu/abs/1983ApJ...270..365M

[36] G. W. Angus, B. Famaey, D. A. Buote, X-ray group and cluster mass profiles in MOND: unexplained mass on the group scale, Monthly Notices of the Royal Astronomical Society 387 (4) (2008) 1470–1480. doi:10.1111/j.1365-2966.2008.13353.x.
URL https://doi.org/10.1111/j.1365-2966.2008.13353.x

[37] P. Tisserand, L. Le Guillou, C. Afonso, J. N. Albert, J. Andersen, R. Ansari, Aubourg, P. Bareyre, J. P. Beaulieu, X. Charlot, et al., Limits on the macho content of the galactic halo from the eros-2 survey of the magellanic clouds, Astronomy Astrophysics 469 (2) (2007) 387–404. doi:10.1051/0004-6361:20066017.
URL http://dx.doi.org/10.1051/0004-6361:20066017

[38] B. J. Carr, S. W. Hawking, Black Holes in the Early Universe, Monthly Notices of the Royal Astronomical Society 168 (2) (1974) 399–415. doi:10.1093/mnras/168.2.399.
URL https://doi.org/10.1093/mnras/168.2.399

[39] B. Carr, F. Kühnel, Primordial black holes as dark matter: Recent developments, Annual Review of Nuclear and Particle Science 70 (1) (2020) 355–394. doi:10.1146/annurev-nucl-050520-125911.
URL https://doi.org/10.1146/annurev-nucl-050520-125911

[40] B. Abbott, R. Abbott, T. Abbott, M. Abernathy, F. Acernese, K. Ackley, C. Adams, T. Adams, P. Addesso, R. Adhikari, et al., Observation of gravitational waves from

a binary black hole merger, Physical Review Letters 116 (6) (Feb 2016). doi:10.1103/physrevlett.116.061102.
URL http://dx.doi.org/10.1103/PhysRevLett.116.061102

[41] S. Bird, I. Cholis, J. B. Muñoz, Y. Ali-Haïmoud, M. Kamionkowski, E. D. Kovetz, A. Raccanelli, A. G. Riess, Did ligo detect dark matter?, Physical Review Letters 116 (20) (May 2016). doi:10.1103/physrevlett.116.201301.
URL http://dx.doi.org/10.1103/PhysRevLett.116.201301

[42] F. Huang, Z.-Y. Zhang, P.-N. Shen, W.-L. Wang, Is d∗ a candidate for a hexaquark-dominated exotic state?, Chinese Physics C 39 (7) (2015) 071001. doi:10.1088/1674-1137/39/7/071001.
URL https://doi.org/10.1088/1674-1137/39/7/071001

[43] G. R. Farrar, G. Zaharijas, Dark Matter and the Baryon Asymmetry of the Universe, 96 (4) (2006) 041302. arXiv:hep-ph/0510079, doi:10.1103/PhysRevLett.96.041302.
URL https://ui.adsabs.harvard.edu/abs/2006PhRvL..96d1302F

[44] M. Bashkanov, D. P. Watts, A new possibility for light-quark dark matter, Journal of Physics G: Nuclear and Particle Physics 47 (3) (2020) 03LT01. doi:10.1088/1361-6471/ab67e8.
URL https://doi.org/10.1088/1361-6471/ab67e8

[45] D. McComas, F. Allegrini, P. Bochsler, M. Bzowski, E. Christian, G. Crew, R. DeMajistre, H. Fahr, H. Fichtner, P. Frisch, et al., Global observations of the interstellar interaction from the interstellar boundary explorer (ibex), science 326 (5955) (2009) 959–962.

[46] Flavor conserving cp violation in invisible axion models, Nuclear Physics B 276 (1) (1986) 241–252. doi:https://doi.org/10.1016/0550-3213(86)90022-2.
URL https://www.sciencedirect.com/science/article/pii/0550321386900222

[47] R. D. Peccei, H. R. Quinn, CP conservation in the presence of pseudoparticles, Phys. Rev. Lett. 38 (1977) 1440–1443. doi:10.1103/PhysRevLett.38.1440.
URL https://link.aps.org/doi/10.1103/PhysRevLett.38.1440

[48] R. D. Peccei, H. R. Quinn, Constraints Imposed by CP Conservation in the Presence of Instantons, Phys. Rev. D 16 (1977) 1791–1797. doi:10.1103/PhysRevD.16.1791.

[49] A simple solution to the strong cp problem with a harmless axion, Physics Letters B 104 (3) (1981) 199–202. doi:https://doi.org/10.1016/0370-2693(81)90590-6.
URL https://www.sciencedirect.com/science/article/pii/0370269381905906

[50] S. Weinberg, A new light boson?, Phys. Rev. Lett. 40 (1978) 223–226. doi:10.1103/PhysRevLett.40.223.
URL https://link.aps.org/doi/10.1103/PhysRevLett.40.223

[51] L. Di Luzio, F. Mescia, E. Nardi, Window for preferred axion models, Physical Review D 96 (7) (Oct 2017). doi:10.1103/physrevd.96.075003.
URL http://dx.doi.org/10.1103/PhysRevD.96.075003

[52] M. Tanabashi, et al., Review of particle physics, Phys. Rev. D 98 (2018) 030001. doi:10.1103/PhysRevD.98.030001.
URL https://link.aps.org/doi/10.1103/PhysRevD.98.030001

[53] D. J. Marsh, Axion cosmology, Vol. 643, Elsevier BV, 2016, p. 1–79. doi:10.1016/j.physrep.2016.06.005.
URL http://dx.doi.org/10.1016/j.physrep.2016.06.005

[54] P. Sikivie, Q. Yang, Bose-Einstein Condensation of Dark Matter Axions, 103 (11) (2009) 111301. arXiv:0901.1106, doi:10.1103/PhysRevLett.103.111301.
URL https://ui.adsabs.harvard.edu/abs/2009PhRvL.103k1301S

[55] I. P. Stern, ADMX, A.-H. collaborations, Axion dark matter searches (2014). doi:10.1063/1.4883465.
URL http://dx.doi.org/10.1063/1.4883465

[56] P. W. Graham, I. G. Irastorza, S. K. Lamoreaux, A. Lindner, K. A. van Bibber, Experimental searches for the axion and axion-like particles, Annual Review of Nuclear and Particle Science 65 (1) (2015) 485–514. doi:10.1146/annurev-nucl-102014-022120.
URL http://dx.doi.org/10.1146/annurev-nucl-102014-022120

[57] H. Primakoff, Photoproduction of neutral mesons in nuclear electric fields and the mean life of the neutral meson, Phys. Rev. 81 (1951) 899. doi:10.1103/PhysRev.81.899.

[58] S. L. Adler, J. Gamboa, F. Méndez, J. López-Sarrión, Axions and "light shining through a wall": A detailed theoretical analysis, Annals of Physics 323 (11) (2008) 2851–2872. doi:10.1016/j.aop.2008.02.001.
URL http://dx.doi.org/10.1016/j.aop.2008.02.001

[59] D. Akerib, et al., First searches for axions and axionlike particles with the lux experiment, Physical Review Letters 118 (26) (Jun 2017). doi:10.1103/physrevlett.118.261301.
URL http://dx.doi.org/10.1103/PhysRevLett.118.261301

[60] A. Banfi, C. Englert, D. Maître, D. Cerdeno, C. Maxwell, N. K. (Ed.), Lecture notes for the 2016 hep school for experimental high energy physics students (2017).

[61] J. Buckley, et al., Cosmic frontier indirect dark matter detection working group summary (2013). arXiv:1310.7040.

[62] L. Bergström, Dark matter evidence, particle physics candidates and detection methods, Annalen der Physik 524 (9-10) (2012) 479–496. doi:10.1002/andp.201200116.
URL http://dx.doi.org/10.1002/andp.201200116

[63] H. Abdalla, A. Abramowski, F. Aharonian, F. Ait Benkhali, A. G. Akhperjanian, T. Andersson, E. O. Angüner, M. Arrieta, P. Aubert, et al., H.e.s.s. discovery of very high energy -ray emission from pks0625354, Monthly Notices of the Royal Astronomical Society 476 (3) (2018) 4187–4198. doi:10.1093/mnras/sty439.
URL http://dx.doi.org/10.1093/mnras/sty439

[64] H. Silverwood, C. Weniger, P. Scott, G. Bertone, A realistic assessment of the CTA sensitivity to dark matter annihilation, Journal of Cosmology and Astroparticle Physics 2015 (03) (2015) 055–055. doi:10.1088/1475-7516/2015/03/055.
URL https://doi.org/10.1088/1475-7516/2015/03/055

[65] S. Adrián-Martínez, A. Albert, M. André, G. Anton, M. Ardid, J.-J. Aubert, T. Avgitas, B. Baret, J. Barrios-Martí, S. Basa, et al., Limits on dark matter annihilation in the sun using the antares neutrino telescope, Physics Letters B 759 (2016)

69–74. doi:10.1016/j.physletb.2016.05.019.
URL http://dx.doi.org/10.1016/j.physletb.2016.05.019

[66] M. Aartsen, K. Abraham, M. Ackermann, J. Adams, J. Aguilar, M. Ahlers, M. Ahrens, D. Altmann, T. Anderson, I. Ansseau, et al., Improved limits on dark matter annihilation in the sun with the 79-string icecube detector and implications for supersymmetry, Journal of Cosmology and Astroparticle Physics 2016 (04) (2016) 022–022. doi:10.1088/1475-7516/2016/04/022.
URL http://dx.doi.org/10.1088/1475-7516/2016/04/022

[67] D. Hooper, L. Goodenough, Dark matter annihilation in the galactic center as seen by the fermi gamma ray space telescope, Physics Letters B 697 (5) (2011) 412–428. doi:https://doi.org/10.1016/j.physletb.2011.02.029.
URL https://www.sciencedirect.com/science/article/pii/S0370269311001742

[68] C. Weniger, A tentative gamma-ray line from dark matter annihilation at the fermi large area telescope, Journal of Cosmology and Astroparticle Physics 2012 (08) (2012) 007–007. doi:10.1088/1475-7516/2012/08/007.
URL http://dx.doi.org/10.1088/1475-7516/2012/08/007

[69] K. N. Abazajian, N. Canac, S. Horiuchi, M. Kaplinghat, Astrophysical and dark matter interpretations of extended gamma-ray emission from the galactic center, Physical Review D 90 (2) (Jul 2014). doi:10.1103/physrevd.90.023526.
URL http://dx.doi.org/10.1103/PhysRevD.90.023526

[70] R. Bartels, S. Krishnamurthy, C. Weniger, Strong support for the millisecond pulsar origin of the Galactic center GeV excess, Phys. Rev. Lett. 116 (5) (2016) 051102. arXiv:1506.05104, doi:10.1103/PhysRevLett.116.051102.

[71] O. Adriani, et al., Observation of an anomalous positron abundance in the cosmic radiation, Nature (2008).
URL https://arxiv.org/abs/0810.4995

[72] A. K. Harding, R. Ramaty, The Pulsar Contribution to Galactic Cosmic Ray Positrons, in: International Cosmic Ray Conference, Vol. 2 of International Cosmic Ray Conference, 1987, p. 92.
URL https://ui.adsabs.harvard.edu/abs/1987ICRC....2...92H

[73] I. Büsching, O. C. de Jager, M. S. Potgieter, C. Venter, A cosmic-ray positron anisotropy due to two middle-aged, nearby pulsars?, The Astrophysical Journal 678 (1) (2008) L39–L42. doi:10.1086/588465.
URL https://doi.org/10.1086/588465

[74] A. Abdo, et al., Constraints on cosmological dark matter annihilation from the fermi-lat isotropic diffuse gamma-ray measurement, Journal of Cosmology and Astroparticle Physics 2010 (04) (2010) 014–014. doi:10.1088/1475-7516/2010/04/014.
URL http://dx.doi.org/10.1088/1475-7516/2010/04/014

[75] T. Damour, L. M. Krauss, A New solar system population of WIMP dark matter, Phys. Rev. Lett. 81 (1998) 5726–5729. arXiv:astro-ph/9806165, doi:10.1103/PhysRevLett.81.5726.

[76] J. Edsjö, J. Elevant, R. Enberg, C. Niblaeus, Neutrinos from cosmic ray interactions in the sun, Journal of Cosmology and Astroparticle Physics 2017 (06) (2017) 033–033. doi:10.1088/1475-7516/2017/06/033.
URL http://dx.doi.org/10.1088/1475-7516/2017/06/033

[77] M. Srednicki, K. A. Olive, J. Silk, High-energy neutrinos from the sun and cold dark matter, Nuclear Physics B 279 (3) (1987) 804–823. doi:https://doi.org/10.1016/0550-3213(87)90020-4.
URL https://www.sciencedirect.com/science/article/pii/0550321387900204

[78] G. Jungman, M. Kamionkowski, K. Griest, Supersymmetric dark matter, Physics Reports 267 (5) (1996) 195–373. doi:https://doi.org/10.1016/0370-1573(95)00058-5.
URL https://www.sciencedirect.com/science/article/pii/0370157395000585

[79] C. P. de los Heros, Status of direct and indirect dark matter searches (2020). arXiv:2001.06193.

[80] M. Aaboud, G. Aad, B. Abbott, O. Abdinov, B. Abeloos, S. H. Abidi, O. S. AbouZeid, N. L. Abraham, H. Abramowicz, et al., Search for dark matter and other new phenomena in events with an energetic jet and large missing transverse momentum using the atlas detector, Journal of High Energy Physics 2018 (1) (Jan

2018). doi:10.1007/jhep01(2018)126.
URL http://dx.doi.org/10.1007/JHEP01(2018)126

[81] M. Aaboud, et al., Combination of searches for invisible higgs boson decays with the atlas experiment, Phys. Rev. Lett. 122 (2019) 231801. doi:10.1103/PhysRevLett.122.231801.
URL https://link.aps.org/doi/10.1103/PhysRevLett.122.231801

[82] M. J. Dolan, T. Ferber, C. Hearty, F. Kahlhoefer, K. Schmidt-Hoberg, Revised constraints and Belle II sensitivity for visible and invisible axion-like particles, Journal of High Energy Physics 2017 (12) (2017) 94. arXiv:1709.00009, doi:10.1007/JHEP12(2017)094.

[83] Review of mathematics, numerical factors, and corrections for dark matter experiments based on elastic nuclear recoil, Astroparticle Physics 6 (1) (1996) 87–112. doi:https://doi.org/10.1016/S0927-6505(96)00047-3.
URL https://www.sciencedirect.com/science/article/pii/S0927650596000473

[84] M. Ibe, W. Nakano, Y. Shoji, K. Suzuki, Migdal effect in dark matter direct detection experiments, Journal of High Energy Physics 2018 (3) (Mar 2018). doi:10.1007/jhep03(2018)194.
URL http://dx.doi.org/10.1007/JHEP03(2018)194

[85] S. Knirck, A. J. Millar, C. A. O'Hare, J. Redondo, F. D. Steffen, Directional axion detection, Journal of Cosmology and Astroparticle Physics 2018 (11) (2018) 051–051. doi:10.1088/1475-7516/2018/11/051.
URL http://dx.doi.org/10.1088/1475-7516/2018/11/051

[86] F. Mayet, et al., A review of the discovery reach of directional dark matter detection, Physics Reports 627 (2016) 1–49, a review of the discovery reach of directional Dark Matter detection. doi:https://doi.org/10.1016/j.physrep.2016.02.007.
URL https://www.sciencedirect.com/science/article/pii/S0370157316001022

[87] T. M. Undagoitia, L. Rauch, Dark matter direct-detection experiments, Journal of Physics G: Nuclear and Particle Physics 43 (1) (2015) 013001. doi:10.1088/0954-3899/43/1/013001.
URL http://dx.doi.org/10.1088/0954-3899/43/1/013001

[88] E. Aprile, J. Aalbers, F. Agostini, M. Alfonsi, L. Althueser, F. Amaro, M. Anthony, F. Arneodo, L. Baudis, B. Bauermeister, et al., Dark matter search results from a one ton-year exposure of xenon1t, Physical Review Letters 121 (11) (Sep 2018). doi:10.1103/physrevlett.121.111302.
URL http://dx.doi.org/10.1103/PhysRevLett.121.111302

[89] X. Cui, et al., Dark matter results from 54-ton-day exposure of pandax-ii experiment, Physical Review Letters 119 (18) (Oct 2017). doi:10.1103/physrevlett.119.181302.
URL http://dx.doi.org/10.1103/PhysRevLett.119.181302

[90] D. Akerib, S. Alsum, H. Araújo, X. Bai, et al., Results from a search for dark matter in the complete lux exposure, Physical Review Letters 118 (2) (Jan 2017). doi:10.1103/physrevlett.118.021303.
URL http://dx.doi.org/10.1103/PhysRevLett.118.021303

[91] R. Ajaj, et al., Search for dark matter with a 231-day exposure of liquid argon using deap-3600 at snolab, Physical Review D 100 (2) (Jul 2019). doi:10.1103/physrevd.100.022004.
URL http://dx.doi.org/10.1103/PhysRevD.100.022004

[92] P. Agnes, et al., Darkside-50 532-day dark matter search with low-radioactivity argon, Physical Review D 98 (10) (Nov 2018). doi:10.1103/physrevd.98.102006.
URL http://dx.doi.org/10.1103/PhysRevD.98.102006

[93] R. Agnese, et al., Results from the super cryogenic dark matter search experiment at soudan, Physical Review Letters 120 (6) (Feb 2018). doi:10.1103/physrevlett.120.061802.
URL http://dx.doi.org/10.1103/PhysRevLett.120.061802

[94] E. Aprile, et al., Light dark matter search with ionization signals in xenon1t, Physical Review Letters 123 (25) (Dec 2019). doi:10.1103/physrevlett.123.251801.
URL http://dx.doi.org/10.1103/PhysRevLett.123.251801

[95] P. Agnes, et al., Low-mass dark matter search with the darkside-50 experiment, Physical Review Letters 121 (8) (Aug 2018). doi:10.1103/physrevlett.121.081307.
URL http://dx.doi.org/10.1103/PhysRevLett.121.081307

[96] R. Agnese, et al., Low-mass dark matter search with cdmslite, Physical Review D 97 (2) (Jan 2018). doi:10.1103/physrevd.97.022002.
URL http://dx.doi.org/10.1103/PhysRevD.97.022002

[97] D. Akerib, et al., Extending light wimp searches to single scintillation photons in lux, Physical Review D 101 (4) (Feb 2020). doi:10.1103/physrevd.101.042001.
URL http://dx.doi.org/10.1103/PhysRevD.101.042001

[98] A. Abdelhameed, et al., First results from the cresst-iii low-mass dark matter program, Physical Review D 100 (10) (Nov 2019). doi:10.1103/physrevd.100.102002.
URL http://dx.doi.org/10.1103/PhysRevD.100.102002

[99] Q. Arnaud, et al., Optimizing edelweiss detectors for low-mass wimp searches, Physical Review D 97 (2) (Jan 2018). doi:10.1103/physrevd.97.022003.
URL http://dx.doi.org/10.1103/PhysRevD.97.022003

[100] R. Agnese, et al., First dark matter constraints from a supercdms single-charge sensitive detector, Physical Review Letters 121 (5) (Aug 2018). doi:10.1103/physrevlett.121.051301.
URL http://dx.doi.org/10.1103/PhysRevLett.121.051301

[101] C. E. Aalseth, et al., Darkside-20k: A 20 tonne two-phase lar tpc for direct dark matter detection at lngs, The European Physical Journal Plus 133 (3) (Mar 2018). doi:10.1140/epjp/i2018-11973-4.
URL http://dx.doi.org/10.1140/epjp/i2018-11973-4

[102] D. Akerib, et al., The lux-zeplin (lz) experiment, Nuclear Instruments and Methods in Physics Research Section A: Accelerators, Spectrometers, Detectors and Associated Equipment 953 (2020) 163047. doi:10.1016/j.nima.2019.163047.
URL http://dx.doi.org/10.1016/j.nima.2019.163047

[103] H. Zhang, A. Abdukerim, W. Chen, X. Chen, Y. Chen, X. Cui, B. Dong, D. Fang, C. Fu, K. Giboni, et al., Dark matter direct search sensitivity of the pandax-4t experiment, Science China Physics, Mechanics Astronomy 62 (3) (Aug 2018). doi:10.1007/s11433-018-9259-0.
URL http://dx.doi.org/10.1007/s11433-018-9259-0

[104] E. Aprile, et al., Physics reach of the XENON1t dark matter experiment., Journal of Cosmology and Astroparticle Physics 2016 (04) (2016) 027–027. doi:10.1088/1475-7516/2016/04/027.
URL https://doi.org/10.1088/1475-7516/2016/04/027

[105] J. Billard, E. Figueroa-Feliciano, L. Strigari, Implication of neutrino backgrounds on the reach of next generation dark matter direct detection experiments, Physical Review D 89 (2) (Jan 2014). doi:10.1103/physrevd.89.023524.
URL http://dx.doi.org/10.1103/PhysRevD.89.023524

[106] F. Ruppin, J. Billard, E. Figueroa-Feliciano, L. Strigari, Complementarity of dark matter detectors in light of the neutrino background, Physical Review D 90 (8) (Oct 2014). doi:10.1103/physrevd.90.083510.
URL http://dx.doi.org/10.1103/PhysRevD.90.083510

[107] E. Bagnaschi, K. Sakurai, M. Borsato, O. Buchmueller, M. Citron, J. C. Costa, A. De Roeck, M. J. Dolan, J. R. Ellis, H. Flächer, et al., Likelihood analysis of the pmssm11 in light of lhc 13-tev data, The European Physical Journal C 78 (3) (Mar 2018). doi:10.1140/epjc/s10052-018-5697-0.
URL http://dx.doi.org/10.1140/epjc/s10052-018-5697-0

[108] I. Samblas, A statistical framework for the characterisation of wimp dark matter with the lux-zeplin experiment, Ph.D. thesis (accessed June 30, 2020).
URL hhttps://spiral.imperial.ac.uk/handle/10044/1/76523

[109] J. Read, The local dark matter density, Journal of Physics G: Nuclear and Particle Physics 41 (6) (2014) 063101.

[110] R. Poole-McKenzie, A. S. Font, B. Boxer, I. G. McCarthy, S. Burdin, S. G. Stafford, S. T. Brown, Informing dark matter direct detection limits with the ARTEMIS simulations, Journal of Cosmology and Astroparticle Physics 2020 (11) (2020) 016–016. doi:10.1088/1475-7516/2020/11/016.
URL https://doi.org/10.1088/1475-7516/2020/11/016

[111] J. Buch, S. C. J. Leung, J. Fan, Using gaia dr2 to constrain local dark matter density and thin dark disk, Journal of Cosmology and Astroparticle Physics 2019 (04) (2019) 026–026. doi:10.1088/1475-7516/2019/04/026.
URL http://dx.doi.org/10.1088/1475-7516/2019/04/026

[112] J. F. Navarro, C. S. Frenk, S. D. M. White, A universal density profile from hierarchical clustering, The Astrophysical Journal 490 (2) (1997) 493–508. doi:10.1086/304888.
URL http://dx.doi.org/10.1086/304888

[113] A. K. Drukier, K. Freese, D. N. Spergel, Detecting cold dark-matter candidates, Phys. Rev. D 33 (1986) 3495–3508. doi:10.1103/PhysRevD.33.3495.
URL https://link.aps.org/doi/10.1103/PhysRevD.33.3495

[114] A. M. Green, Astrophysical uncertainties on the local dark matter distribution and direct detection experiments, Journal of Physics G: Nuclear and Particle Physics 44 (8) (2017) 084001. doi:10.1088/1361-6471/aa7819.
URL http://dx.doi.org/10.1088/1361-6471/aa7819

[115] J. Bland-Hawthorn, O. Gerhard, The galaxy in context: Structural, kinematic, and integrated properties, Annual Review of Astronomy and Astrophysics 54 (1) (2016) 529–596. doi:10.1146/annurev-astro-081915-023441.
URL http://dx.doi.org/10.1146/annurev-astro-081915-023441

[116] G. Monari, B. Famaey, I. Carrillo, T. Piffl, M. Steinmetz, R. F. G. Wyse, F. Anders, C. Chiappini, K. Janßen, The escape speed curve of the galaxy obtained from gaia dr2 implies a heavy milky way, Astronomy Astrophysics 616 (2018) L9. doi:10.1051/0004-6361/201833748.
URL http://dx.doi.org/10.1051/0004-6361/201833748

[117] A. J. Deason, A. Fattahi, V. Belokurov, N. W. Evans, R. J. J. Grand, F. Marinacci, R. Pakmor, The local high-velocity tail and the galactic escape speed, Monthly Notices of the Royal Astronomical Society 485 (3) (2019) 3514–3526. doi:10.1093/mnras/stz623.
URL http://dx.doi.org/10.1093/mnras/stz623

[118] N. W. Evans, C. A. J. O'Hare, C. McCabe, Shm^{++}: A refinement of the standard halo model for dark matter searches in light of the gaia sausage (2018). arXiv:1810.11468.

[119] L. Necib, M. Lisanti, V. Belokurov, Inferred evidence for dark matter kinematic substructure with sdss–gaia, The Astrophysical Journal 874 (1) (2019) 3. doi:10.3847/1538-4357/ab095b.
URL http://dx.doi.org/10.3847/1538-4357/ab095b

[120] N. Bozorgnia, A. Fattahi, C. S. Frenk, A. Cheek, D. G. Cerdeño, F. A. Gómez, R. J. Grand, F. Marinacci, The dark matter component of the gaia radially anisotropic substructure, Journal of Cosmology and Astroparticle Physics 2020 (07) (2020) 036–036. doi:10.1088/1475-7516/2020/07/036.
URL http://dx.doi.org/10.1088/1475-7516/2020/07/036

[121] R. H. Helm, Inelastic and elastic scattering of 187-mev electrons from selected even-even nuclei, Phys. Rev. 104 (1956) 1466–1475. doi:10.1103/PhysRev.104.1466.
URL https://link.aps.org/doi/10.1103/PhysRev.104.1466

[122] J. Hisano, Effective theory approach to direct detection of dark matter, Les Houches Lect. Notes 108 (2020). arXiv:1712.02947, doi:10.1093/oso/9780198855743.003.0011.

[123] H. Georgi, Effective field theory, Annual review of nuclear and particle science 43 (1) (1993) 209–252.
URL http://www.people.fas.harvard.edu/~hgeorgi/review.pdf

[124] C. P. Burgess, Introduction to Effective Field Theories and Inflation, Les Houches Lect. Notes 108 (2020). doi:10.1093/oso/9780198855743.003.0004.

[125] G. Buchalla, O. Catà, C. Krause, On the power counting in effective field theories, Physics Letters B 731 (2014) 80–86. doi:10.1016/j.physletb.2014.02.015.
URL http://dx.doi.org/10.1016/j.physletb.2014.02.015

[126] A. L. Fitzpatrick, W. Haxton, E. Katz, N. Lubbers, Y. Xu, The effective field theory of dark matter direct detection, Journal of Cosmology and Astroparticle Physics 2013 (02) (2013) 004–004. doi:10.1088/1475-7516/2013/02/004.
URL http://dx.doi.org/10.1088/1475-7516/2013/02/004

[127] N. Anand, A. L. Fitzpatrick, W. Haxton, E. Katz, N. Lubbers, Y. Xu, DMFormFactor Mathematica package, Version 6.0, https://www.ocf.berkeley.edu/~nanand/software/dmformfactor/ (2013–2015).

[128] G. Barello, S. Chang, C. A. Newby, A model independent approach to inelastic dark matter scattering, Physical Review D 90 (9) (Nov 2014). doi:10.1103/physrevd.90.094027.
URL http://dx.doi.org/10.1103/PhysRevD.90.094027

[129] D. Smith, N. Weiner, Inelastic dark matter, Physical Review D 64 (4) (Jul 2001). doi:10.1103/physrevd.64.043502.
URL http://dx.doi.org/10.1103/PhysRevD.64.043502

[130] P. W. Graham, R. Harnik, S. Rajendran, P. Saraswat, Exothermic dark matter, Physical Review D 82 (6) (Sep 2010). doi:10.1103/physrevd.82.063512.
URL http://dx.doi.org/10.1103/PhysRevD.82.063512

[131] N. Larsen, An effective field theory analysis of the first lux dark matter search, Ph.D. thesis, Yale University (2016).

[132] D. Ma, M. Hossain, A. Chow, M. Arshad, R. M. Battson, R. D. Sanders, H. Mehmet, A. D. Edwards, N. P. Franks, M. Maze, Xenon and hypothermia combine to provide neuroprotection from neonatal asphyxia, Annals of neurology 58 (2) (2005) 182–193. doi:https://doi.org/10.1002/ana.20547.

[133] B. Drayer, S. Wolfson, O. Reinmuth, M. Dujovny, M. Boehnke, E. Cook, Xenon enhanced ct for analysis of cerebral integrity, perfusion, and blood flow., Stroke 9 (2) (1978) 123–130. doi:https://doi.org/10.1161/01.str.9.2.123.

[134] T. Yamashita, Y. Nagatsugu, H. Ishihara, Y. Shiroyama, Y. Wakuta, S. Kashiwagi, Comparison of xe-ct/cbf and quantitative ecd-spelt, Acta Neurologica Scandinavica 93 (1996) 6–9. doi:https://doi.org/10.1111/j.1600-0404.1996.tb00531.x.

[135] V. Chepel, M. Lopes, A. Kuchenkov, R. Ferreira Marques, A. Policarpo, Performance study of liquid xenon detector for pet, Nuclear Instruments and Methods in Physics Research Section A: Accelerators, Spectrometers, Detectors and Associated Equipment 392 (1) (1997) 427–432, position-Sensitive Detectors Conference 1996. doi:https://doi.org/10.1016/S0168-9002(97)00196-4.
URL https://www.sciencedirect.com/science/article/pii/S0168900297001964

[136] L. Gallego Manzano, et al., Xemis: A liquid xenon detector for medical imaging, Nuclear Instruments and Methods in Physics Research Section A: Accelerators, Spectrometers, Detectors and Associated Equipment 787 (2015) 89–93, new Developments in Photodetection NDIP14. doi:https://doi.org/10.1016/j.nima.2014.11.040.
URL https://www.sciencedirect.com/science/article/pii/S016890021401328X

[137] N. G. Basov, V. A. Danilychev, Y. M. Popov, Stimulated emission in the vacuum ultraviolet region, Soviet Journal of Quantum Electronics 1 (1) (1971) 18–22. doi:10.1070/qe1971v001n01abeh003011.
URL https://doi.org/10.1070/qe1971v001n01abeh003011

[138] V. Chepel, H. Araújo, Liquid noble gas detectors for low energy particle physics, Journal of Instrumentation 8 (04) (2013) R04001–R04001. doi:10.1088/1748-0221/8/04/r04001.
URL https://doi.org/10.1088/1748-0221/8/04/r04001

[139] E. Lifshitz, LD, S. L. (JB), Quantum Mechanics; Non-relativistic Theory, Pergamon Press, 1965. doi:https://doi.org/10.2307/3610674.

[140] D. Akerib, et al., Results of a search for sub-gev dark matter using 2013 lux data, Physical Review Letters 122 (13) (Apr 2019). doi:10.1103/physrevlett.122.131301.
URL http://dx.doi.org/10.1103/PhysRevLett.122.131301

[141] E. Aprile, et al., Search for light dark matter interactions enhanced by the migdal effect or bremsstrahlung in xenon1t, Physical Review Letters 123 (24) (Dec 2019). doi:10.1103/physrevlett.123.241803.
URL http://dx.doi.org/10.1103/PhysRevLett.123.241803

[142] T. Takahashi, S. Konno, T. Hamada, M. Miyajima, S. Kubota, A. Nakamoto, A. Hitachi, E. Shibamura, T. Doke, Average energy expended per ion pair in liquid xenon, Phys. Rev. A 12 (1975) 1771–1775. doi:10.1103/PhysRevA.12.1771.
URL https://link.aps.org/doi/10.1103/PhysRevA.12.1771

[143] S. Kubota, M. Hishida, J. Raun, Evidence for a triplet state of the self-trapped exciton states in liquid argon, krypton and xenon, Journal of Physics C: Solid State Physics 11 (12) (1978) 2645–2651. doi:10.1088/0022-3719/11/12/024.
URL https://doi.org/10.1088/0022-3719/11/12/024

[144] T. Doke, A. Hitachi, J. Kikuchi, K. Masuda, H. Okada, E. Shibamura, Absolute scintillation yields in liquid argon and xenon for various particles, Japanese Journal of Applied Physics 41 (Part 1, No. 3A) (2002) 1538–1545. doi:10.1143/jjap.41.1538.
URL https://doi.org/10.1143/jjap.41.1538

[145] C. E. Dahl, The physics of background discrimination in liquid xenon, and first results from Xenon10 in the hunt for WIMP dark matter, Ph.D. thesis, Princeton University (Jun. 2009).
URL https://ui.adsabs.harvard.edu/abs/2009PhDT.....3D

[146] E. Aprile, T. Doke, Liquid xenon detectors for particle physics and astrophysics, Reviews of Modern Physics 82 (3) (2010) 2053–2097. doi:10.1103/revmodphys.82.2053.
URL http://dx.doi.org/10.1103/RevModPhys.82.2053

[147] J. Meija, et al., Commission on atomic weights and isotopic abundances report for the international union of pure and applied chemistry (2016). doi:https://doi.org/10.1515/pac-2015-0503.

[148] R. Platzman, Total ionization in gases by high-energy particles: An appraisal of our understanding, The International Journal of Applied Radiation and Isotopes 10 (2) (1961) 116–127. doi:https://doi.org/10.1016/0020-708X(61)90108-9.
URL https://www.sciencedirect.com/science/article/pii/0020708X61901089

[149] U. Rössler, Interpretation of far uv spectra in solid rare gases from calculated density of states, physica status solidi (b) 45 (2) (1971) 483–491. doi:https://doi.org/10.1002/pssb.2220450211.

[150] W. Shockley, Problems related to p-n junctions in silicon, Solid-State Electronics 2 (1) (1961) 35–67. doi:https://doi.org/10.1016/0038-1101(61)90054-5.
URL https://www.sciencedirect.com/science/article/pii/0038110161900545

[151] T. Doke, A. Hitachi, S. Kubota, A. Nakamoto, T. Takahashi, Estimation of fano factors in liquid argon, krypton, xenon and xenon-doped liquid argon, Nuclear Instruments and Methods 134 (2) (1976) 353–357. doi:https://doi.org/10.1016/0029-554X(76)90292-5.
URL https://www.sciencedirect.com/science/article/pii/0029554X76902925

[152] R. A. Muller, S. E. Derenzo, G. Smadja, D. B. Smith, R. G. Smits, H. Zaklad, L. W. Alvarez, Liquid-Filled Proportional Counter, 27 (8) (1971) 532–535. doi:10.1103/PhysRevLett.27.532.

[153] S. E. Derenzo, T. S. Mast, H. Zaklad, R. A. Muller, Electron avalanche in liquid xenon, Phys. Rev. A 9 (1974) 2582–2591. doi:10.1103/PhysRevA.9.2582.

[154] A. Lansiart, A. Seigneur, J.-L. Moretti, J.-P. Morucci, Development research on a highly luminous condensed xenon scintillator, Nuclear Instruments and Methods 135 (1) (1976) 47–52. doi:https://doi.org/10.1016/0029-554X(76)90824-7.
URL https://www.sciencedirect.com/science/article/pii/0029554X76908247

[155] T. Doke, Recent developments of liquid xenon detectors, Nuclear Instruments and Methods in Physics Research 196 (1) (1982) 87–96. doi:https://doi.org/10.1016/0029-554X(82)90621-8.
URL https://www.sciencedirect.com/science/article/pii/0029554X82906218

[156] S. Suzuki, T. Doke, A. Hitachi, A. Yunoki, K. Masuda, T. Takahashi, Photoionization effect in liquid xenon doped with triethylamine (tea) or trimethylamine (tma), Nuclear Instruments and Methods in Physics Research Section A: Accelerators, Spectrometers, Detectors and Associated Equipment 245 (1) (1986) 78–81. doi:https://doi.org/10.1016/0168-9002(86)90260-3.
URL https://www.sciencedirect.com/science/article/pii/0168900286902603

[157] H. Wang, Xenon as a detector for dark matter search, Physics Reports 307 (1) (1998) 263–267. doi:https://doi.org/10.1016/S0370-1573(98)00058-1.
URL https://www.sciencedirect.com/science/article/pii/S0370157398000581

[158] S. Kubota, M. Hishida, M. Suzuki, J.-Z. Ruan, Dynamical behavior of free electrons in the recombination process in liquid argon, krypton, and xenon, Physics Review B 20 (8) (1979) 3486–3496. doi:10.1103/PhysRevB.20.3486.
URL https://ui.adsabs.harvard.edu/abs/1979PhRvB..20.3486K

[159] W. H. Lippincott, K. J. Coakley, D. Gastler, A. Hime, E. Kearns, D. N. McKinsey, J. A. Nikkel, L. C. Stonehill, Scintillation time dependence and pulse shape discrimination in liquid argon, 78 (3) (2008) 035801. arXiv:0801.1531, doi:10.1103/PhysRevC.78.035801.

[160] J. Lindhard, M. Scharff, H. E. Schioett, RANGE CONCEPTS AND HEAVY ION RANGES (NOTES ON ATOMIC COLLISIONS, II), Vol. 33, 1963.
URL https://www.osti.gov/biblio/4153115

[161] J. N. Marx, D. R. Nygren, The Time Projection Chamber, Phys. Today 31N10 (1978) 46–53. doi:10.1063/1.2994775.

[162] M. Schenk, Studies with a liquid argon time projection chamber: Addressing technological challenges of large-scale detectors, 2015. doi:10.1007/978-3-658-09430-0.

[163] C. Rubbia, The Liquid Argon Time Projection Chamber: A New Concept for Neutrino Detectors (5 1977).
URL http://cdsweb.cern.ch/record/117852/files/CERN-EP-INT-77-8.pdf

[164] K. Kleinknecht, Detectors for Particle Radiation, 1999.
URL https://ui.adsabs.harvard.edu/abs/1999dpr..book.....K

[165] H. Cao, A study of nuclear recoils in Liquid Argon Time Projection Chamber for the direct detection of WIMP dark matter, Ph.D. thesis, Princeton U. (2014). doi:10.2172/1182552.

[166] B. J. Mount, et al., LUX-ZEPLIN (LZ) Technical Design Report, Tech. rep. (3 2017). arXiv:1703.09144.

[167] J. Thomas, D. A. Imel, Recombination of electron-ion pairs in liquid argon and liquid xenon, Phys. Rev. A 36 (1987) 614–616. doi:10.1103/PhysRevA.36.614.
URL https://link.aps.org/doi/10.1103/PhysRevA.36.614

[168] T. Doke, et al., Let dependence of scintillation yields in liquid argon, Nuclear Instruments and Methods in Physics Research Section A: Accelerators, Spectrometers, Detectors and Associated Equipment 269 (1) (1988) 291–296. doi:https://doi.org/10.1016/0168-9002(88)90892-3.
URL https://www.sciencedirect.com/science/article/pii/0168900288908923

[169] R. Davis, D. S. Harmer, K. C. Hoffman, Search for neutrinos from the sun, Phys. Rev. Lett. 20 (1968) 1205–1209. doi:10.1103/PhysRevLett.20.1205.
URL https://link.aps.org/doi/10.1103/PhysRevLett.20.1205

[170] J. Heise, The sanford underground research facility at homestake, AIP Publishing LLC, 2014. doi:10.1063/1.4883449.
URL http://dx.doi.org/10.1063/1.4883449

[171] F. Gray, C. Ruybal, J. Totushek, D.-M. Mei, K. Thomas, C. Zhang, Cosmic ray muon flux at the sanford underground laboratory at homestake, Nuclear Instruments and Methods in Physics Research Section A: Accelerators, Spectrometers, Detectors and Associated Equipment 638 (1) (2011) 63–66. doi:10.1016/j.nima.2011.02.032.
URL http://dx.doi.org/10.1016/j.nima.2011.02.032

[172] D. Robertson, M. Couder, U. Greife, F. Strieder, M. Wiescher, Underground nuclear astrophysics studies with CASPAR, in: European Physical Journal Web of Conferences, Vol. 109 of European Physical Journal Web of Conferences, 2016, p. 09002. doi:10.1051/epjconf/201610909002.

[173] D. Akerib, et al., The large underground xenon (lux) experiment, Nuclear Instruments and Methods in Physics Research Section A: Accelerators, Spectrometers, Detectors and Associated Equipment 704 (2013) 111–126. doi:10.1016/j.nima.2012.11.135.
URL http://dx.doi.org/10.1016/j.nima.2012.11.135

[174] M. Collaboration, The MAJORANA DEMONSTRATOR neutrinoless double-beta decay experiment (2013). arXiv:1308.1633.

[175] D. Akerib, C. Akerlof, D. Akimov, S. Alsum, H. Araújo, I. Arnquist, M. Arthurs, X. Bai, A. Bailey, J. Balajthy, et al., Identification of radiopure titanium for the lz dark matter experiment and future rare event searches, Astroparticle Physics 96 (2017) 1–10. doi:10.1016/j.astropartphys.2017.09.002.
URL http://dx.doi.org/10.1016/j.astropartphys.2017.09.002

[176] F. Neves, A. Lindote, A. Morozov, V. Solovov, C. Silva, P. Bras, J. Rodrigues, M. Lopes, Measurement of the absolute reflectance of polytetrafluoroethylene (ptfe) immersed in liquid xenon, Journal of Instrumentation 12 (01) (2017) P01017–P01017. doi:10.1088/1748-0221/12/01/p01017.
URL http://dx.doi.org/10.1088/1748-0221/12/01/P01017

[177] K. Lung, K. Arisaka, A. Bargetzi, P. Beltrame, A. Cahill, T. Genma, C. Ghag, D. Gordon, J. Sainz, A. Teymourian, et al., Characterization of the hamamatsu

r11410-10 3-in. photomultiplier tube for liquid xenon dark matter direct detection experiments, Nuclear Instruments and Methods in Physics Research Section A: Accelerators, Spectrometers, Detectors and Associated Equipment 696 (2012) 32–39. doi:10.1016/j.nima.2012.08.052.
URL http://dx.doi.org/10.1016/j.nima.2012.08.052

[178] D. Akerib, X. Bai, E. Bernard, A. Bernstein, A. Bradley, D. Byram, S. Cahn, M. Carmona-Benitez, D. Carr, J. Chapman, et al., An ultra-low background pmt for liquid xenon detectors, Nuclear Instruments and Methods in Physics Research Section A: Accelerators, Spectrometers, Detectors and Associated Equipment 703 (2013) 1–6. doi:10.1016/j.nima.2012.11.020.
URL http://dx.doi.org/10.1016/j.nima.2012.11.020

[179] D. Akerib, C. Akerlof, S. Alsum, H. Araújo, M. Arthurs, X. Bai, A. Bailey, J. Balajthy, S. Balashov, D. Bauer, et al., Projected wimp sensitivity of the lux-zeplin (lz) dark matter experiment, arXiv preprint arXiv:1802.06039 (2018).

[180] M. Yeh, A. Garnov, R. Hahn, Gadolinium-loaded liquid scintillator for high-precision measurements of antineutrino oscillations and the mixing angle, 13, Nuclear Instruments and Methods in Physics Research Section A: Accelerators, Spectrometers, Detectors and Associated Equipment 578 (1) (2007) 329 – 339. doi:https://doi.org/10.1016/j.nima.2007.03.029.
URL http://www.sciencedirect.com/science/article/pii/S0168900207006511

[181] F. An, A. Balantekin, H. Band, M. Bishai, S. Blyth, D. Cao, G. Cao, J. Cao, W. Cen, Y. Chan, et al., Measurement of electron antineutrino oscillation based on 1230 days of operation of the daya bay experiment, Physical Review D 95 (7) (Apr 2017). doi:10.1103/physrevd.95.072006.
URL http://dx.doi.org/10.1103/PhysRevD.95.072006

[182] D. Akerib, H. Araújo, X. Bai, A. Bailey, J. Balajthy, E. Bernard, A. Bernstein, A. Bradley, D. Byram, S. Cahn, et al., Radiogenic and muon-induced backgrounds in the lux dark matter detector, Astroparticle Physics 62 (2015) 33–46. doi:10.1016/j.astropartphys.2014.07.009.
URL http://dx.doi.org/10.1016/j.astropartphys.2014.07.009

[183] D. Akerib, H. Araújo, X. Bai, A. Bailey, J. Balajthy, P. Beltrame, E. Bernard, A. Bernstein, T. Biesiadzinski, E. Boulton, et al., Chromatographic separation of radioactive noble gases from xenon, Astroparticle Physics 97 (2018) 80–87. doi:10.1016/j.astropartphys.2017.10.014.
URL http://dx.doi.org/10.1016/j.astropartphys.2017.10.014

[184] D. Akimov, J. B. Albert, P. An, C. Awe, P. S. Barbeau, B. Becker, V. Belov, A. Brown, A. Bolozdynya, B. Cabrera-Palmer, et al., Observation of coherent elastic neutrino-nucleus scattering, Science 357 (6356) (2017) 1123–1126. doi:10.1126/science.aao0990.
URL http://dx.doi.org/10.1126/science.aao0990

[185] F. Hasert, et al., Observation of neutrino-like interactions without muon or electron in the gargamelle neutrino experiment, Physics Letters B 46 (1) (1973) 138 – 140. doi:https://doi.org/10.1016/0370-2693(73)90499-1.
URL http://www.sciencedirect.com/science/article/pii/0370269373904991

[186] L. W. Kastens, S. B. Cahn, A. Manzur, D. N. McKinsey, Calibration of a liquid xenon detector withkr83m, Physical Review C 80 (4) (Oct 2009). doi:10.1103/physrevc.80.045809.
URL http://dx.doi.org/10.1103/PhysRevC.80.045809

[187] W. Taylor, Lux-Zeplin Collaboration, D-D Neutron Generator Calibrations and Hardware in the LUX-ZEPLIN Dark Matter Search Experiment, in: APS April Meeting Abstracts, Vol. 2016 of APS Meeting Abstracts, 2016, p. C16.007.
URL https://ui.adsabs.harvard.edu/abs/2016APS..APRC16007T

[188] adelphitech.com, DD-108M Neutron Generator Operation Manual (accessed Dec 15 2020).
URL http://www.adelphitech.com

[189] L. Collaboration, D. S. Akerib, S. Alsum, H. M. Araújo, X. Bai, A. J. Bailey, J. Balajthy, P. Beltrame, E. P. Bernard, et al., Low-energy (0.7-74 kev) nuclear recoil calibration of the lux dark matter experiment using d-d neutron scattering kinematics (2016). arXiv:1608.05381.

[190] C. Faham, V. Gehman, A. Currie, A. Dobi, P. Sorensen, R. Gaitskell, Measurements of wavelength-dependent double photoelectron emission from single photons

in vuv-sensitive photomultiplier tubes, Journal of Instrumentation 10 (09) (2015) P09010–P09010. doi:10.1088/1748-0221/10/09/p09010.
URL http://dx.doi.org/10.1088/1748-0221/10/09/P09010

[191] C. Silva, J. Pinto da Cunha, A. Pereira, V. Chepel, M. I. Lopes, V. Solovov, F. Neves, Reflectance of polytetrafluoroethylene for xenon scintillation light, Journal of Applied Physics 107 (6) (2010) 064902. doi:10.1063/1.3318681.
URL http://dx.doi.org/10.1063/1.3318681

[192] B. López Paredes, H. Araújo, F. Froborg, N. Marangou, I. Olcina, T. Sumner, R. Taylor, A. Tomás, A. Vacheret, Response of photomultiplier tubes to xenon scintillation light, Astroparticle Physics 102 (2018) 56–66. doi:10.1016/j.astropartphys.2018.04.006.
URL http://dx.doi.org/10.1016/j.astropartphys.2018.04.006

[193] D. Akerib, S. Alsum, H. Araújo, X. Bai, A. Bailey, J. Balajthy, P. Beltrame, E. Bernard, A. Bernstein, T. Biesiadzinski, et al., Signal yields, energy resolution, and recombination fluctuations in liquid xenon, Physical Review D 95 (1) (Jan 2017). doi:10.1103/physrevd.95.012008.
URL http://dx.doi.org/10.1103/PhysRevD.95.012008

[194] E. M. Gushchin, A. A. Kruglov, V. V. Litskevich, A. N. Lebedev, I. M. Obodovskiĭ, S. V. Somov, Electron emission from condensed noble gases, Soviet Journal of Experimental and Theoretical Physics 49 (1979) 856.
URL https://ui.adsabs.harvard.edu/abs/1979JETP...49..856G

[195] G. Cowan, K. Cranmer, E. Gross, O. Vitells, Power-constrained limits (2011). arXiv:1105.3166.

[196] D. Akerib, C. Akerlof, A. Alqahtani, S. Alsum, T. Anderson, N. Angelides, H. Araújo, J. Armstrong, M. Arthurs, X. Bai, et al., Simulations of events for the lux-zeplin (lz) dark matter experiment, Astroparticle Physics 125 (2021) 102480. doi:10.1016/j.astropartphys.2020.102480.
URL http://dx.doi.org/10.1016/j.astropartphys.2020.102480

[197] W. Turner, A. Baxter, H. J. Birch, B. Boxer, S. Burdin, E. Fraser, A. Greenall, S. Powel, P. Sutcliffe, Optical calibration system for the lux-zeplin (lz) outer detector (2021). arXiv:2102.06281.

[198] sinogerman.brinkster.net, BL–LBVB5N15C Series Datasheet (accessed May 14, 2019).
URL http://sinogerman.brinkster.net/brite-led/PDF/BL-LBVB5N15C%20series%20datasheet.pdf

[199] W. Beriguete, et al., Production of a gadolinium-loaded liquid scintillator for the daya bay reactor neutrino experiment, Nuclear Instruments and Methods in Physics Research Section A: Accelerators, Spectrometers, Detectors and Associated Equipment 763 (2014) 82 – 88. doi:https://doi.org/10.1016/j.nima.2014.05.119.
URL http://www.sciencedirect.com/science/article/pii/S0168900214006834

[200] hamamatsu.com, Hamamatsu S5971 Datasheet (accessed May 14, 2019).
URL https://www.hamamatsu.com/resources/pdf/ssd/s5971_etc_kpin1025e.pdf

[201] ti.com, Burr-Brown IVC102 Datasheet (accessed May 14, 2019).
URL https://www.ti.com/lit/ds/symlink/ivc102.pdf?ts=1609745841820

[202] i fiberoptics.com, Mitsubishi Chemicals, Super Eska Duplex Optical Fiber Cable (accessed February 1, 2019).
URL https://i-fiberoptics.com/fiber-detail.php?id=15&sum=80

[203] R. Alves, et .al, The calibration system for the photomultiplier array of the SNO+ experiment, Journal of Instrumentation (JINST) 10 (2015) 03002. arXiv:1411.4830.

[204] D. S. Akerib, et al., Constraints on Effective Field Theory Couplings Using 311.2 days of LUX Data (2021). arXiv:2102.06998.

[205] D. S. Akerib, et al., Radio-assay of titanium samples for the lux experiment (2012). arXiv:1112.1376.

[206] M. Szydagis, et al., Noble element simulation technique (Jun. 2020). doi:10.5281/zenodo.3905382.
URL https://doi.org/10.5281/zenodo.3905382

[207] D. Akerib, et al., Improved modeling of β electronic recoils in liquid xenon using lux calibration data, Journal of Instrumentation 15 (02) (2020) T02007–T02007.

doi:10.1088/1748-0221/15/02/t02007.
URL http://dx.doi.org/10.1088/1748-0221/15/02/T02007

[208] D. S. A. et al., An effective field theory analysis of the first lux dark matter search (2020). arXiv:2003.11141.

[209] Multiphysics software for optimizing designs. arXiv:https://www.comsol.com/.
URL https://www.comsol.com/

[210] D. Akerib, et al., 3d modeling of electric fields in the LUX detector, Journal of Instrumentation 12 (11) (2017) P11022–P11022. doi:10.1088/1748-0221/12/11/p11022.
URL https://doi.org/10.1088/1748-0221/12/11/p11022

[211] D. S. Akerib, et al., Tritium calibration of the lux dark matter experiment, Phys. Rev. D 93 (2016) 072009. doi:10.1103/PhysRevD.93.072009.
URL https://link.aps.org/doi/10.1103/PhysRevD.93.072009

[212] D. S. Akerib, et al., Improved measurements of the β-decay response of liquid xenon with the lux detector, Phys. Rev. D 100 (2019) 022002. doi:10.1103/PhysRevD.100.022002.
URL https://link.aps.org/doi/10.1103/PhysRevD.100.022002

[213] D. S. Akerib, S. Alsum, H. M. Araújo, X. Bai, A. J. Bailey, J. Balajthy, P. Beltrame, E. P. Bernard, et al., ^{83m}Kr calibration of the 2013 lux dark matter search, Phys. Rev. D 96 (2017) 112009. doi:10.1103/PhysRevD.96.112009.
URL https://link.aps.org/doi/10.1103/PhysRevD.96.112009

[214] M. Szydagis, N. Barry, K. Kazkaz, J. Mock, D. Stolp, M. Sweany, M. Tripathi, S. Uvarov, N. Walsh, M. Woods, NEST: a comprehensive model for scintillation yield in liquid xenon, Journal of Instrumentation 6 (10) (2011) P10002–P10002. doi:10.1088/1748-0221/6/10/p10002.
URL https://doi.org/10.1088/1748-0221/6/10/p10002

[215] P. Sorensen, C. E. Dahl, Nuclear recoil energy scale in liquid xenon with application to the direct detection of dark matter, Physical Review D 83 (6) (Mar 2011). doi:10.1103/physrevd.83.063501.
URL http://dx.doi.org/10.1103/PhysRevD.83.063501

[216] J. R. Klein, A. Roodman, Blind analysis in nuclear and particle physics, Annual Review of Nuclear and Particle Science 55 (1) (2005) 141–163. arXiv:https://doi.org/10.1146/annurev.nucl.55.090704.151521, doi:10.1146/annurev.nucl.55.090704.151521.
URL https://doi.org/10.1146/annurev.nucl.55.090704.151521

[217] E. Aprile, et al., Dark matter results from 225 live days of xenon100 data, Physical Review Letters 109 (18) (Nov 2012). doi:10.1103/physrevlett.109.181301.
URL http://dx.doi.org/10.1103/PhysRevLett.109.181301

[218] R. Agnese, et al., Search for low-mass weakly interacting massive particles with supercdms, Physical Review Letters 112 (24) (Jun 2014). doi:10.1103/physrevlett.112.241302.
URL http://dx.doi.org/10.1103/PhysRevLett.112.241302

[219] V. N. Lebedenko, et al., Results from the first science run of the zeplin-iii dark matter search experiment, Physical Review D 80 (5) (Sep 2009). doi:10.1103/physrevd.80.052010.
URL http://dx.doi.org/10.1103/PhysRevD.80.052010

[220] D. Akerib, et al., Position reconstruction in LUX, Journal of Instrumentation 13 (02) (2018) P02001–P02001.
URL https://doi.org/10.1088/1748-0221/13/02/p02001

[221] E. Aprile, et al., Xenon1t dark matter data analysis: Signal and background models and statistical inference, Phys. Rev. D 99 (2019) 112009. doi:10.1103/PhysRevD.99.112009.
URL https://link.aps.org/doi/10.1103/PhysRevD.99.112009

[222] E. Aprile, et al., Effective field theory search for high-energy nuclear recoils using the xenon100 dark matter detector, Physical Review D 96 (4) (Aug 2017). doi:10.1103/physrevd.96.042004.
URL http://dx.doi.org/10.1103/PhysRevD.96.042004

[223] J. Neyman, Outline of a Theory of Statistical Estimation Based on the Classical Theory of Probability, Phil. Trans. Roy. Soc. Lond. A 236 (767) (1937) 333–380. doi:10.1098/rsta.1937.0005.

[224] G. Cowan, K. Cranmer, E. Gross, O. Vitells, Asymptotic formulae for likelihood-based tests of new physics, The European Physical Journal C 71 (2) (Feb 2011). doi:10.1140/epjc/s10052-011-1554-0.
URL http://dx.doi.org/10.1140/epjc/s10052-011-1554-0

[225] E. Aprile, et al., First dark matter search results from the xenon1t experiment, Physical Review Letters 119 (18) (Oct 2017). doi:10.1103/physrevlett.119.181301.
URL http://dx.doi.org/10.1103/PhysRevLett.119.181301

[226] W. Verkerke, D. Kirkby, The roofit toolkit for data modeling (07 2003). doi:10.1142/9781860948985_0039.

[227] L. Moneta, K. Belasco, K. Cranmer, S. Kreiss, A. Lazzaro, D. Piparo, G. Schott, W. Verkerke, M. Wolf, The roostats project (2011). arXiv:1009.1003.